MINISTÉRIO DA EDUCAÇÃO
UNIVERSIDADE FEDERAL DO RIO GRANDE DO SUL
PROGRAMA DE PÓS-GRADUAÇÃO EM ENGENHARIA MECÂNICA

# EXPERIMENTAL CHARACTERIZATION AND CONSTITUTIVE MODELING OF VISCOPLASTIC EFFECTS IN HIGH STRAIN-RATE DEFORMATION OF POLYCRYSTALLINE FCC METALS

por

Tiago dos Santos

Tese para obtenção do Título de

Doutor em Engenharia

Porto Alegre, dezembro de 2016

EXPERIMENTAL CHARACTERIZATION AND CONSTITUTIVE MODELING OF VISCOPLASTIC EFFECTS IN HIGH STRAIN-RATE DEFORMATION OF POLYCRYSTALLINE FCC METALS

por

Tiago dos Santos
Mestre em Engenharia Mecânica

Tese submetida ao Programa de Pós-Graduação em Engenharia Mecânica, da Escola de Engenharia da Universidade Federal do Rio Grande do Sul, como parte dos requisitos necessários para a obtenção do Título de

Doutor em Engenharia

Área de concentração: Mecânica dos Sólidos

Orientador: Prof. Dr. Rodrigo Rossi

Coorientador: Prof. Dr. Samir Maghous

Aprovada por:

Prof.ª Dr.ª Cintia C. Petry Mazzaferro (PROMEC/UFRGS - Porto Alegre - Brasil)

Prof. Dr. Jakson Manfredini Vassoler (PROMEC/UFRGS - Porto Alegre - Brasil)

Prof. Dr. Eduardo Bittencourt (PPGEC/UFRGS - Porto Alegre - Brasil)

Prof. Dr. Miguel Vaz Júnior (PPGEM/UDESC - Joinville - Brasil)

Prof. Dr. Jakson Manfredini Vassoler
Coordenador do PROMEC

Porto Alegre, 02 de dezembro de 2016

*The man who cannot occasionally imagine events and conditions of existence that are contrary to the causal principle as he knows it will never enrich his science by the addition of a new idea.*

Max Planck (1858-1947)

## AGRADECIMENTOS

Primeiramente agradeço a Deus, à minha família e amigos. Especialmente aos meus pais Miguel e Marivete por todo apoio, suporte e valores que me trouxeram até aqui. Agradeço às minhas avós Eleide e Mafalda, e ao meu tio Luis Carlos por toda a ajuda e amizade. Um especial agradecimento à minha companheira Érica, por todo amor, companheirismo, compreensão e apoio constantes. Gostaria de agradecer à CAPES (Coordenação de Aperfeiçoamento de Pessoal de Nível Superior) pelo suporte financeiro durante o curso de doutorado. Especificamente ao PDSE (Programa de Doutorado Sanduíche no Exterior) sob o processo de número BEX 7023/15-4. Gostaria de agradecer ao meu orientador Professor Rodrigo Rossi, pelas grandes oportunidades, pelo desafio e confiança, permanente orientação, ajuda e amizade durante todo o tempo que estamos trabalhando juntos. Agradeço ao meu coorientador Professor Samir Maghous, por aceitar participar na realização deste trabalho, por sua constante orientação, ajuda e amizade ao longo de todo este período. Agradeço ao Professor Pedro Rosa do Instituto Superior Técnico de Lisboa pela acolhida durante meu período de doutorado sanduíche em Portugal, pela disposição, entusiasmo e empenho na realização desta tese, pela orientação e amizade. Agradeço também aos meus colegas de laboratório portugueses Leandro Fernandes, Alcino Reis e Olivier Marques pelo companheirismo e amizade. Em especial ao Leandro, pela valiosa ajuda na realização das atividades experimentais. Sou grato aos meus colegas do PROMEC/UFRGS pela amizade e companheirismo. Principalmente ao Gustavo Ramos, Martin Geier, Rudimar Mazzochi e Gilmar Mazzochi. Em especial ao Gustavo, com o qual tiver o prazer de conviver durante grande parte do meu curso de mestrado e também de doutorado. Agradeço aos professores membros da comissão de avaliação pelas valiosas contribuições quanto ao desenvolvimento do presente trabalho.

## RESUMO

O presente trabalho tem como objetivo a caracterização experimental e modelagem constitutiva do comportamento de metais CFC (Cúbicos de Face Centrada) policristalinos quando submetidos a altas taxas de deformação. O material empregado no desenvolvimento do trabalho é uma liga de alumínio comercialmente pura: o alumínio AA1050. No âmbito da presente investigação, os experimentos são conduzidos à temperatura ambiente. O desenvolvimento experimental tem por objetivo evidenciar as principais características constitutivas que descrevem o comportamento macroscópico desta classe de metais quando submetidos a processos de deformação envolvendo altas taxas de deformação: (i) o endurecimento induzido pela deformação; (ii) o endurecimento induzido pela taxa de deformação; e (iii) a sensibilidade instantânea em relação à taxa de deformação. Para a caracterização de cada uma destes aspectos constitutivos, são realizados experimentos específicos utilizando equipamentos desenvolvidos, em sua maioria, no contexto da presente investigação. De forma geral, os experimentos consistem em ensaios de compressão envolvendo uma ampla faixa de taxas de deformação, variando desde condições *quasi*-estáticas a taxas na ordem de $10^4\,\mathrm{s}^{-1}$. Os resultados experimentais, juntamente com evidências experimentais macro e microscópicas disponíveis na literatura, dão suporte ao desenvolvimento de um modelo constitutivo elasto-viscoplástico. A formulação constitutiva segue uma abordagem semi-física, na qual a escolha das variáveis inelásticas e proposição de suas regras de evolução são qualitativamente guiadas por considerações metalúrgicas baseadas no acúmulo e organização de discordâncias. O modelo proposto, embora consista em uma abordagem simplificada quando comparado a modelos de base física, é capaz de representar separadamente cada uma das características constitutivas destacadas anteriormente. Com base nos resultados experimentais aqui obtidos, o modelo elasto-viscoplástico proposto é então ajustado e posteriormente validado. Na sequência é desenvolvida a formulação numérica relacionada ao modelo proposto. A abordagem como um todo é inserida em um contexto de deformações finitas seguindo uma descrição Lagrangiana Total. O desenvolvimento numérico descreve o procedimento utilizado para solução de problemas de equilíbrio não lineares seguindo uma formulação incremental implícita empregando o método dos elementos finitos. Em um contexto local, é utilizado um esquema de integração implícito seguindo um mapeamento exponencial. A linearização das equações de mapeamento de retorno possibilita a derivação analítica do módulo tangente consistente. O modelo constitutivo, bem como o procedimento numérico, são utilizados para a solução de problemas numéricos clássicos como: ensaio de compressão em condições de deformações homogêneas, e compressão envolvendo contato com atrito. As simulações numéricas avaliam tanto a capacidade constitutiva do modelo proposto em descrever o comportamento de estruturas quando deformadas sob condições envolvendo

elevadas taxas de deformação, quanto à eficiência do procedimento numérico a partir de análises de convergência. Em conclusão, com o procedimento experimental adotado é possível evidenciar as principais características macroscópicas inerentes ao comportamento de metais quando submetidos a processos de deformação envolvendo altas velocidades. Além disso, com base nos resultados analíticos e numéricos, observa-se que o modelo constitutivo proposto é capaz de reproduzir de forma satisfatória os comportamentos evidenciados experimentalmente.

Palavras-chave: Caracterização experimental; Altas taxas de deformação; Deformações Finitas; Materiais elasto-viscoplásticos; Modelagem numérica.

**ABSTRACT**

The present work aims at performing the experimental characterization and constitutive modeling associated with the mechanical behavior of polycrystalline FCC (Face Centered Cubic) metals when subjected to high strain-rate deformations. The material to be employed in the experiments is a commercially pure aluminum alloy: aluminum AA1050. Within the present investigation context, experiments are performed at room temperatures. The primary objective of the laboratory experiments is to assess the main constitutive features associated with the macroscopic mechanical behavior observed for FCC metals subjected to high strain-rate deformation processes: (i) strain-hardening; (ii) strain-rate-hardening; and (iii) instantaneous rate-sensitivity. In order to characterize each constitutive feature, experiments using equipments specifically devised to achieve the objectives are performed. The laboratory investigation consists of compression tests involving a wide strain-rate range, from quasi-static conditions to strain-rates of the order of $10^4\,\mathrm{s}^{-1}$. Experimental results together with micro and macroscopic experimental evidences available in the literature give support to the development of a elastic-viscoplastic model. The stress-strain formulation follows a semi-physical approach, in which inelastic variables and their evolution equations are qualitatively motivated by metallurgical considerations based on the storage and arrangement of dislocations. Although its simplified nature when compared to physically-based models, the proposed model is capable of representing separately each one of the constitutive features highlighted early. In addition, in analogy to the stress-strain proposition, a model describing the material hardness evolution in terms of strain and strain-rate histories is also provided. Based on the obtained experimental results, the proposed elastic-viscoplastic and hardness evolution models are adjusted and then validated. The corresponding stress-strain numerical formulation is developed in a subsequent step. The approach as a whole is integrated into finite strain framework following a Total Lagrangian description. The procedure employed to solve nonlinear equilibrium problem follows an implicit incremental formulation implemented in the context of the finite element method. At a local level, an implicit integration scheme based on an exponential mapping is adopted. From linearization of return mapping equations, an analytical consistent tangent modulus is obtained. Both constitutive model and numerical approach are employed to simulated classical problems: a compression test involving homogeneous deformation and a compression test involving contact and frictional conditions. Numerical simulations evaluate the constitutive capabilities associated with the proposed model when predicting the structural behavior at high strain-rate loadings. Furthermore, numerical efficiency and robustness related to the present procedure are also assessed by means of convergence analysis. While the adopted experimental procedure gave fundamental evidences of the main macroscopic features inherent in the metallic

material behavior when subjected to high strain-rate deformations, the analytical and numerical results demonstrated that the proposed constitutive model is able to suitably reproduce the observed behavior.

Key-words: Experimental characterization; High strain-rates; Finite strains; Elastic-viscoplastic materials; Numerical modeling.

## CONTENTS

## LIST OF FIGURES

## LIST OF TABLES

## LIST OF SYMBOLS

### Roman scalar, vector, and tensor symbols

| | |
|---|---|
| $A$ | Isotropic hardening variable, Pa |
| $A_1$ | Isotropic hardening variable associated with Stages II and III, Pa |
| $A_2$ | Isotropic hardening variable associated with Stage IV, Pa |
| $A_\infty$ | Rate-dependent nonlinear hardening saturation parameter, Pa |
| $A_\infty^{lwr}$ | Lower reference value of $A_\infty$, Pa |
| $A_\infty^{up}$ | Upper reference value of $A_\infty$, Pa |
| $\bar{A}_\infty$ | Effective strain-rate-history dependent value of $A_\infty$, Pa |
| $A_{HAB}$ | Hardening due to high angle GNBs, Pa |
| $A_{LAB}$ | Hardening due to low angle boundaries (IDBs and GNBs), Pa |
| $A_s$ | Current cross section area of the compression specimem, $m^2$ |
| $b$ | Magnitude of Burgers vector, m |
| $B$ | Damping coefficient associated with dislocation drag, Pa.s |
| $\boldsymbol{b}$ | Body force vector in the current configuration, $N/m^3$ |
| $\bar{\boldsymbol{b}}$ | Body force vector in the reference configuration, $N/m^3$ |
| $c$ | Linear hardening-rate parameter |
| $c_p$ | Specific heat at constant pressure, J/(kg.K) |
| $\boldsymbol{C}$ | Right Cauchy-Green strain tensor, m/m |
| $d$ | Current specimen diameter, m |
| $d_0$ | Initial specimen diameter, m |
| $\bar{d}$ | Mean distance traveled by a mobile dislocation, m |
| $d_r$ | Spacing between short-range barriers, m |
| $d_{sr}$ | Width of a short-range barrier, m |
| $D_C$ | Average size of low angle dislocation cells, m |

| | |
|---|---|
| $D_{GNB}$ | Spacing between geometrically necessary boundaries, m |
| $D_{HAB}$ | Average spacing between high angle boundaries, m |
| $D_{IDB}$ | Spacing between incidental dislocation boundaries, m |
| $\boldsymbol{D}$ | Strain-rate tensor given in the current configuration, 1/s |
| $\bar{\boldsymbol{D}}$ | Strain-rate tensor in the intermediate configuration, 1/s |
| $e$ | Specific internal energy in the reference configuration, J/kg |
| $E$ | Young modulus, Pa |
| $\boldsymbol{E} = \boldsymbol{E}^{(0)}$ | Hencky strain tensor, m/m |
| $f\left(\bar{\boldsymbol{\tau}}, A\right)$ | Yield function, Pa |
| $F$ | Current compression force applied to the specimen, N |
| $\boldsymbol{F}$ | Deformation gradient tensor, m/m |
| $G_0$ | Total thermal activation energy, J |
| $\Delta G$ | Thermal activation energy supplied by a given temperature, J |
| $\bar{H}$ | Hardening modulus associated with $\alpha_1$, Pa |
| $\tilde{H}$ | Hardening modulus associated with $\alpha_2$, Pa |
| $H_V$ | Material microhardness (Vickers indenter), Pa |
| $\boldsymbol{I}$ | Second-order identity tensor |
| $\mathbb{I}$ | Forth-order identity tensor |
| $J$ | Deformation Jacobian, $m^3/m^3$ |
| $k$ | Boltzmann constant, J/K |
| $K$ | Kinetic energy of the body $\mathcal{B}$, J |
| $l$ | Current specimen length, m |
| $l_0$ | Initial specimen length, m |
| $\boldsymbol{l}_i$ | Vector of Lagragian principal directions of strain |
| $l_d$ | Length of a mobile dislocation, m |

| | |
|---|---|
| $\boldsymbol{L}$ | Velocity gradient tensor given in the current configuration, 1/s |
| $\bar{\boldsymbol{L}}$ | Velocity gradient tensor in the intermediate configuration, 1/s |
| $m$ | Rate-sensitivity parameter |
| $M$ | Taylor factor: from 2.4 to 3.2 for FCC metals, Pa |
| $n_d$ | Dimension of the vector field considered |
| $n_e$ | Number of finite elements |
| $n_{int}$ | Number of internal variables |
| $n_n$ | Number of nodes of a finite element |
| $n_N$ | Number of nodes of the global FE mesh |
| $N$ | Number of time subintervals |
| $N_A$ | Derivative of yield function $f$ with respect to $A$ |
| $N_i^{(e)}(\boldsymbol{X})$ | Interpolation function of the element $(e)$ associated with the node $i$ |
| $N_i^g(\boldsymbol{X})$ | Global interpolation function associated with the global node $i$ |
| $\boldsymbol{n}$ | Unit outward normal vector in the current configuration |
| $\boldsymbol{N}$ | Unit outward normal vector in the reference configuration |
| $\boldsymbol{N}_{\bar{\boldsymbol{\tau}}}$ | Derivative of yield function $f$ with respect to tensor $\bar{\boldsymbol{\tau}}$ |
| $O_{(\cdot)}$ | Vicinity of point $(\cdot)$ |
| $P$ | Spatial point |
| $P_0$ | Material point |
| $\boldsymbol{P}$ | First Piola-Kirchhoff stress tensor, Pa |
| $\boldsymbol{P}^S$ | Second Piola-Kirchhoff stress tensor, Pa |
| $Q$ | Heat received by the body $\mathcal{B}$, J/s |
| $\bar{\boldsymbol{q}}$ | Heat flux in the reference configuration, J/(s.m$^2$) |
| $\bar{r}$ | Heat generation in the reference configuration, J/(kg.s) |
| $R(A)$ | Yield domain radius, Pa |

| | |
|---|---|
| $\boldsymbol{R}$ | Rotation tensor |
| $s$ | Specific internal entropy in the reference configuration, J/(kg.K) |
| $s_i$ | Specific entropy production rate in the reference configuration, J/(kg.K) |
| $S$ | Internal entropy of the body $\mathcal{B}$ (state function), J/K |
| $S_i$ | Entropy produced in the body $\mathcal{B}$ (irreversible part of $S$), J/K |
| $S_r$ | Entropy supplied to the body $\mathcal{B}$ (reversible part of $S$), J/K |
| $t$ | Current time instant, s |
| $t_0$ | Initial time instant, s |
| $t_f$ | Final time instant, s |
| $t_n$ | Initial time instant of incremental time interval, s |
| $t_{n+1}$ | Final instant of incremental time interval, s |
| $t_r$ | Running time of a mobile dislocation, s |
| $t_w$ | Waiting time of a mobile dislocation, s |
| $\boldsymbol{t}$ | Traction vector in the current configuration, $\mathrm{N/m^2}$ |
| $\bar{\boldsymbol{t}}$ | Traction vector in the reference configuration, $\mathrm{N/m^2}$ |
| $U$ | Internal energy of the body $\mathcal{B}$, J |
| $\boldsymbol{u}$ | Displacement vector, m |
| $\bar{\boldsymbol{u}}$ | Prescribed displacement vector, m |
| $\boldsymbol{U}$ | Right stretch tensor, m/m |
| $\bar{v}_d$ | Mean velocity of a mobile dislocation, m/s |
| $\bar{v}_r$ | Mean running velocity of a mobile dislocation, m/s |
| $V^*$ | Activation volume, $\mathrm{m^3}$ |
| $\boldsymbol{V}$ | Left stretch tensor |
| $\dot{w}_0$ | Rate of work per unit of volume, $\mathrm{J/(s.m^3)}$ |
| $W$ | Work done on the body $\mathcal{B}$, J |

| | |
|---|---|
| $\boldsymbol{W}$ | Spin tensor in the current configuration, 1/s |
| $\bar{\boldsymbol{W}}$ | Spin tensor in the intermediate configuration, 1/s |
| $\boldsymbol{x}$ | Current position vector, m |
| $\boldsymbol{X}$ | Reference position vector, m |

**Greek scalar, vector, and tensor symbols**

| | |
|---|---|
| $\alpha$ | Isotropic hardening internal variable, m/m |
| $\alpha_1$ | Internal variable associated with Stages II and III, m/m |
| $\alpha_2$ | Internal variable associated with Stage IV, m/m |
| $\boldsymbol{\alpha}$ | Set of $n_{int}$ internal variables |
| $\beta_{TQ}$ | Taylor-Quinney coefficient |
| $\beta_i\left(\dot{\varepsilon}\right)$ | Rate-dependent parameter related to $\delta$ and $A_\infty$ |
| $\delta$ | Rate-dependent nonlinear hardening-rate parameter |
| $\delta^{lwr}$ | Lower reference value of $\delta$ |
| $\delta^{up}$ | Upper reference value of $\delta$ |
| $\delta_{ij}$ | Kronecker's delta |
| $\varepsilon$ | Accumulated viscoplastic strain, m/m |
| $\dot{\varepsilon}_{up}, \dot{\varepsilon}_{lwr}$ | Upper and lower reference strain-rates, 1/s |
| $\vartheta$ | Viscosity parameter of Perzyna and Peric models, s |
| $\vartheta_1, \vartheta_2$ | Viscosity parameters of modified Peric model, s |
| $\boldsymbol{\eta}$ | Virtual displacement vector, m |
| $\Phi_0$ | Dissipation per unit of reference volume, J/(s.m$^3$) |
| $\phi$ | Flow potential, Pa |
| $\boldsymbol{\varphi}$ | Deformation mapping function |
| $\boldsymbol{\varphi}_t$ | Deformation mapping functions for a given time instant $t$ |
| $\kappa$ | Bulk modulus, Pa |

| | |
|---|---|
| $\dot{\lambda}$ | Viscoplastic multiplier, 1/s |
| $\lambda_i^e$ | Eigenvalues of $\boldsymbol{U}^e$, m/m |
| $\Delta\lambda$ | Incremental viscoplastic multiplier, m/m |
| $\mu$ | Shear modulus, Pa |
| $\nu$ | Poisson coefficient |
| $\omega$ | Frequency at which a thermal energy $\Delta G$ is supplied, rad/s |
| $\omega_0$ | Frequency of the thermal oscillation of a dislocation, rad/s |
| $\Omega$ | Open current domain |
| $\Omega_0$ | Open reference domain |
| $\bar{\Omega}$ | Closed current domain |
| $\bar{\Omega}_0$ | Closed reference domain |
| $\partial\Omega$ | Current domain boundary |
| $\partial\Omega_0$ | Reference domain boundary |
| $\partial\Omega^u$ | Essential boundary in the current configuration |
| $\partial\Omega_0^u$ | Essential boundary in the reference configuration |
| $\partial\Omega^t$ | Natural boundary in the current configuration |
| $\partial\Omega_0^t$ | Natural boundary in the reference configuration |
| $\Omega_0^{(e)}$ | Reference domain of the finite element $(e)$ |
| $\psi$ | Specific Helmholtz free-energy per unit of reference volume, J/kg |
| $\rho$ | Specific mass in the current configuration, kg/m$^3$ |
| $\rho_0$ | Specific mass in the reference configuration, kg/m$^3$ |
| $\rho_d$ | Density of dislocations m/m$^3$ |
| $\rho_m$ | Density of mobile dislocations m/m$^3$ |
| $\sigma_{flow}$ | Unidimensional flow stress, Pa |
| $\sigma_v$ | Viscous stress due to thermal activation mechanisms, Pa |

| | |
|---|---|
| $\sigma_{vd}$ | Viscous stress due to dislocation drag, Pa |
| $\sigma_y$ | Initial yield stress, Pa |
| $\boldsymbol{\tau}$ | Kirchhoff stress tensor, Pa |
| $\bar{\boldsymbol{\tau}}$ | Rotated Kirchhoff stress tensor, Pa |
| $\theta$ | Absolute temperature, K |
| $\theta_{GNB}$ | Misorientations angle of geometrically necessary boundaries, rad |
| $\theta_{IDB}$ | Misorientations angle of incidental dislocation boundaries, rad |
| $\theta_{mis}$ | Misorientations angle of dislocation boundaries, rad |
| $\Theta\left(\langle f \rangle, A\right)$ | Overstress function |
| $\Theta^{-1}\left(\dot{\lambda}, A\right)$ | Inverse of the overstress function |
| $\xi_i$ | Parameter of function $\beta_i\left(\dot{\varepsilon}\right)$ |

**Roman fourth-order tensor symbols**

| | |
|---|---|
| $\mathbb{D}^e$ | Hyperelastic modulus, Pa |
| $\mathbb{D}_{n+1}$ | Material dependent term of modulus $\tilde{\mathbb{D}}_{n+1}$, Pa |
| $\tilde{\mathbb{D}}_{n+1}$ | Consistent tangent operator, Pa |
| $\mathbb{M}$ | Continuum tangent modulus, Pa |
| $\mathbb{M}_{n+1}$ | Consistent tangent modulus, Pa |
| $\mathbb{P}_{n+1}, \mathbb{Q}_{n+1}$ | Geometric terms of modulus $\tilde{\mathbb{D}}_{n+1}$, m/m |

**Roman set and space symbols**

| | |
|---|---|
| $\mathcal{B}$ | Deformable continuum body |
| $\mathcal{I}$ | Time interval of interest |
| $\mathcal{K}$ | Set of kinematically admissible displacements |
| $\mathcal{M}^n$ | Set of every quadratic tensor of order $n$ |
| $\mathcal{M}^n_+$ | Set of every non-singular quadratic tensor of order $n$ |
| $\mathcal{O}^n_+$ | Set of every proper orthogonal tensor of order $n$ |

| | |
|---|---|
| $\mathcal{R}^n$ | Euclidean space of order $n$ |
| $\mathcal{R}_{>0}$ | Set of positive real numbers |
| $\mathcal{R}_{\geq 0}$ | Space of non-negative real numbers |
| $\mathcal{S}^n$ | Set of every symmetric tensor of order $n$ |
| $\mathcal{S}^n_>$ | Set of every symmetric, positive, definite tensor of order $n$ |
| $\mathcal{V}$ | Set of kinematically admissible virtual displacements |
| $\bar{\mathcal{Y}}$ | Closed yield domain |
| $\partial\mathcal{Y}$ | Yield surface |

**Roman functional symbols**

| | |
|---|---|
| $\mathscr{R}(\boldsymbol{u}, \boldsymbol{\eta})$ | Virtual work functional, J |

**Roman FEM matrix notation**

| | |
|---|---|
| $\mathsf{A}$ | FE assembling operator |
| $\vec{\eta}$ | Global vector of nodal virtual displacements, m |
| $\vec{f}_{ext}$ | Global vector of nodal external forces, N |
| $\vec{f}^{(e)}_{ext}$ | Local vector of nodal external forces, N |
| $\vec{f}_{int}$ | Global vector of nodal internal forces, N |
| $\vec{f}^{(e)}_{int}$ | Local vector of nodal internal forces, N |
| $\mathsf{G}^g$ | Global FE gradient operator, 1/m |
| $\mathsf{G}^{(e)}$ | Local FE gradient operator, 1/m |
| $\mathsf{K}_T$ | Global tangent stiffness matrix, N/m |
| $\mathsf{K}^{(e)}_T$ | Local tangent stiffness matrix, N/m |
| $\mathsf{N}^g$ | Global interpolation matrix |
| $\mathsf{N}^{(e)}$ | Local interpolation matrix |
| $\vec{P}$ | Global vector containing firts P-K stress values, Pa |
| $\vec{u}$ | Global vector of nodal displacements, m |

**Math Operators, subscripts, and superscripts**

| | |
|---|---|
| $\det(\cdot)$ | Determinant operator |
| $Dg(u)[x]$ | Directional derivative of $g$ at $u$ in the direction of $x$ |
| $\mathrm{div}_{\boldsymbol{X}}(\cdot)$ | Material divergent operator, 1/m |
| $\mathrm{div}_{\boldsymbol{x}}(\cdot)$ | Spatial divergent operator, 1/m |
| $\exp(\cdot)$ | Exponential operator |
| $\nabla_{\boldsymbol{X}}(\cdot)$ | Material gradient operator, 1/m |
| $\nabla_{\boldsymbol{x}}(\cdot)$ | Spatial gradient operator, 1/m |
| ${}^{h}(\cdot)$ | FEM approximation of field $(\cdot)$ |
| $\Delta(\cdot)$ | Increment of $(\cdot)$ |
| $(\cdot)^{-1}$ | Inverse operator |
| $\ln(\cdot)$ | Natural logarithm operator |
| $(\cdot)^{e}$ | Elastic part of $(\cdot)$ |
| $(\cdot)^{vp}$ | Viscoplastic part of $(\cdot)$ |
| $(\cdot)_{\infty}$ | Saturation value of $(\cdot)$ |
| $\dot{(\cdot)} = \frac{D}{Dt}(\cdot)$ | Material derivative operator, 1/s |
| $(t_n, t_{n+1}]$ | Incremental time interval |
| $\mathrm{tr}(\cdot)$ | Trace operator |
| $(\cdot)^{T}$ | Transpose operator |
| $(\cdot)^{D}$ | Deviatoric part of stress tensor $(\cdot)$ |
| $(\cdot)_{d}$ | Deviatoric part of strain tensor $(\cdot)$ |
| $(\cdot)^{k}$ | Value of $(\cdot)$ at iteration $k$ |
| $(\cdot)^{k+1}$ | Value of $(\cdot)$ at iteration $k+1$ |
| $(\cdot)_{n}$ | Value of $(\cdot)$ at $t_n$ |
| $(\cdot)_{n+1}$ | Value of $(\cdot)$ at $t_{n+1}$ |

| | |
|---|---|
| $\|\cdot\|$ | Euclidean norm |
| $(\cdot)_{n+1}^{trial}$ | Trial elastic value of $(\cdot)$ at $t_{n+1}$ |
| $(\cdot)_v$ | Volumetriv part of strain tensor $(\cdot)$ |
| $(\cdot)_i$ | Initial value of $(\cdot)$ |

# 1 INTRODUCTION

In many engineering applications, metallic materials and structures are subjected to extreme straining and loading-rate conditions. These service conditions are present in many manufacturing processes, such as high speed machining [Neugebauer et al., 2011; Silva et al., 2014] (Figure 1(a)), forming [Geier et al., 2014], and compaction of metallic components [Mamalis et al., 2004; dos Santos et al., 2015a]. In addition, high strain-rates are also observed in analysis of structural crashworthiness in the automotive and aerospace industries, terminal ballistics research for safety and military activities, among several others. Examples of typical structures of aerospace, automotive, military/civil engineering, oil and gas, and naval industries activities [Rodríguez-Martínez, 2010; Rusinek and Jankowiak, 2014] are shown in Figures 1.1(b)-(g), respectively. In summary, high strain-rates are present in a large variety of modern industrial processes.

Although high speed machining is widely diffused in metal industry, this kind of manufacturing processes are still matter of recent investigations, aiming at predicting cutting efforts, designing machining tools, describing characteristics associated with finished products, such as surface quality and residual stresses in machined surfaces [Neugebauer et al., 2011; Miguélez et al., 2013; Wang et al., 2015]. The aerospace industry is constantly seeking for new materials capable of supporting high velocity conditions (and high temperature variations) while allowing for aircraft mass reduction [Arias et al., 2014]. The employment of materials for energy absorption in impact applications is an important subject associated with the automotive designing. This topic is directly related to passenger security issues and also to governmental costs due to traffic-accidents. In the military or safety industries, strength materials capable of absorbing impact energy are of great importance for armor designing and ballistic applications. In civil engineering activities, materials and structures experience dynamic conditions when they are exposed, for instance, to seismic events. In structural design activities related to oil and gas industries, it is necessary to account for accidental loadings due to collisions and falling objects, explosions and fragments penetrations [Rodríguez-Martínez, 2010], or process involving dynamic rupture of pipelines [Mirzaei et al., 2015]. In addition to those (mechanical, civil, aerospace, naval,...) engineering applications, deformation processes involving high velocities have proved to be a useful alternative in activities associated with materials design and processing. For example, in plastic deformation-induced grain-refinement processes, there are evidences that, for a given straining level, increasing the imposed strain-rate results in smaller grains. This feature allows increasing both ductility and strength of worked material [Zhang and Shim, 2010; Huang and Tao, 2011; Luo et al., 2012b].

In addition to reducing production time, other advantages can be verified by employing high velocities in manufacturing processes. For example, by increasing the cutting-speed


Figure 1.1: Engineering applications in which metallic alloys can be subjected to wide strain and strain-rate ranges during service or accidental conditions. (a) High speed machining processes; (b) Aerospace industry; (c) Automotive industry; (d) Military applications; (e) Civil engineering applications; (f) Oil and gas (offshore) industries; (g) Naval industry. Source: Rodríguez-Martínez, 2010.

in machining processes, a better surface quality can be reached in machined components [Korkut et al., 2004; Lima et al., 2005]. In processes as cold stamping, bending, or forging, an increase in strain-rate allows plastically processing materials with low formability, or consequently reducing the number of forming steps and thus the number of tools involved in the process [Orava, 1973; Ma et al., 2014]. However, due to higher efforts, increasing the deformation velocity demands the utilization of more robust and powerful machines, what clearly increases the cost of equipments. Furthermore, high velocity operation conditions induce higher vibrations and tool wear, what leads to an increase in frequency of machine stops for maintenance. In addition, higher vibrations and wave propagations difficult the utilization of data acquisition systems to monitor desired process parameters.

The significant increase in engineering applications involving extreme mechanical loading conditions, such as severe plastic deformations and high strain-rates, has motivated

many investigations concerning to dynamic behavior of metals. Although many efforts and resources have been focused in such investigations, there are many subjects which are still matter of discussion in academic and industrial environments. However, investigations have generally evidenced that material response (in terms of flow[1] stress, yield stress, or material hardness, for example) is strongly influenced by the associated deformation-history experienced by the material. Deformation-history, in addition to associated strain path, includes both strain-rate and temperature histories [Zener and Hollomon, 1944; Klepaczko, 1975; Chiem and Duffy, 1983; Tanner and McDowell, 1999; Rodríguez-Martínez et al., 2011]. Moreover, an increase in flow stress rate-sensitivity is evidenced when imposed strain-rate exceeds values of $10^3\,\mathrm{s}^{-1}$ [Lindholm, 1964; Campbell, 1972; Follansbee and Kocks, 1988; Gao and Zhang, 2012]. These aspects concerning material behavior depending on past deformation-histories, and instantaneous rate-sensitivity are better discussed in Section 1.3.

In general, investigations on the dynamic behavior of metals aim at simulating manufacturing processes or engineering applications in which those extreme conditions in terms of straining, loading-rate, and temperature are evidenced. However, these simulations require to be able of predicting the material behavior under desired service conditions. For this purpose two major challenges have to be overcome. The first one is associated with experimental characterization of material behavior under high strain-rate loading conditions. This task depends directly on the ability of designing laboratory machines which are capable of reproducing the conditions and of acquiring quantities of interest associated with a given deformation process. The second challenge is related to choose or propose suitable constitutive models, which are able of predicting material response evidenced experimentally. As it will be shown latter, both experimental and constitutive issues are still subject of recent investigations in the current literature.

Motivated by the large number of engineering applications involving high velocity plastic deformation of metallic materials, and in order to contribute on the two major challenges cited above, the present work has the aim of performing both experimental characterization and constitutive modeling of *quasi*-static and high strain-rate mechanical behavior of polycrystalline FCC metals under finite strain conditions at room temperature. Specifically, the material chosen for the study is an aluminum AA1050 (99.5% wt) in an annealed condition. It is worth mentioning that commercially pure aluminum, in addition to be widely employed in many applications as in manufacturing of equipments for chemical and food industries, can be taken as a reference material for subsequent analysis of more complex alloys employed in high strength structural applications, as in automotive, aerospace, naval, and military industries. Based on the preceding proposal,

[1]Throughout the present work a differentiation between flow and yield stress is considered. Flow stress refers to the overall stress response, i.e., it comprises the contribution due to current material strength and due to instantaneous strain-rate and temperature effects. In contrast, term yield stress refers to current material strength, which results from the current material microstructure.

the principal objectives related to the present study are outlined in the following.

## 1.1 Objectives

The main goal of the present work is to perform both experimental and constitutive characterization of mechanical behavior of polycrystalline FCC metals, specifically the aluminum AA1050, considering large strain cold deformations in a wide strain-rate range.

### 1.1.1 Specific objectives

In order to comply with the main goal, specific tasks have to be achieved:

- Performing the mechanical characterization of an aluminum AA1050 by means of compression and microhardness tests. During compressions, specimens have to be subjected to finite strains performed at strain-rates covering a wide range: from *quasi*-static conditions to strain-rates in the order of $10^4\,\mathrm{s}^{-1}$;
- From experiments, evidencing the main constitutive features associated with high strain-rate mechanical behavior of polycrystalline FCC metals under finite strains and at room temperature:
  - (i) *strain-hardening* will be evidenced by means of *quasi*-static compressions;
  - (ii) *strain-rate-hardening* will be evidenced by means of incremental compressions, considering distinct constant strain-rates (from $10^{-2}\,\mathrm{s}^{-1}$ to $1.1\times10^4\,\mathrm{s}^{-1}$), and microhardness tests performed between each deformation increment;
  - (iii) *instantaneous rate-sensitivity* will be characterized by continuous compressions under moderate strains at strain-rates from $10^{-2}\,\mathrm{s}^{-1}$ to $4\times10^3\,\mathrm{s}^{-1}$, where instantaneous flow stress is monitored;
- Evidencing strain-rate-history effects on both material hardening and material hardness evolution by means of sequential strain-rate experiments: decremental strain-rate tests, and strain-rate jump tests;
- Considering obtained experimental evidences, as well as macroscopic and microscopic data available in the literature, proposing an isothermal semi-physical[2] elastic-viscoplastic model, within a finite strain framework, capable of representing

[2]Term *semi-physical* can be used to designate phenomenological models which take into account for microstructural changes by introducing internal variables which do not correspond directly to physical identities (e.g., dislocation densities), but they are seen as effective microstructural features, whose hardening contribution and corresponding evolution are qualitatively based upon metallurgical and experimental results obtained from previous physically-based investigations [Molinari and Ravichandran, 2005; Rusinek and Jankowiak, 2014]. Along the present work, term *semi-physical model* is equivalent to terms *phenomenological model* and *simplified model*, in reference to the corresponding physical simplification employed by this kind of constitutive approach.

obtained experimental results reasoning on preceding constitutive features: strain-hardening, strain-rate-hardening, and instantaneous rate-sensitivity;

- Proposing an alternative constitutive formulation for directly modeling the effects of strain and strain-rate histories on the material hardness evolution. This alternative proposition is intended to model engineering applications in which the material hardness has to be predicted or monitored;

- Calibrating and validating the proposed models considering obtained experimental data;

- Developing both the global and local numerical formulations related to the proposed finite strain elastic-viscoplastic formulation, with the aim of integrating the constitutive proposal into a finite element framework, in order to solve structural engineering problems;

- Performing numerical simulations on compression tests considering homogeneous deformation and frictional conditions, with the aim of demonstrating corresponding constitutive capacity and numerical aspects, such as local and global convergence behavior, associated with the developed constitutive model and corresponding numerical solution strategies.

It is of great importance to mention that the experimental part of this work was developed at the *Instituto Superior Técnico* (IST) of Lisbon, Portugal, under the supervision of Professor Pedro Rosa, who designed the new equipments to be presented through the work. Although the experimental development has initiated approximately one year before, the final phase of equipment assembling as well as the experimental tests were carried out during a period of approximately ten months the student Tiago dos Santos have worked at IST under the guidance of Professor Pedro Rosa.

Having established the main objectives, specific topics concerning the (visco)plastic deformation of metallic materials are discussed in the following sections. Such a discussion encompasses aspects on experimental characterization, macroscopic experimental observations, metallurgical aspects, and constitutive modeling of high strain-rate mechanical behavior of metals.

## 1.2 High strain-rate mechanical characterization of materials

In order to properly predict a given material behavior, associated material characterization have to be performed, from a practical point of view, considering strain and strain-rate regimes similar to those observed in the desired manufacturing process or engineering application. For this purpose, one needs to seek for experimental apparatus and methods, which are capable of reproducing the same order of magnitude for the specific

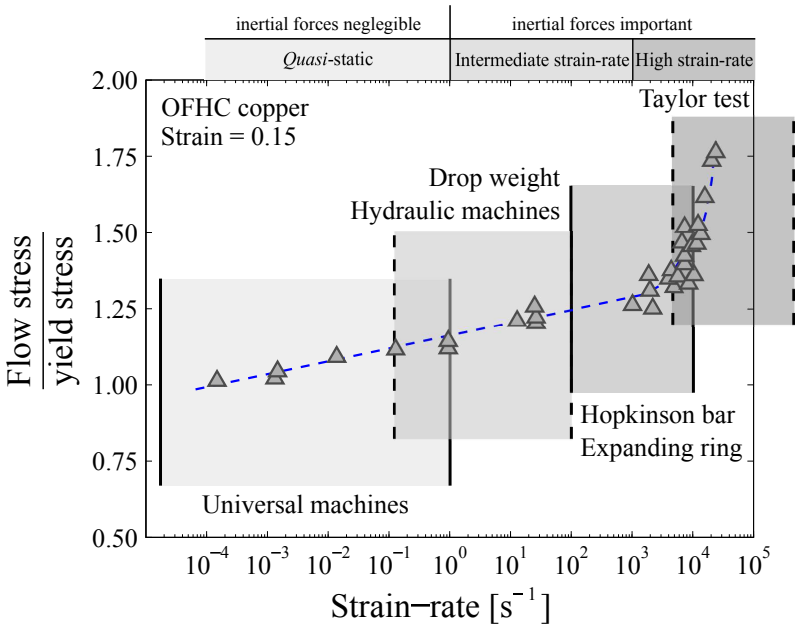


Figure 1.2: Classification of experimental equipments considering strain-rate ranges. See also Meyers, 1994, Rusinek and Jankowiak, 2014, and Silva et al., 2013, 2014. Experimental flow stress data are those of Follansbee and Kocks, 1988, for an annealed high purity copper at a given strain of 0.15.

deformation characteristics to which the material will be subjected. Figure 1.2 classifies some testing machines in terms of their strain-rate ranges. These application domains can be classified into three regimes: (i) *quasi*-static; (ii) intermediate strain-rate; and (iii) high strain-rate. The first testing strain-rate regime, $10^{-4} - 10^{0}\,\mathrm{s}^{-1}$, can be reached by means of conventional universal testing machines, and due to the low velocity conditions, inertial effects can be neglected [Meyers, 1994, Ch. 12]. In order to reach intermediate strain-rate conditions, $10^{0} - 10^{2}\,\mathrm{s}^{-1}$, servo-hydraulic testing machines or dropping weight systems can be used. In this intermediate strain-rate tests, inertial effects become important. These effects are due to elastic wave propagation along specimen and machine structure. On one hand, universal servo-hydraulics machines and systems based on a dropping weight are commercial equipments, which may be acquired from an appropriate manufacturer. On the other hand, these equipments are capable of performing tests considering a maximum strain-rate in order of $10^{2}\,\mathrm{s}^{-1}$, see Figure 1.2 and reference [Meyers, 1994, Ch. 12].

In order to characterize the material behavior under strain-rates greater than $10^{2}\,\mathrm{s}^{-1}$, or considering a high strain-rate regime, $10^{3} - 10^{5}\,\mathrm{s}^{-1}$, non-conventional equipments have to be used for reproducing the desired testing conditions. The most used equipments in dynamic tests considering strain-rates exceeding $10^{2}\,\mathrm{s}^{-1}$ are described below[3]. Under high strain-rate conditions, in addition to elastic wave propagation, inertial effects can involve plastic wave propagating along specimen [Meyers, 1994, Ch. 12].

[3]For more details on experimental and general aspects associated with dynamic behavior of materials, see, e.g., works of Meyers, 1994, and Ramesh, 2008.

***Hopkinson bar test*** [Hopkinson, 1914; Kolsky and Douch, 1962] is the most used machine in dynamic plasticity characterization, employing strain-rates within the range of $10^2 - 10^4\,\mathrm{s}^{-1}$. Figure 1.3(a) shows a schematic representation describing how *Hopkinson* bar works. Depending on the apparatus, the striker bar can be fired with a velocity between 2.5 and 25 $\frac{\mathrm{m}}{\mathrm{s}}$. The bar impacts against the incident bar, then an elastic wave propagates along that until reaching the specimen to be tested, which is therefore strained. Part of elastic wave is transmitted through the transmitter bar, and the remaining one is reflected back to the incident bar. These wave propagations along the bars are monitored by means of strain gauges. Desired quantities as force and displacement are then post calculated based on elastic wave propagation theory. As characteristic, tests are performed under *quasi*-constant strain-rates;

***Expanding ring test*** (see, e.g., Meyers, 1994, Ch. 12) is an experimental procedure used to determine the stress-strain response of a material subjected to strain-rates lower than $10^4\,\mathrm{s}^{-1}$. This method consists of expanding a ring-specimen in its radial direction. Ring expansion is performed by employing extreme loading conditions using, e.g., explosives or electromagnetic systems, see Figure 1.3(b). High speed cameras or optical sensors are used in order to monitor the associated deformation process. The advantage related to this procedure is the ability of obtaining stress-strain curves employing high strain-rates. However, the expanding ring test has experimental difficulties, e.g., maintaining a *quasi*-constant strain-rate during the test. As a characteristic, imposed strain-rate is higher in the beginning of experiment, and it is progressively lowered as the imposed strain increases;

***Taylor test*** [Taylor, 1948] is an experimental method in which the specimen is a bar, which is accelerated and then collides against a "rigid" plate, see Figure 1.3(c). Due to impact, elastic as well as plastic waves propagate along the bar, and the specimen undergoes non-homogeneous plastic deformations. Determination of apparent yield stress is done considering analytical expressions reasoning on a rigid-plastic unidimensional analysis. However, in general cases, mainly when high velocities are employed, associated deformed configuration predicted by this simplified analysis does not coincide with that observed experimentally at the end of deformation process. Thus, modifications of the original approach, as that of Erlich et al., 1982, were proposed in order to obtain satisfactory stress-strain relationships even when considering strain-rates in the order of $10^4 - 10^5\,\mathrm{s}^{-1}$. Representation of strain-rate vs. strain curve related to *Taylor* test showed in Figure 1.3(c) was based on work of Brünig and Driemeier, 2007;

***Electromagnetic cam-driven machine*** [Silva et al., 2012, 2013] is an experimental apparatus in which high strain-rate compression tests can be performed. This machine was proposed in order to allow imposing different strain-rate-histories during

compression testing. That is, the preceding experimental procedures have specific loading-histories, whereas the *Hopkinson* bar test has a *quasi*-constant strain-rate-history during deformation, and the expanding ring test has a loading-history in which the strain-rate decreases with imposed strain. The experimental apparatus proposed by Silva et al., 2012, 2013 consists of an electromagnetic actuator driving a cam-follower device, which in turn performs the specimen compression by means of a movable compression platen, see Figure 1.4(a). Achieved by changing the cam profile, the foremost advantage of this testing machine is the flexibility of designing specific strain-rate vs. strain relationships according to the desired test to be performed. Figure 1.4(b) shows different kinematic operating conditions that were obtained by means of logistic (type A), root (type B), and linear (type C) cam profiles. The machine flexibility allows to reproduce the working conditions which are commonly found in real manufacturing processes. This experimental procedure allows imposing strain-rates reaching $10^3\,\mathrm{s}^{-1}$;

***Gas gun machine test*** (see, e.g., Meyers, 1994, Ch. 12) is another kind of high strain-rate testing equipment. In a concise description, it consists of a pressure vessel, a barrel (or a tube), and a target chamber. The high pressure gas is loaded in the high pressure vessel and the projectile, mounted in a sabot, is placed in the barrel. A valve is released and the high pressure gas drives the projectile, which is accelerated in the barrel and impacts the target chamber. The principal advantages of guns over other techniques are the reproducibility of results, the excellent planarity and parallelism at impact, and the relative ease to use sophisticated instrumentation and diagnostics. One uses light gases for maximum velocity; hydrogen and helium are preferred, although air can also be used. The maximum velocity can be calculated from the maximum rate of expansion of the gas. For example, using helium, the projectile can accelerate to a velocity of $1200\,\frac{m}{s}$, thus providing strain-rates reaching magnitudes as high as $10^5\,\mathrm{s}^{-1}$. A simplified gas gun machine using air and a novel instrumented target chamber is used in the present work. However, our tests are limited to maximum velocities of $70\,\frac{m}{s}$, and thus to strain-rates in the order of magnitude of $10^4\,\mathrm{s}^{-1}$. Detailed descriptions on the instrumented chamber and on the gas gun machine used here are given respectively in Subsections 2.2.1 and 2.2.2.

The vast majority of high strain-rate experiments has the goal of monitor the instantaneous stress (flow stress) response corresponding to given strain, strain-rate, and temperature histories. In order to be able of assessing the current material strength (yield stress) induced by the whole load-history, a *quasi*-static reload starting from the current deformed condition has to be performed [Follansbee and Kocks, 1988; Tanner and McDowell, 1999; Farbaniec et al., 2012]. This task increases difficulties related to experimental characterization. For example, the *quasi*-static reloading is a destructive

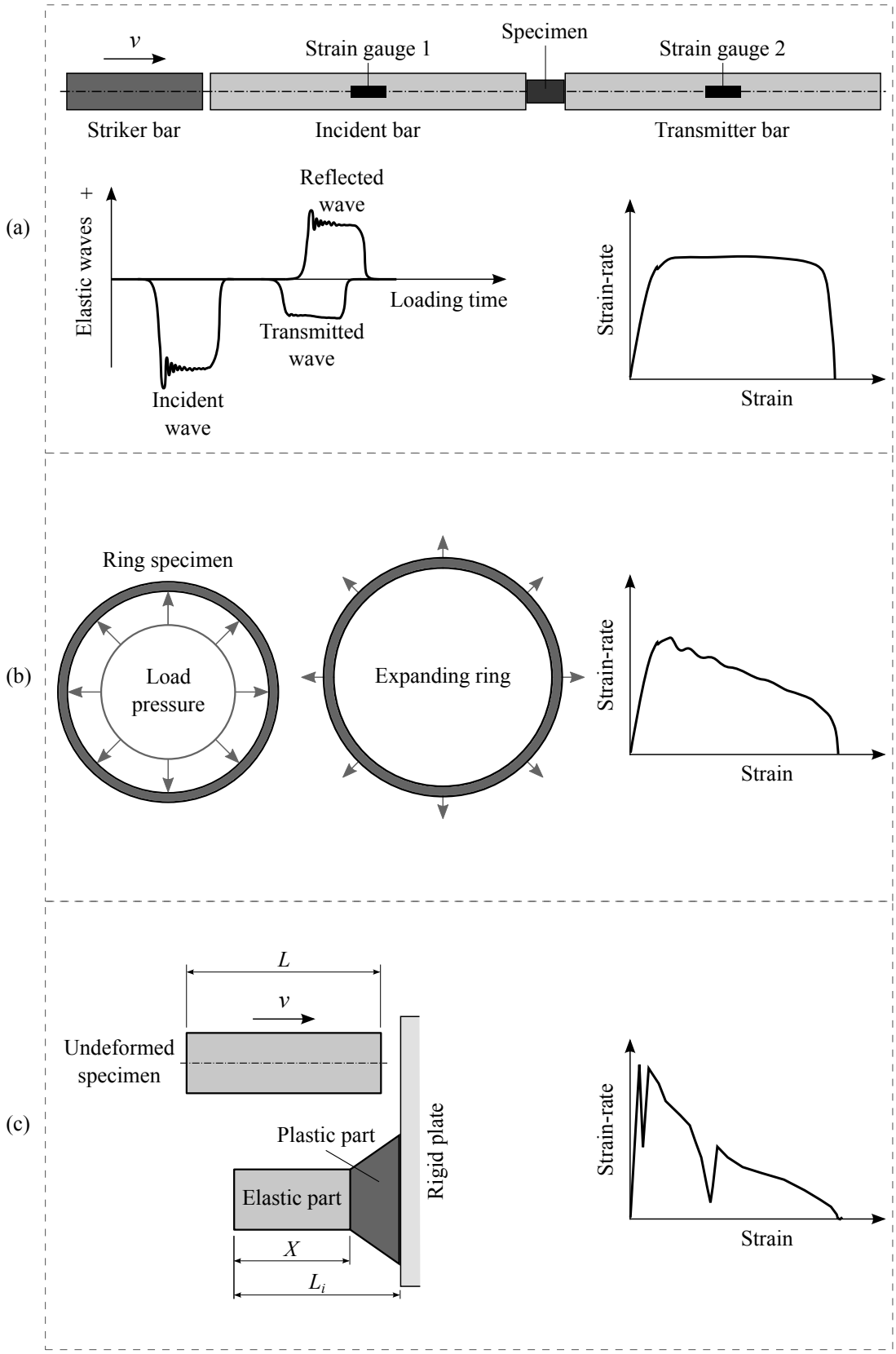


Figure 1.3: Schematic representation of some high strain-rate tests, and associated strain-rate vs. strain loading paths: (a) *Hopkinson* bar; (b) Expanding ring; and (c) *Taylor* tests. See also Meyers, 1994.

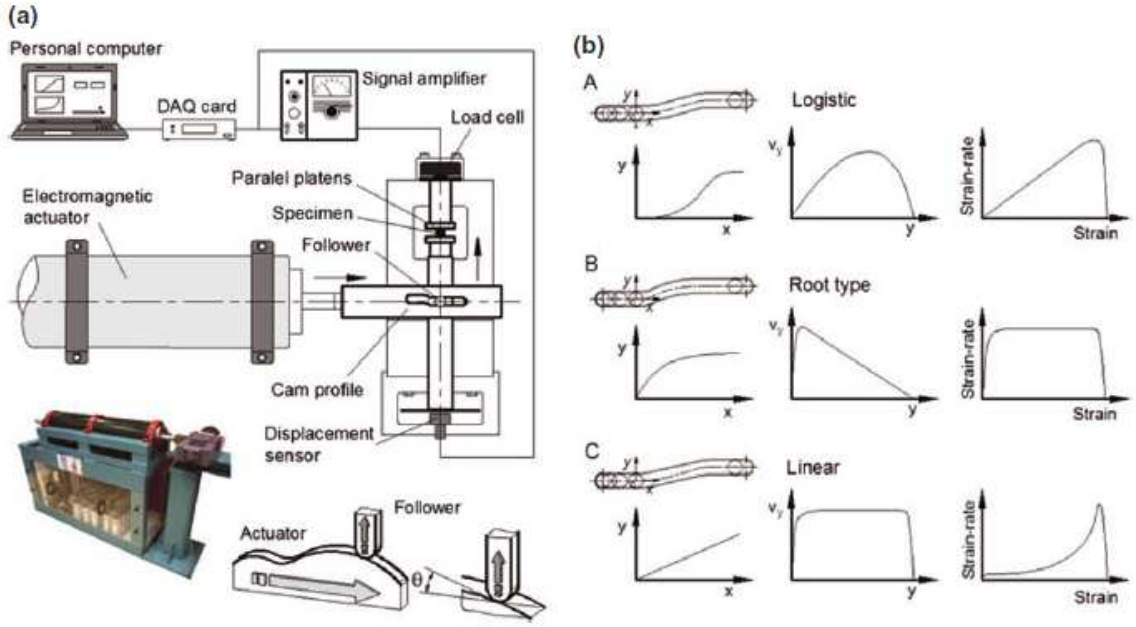


Figure 1.4: Electromagnetic actuator and cam-follower tool. (a) Schematic representation, nomenclature, photograph of the equipment and details of the cam profiles and follower. (b) Follower displacement vs. actuator displacement; Follower velocity vs. its displacement; Strain-rate vs. imposed strain on material specimen, considering three different types of cam profiles: A - Logistic, B - Root type, and C - Linear cam. [Silva et al., 2014].

test, restrained specimen can not be used for a characterization considering a constant strain-rate. Accordingly, the number of work pieces used in experiments is significantly increased. A nondestructive alternative to assess the strain and strain-rate induced material strength is performing hardness (indentation) tests between constant strain-rate deformation increments. However, to be able of estimating the current material strength from hardness measurements, a correlation between current yield stress and corresponding material hardness has to be established [Johnson, 1970; Qiao et al., 2009; Tiryakioglu et al., 2015]. Examples of works investigating strain, strain-rate, and temperature effects on hardness evolution of metallic materials are: Li et al., 2009, Zhang and Shim, 2010, and Huang and Tao, 2011. However, these studies have performed only *quasi*-constant strain-rate deformations, they have not considered sequential strain-rate tests to assess, for example, strain-rate-history effects on corresponding hardness evolution.

## 1.3 Strain-rate influence on phenomenological behavior of metals

Many investigations have been performed, at both micro- and macro-scales, with the aim of understanding a specific material behavior when subjected to severe plastic deformations and high strain-rates. As far as the macroscopic plastic deformation of metals is concerned, three rate-dependent phenomena can be highlighted [Lemaitre and Chaboche, 1990; Ottosen and Ristinmaa, 2005; de Souza Neto et al., 2008]: (i) the *strain-rate-*

*dependence* of flow stress; (ii) *creep* phenomenon; and (iii) phenomenon of stress *relaxation*; which are showed respectively in Figures 1.5(a)-(c). Figure 1.5(a) shows schematic unidimensional stress-strain curves obtained from tests performed under different strain-rates. An important aspect to be observed is that both current flow stress and associated material hardening behavior are influenced by the applied loading-rate, in the sense that increasing the imposed strain-rate, higher stress levels are reached.

Creep phenomenon, Figure 1.5(b), can be evidenced when a specimen is loaded at different stress levels, which are then maintained constant during long periods of time. In such cases, even at a constant stress, the material experiences a continuous plastic flow that is accelerated for higher stress values. For moderate and high stress levels, three creep stages can be observed in curves of Figure 1.5(b): (i) primary creep is the branch starting from origin which has a continuously decreasing strain-rate; (ii) secondary creep

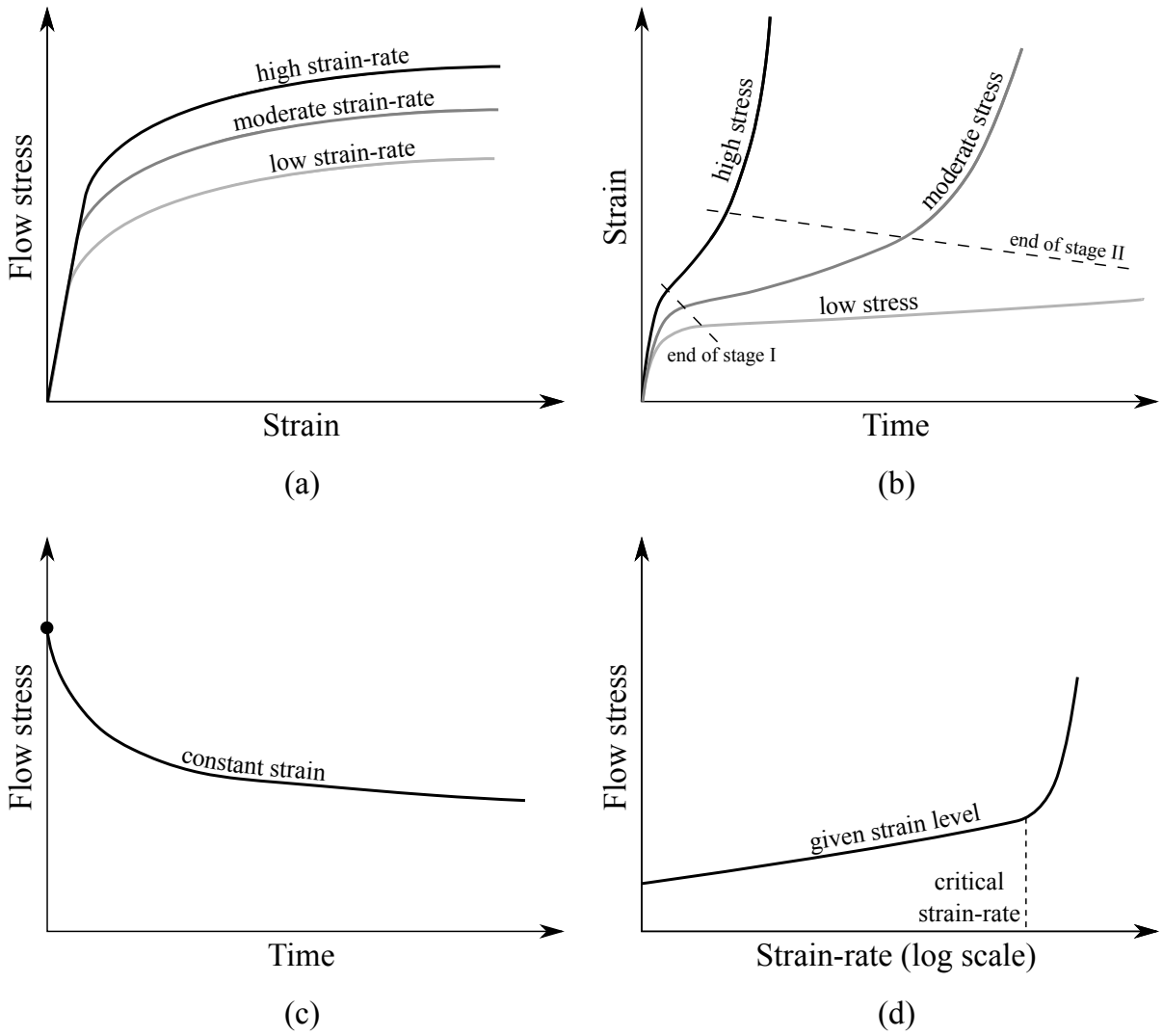


Figure 1.5: Schematic representation of viscoplastic phenomena: (a) Flow stress rate-dependence; (b) Creep under constant stress; (c) Stress relaxation under constant strain; (d) Change in flow stress rate-sensitivity at a critical strain-rate.

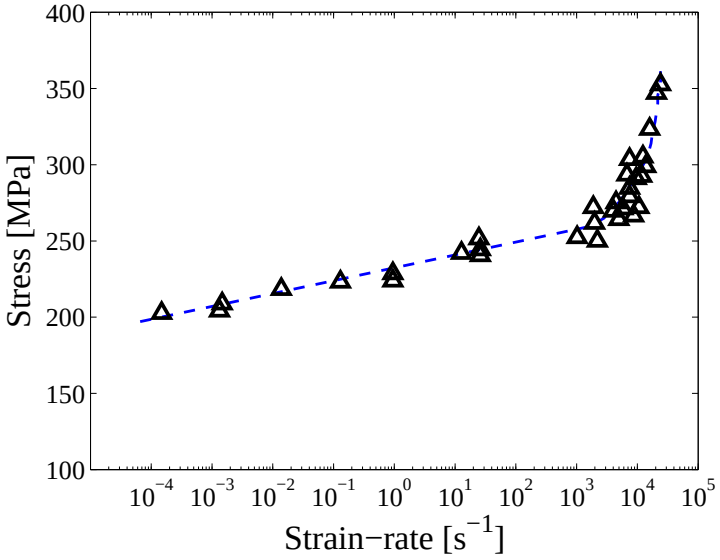


Figure 1.6: Experimental data on the flow stress rate-sensitivity observed in a high purity copper for a true strain level of 0.15 at room temperature. Source: Adapted from Follansbee and Kocks, 1988.

is the stage in which there is a *quasi*-constant (and *quasi*-null) strain-acceleration; and (iii) tertiary creep, which is characterized by high strain-rates which leads to the material rupture [Lemaitre and Chaboche, 1990; Ottosen and Ristinmaa, 2005; de Souza Neto et al., 2008]. For lower stress levels, material strain tends to stabilize during secondary stage. Constitutive prediction of creep behavior of metals is of great importance for high temperature applications ($T > \frac{1}{3}T_m$, where $T_m$ is the melting temperature), in which the material is subjected to high loads during a long time, such as is observed in aerospace turbines.

The stress relaxation phenomenon (Figure 1.5(c)) can be observed in a simple tensile-relaxation test, in which the specimen is subjected to a prescribed strain level imposed at a finite strain-rate. As long as the applied strain is kept constant, a decrease in the stress level is observed in the course of time. The stress value tends asymptotically to an equilibrium stress. The set of prescribed strain and corresponding equilibrium stress, attainable by means of relaxation processes, forms an equilibrium stress-strain curve [Haupt and Lion, 1995; Haupt, 2000]. The stress relaxation phenomenon is important, particularly in high velocity mechanical forming processes, the mechanical component is maintained at constant strain level after the loading phase to reduce spring-back effects.

Furthermore, there are experimental evidences showing that associated flow stress rate-sensitivity of metallic materials can increase even at room temperatures when imposed strain-rates exceed a given critical value [Follansbee, 1986; Follansbee and Kocks, 1988]. This behavior is schematically showed in Figure 1.5(d), and experimental results obtained by Follansbee and Kocks, 1988, considering an annealed high purity copper (99.99% wt.), and using the *Hopkinson* bar, are shown in Figure 1.6. This figure assesses the strain-rate

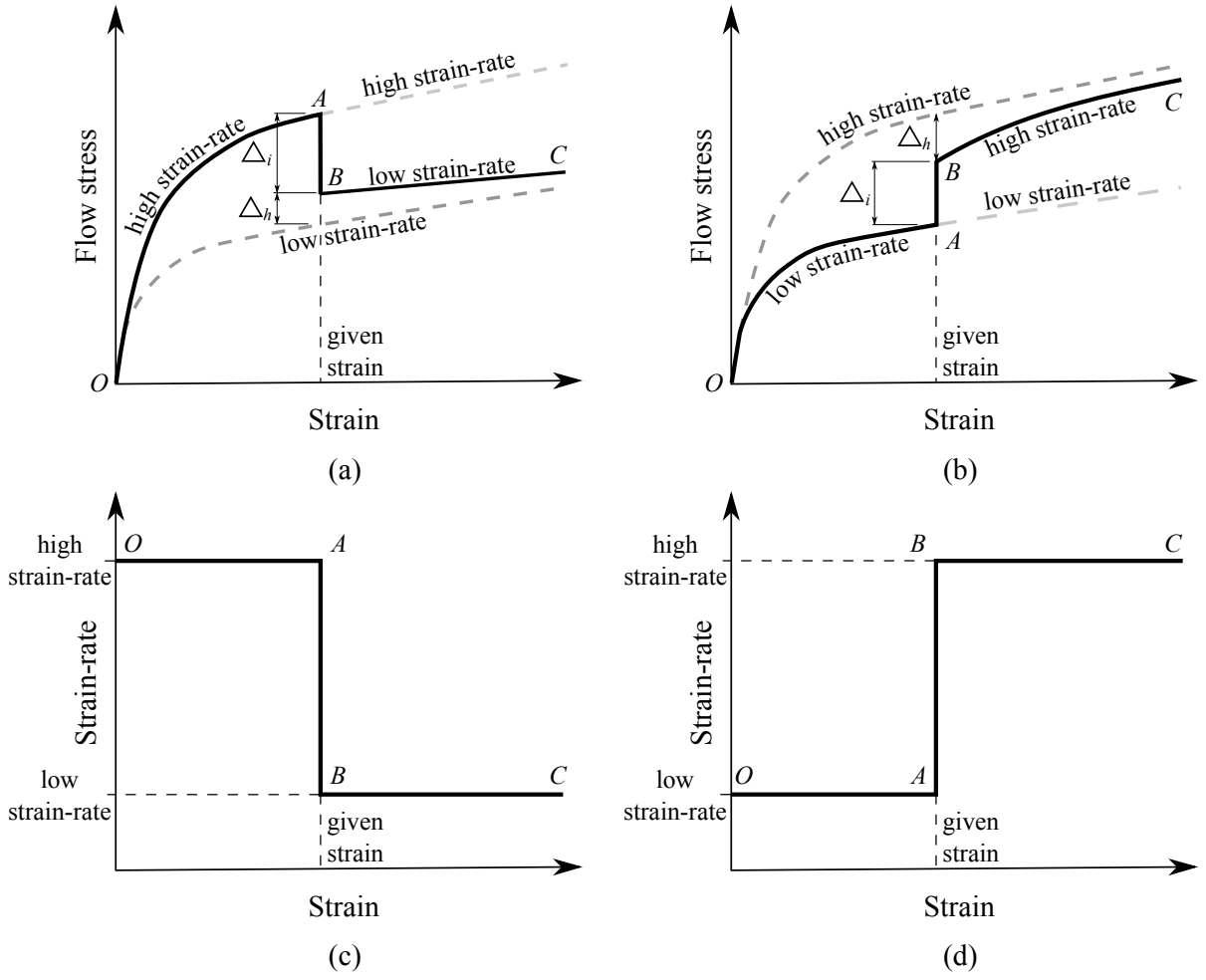


Figure 1.7: Schematic representation of strain-rate sequential tests: (a) Flow stress-strain curve associated with decremental strain-rate-history (c); (b) Flow stress-strain curve associated with jump strain-rate-history (d). Gray dashed-lines are associated low and high strain-rate monotonic flow stress-strain curves. After Klepaczko, 1975.

influence on flow stress response of this material considering a given true strain level of 0.15 at room temperature. In this case, mentioned critical value of strain-rate, above which an abrupt increase in material rate-sensitivity is observed, is around $10^3\,\mathrm{s}^{-1}$.

In addition to instantaneous effects, that could be verified by means of constant strain-rate loadings, experimental results have evidenced loading-history effects, which revel the dependence of material response with respect to strain-rate (or temperature) histories associated with a given deformation process [Klepaczko, 1975; Chiem and Duffy, 1983; Rashid et al., 1992; Tanner and McDowell, 1999]. *Strain-rate-history effects* can be evidenced from strain-rate-sequential tests, in which the material is strained to a certain level according to a given constant strain-rate, which is then "instantaneously" switched to a higher or lower level, as showed schematically in Figures 1.7(c) and (d), respectively for a decremental strain-rate test and for a strain-rate jump test. Flow stress-strain results of a given sequential test are showed in Figures 1.7(a) and (b) (after Klepaczko, 1975),

resulting from associated imposed strain-rate-histories of Figures 1.7(c) and (d), respectively. In both decremental and jump tests, at point $A$, where the imposed strain-rate is abruptly changed, a jump, $\triangle_i$, in the current flow stress is observed in both Figures 1.7(a) and (b). This behavior can be attributed to the instantaneous rate effects, associated with thermally activated mechanisms and viscous drag resistance [Klepaczko, 1975; Rashid et al., 1992]. However, when comparing the current flow stress response at point $B$ (i.e, right after the instantaneous stress change) with a monotonic loading curve in which the second strain-rate (a lower strain-rate for the decremental test, and a higher strain-rate for the jump test) was imposed from the initial state $O$, a strain-rate-induced hardening $\triangle_h$ is evidenced, see Figures 1.7(a) and (b). The current flow stress state at point $B$ does not recover the monotonic curve considering the second strain-rate. This behavior indicates that the current stress response, instead of being a state function of loading parameters as strain, strain-rate and temperature, is dependent on the previous loading-histories experienced by the deformed material. The strain-rate-induced hardening $\triangle_h$ can be attributed to the influence of previously imposed strain-rate on the material microstructural evolution, e.g., an increase in the density of stored dislocations induced by an increase of imposed loading-rate [Klepaczko, 1975; Rashid et al., 1992].

In summary, keeping in mind this brief discussion, one can observe that the imposed strain-rate has a major influence on macroscopic material response. Related phenomenological features, including the sharp rate-sensitivity change observed at high strain-rates (Figure 1.5(d) and Figure 1.6) as well as associated strain-rate-history effects (Figures 1.7(a) and (b)) have motivated many fundamental investigations in order to identify microscopic mechanisms responsible for rate-dependent phenomena observed in plastic deformation of metals. These investigations were intended to provide a better understanding on material behavior of metals when subjected to high strain-rate loadings, and then to be able of providing support for proposing suitable constitutive models capable of properly predicting experimental results under desired loading conditions. In order to advance toward a better understanding on fundamental mechanisms responsible for the rate-dependent experimental observations described earlier, and then to support future constitutive developments in this work, the following section outlines important metallurgical aspects concerning the material microstructural evolution induced by both *quasi*-static and high strain-rate plastic deformation of metals.

## 1.4 Metallurgical aspects of plastic deformation process

Although the constitutive model to be developed in this work consists of a phenomenological (or semi-physical) approach, in order to be guided by micro-mechanical features, this section is intended to bring out a brief discussion on metallurgical aspects inherent to plastic deformation of metallic materials. The present analysis is restricted to "pure" *face*

*centered cubic* (FCC) metals with moderate to high *stacking fault energy* (SFE) (such as copper, nickel, and aluminum) at room temperature.

The plastic deformation of metals involves permanent or irreversible changes on the geometry of mechanical structures. The way the material responds to the imposed loadings (stress and strains) depends on its initial microstructure and crystallographic texture, and also, on how these characteristics evolve with deformation. To properly understand and predict the plastic behavior of metals, relationships between the current microstructural and mechanical response, such as the current yield stress, have to be established. Aiming at correlating key microstructural parameters with desired mechanical proprieties, many investigations have been performed. A rich bibliography on these metallurgical investigations can be found in recent textbooks as those of Hull and Bacon, 2011, Argon, 2012, François et al., 2012, Kubin, 2013, and Hansen and Barlow, 2014.

Following a physically-based or metallurgical thought, correlating the macroscopic mechanical response of a given material to microstructural aspects demands the knowledge of the fundamental mechanisms governing the material plastic behavior under the physical and loading conditions of interest. Under low temperature ($T \leq \frac{1}{3}T_m$) applications, the plastic behavior of "pure" FCC metals with moderate to high SFE is governed by the relative sliding between specific (compact) crystallographic planes along preferable directions in which the resolved shear stress reaches a threshold value [Taylor, 1934a,b; Schmid and Boas, 1935]. In fact, the relative crystallographic sliding is facilitated by the motion of dislocations along the directions with the highest atomic densities [McClintock and Argon, 1966; Dieter, 1986; Hull and Bacon, 2011; Hansen and Barlow, 2014]. Both compact crystallographic planes and preferable directions constitute the so-called *slip systems*. Considering the mentioned mechanism, the plastic flow occurs by means of superimposed pure shear deformations, without significantly changing the structural ordering and arrangement of atoms, and consequently without significantly changing the material volume [McClintock and Argon, 1966; Dieter, 1986; Hull and Bacon, 2011; Hansen and Barlow, 2014].

### 1.4.1 Strain-hardening behavior

This subsection presents a succinct discussion on the material hardening behavior and corresponding microstructural evolution considering *quasi*-static deformation processes. As the plastic deformation evolves an increase in the material resistance is evidenced, requiring a higher stress to proceed with deformation. This behavior is denominated strain-hardening, which refers to the deformation-induced increase on material strength. As it can be observed in Figure 1.8, the hardening behavior of metals and their alloys is typically characterized by a distinct number of deformation stages [Nes, 1997; Kocks and Mecking, 2003; Argon, 2012; Hansen and Barlow, 2014]:

- *Stage I* is known as the easy slip stage, once at this phase the material presents a low hardening-rate. At this stage there are few dislocations stored in the material structure, consequently the plastic flow occurs in a single (primary) slip system, at which the higher resolved shear stress is reached. The deformation Stage I is not observed in the stress-strain behavior of polycrystalline FCC metals;

- *Stage II* is characterized by a nearly constant hardening-rate, see Figure 1.8(b). At this stage, due to an increase in the dislocation density and thus in the slip resistance of the primary system, multiples slip systems are then activate. For metals with high SFE (as aluminum) the deformation Stage II is almost nonexistent at room temperature;

- *Stage III* is featured by a nonlinear evolution in the stress-strain curve, as shown in Figure 1.8(a). At this stage, the material presents a quick reduction in associated hardening-rate as the stress level increases. Different microstructural mechanisms can promote the transition between Stages II and III. One of the most important is the cross slipping of mobile dislocations. At the end of Stage II, due to a high amount of stored dislocations and consequently internal stresses, some dislocations can change their original slip planes and thus annihilate when interacting with dislocations with opposite sign. The deformation Stage III is characterized by a competition between the accumulation and annihilation of dislocations;

- *Stage IV* is characterized by a nearly constant low hardening-rate (Figure 1.8(b)). This stage can extend itself until high deformation levels. Its end is featured by a decrease in observed hardening-rate to a *quasi*-null value, characterizing the beginning of deformation Stage V. Metallurgical aspects associated with Stage IV are less understood than the preceding stages (I, II, and III). Although some interpretation relying on the formation of new sub/grains induced by an increase in the misorientation between dislocation cells at advanced stages of straining [Argon and Haasen, 1993; Nes, 1997; Kocks and Mecking, 2003], other authors attribute the hardening behavior of Stage IV to formation of lamellar or fibrous structures [Hughes et al., 1997; Hansen and Barlow, 2014]. Furthermore, this stage can also be related to dislocation debris acting as obstacles to dislocation glide [Rollett et al., 1989]..

In a underlying scale, the hardening behavior of metals is controlled by the interaction, storage, and arrangement of dislocation structures. Thus, the distinct deformation stages can be related to microstructural evolution induced by increasing both stress and strain levels. In a succinct manner, the arrangement of dislocation in a FCC material with moderate to high SFE evolves from a planar configuration at Stage II to a three-dimensional cell structure at Stage III. At all strain levels, the structural subdivision occurs in a form of elongated, alternately misoriented domains of a specific orientation. For example, for a

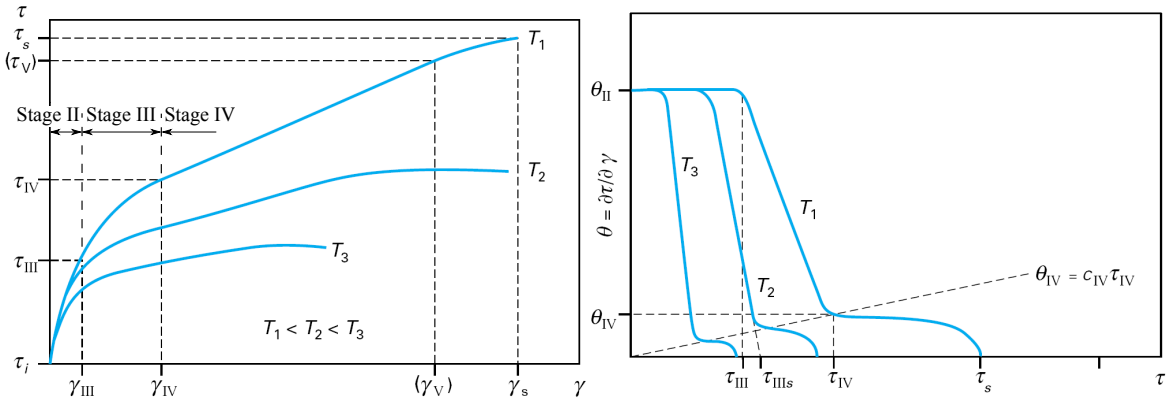


Figure 1.8: Schematic representation of the deformation stages evidenced during the plastic flow of polycrystalline FCC metals [Nes, 1997]: (a) Shear stress ($\tau$) vs. shear stain ($\gamma$) curves for different temperatures ($T_i$); (b) Hardening-rate ($\theta$) vs. shear stress ($\tau$) level for different temperatures ($T_i$). Subscripts II, III, IV and V refer to corresponding deformation stage. $(\cdot)_s$ stands for the saturation value of quantity $(\cdot)$. Constant $c_{IV}$ correlates the hardening-rate and saturation stress associated with Stage IV. Source: Nes, 1997.

rolling process, a lamellar structure is obtained, while for a cylindrical extrusion process, a fibrous configuration is reached [Hansen et al., 2001; Hansen and Barlow, 2014]. A schematic representation describing the microstructural evolution due to imposed plastic deformation is showed in Figure 1.9, where a simple compression test is considered. A brief description on each deformation phase is given in next subsections.

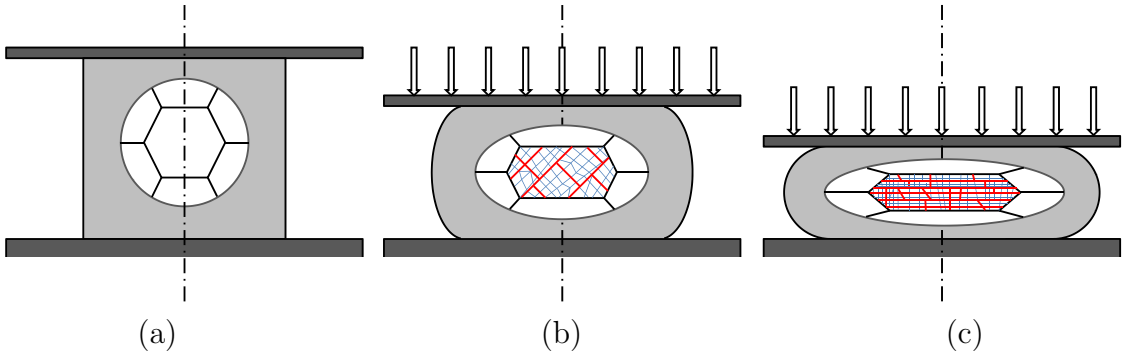


Figure 1.9: Schematic representation on the microstructural evolution considering a simple compression test. (a) Undeformed specimen; (b) Specimen subjected to small or moderate strain levels: Formation of incidental dislocation boundaries (IDBs) (thin lines) and deformation bands (thick lines), such as geometrically necessary boundaries (GNBs) and micro-bands (MBs), nearly aligned with the direction of the highest shear stress; (c) Specimen subjected to large strains: Formation of lamellar structures (thick lines), almost transversally aligned with the load direction.

### 1.4.2 Deformation-induced microstructural evolution

In a general way, dislocations formed during deformation are organized according to characteristic patterns which assume the form of *dislocation boundaries* (DBs). These boundaries can form spatial structures (in "pure" metals with moderate to high SFE), or extended planar boundaries (in "pure" metals with low SFE, or in metallic alloys). Some authors suggest that these configurations represent *low energy dislocation structures* (LEDS). This line of thought follow ideas and works of researchers like *Kuhlmann-Wilsdorf*, *Hughes*, *Hansen* and co-authors [Kuhlmann-Wilsdorf and Merwe, 1982; Kuhlmann-Wilsdorf and Hansen, 1991; Bay et al., 1992; Liu et al., 1998; Hughes and Hansen, 2000; Hansen and Barlow, 2014].

The crystallographic orientations of the regions on both side of a DB are rotated with respect to each other. The resulting rotation angle is called misorientation angle

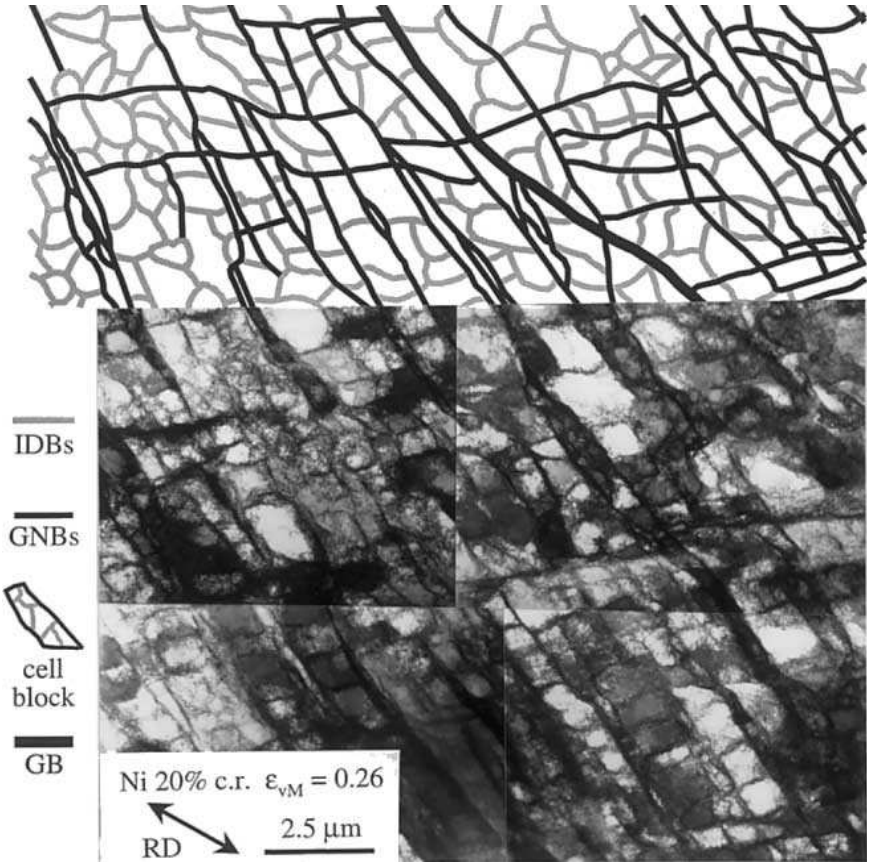


Figure 1.10: TEM micrography of the dislocation microstructure typical of deformation Stage III, shown here for pure nickel following a 20% reduction by cold rolling (cr) (equivalent *von Mises* $\varepsilon_{\mathrm{vM}} = 0.26$). At the top of figure is a tracing of the underlying and adjacent micrograph to illustrate the cell block structure composed of IDBs and GNBs. Long GNBs are nearly parallel to the main {111} slip plane and inclined to the rolling direction (RD). Sections of two grains are visible with a grain boundary (GB) running diagonally. Viewing plane is the longitudinal section containing the normal and rolling directions. Source: Hughes, 2001.

$\theta_{mis}$. There are two types of DBs which are formed and subdivided in two scales. In the smaller scale, there are nearly equiaxed dislocation cells. These dislocation boundaries, which are denominated incidental dislocation boundaries (IDBs), can be formed formed by the mutual and statistical trapping of glide dislocations. The larger scale is constituted by extended boundaries separating two cell blocks (CBs). These boundaries accommodate strain incompatibilities between two neighbor CBs, and thus are called geometrically necessary boundaries (GNBs), as illustrated by schematic representation of Figure 1.9 and micrography of Figure 1.10.

While the formation and morphology of dislocation cells have been described qualitatively, the next step towards a constitutive description is identifying and quantifying key structural parameters in order to introduce them in a constitutive law. The dislocation density $\rho_d$, the boundary spacing ($D_{IDB}$ for IDBs and $D_{GND}$ for GNBs, see Figure 1.11), and the misorientation angles ($\theta_{IDB}$ for IDBs and $\theta_{GND}$ for GNBs, see Figure 1.11) have been used as key microstructural features to estimate the current yield stress of metals (see, e.g., Hughes and Hansen, 2000). Both boundary spacing and misorientation angles related to IDBs and GNBs are schematically represented in Figure 1.11.

At small and moderate strains, the GNBs are formed by dense dislocation walls

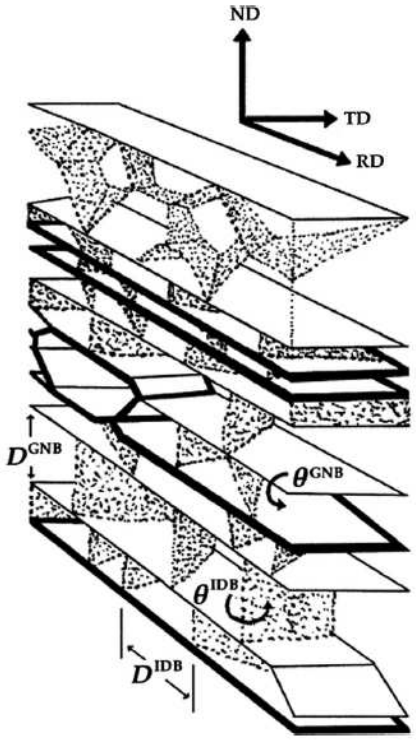


Figure 1.11: Schematic representation of a deformation microstructure showing the key structural parameters. Lamellae of extended GNBs are linked by low-angle IDBs (bamboo-type structure). High-angle ($\theta_{mis} > 15°$) GNBs are represented by thick lines, and those with medium-angle ($3° < \theta_{mis} < 15°$) by medium lines. Source: Hughes and Hansen, 2000.

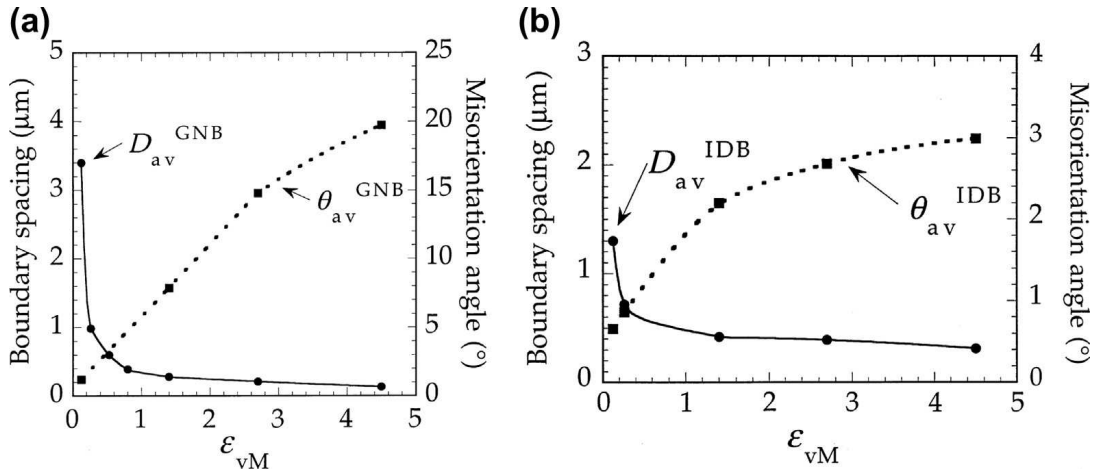


Figure 1.12: Boundary spacing and misorientation angles as a function of equivalent *von Mises* strain for a cold-rolled nickel: (a) GNBs and (b) IDBs. Source: Hughes and Hansen, 2000.

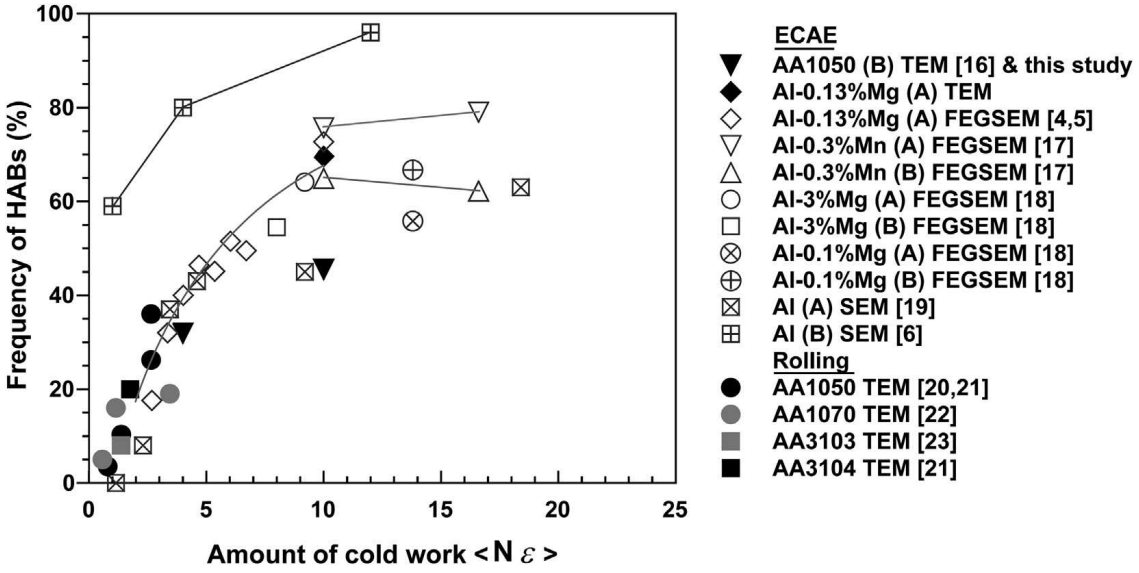


Figure 1.13: Fraction of HABs in aluminum alloys deformed by angular extrusion and rolling. Source: Mishin et al., 2003.

(DDWs) and by *micro-bands* (MBs). These nearly planar boundaries are organized in groups almost parallels to the macroscopic planes containing the direction of higher shear stress [Bay et al., 1992; Hughes et al., 1998], see also Figure 1.9(b). As the strain proceeds to larger levels, both DDWs and MBs give rise to lamellar boundaries (LBs), which are approximately transversal to the principal stress directions [Bay et al., 1992], see Figure 1.9(c).

On one hand, at low and medium deformation levels, CBs contain many dislocation cells. On the other hand, as the plastic straining increases, the number of cell per CB decreases, what occurs due to a reduction in boundaries spacing ($D_{IDB}$ and $D_{GNB}$). However, the spacing between GNBs decay faster than those associated with IDBs [Hughes and Hansen, 2000], see Figure 1.12. Running in parallel with the microstructural refinement,

is the mutual storage of dislocation within boundaries. The dislocation storage increases both IDB and GNB misorientation angles [Hughes and Hansen, 2000], see Figure 1.12. In a way that, in large strains processes, the misorientation can exceed 15°, meaning that this boundaries become high-angle boundaries (HABs), which in their turn are compared to the original grain boundaries [Hansen, 2004]. The fraction of HABs can reach about $70 - 80\%$ [Mishin et al., 2003], see Figure 1.13.

The preceding analysis presents some experimental results and observations related to *quasi*-static deformation processes. In order to proceed with the present analysis, which is intended to evidence the high strain-rate behavior of metals, effects of plastic deformation velocity on the microstructural evolution are therefore described in the sequel.

### 1.4.3 Strain-rate-induced microstructural evolution

As explained in Subsection 1.4.2, dislocation structures in FCC metals deformed under *quasi*-static loadings tend to organize themselves in cellular structures (at small strains), which evolve to lamellar structures as the plastic deformation increases. Some researchers [Huang and Tao, 2011; Luo et al., 2012a,b] have observed that those morphological features are also evidenced in aluminum and nickel samples (high SFE metals), even when subjected to dynamic loadings, involving strain-rates in the order of $10^3\,\mathrm{s}^{-1}$. Figures 1.14 and 1.15 show respectively typical cellular and lamellar structures formed in nickel specimens under dynamic plastic deformation. From a constitutive point of view, the fact that in both *quasi*-static and high strain-rate conditions the microstructure formed during deformation follows a similar organization pattern is of great importance, because in this way the same microstructural features can be taken as key parameters when proposing a constitutive model. Based on discussion of Subsection 1.4.2, those key microstructural parameters can be identified as: the dislocation density $\rho_d$, boundary spacing $D_{IDB,GND}$, and misorientation angle of dislocation boundaries $\theta_{IDB,GND}$.

Many experimental investigations have been performed to identify and understand how the imposed strain-rate influences the microstructural evolution and the macroscopic response of metallic materials. Among the most important contributions on this subject along the years, some works are referenced: Leslie, 1973, Orava, 1973, Chiem and Duffy, 1983, Duffy, 1983, Cheval and Priester, 1989, Shankaranarayan and Varma, 1995, Bhattacharyya et al., 2005, Dirras et al., 2010, Zhang and Shim, 2010, Huang and Tao, 2011, Rusty Gray III, 2012, Luo et al., 2012a,b, Baig et al., 2013, Pandey et al., 2013, Bodelot et al., 2015, Vilamosa et al., 2015, and Yang et al., 2015, to cite a few.

Although there exist aspects not well understood on the strain-rate influence on material response and its microstructural evolution, some common evidences about the microstructural rate-sensitivity of metallic materials can be pointed out. For example, studies have indicated that by increasing the imposed strain-rate, more refined dislocation substructures can be produced by plastic deformation. In other words, by increasing the

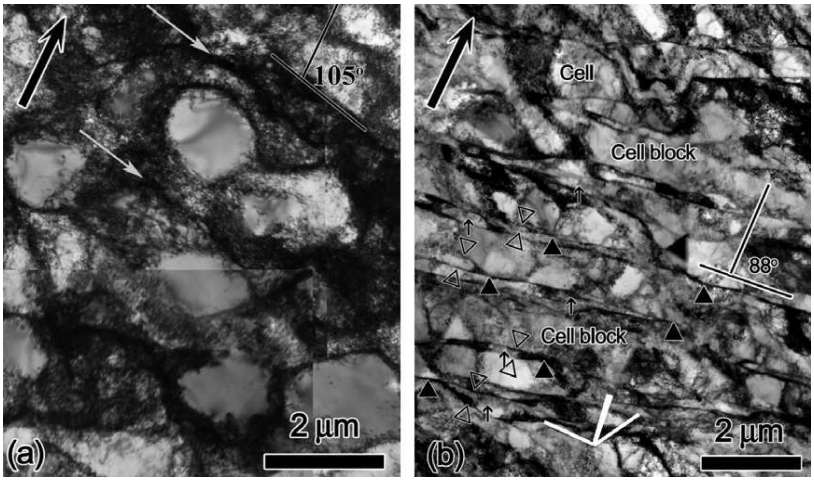


(a) (b)

Figure 1.14: Typical microstructures of nickel samples after dynamic plastic deformation with a strain level of 0.3: (a) Cellular structure and (b) extended dislocation boundaries are dominating features. Extended dislocation boundaries, composed by DDWs (black triangles) and MBs (empty triangles), are near perpendicular to the compression direction (black arrows) and coincide with the traces of planes {111}. In figure (b) white lines indicate the traces of planes {111}. Source: Luo et al., 2012b.

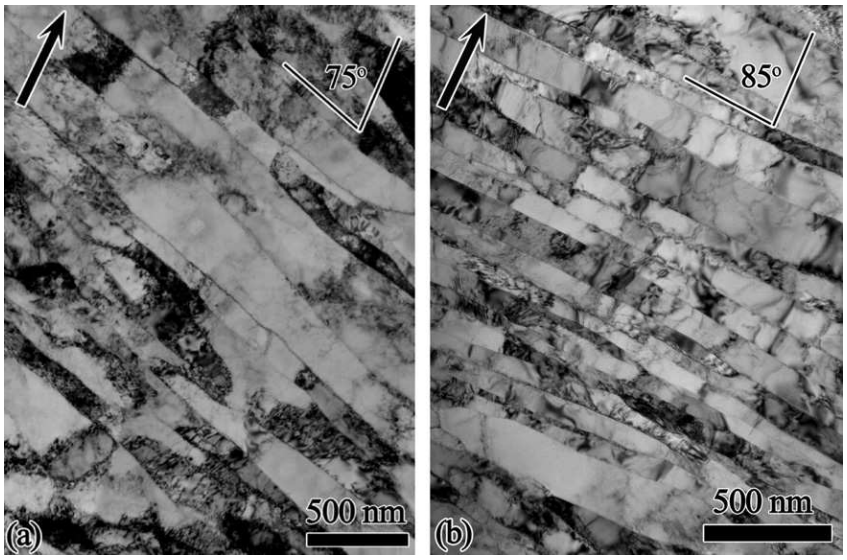


(a) (b)

Figure 1.15: Deformed microstructures of nickel subjected to dynamic plastic deformations with strains levels of (a) 1.7 and (b) 2.3. Thin lamellar boundaries define regions subdivided by dislocation boundaries which interconnect the lamellae. There is low dislocation density between the boundaries. The lamellar boundaries are near perpendicular ($75 - 85°$) to the compression direction (black arrows). Source: Luo et al., 2012b.

strain-rate, one can increase the density of dislocations stored, and thus decrease the size of sub/grains, the spacing between and the width of lamellar boundaries formed due to plastic straining [Huang and Tao, 2011; Rusty Gray III, 2012; Luo et al., 2012a]. In

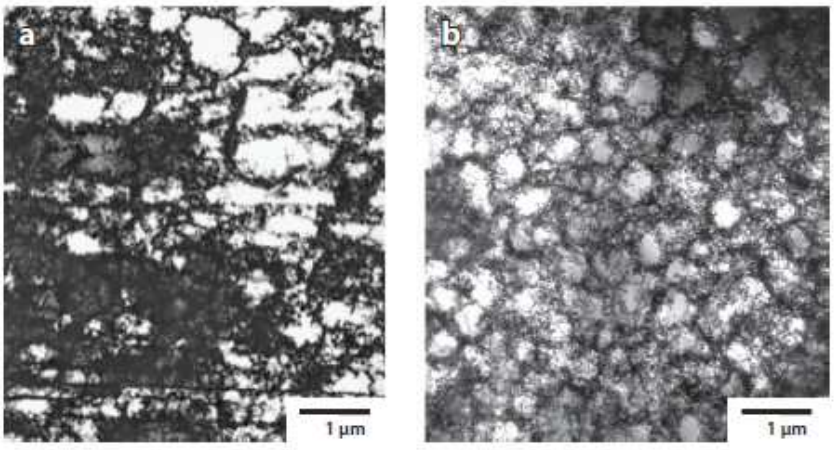


(a) (b)

Figure 1.16: Dislocation cells formed in copper samples deformed according to (a) *quasi*-static strain of $\approx 0.1$ and (b) dynamic plastic deformation of $\approx 0.0825$. Source: Rusty Gray III, 2012.

addition to reducing the cell size, increasing the velocity deformation can produce more homogeneous distributions of sub/grains throughout the sample. Furthermore, there are experimental results evidencing a strain-rate-induced increase in the misorientation angles of IDBs [Rusty Gray III, 2012; Luo et al., 2012a,b]. An example of strain-induced microstructural refinement is shown in Figure 1.16, where dislocation cell structures formed in copper samples subjected to both *quasi*-static and dynamic loadings are displayed.

Experimental results [Zhang and Shim, 2010; Huang and Tao, 2011; Luo et al., 2012b] and dislocation dynamics simulations [Shehadeh et al., 2005] have indicated that, when subjected to high strain-rate deformation processes, dislocation structures tend to accommodate the imposed plastic deformation and associated restrictions on the slipping velocity by increasing their nucleation and multiplication rates. This behavior increases both the density and interaction of stored dislocations, what inhibits dynamic recovery and dislocation annihilation mechanisms, thus increasing the dislocation population.

As already discussed, the increase in strain-rate leads to a reduction in the sub/grain size. Beyond a certain strain level, by increasing their misorientation angles, the subgrains and dislocation cells formed during the deformation may give rise to new grains (dynamic recrystallization) with low ($\theta_{mis} < 5°$), medium ($5° \leq \theta_{mis} \leq 15°$) or even high-angle ($\theta_{mis} > 15°$) boundaries [Zhang and Shim, 2010; Huang and Tao, 2011; Luo et al., 2012b]. The increase in the misorientation angle associated with IDBs is due to a greater number of dislocations trapped within the cell interiors [Luo et al., 2012b].

Macroscopic features associated with metallic materials, such as the strength (yield and flow stress), hardness, ductility, among others, are generally controlled by the current microstructural configuration: dislocation density, sub/grain size, crystallographic misorientation, etc. An example of this correlation between microscopic and macroscopic

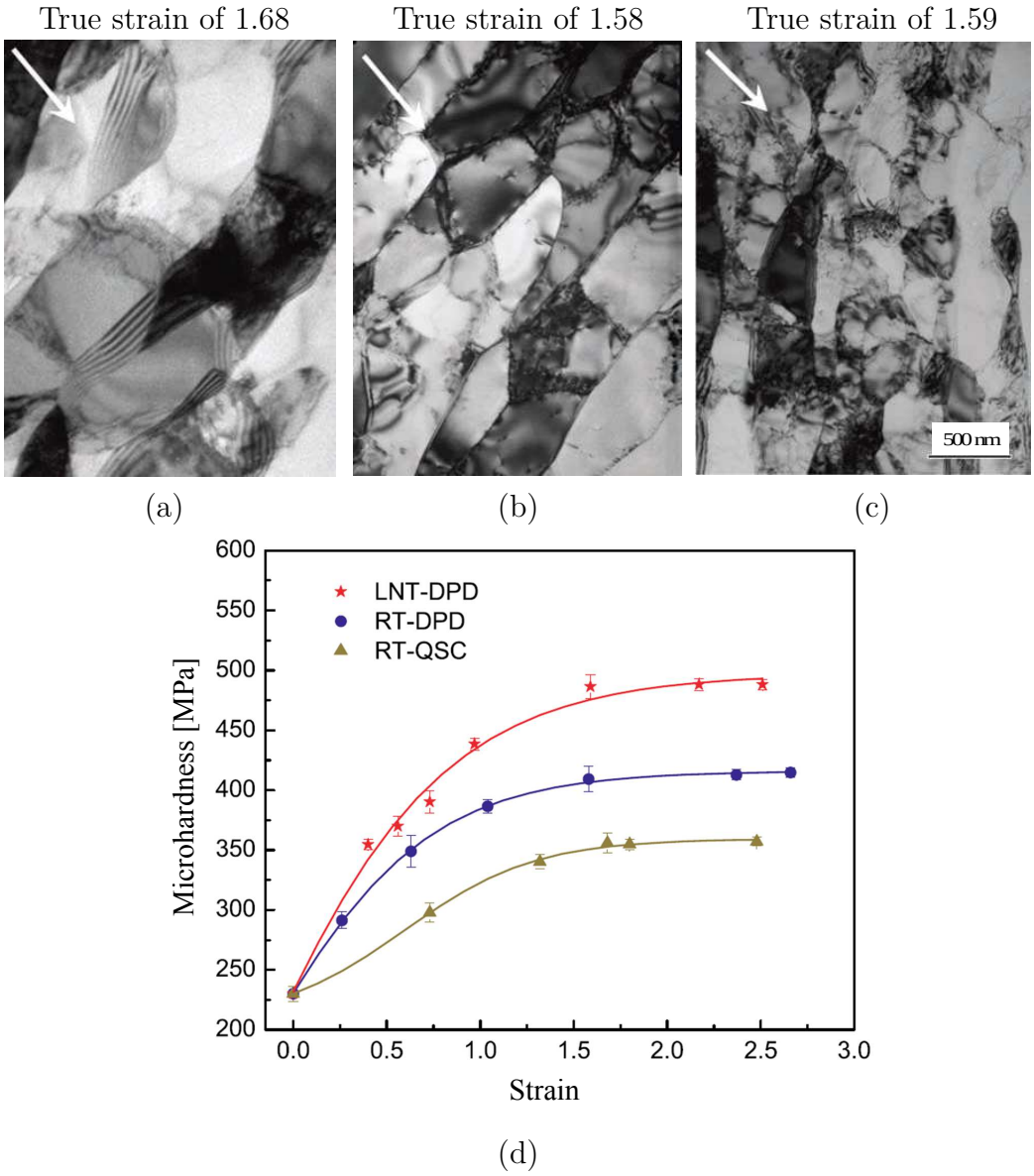


Figure 1.17: TEM micrography showing strain-rate (and temperature) influence on strain-induced grain refinement considering aluminum AA1050 samples: (a) RT-QSC: Room temperature *quasi*-static loading; (b) RT-DPD: Room temperature, dynamic plastic deformation, strain-rate in the order of $10^3\,s^{-1}$; (c) LNT-DPD: Cryogenic temperature (liquid nitrogen temperature), dynamic plastic deformation, strain-rate in the order of $10^3\,s^{-1}$; (d) Vickers microhardness in terms of imposed strain considering RT-QSC, RT-DPD, and LNT-DPD loading conditions. Source: Adapted from Huang and Tao, 2011.

features is the well-known *Hall-Petch* rule [Hall, 1951; Petch, 1953], which states that by refining the grain size, one can increase the obtained material strength. In this manner, if the imposed strain-rate has a major influence on the microstructural evolution of metallic materials, as earlier discussed in Section 1.3, it should strongly influence the related macroscopic behavior. Figures 1.17(a)-(c) show experimental results obtained by Huang and Tao, 2011, on aluminum AA1050 samples, evidencing that increasing the

deformation-rate (or decreasing the temperature) produces a more efficient strain-induced grain refinement. The authors have confirmed the strengthening promoted by the deformation velocity by means of microhardness tests. Results shown in Figure 1.17(d) provide evidence of an increase in material hardness due to an increase in imposed strain-rate. It is worth mentioning that similar effects can also be obtained by reducing the testing temperature [Li et al., 2009; Zhang and Shim, 2010; Huang and Tao, 2011]. After identifying and qualitatively evaluating some key microstructural parameters, the next subsection correlates these features with the current material strength, in order to provide constitutive fundamentals for developing a suitable plasticity model.

### 1.4.4 Current yield stress constitutive relationships

As explained in Subsections 1.4.1 to 1.4.3, the deformation stages observed in metallic materials correlate with the current material microstructure. This fact suggests that relationships between the current yield stress and microstructural parameters can be formulated. As pointed out in preceding discussions, the dislocation density, and parameters associated with dislocation boundaries, as their spacing and misorientation angles, can be taken as governing microstructural features. In order to comply with this constitutive task, the ideas introduced by researchers such as *Kuhlmann-Wilsdorf*, *Hughes*, *Hansen* and co-authors [Kuhlmann-Wilsdorf, 1989; Bay et al., 1992; Hughes and Hansen, 2000; Hansen, 2004; Hansen and Barlow, 2014] are followed. This approach is based on strengthening contributions due to low angle ($\theta < 15°$) IDBs and GNBs in a CB structure from low to moderate strains (Stages II and III), and high angle ($\theta \geq 15°$) lamellar (or fibrous) structure formed at large strains (Stage V) [Hansen, 2004; Hansen and Barlow, 2014]. Accordingly, the current macroscopic yield stress can be given by the following equation [Kuhlmann-Wilsdorf and Hansen, 1991; Hansen, 2004; Gazder et al., 2008]:

$$\bar{R} = \sigma_y + A_{LAB} + A_{HAB}, \tag{1.1}$$

where $\sigma_y$ can be taken as the initial yield stress of a fully annealed material, $A_{LAB}$ and $A_{GNB}$ are hardening contributions related with LABs (Low Angle Boundaries) and HABs (High Angle Boundaries), respectively.

Considering a polycrystalline metal, in which the formation of dislocation cells governs the hardening behavior, experimental evidences have demonstrated that there exists an empirical relationship between $A_{LAB}$ and an average cell size $D_C$ [Kuhlmann-Wilsdorf and Hansen, 1991]:

$$A_{LAB} = \frac{k_1 \mu b}{D_C} \rightarrow A_{LAB} \propto \frac{1}{D_C}, \tag{1.2}$$

where $\mu$ is the elastic shear modulus, $b$ is the *Burgers* vector magnitude, and $k_1$ is a constant. Regarding term $A_{HAB}$, high angle boundaries have shown to present a hardening

contribution equivalent to that due to ordinary grain boundaries [Hansen, 2004]. Then, hardening variable $A_{HAB}$ can be given according to a *Hall-Petch* relationship [Hall, 1951; Petch, 1953; Kuhlmann-Wilsdorf and Hansen, 1991; Hansen, 2004]:

$$A_{HAB} = \frac{\bar{k}_2}{\sqrt{D_{HAB}}} = k_2\mu\sqrt{\frac{b}{D_{HAB}}} \rightarrow A_{HAB} \propto \sqrt{\frac{1}{D_{HAB}}}, \tag{1.3}$$

where $D_{HAB}$ is the spacing between HABs and $\bar{k}_2 \coloneqq k_2\mu\sqrt{b}$ is a constant. Then, Eq. (1.1) can be rewritten as

$$\bar{R} = \sigma_y + \mu\left(\frac{k_1 b}{D_C} + k_2\sqrt{\frac{b}{D_{HAB}}}\right). \tag{1.4}$$

In a simplified modeling devoted to monotonic loadings, a single isotropic hardening variable $A = A_{LAB} + A_{HAB}$ is commonly assumed:

$$\bar{R} = \sigma_y + A. \tag{1.5}$$

In the constitutive formulation to be developed in the present work, current material strength shall be given according to Eq. (1.5). But to simplify the notation, the isotropic hardening variable is considered to be given by $A = A_1 + A_2$. Although assumed hardening variables $A_1 \equiv A_{LAB}$ and $A_2 \equiv A_{HAB}$ may be related to microstructural parameters, the constitutive model to be formulated hereafter represents both strain and strain-rate hardening by means of phenomenological constitutive equations. Variable $A_1$ is assumed to govern the hardening behavior from small to moderate strain levels (at Stages II and III), and to correlate with an internal variable $\alpha_1 \propto \frac{1}{D_C}$, such that

$$A_1 \propto \alpha_1. \tag{1.6}$$

In contrast, $A_2$ is assumed to represent the *quasi*-linear hardening behavior at larger strains (at Stage V), and to be given in terms of an internal variable $\alpha_2 \propto \sqrt{\frac{1}{D_{HAB}}}$:

$$A_2 \propto \alpha_2. \tag{1.7}$$

Although internal variables $\alpha_1$ and $\alpha_2$ are assumed to have a correlation with physical features as $D_C$ and $D_{HAB}$, in the present work they are seen as effective parameters describing the macroscopic material hardening at Stages II, III, and at Stage IV, respectively. Accordingly, phenomenological evolution equations for $\alpha_1$ and $\alpha_2$, accounting for strain and strain-rate effects, will be addressed in this work.

In preceding topics, a metallurgical discussion on aspects associated with strain and strain-rate-induced hardening behavior have been provided. The last one refers to the

microstructural rate-sensitivity. However, there is still the rate-sensitivity corresponding to instantaneous rate-effects on the current flow stress. In metallic materials this instantaneous rate-sensitivity is associated with two main mechanisms: (i) thermally activated dislocation kinetics until moderate strain-rates; and (ii) dislocation drag mechanisms for greater strain-rates [Kocks et al., 1975; Meyers, 1994; Nemat-Nasser, 2009; François et al., 2012]. These two aspects are better discussed in the sequel.[4]

### 1.4.5 Thermal activation and dislocation drag mechanisms

While moving through the crystalline lattice, a dislocation continuously faces numerous barriers. The motion of dislocations is opposed by short-range (e.g., the *Peierls-Nabarro* resistance and dislocations trapping the slip plane) and long-range (e.g., the elastic field due to other defects as grain boundaries and far field forest of dislocations) obstacles. In addition, the dislocation must overcome any drag resistance that may act on it as the dislocation moves from one set of short-range barriers to the next. Therefore the energetic resistance to be overcome by a dislocation to move a given distance is the combination of short and long-range energy barriers [Kocks et al., 1975; Meyers, 1994], as schematically shown in Figure 1.18(b). While short-range obstacles can be overcome with the add of thermal activation (or oscillation) mechanisms, long-range barriers do not directly depend on the temperature or on the plastic strain-rate. In fact, following a simplified isothermal approach, the athermal resistance can be assumed to be approximately equal to the mechanical strength, $\sigma_y + A$, due to the current microstructural configuration given explicitly in Eq. (1.5). Keeping in mind the preceding discussion on strain and strain-rate-induced hardening, the temperature and strain-rate influence on long-range resistance occurs only in a indirect way, by means of temperature and strain-rate dependent microstructural evolution. However, in order to complete the present metallurgical discussion on constitutive aspects associated with the plastic deformation of metals, the underlying mechanisms responsible for the instantaneous flow stress rate-sensitivity still have to be addressed. With this purpose, the overall flow stress response can be written as

$$\sigma_{flow} = \sigma_y + A + \sigma_v, \tag{1.8}$$

where $\sigma_v$ is the viscous stress, which in this simplified discussion corresponds to the strength due to short-range barriers.

In order to correlate the viscous stress $\sigma_v$ with imposed inelastic strain-rate, one can consider the mobile dislocation of Figure 1.18(a), which moves a distance $\bar{d} = d_r + d_{sr}$ from point 1 to position 2. During the motion the dislocation has to overcome the overall

[4]This explanation consists of a simplified discussion about thermally activated dislocation kinetics and dislocation drag mechanisms. However, for an in depth discussion on these subjects, works of Kocks et al., 1975, Meyers, 1994, Nemat-Nasser, 2009, and François et al., 2012, are referenced.

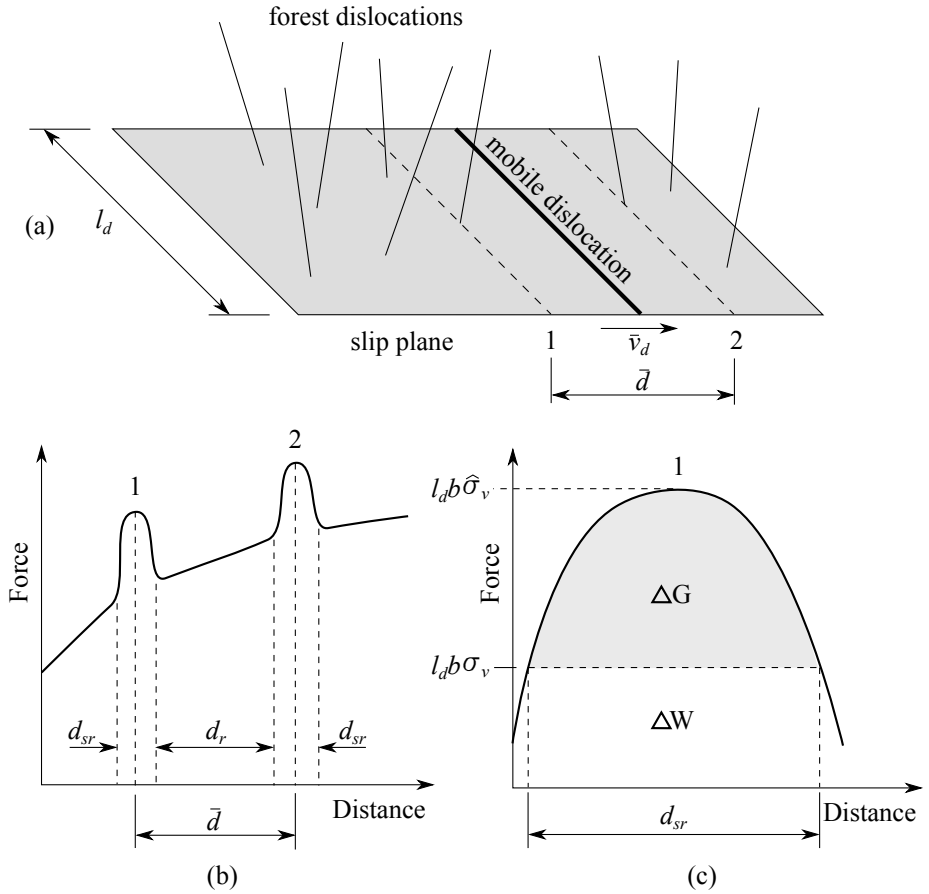


Figure 1.18: (a) Mobile dislocation traveling from obstacle 1 to 2; (a) Overall energy barrier to be overcome by the mobile dislocation; (c) Detail of the energetic short-range barrier at position 1. See also Kocks et al., 1975.

energetic barrier illustrated in Figure 1.18(b). The short-range energetic barrier opposing the dislocation motion at position 1 is detailed in Figure 1.18(c). Thus focusing on the viscous stress $\sigma_v$, supposing that the total energy needed to overcome the obstacle 1 is $G_0$, and that the thermal oscillation is capable of supplying an energy $\Delta G < G_0$, thus the remaining amount of energy is the work to be performed by $\sigma_v$ to cross the barrier width $d_{sr}$:

$$\Delta G = G_0 - \sigma_v V^*, \tag{1.9}$$

where $V^* := b d_{sr} l_d$ is the activation volume needed to overcome this obstacle, $l_d$ is the dislocation length, and $b$ is the *Burgers* vector magnitude. For a given temperature, the frequency at which the energy $\Delta G$ is supplied by the corresponding thermal oscillation is

$$\omega = \omega_0 \exp\left(-\frac{\Delta G}{k\theta}\right), \tag{1.10}$$

where $k$ is the *Boltzmann* constant, $\theta$ is the absolute temperature and $\omega_0$ is the thermal oscillation frequency of this dislocation. Notice that, the higher the temperature the higher the frequency at which $\Delta G$ is supplied. The time the dislocation takes to move

the distance $\bar{d}$ is $\Delta t$. This time is composed by the period during which the dislocation waits for a successful attempt to overcome the barrier 1, $t_w$ (waiting time), and by the time taken to travel from point 1 to 2, $t_r$ (running time), thus

$$\Delta t = t_w + t_r. \tag{1.11}$$

The waiting period is given by

$$t_w = \frac{1}{\omega} = \frac{1}{\omega_0} \exp\left(\frac{\Delta G}{k\theta}\right). \tag{1.12}$$

From low to moderate strain-rates one has $t_w \gg t_r$, thus $\Delta t \approx t_w$ [Kocks et al., 1975; Meyers, 1994]. Consequently, the mean dislocation velocity within the distance $\bar{d}$ can be expressed as

$$\bar{v}_d = \frac{\bar{d}}{t_w} = \bar{d}\omega_0 \exp\left(-\frac{\Delta G}{k\theta}\right). \tag{1.13}$$

Therefore knowing the *Orowan* kinetic equation [Orowan, 1945]

$$\dot{\varepsilon} = \rho_m b \bar{v}_d, \tag{1.14}$$

we obtain an expression for the rate of plastic strain $\dot{\varepsilon}$ due to the motion of a density $\rho_m$ of mobile dislocations traveling the distance $\bar{d}$:

$$\dot{\varepsilon} = \dot{\varepsilon}_0 \exp\left(-\frac{\Delta G}{k\theta}\right), \tag{1.15}$$

where $\dot{\varepsilon}_0 \coloneqq \rho_m b \bar{d} \omega_0$ can be seen as a reference plastic strain-rate. Expression (1.15) consists of a kinetic equation representing the plastic flow at a constant structure. The main task is to express the energy barrier $\Delta G$ in terms of the stress $\sigma_v = \sigma_{flow} - (\sigma_y + A)$ and the temperature. A general expression for $\Delta G$ was proposed by Kocks et al., 1975, which reads

$$\Delta G = G_0 \left[1 - \left(\frac{\sigma_v}{\hat{\sigma}_v}\right)^p\right]^q, \tag{1.16}$$

in which $0 < p \leq 1$ and $1 \leq q \leq 2$ are parameters depending on the energy barrier profile controlled by the kind of obstacle and material structure. In general, $\sigma_v$ is a state function of both temperature and strain-rate, being $\hat{\sigma}_v$ the viscous stress at $\theta \to 0\,K$. Equations (1.15) and (1.16) complete the kinetic description of the plastic flow governed by thermal activation mechanisms. This proposal fits into a physically-based approach. However, simplified kinetic equations were proposed by some authors in order to deal with isothermal problems and avoid the determination of material strength at $\theta \to 0\,K$. Proposals of Perzyna, 1966, 1986, Perić, 1993, and Bodner and Rubin, 1994, can be cited as examples.

Thermal activation mechanisms control the plastic flow from low to intermediate strain-rates ($\approx 10^3\,\mathrm{s}^{-1}$). However, when strain-rates approaching $10^4\,\mathrm{s}^{-1}$ are imposed, the viscous drag resistance becomes pronounced, and effective stresses higher than $\sigma_v$ are needed to proceed with plastic deformation. In this case, the flow stress can be given by

$$\sigma_{flow} = \sigma_y + A + \sigma_v + \sigma_{vd}, \tag{1.17}$$

where $\sigma_{vd}$ is the viscous drag resistance opposing the dislocation motion from one short-range obstacle to the next, e.g., from 1 to point 2 of Figure 1.18(a). In a very simplified way, $\sigma_{vd}$ can be correlated with the dislocation running velocity $\bar{v}_r$ by a linear relationship:

$$\bar{v}_r = \frac{b}{B}\sigma_{vd}, \tag{1.18}$$

where $B$ is a damping coefficient. Consequently, in a situation where very high strain-rates are imposed, the viscous drag resistance controls the dislocation motion, $\bar{v}_d \approx \bar{v}_r$, and then, using Eq. (1.14), the strain-rate reads [Kocks et al., 1975; Meyers, 1994; Nemat-Nasser, 2009]

$$\dot{\varepsilon} = \frac{\rho_m b^2}{B}\sigma_{vd}. \tag{1.19}$$

In fact, in a general plastic deformation process, mainly from moderate to high strain-rates, the inelastic flow is controlled by a combination of thermal activation and viscous drag mechanisms. Thus, a constitutive proposal to be employed from low to high strain-rate regimes has to comply with this task. There are physically-based kinetic equations dealing simultaneously with these two mechanisms [Regazzoni et al., 1987; Nemat-Nasser and Li, 1998; Gao and Zhang, 2012; Rodríguez-Martínez et al., 2011]. However, phenomenological approaches as those previously cited [Perzyna, 1966, 1986; Perić, 1993; Bodner and Rubin, 1994], do not account in general for viscous drag mechanisms. Thus, in order to comply with this modeling task, the model proposed by Perić, 1993 is modified. Model of Perić, 1993, circumvents some numerical problems associated with the model of Perzyna, 1966, 1986.

## 1.5 High strain-rate constitutive modeling of metals

According to the preceding discussion, a suitable constitutive model to predict high strain-rate behavior of metals should account at least for strain and strain-rate-history effects, since corresponding material hardening (mainly of FCC metals) is strongly rate-dependent at high velocity conditions [Klepaczko, 1975; Chiem and Duffy, 1983; Tanner and McDowell, 1999; Huang and Tao, 2011; Luo et al., 2012a]. However, a constitutive model to be employed in large scale engineering computations should incorporate suitable constitutive capabilities, while keeping it simple enough to be experimentally and

numerically “attractive”.

In general, the great majority of Internal State Variable (ISV) viscoplastic models (e.g., those of Perzyna, 1966, 1971, Perić, 1993, Ristinmaa and Ottosen 1998, Simo et al. 1988, and Alfano et al., 2001) are proposed in order to account for instantaneous rate-effects during plastic deformation. But they disregard the hardening dependence on strain-rate. However, as previously discussed in Subsection 1.4.3 and evidenced by experiments of Subsection 2.2.3, accounting for rate-dependent microstructural evolution, even following a macroscopic description, becomes an important feature within a high strain-rate constitutive formulation. In this sense, a variety of ISV models accounting for strain-rate-history effects have been proposed in the literature. In this context, relevant references include the works of Bodner and Partom, 1975, Anand, 1985, Klepaczko and Chiem, 1986, Follansbee and Kocks, 1988, Tong et al., 1992, Bodner and Rubin, 1994, Molinari and Ravichandran, 2005, and recently those of Rusinek et al., 2010, Gao and Zhang, 2012, Vilamosa et al., 2016, and Yan et al., 2016. See also reviews on high strain-rate constitutive modeling, as those of Meyers, 1994, Chaboche, 2008, Klepaczko, 2009, Rusinek and Jankowiak, 2014, and Xu and Huang, 2015.

Tanner and McDowell, 1999, investigated experimentally loading-history effects on response of annealed high purity copper at various strain-rates and temperatures. In a subsequent work, Tanner et al., 1999, calibrated and compared the JC [Johnson and Cook, 1983], the MTS (*Mechanical Threshold Stress*) [Follansbee and Kocks, 1988], and the BCJ [Bamman et al., 1996] models. These authors concluded that the BCJ model provides a better performance than that presented by the MTS model. However, specifically on room temperature decremental strain-rate test, comparison results have shown some scattering between predictions and experiments, for both MTS and BCJ models. Comparisons between phenomenological and physically-based constitutive models [Johnson and Cook, 1983; Zerilli and Armstrong, 1992; Nemat-Nasser and Li, 1998; Khan et al., 2004; Voyiadjis and Abed, 2005; Rusinek et al., 2010] considering FCC metals were also performed by Xu and Huang, 2015 employing a high purity copper. As a result, physically-based models, i.e., based on the MTS approach [Follansbee and Kocks, 1988; Nemat-Nasser and Li, 1998; Rusinek et al., 2010], have presented a better description of the high strain-rate, large deformation behavior of FCC metals. This class of physically-based models allows for a detailed description of both material behavior and its current state, thus providing an appropriate framework for capturing loading-history effects. However, these models require complex optimization algorithms and large computational efforts to find associated model constants, see for instance comments of Gao and Zhang, 2012.

Since a detailed physically-based description increase the model complexity and the number of constants to be adjusted (see also discussion of Rusinek and Jankowiak, 2014), and seeking for the formulation simplicity, researchers [Bodner and Rubin, 1994; Molinari and Ravichandran, 2005; Rodríguez-Martínez et al., 2009; dos Santos et al., 2016] have

Table 1.1: Constitutive characteristics of selected models. Source: dos Santos et al., 2016.

| Model | SRH | Stage IV | Temp. | AS | Number of parameters | | | |
|---|---|---|---|---|---|---|---|---|
| | | | | | Total | Phys. | Ref. | Adjust. |
| dos Santos et al., 2016 | √ | √ | × | √ | 10 | 0 | 2 | 8 |
| MR | √ | × | √ | √ | 14 | 0 | 4 | 10 |
| BPR | √ | × | × | × | 9 | 0 | 2 | 7 |
| MTS | √ | √/× | √ | × | 14 | 3 | 2 | 9 |

proposed semi-physical constitutive models, which possesses a lower number of material parameters and require few experiments to identify them. Bodner and Partom, 1975, proposed an elastic-viscoplastic model (BP model) to predict the behavior of metals at different strain-rate and temperature histories within the context of continuum mechanics. Estrin and Mecking, 1986, extended the BP model to predict strain-rate-induced microstructural evolution by letting the internal variable saturation and hardening-rate to be rate-dependent. Some years after, Bodner and Rubin, 1994, proposed an isothermal modified BP model to account for extensive strain-hardening and strain-rate-induced hardening in copper at room temperature.

Aiming at providing a simplified viscoplastic model, Molinari and Ravichandran, 2005, proposed a high strain-rate constitutive formulation based on a single internal variable, which represents an effective microstructural feature. Although this model fits into a macroscopic phenomenological approach, the choice of the internal variable and its evolution were based on microstructural mechanisms, such as dislocation generation and annihilation processes and associated formation of dislocation cells, following ideas developed in physically-based models as those of Klepaczko and Chiem, 1986, Estrin and Mecking, 1984, and Nes, 1997. Thereby, the model proposed by Molinari and Ravichandran, 2005, is capable of accounting in a phenomenological manner for rate effects on the material strength, providing reasonable results in reproducing experimental data for copper tests under different strain-rates, temperatures, and strain-rate jumps. However, as the internal variable evolution saturates at a given strain level, the model is not able in its original form to account for strain-hardening at advanced strains, i.e., during deformation Stage IV. In this sense, in order to provide a simple constitutive alternative suitable to account for rate-dependent strain-hardening behavior of polycrystalline FCC metals, dos Santos et al., 2016, recently proposed a viscoplastic formulation within the ISV thermodynamics framework. Proposed phenomenological constitutive model showed very good agreement with experimental data of annealed high purity copper obtained during large strain, high strain-rate cold deformation processes. The model proposed by dos Santos et al., 2016, fits into a semi-physical context, once the internal state variable and its evolution were also based on dislocation dynamics processes.

With the aim of summarizing the present discussion on viscoplastic modeling and providing a clear visualization on some of mentioned viscoplastic proposals, some single internal variable models are highlighted in Table 1.1, namely the models of Bodner and Rubin, 1994, (BPR), Molinari and Ravichandran, 2005, (MR), Follansbee and Kocks, 1988, (MTS). This table also presents characteristics related to the model [dos Santos et al., 2016] that will be taken as basis in this work. Both the BPR and MR models consist of simplified formulations widely employed in viscoplastic modeling of loading-history effects. The MTS model is introduced to compare the simplified ones with a physically-based model. Comparison presented in Table 1.1 consists of assessing some constitutive features related to those models, namely the ability of representing the deformation Stage IV, strain-rate (SRH), and temperature (Temp.) history effects, as well as the simplicity of the internal variable evolution equation, i.e., if it allows an analytic solution (AS). Furthermore, the number of material parameters, which are classified as physical (Phys.), adjustable (Adjust.), and non-adjustable or reference (Ref.) parameters, are also assessed. Unidimensional constitutive formulations related to each of the selected models are shown in Table A.1 presented in Appendix A, where constitutive equations associated with unidimensional flow stress ($\sigma_{flow}$), internal state variable and its evolution, as well as strain-rate-history effects and related model parameters are addressed.

All models of Table 1.1 should be able of representing strain-rate-history effects. However, the MR, BPR, and MTS models in their original form cannot account for constant hardening-rate at larger strains (the deformation Stage IV). The MTS model, in a first stage can prevents the stress saturation at given strain level. But, as discussed by Kok et al., 2002, this model saturates with strain. In this table, only the MR and MTS models are able of modeling thermal effects. Furthermore, among the models analyzed, those of Molinari and Ravichandran, 2005, and dos Santos et al., 2016, allow to obtain analytical expressions for the ISV evolution. Concerning the number of parameters, the BPR model exhibits the lower number of constants to be adjusted. However, as discussed earlier, this model does not account for hardening in Stage IV, and it seems that at least one parameter is needed to perform this task. Among the simplified models, the MR model (under isothermal condition) and that proposed by dos Santos et al., 2016, have 8 parameters to be calibrated.

In order to provide constitutive comparisons related to the viscoplastic proposals cited above, Appendix A compares the model proposed by dos Santos et al., 2016, with models of Follansbee and Kocks, 1988, Bodner and Rubin, 1994, Bamman et al., 1996, and of Molinari and Ravichandran, 2005, in predicting decremental strain-rate experiments for an annealed high purity copper. In a general way, the model proposed by dos Santos et al., 2016 presents better predictions within the conditions considered. Although the model of dos Santos et al., 2016, has been developed within the context of the present thesis, its calibration was performed by employing experimental results available in the

literature [Nemat-Nasser and Li, 1998; Tanner and McDowell, 1999; Jordan et al., 2013]. Therefore, the present work aims at obtaining original experimental data (considering a commercially pure aluminum), and then improving the model recently formulated [dos Santos et al., 2016] in order to properly representing the experimental observations. As a result of this improvement, the formulation previously published [dos Santos et al., 2016] will be a particular case of the viscoplastic model to be developed here. The detailed work proposal is provided in the following section.

## 1.6 Work outline

In Chapter 2, material details, experimental equipments and procedures are described. Experimental development is devoted to characterize specific constitutive features: strain-hardening, strain-rate-hardening and instantaneous rate-sensitivity. Corresponding experimental results are presented in Section 2.3. *Quasi*-static material behavior is identified considering strain-induced evolution of both flow stress and material hardness. Considering those results, an empirical correlation between current yield stress and material hardness is proposed. The strain-rate-hardening feature, which is intimately related to material microstructure evolution and its current state, is macroscopically assessed by evaluating strain-rate effects on material hardness. Considering obtained material hardness data, and using the yield stress-material hardness correlation, current (rate-dependent) material strength is therefore estimated. Instantaneous rate-sensitivity is assessed by means of high velocity compressions employing constant strain-rates. As a result, experimental high strain-rate flow stress-strain curves are then obtained. Strain-rate-history effects on the behavior of tested material are identified by performing sequential strain-rate experiments, namely, decremental strain-rate tests, and strain-rate jump tests, thus evaluating corresponding flow stress and material hardness evolution.

Chapter 3 describes the finite strain framework employed for modeling the mechanical behavior of an elastic-viscoplastic body. Some continuum mechanics background considering a *Total Lagrangian* finite strain framework is presented in Section 3.1. These fundamentals consists of describing equilibrium equations as well as associated boundary conditions, and further stating thermodynamic principles to be complied with by the viscoplastic constitutive model to be developed in Section 3.2. Having as reference the obtained experimental results, an elastic-viscoplastic model is then proposed. Constitutive formulation generalizes the model proposed by dos Santos et al., 2016, which proved to be a suitable simplified alternative in modeling finite strain, high strain-rate cold deformation of an annealed high purity copper [Nemat-Nasser and Li, 1998; Tanner and McDowell, 1999; Jordan et al., 2013]. The present development is intended to provide a phenomenological constitutive framework for modeling the rate-dependent strain-hardening behavior of polycrystalline FCC metals. Constitutive development assumes a homogeneous mate-

rial possessing both elastic and inelastic isotropy, and it follows a macroscopic phenomenological (or semi-physical) framework. This constitutive formulation adopts a *von Mises* plasticity employing a strain-rate dependent isotropic hardening whose evolution equations follow the *overstress* framework of Perzyna, 1966, 1971.[5] The isotropic hardening is taken into account by two scalar internal variables, which can be interpreted as effective microstructural features. A new phenomenological viscoplastic function accounting for thermally-activated and viscous drag mechanisms is also proposed.

Following with material behavior characterization, experimental data presented in Section 2.3 are used to adjust model parameters in Chapter 4. Model calibration is performed considering subsequent steps, what allows identifying separately each constitutive feature as well as verifying graphically the adjusted constants. This fact permits to employ simpler and more efficient gradient-based local algorithms as an alternative to global strategies. Calibrated model is therefore validated considering sequential strain-rate experimental results reasoning on both flow stress and material hardness.

Chapter 5 presents both global and local numerical formulations. Section 5.1 outlines the global strategy adopted for solving associated equilibrium problem satisfying imposed boundary conditions. Time discretization follows an implicit strategy and space discretization is carried out by using the Finite Element Method (FEM). Obtained nonlinear incremental boundary value problem is iteratively solved by the *Newton-Raphson* method. Section 5.2 describes the local incremental constitutive formulation. Present approach follows standard works on isotropic finite strain (visco)plasticity, as those of Eterovic and Bathe, 1990, and Weber and Anand, 1990, thus employing an exponential implicit integration scheme. Related nonlinear equations are solved by using an elastic predictor-plastic corrector algorithm. Therefore, adopted numerical strategy furnishes incremental elastic-viscoplastic solutions associated with each reversible or irreversible deformation increment. From linearization of corresponding return mapping equations, an analytical consistent tangent operator is obtained, which is then employed in the iterative solution of related global equilibrium equations using FEM.

In Chapter 6 numerical results obtained by using the present approach are therefore presented. Numerical simulations consists of compression tests considering both homogeneous deformation and frictional billet upsetting. Numerical tests have the aim of demonstrating corresponding model capabilities and numerical robustness. Our conclusions and comments are given in Chapter 7.

Appendix A provides the uniaxial flow stress formulations corresponding to viscoplastic models outlined in Table 1.1. In addition, this appendix also compares some viscoplas-

[5]We have also to mention that there are other viscoplastic framework in which a phenomenological or even physically-based model can be embedded, e.g., the overstress model of *Duvaut-Lions* [Duvaut and Lions, 1976; Simo et al., 1988; dos Santos et al., 2015b], that of *Krempl* [Krempl and Gleason, 1996; Krempl, 1996], or the consistency model of *Wang* [Wang et al., 1997]. A comparison between models of *Perzyna* and of *Wang* was done by Zaera and Fernández-Sáez, 2006.

tic model in predicting experimental results obtained from decremental strain-rate tests for high purity copper samples. Appendix B describes numerical aspects related to the numerical strategy adopted in solving both global and local problems as well as model calibration. Specifically, topic B.5 presents a qualitative finite element analysis (using software *Abaqus*) on the dynamic behavior of the developed compression tool.

# 2 EXPERIMENTAL PROCEDURES AND RESULTS

This chapter reports aspects related to the employed material (aluminum AA1050) and it provides construction and technical characteristics associated with the developed and used equipments. Furthermore, experimental procedures used to characterize the desired material behavior and corresponding results are also presented.

## 2.1 Employed material

Chemical composition of aluminum AA1050 (99.5% wt) to be employed in this work is given in Table 2.1. Cylindrical specimens with nominal dimensions of Ø6 × 6 mm were cut from a cold-rolled plate using wire electrical discharge machining and finished by turning. End faces of the specimens had smooth concentric circular patterns and cutting parameters were set in order to obtain an initial average surface roughness (Ra) below 0.3 $\mu$m. The material employed in experiments has been annealed at 450 °C during 2 h, followed by a natural cooling in air. The initial grain size of the samples after annealing were measured by metallographic examination and it was found to varies from 100 to 300 $\mu m$. Corresponding specimen dimensions and material metallography are showed in Figure 2.1.

Table 2.1: Chemical composition of aluminum AA1050.

| Element | Cu | Mg | Si | Fe | Mn | Zn | Ti | Al |
|---|---|---|---|---|---|---|---|---|
| % weight (max.) | 0.05 | 0.05 | 0.25 | 0.4 | 0.05 | 0.07 | 0.05 | Balance |

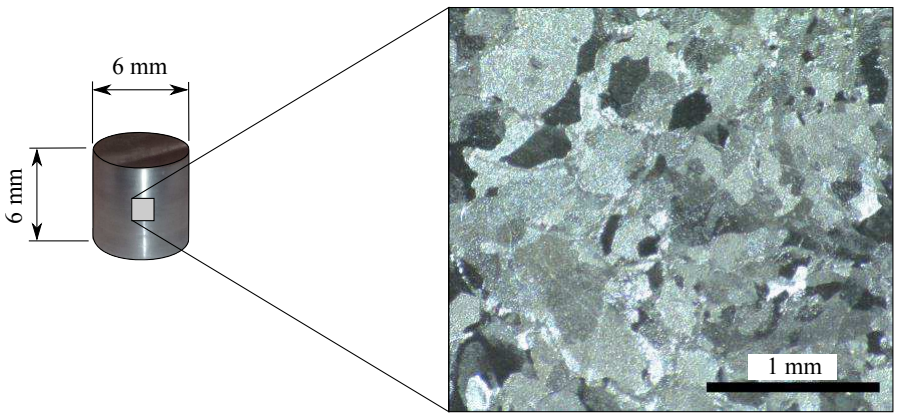


Figure 2.1: Optical micrography of annealed aluminum AA1050. Sample was chemically etched by using a modified *Poulton* solution. For details on the metallographic analysis see Reis et al., 2016.

## 2.2 Experimental equipments

This section is intended to outline the experimental equipments developed at the *Instituto Superior Técnico* of Lisbon, Portugal, under the supervision of Professor Pedro Rosa, for characterizing the *quasi*-static and dynamic material behavior, reasoning on constitutive features as strain-hardening, strain-rate-hardening and viscous effects.

Material characterization is performed by means of compression tests. For this purpose specific experimental apparatus were developed: (i) a new compression tool dedicated to compression testing; and (ii) a gas gun machine to perform high strain-rate compressions. Developed and commercial experimental equipments used in material characterization are better described in the following subsections.

### 2.2.1 Compression tool

In order to perform the corresponding experiments, an instrumented compression tool is developed. This tool is dedicated to compression testing of cylindrical specimens with both diameters and heights varying from 2 mm to 8 mm. However, here specimens with nominal dimensions of $\emptyset 6 \times 6$ mm are used. The aim of this development is to obtain a proper rigid compression tool, in which both displacement and load measurements associated with compressions are carried out as close as possible to the experimented specimen. By making that, experimental errors associated with deformation of tools and testing machine structure are strongly reduced. Developed compression tool is shown in Figure 2.2. The whole apparatus consists of a high strength steel cylindrical chamber, where two compression platens are assembled: (i) a fix one, which is positioned over a piezoelectric load cell (*Kistler* 9137B, maximum load of 80 kN); and (ii) a mobile one, which is guided by rubber O-rings, and where the load is applied. The compression platens utilized in the experimental tests have been machined and polished in order to limit the average values of surface roughness (Ra) in the range $0.07 - 0.15\,\mu$m. At the described compression platens, copper spiral coils are attached, which compose the developed displacement sensor described in subsequent topic. To the load cell, following recommendations from the manufacturer, a preload of 10 kN is applied [Kis, 2016]. Then, in order to reduce associated preload loss during compression, *Belleville* washers are assembled with the preload bolt. Furthermore, the load cell is aligned by using a polymeric guide.

The primary coil, assembled in the fixed compression platen, is connected to a function generator (*Thurlby Thandar instruments* TG120), which provides an alternate electric current of 10 MHz with an electric potential of 20 V. In order to avoid short-circuit due to its low electric resistance of $\sim 1\,\Omega$, the primary coil is connected in series with a resistor of $20\,\Omega$. The secondary coil is connected to a full-bridge diode (1N5819) rectifier with a capacitor of $0.21\,\mu$F, whose output, by means of a BNC connecting board (*National Instruments* BNC-2120), is connected to a Data Acquisition (DAQ) board (*Na-*

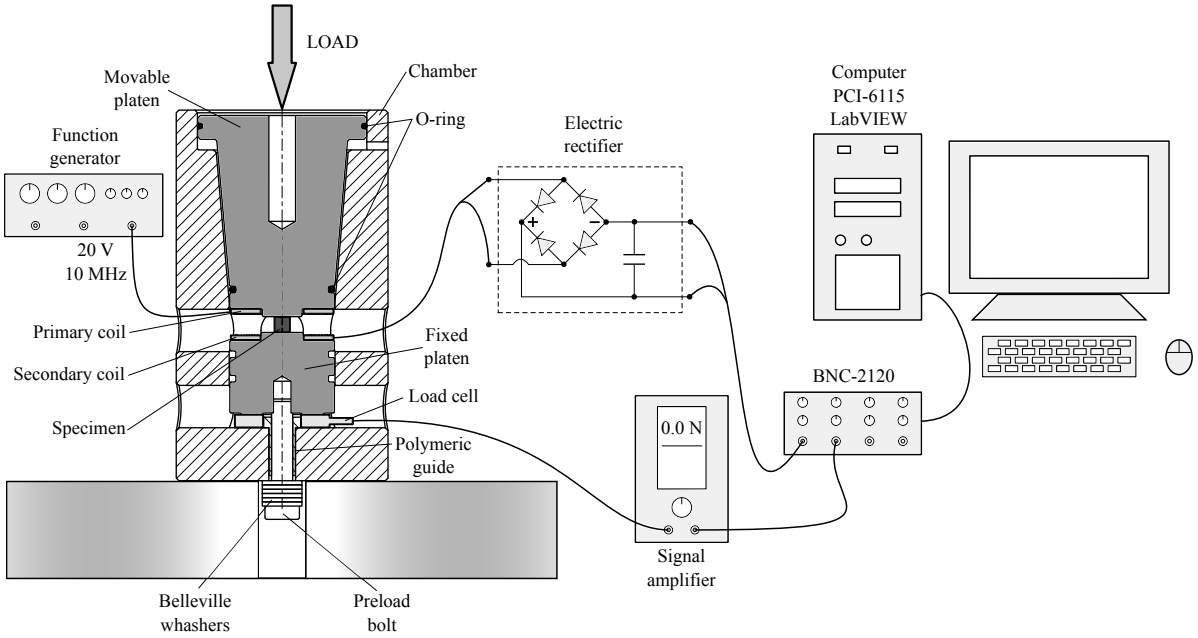


Figure 2.2: Schematic representation of compression tool and associated data acquisition.

*tional Instruments* PCI-6115, 12-Bit, 10 MS/s/ch), to which the signal amplifier (*Kistler* type 5015A, 1 MS/s) of the piezoelectric load cell is also connected. Acquired data are processed by using the software *LabView* installed in a dedicated computer.

Displacement sensor

The displacement sensor is composed by two copper spiral coils built from printed circuit boards (PCBs), see schematic representation of Figure 2.3(a). This sensor works by an inductive action. In order to allow high velocity compression tests, an alternated electric current of 10 MHz with an electric potential of 20 V is furnished to the primary coil. Due to the electromagnetic coupling between the coils, an alternate electric current is induced in the secondary one. The electric potential associated with the induced charge depends on the distance $l$ between the coils, see Figure 2.3(b). In this case, the distance is the specimen height. In this manner, to measure the current specimen height during compression, the electric potential $V_e$ measured at the rectifier output is correlated with associated distance $l$ by means of calibration curve obtained *a priori* (see Figure 2.4). The correlation follows the functional form:

$$l = a_0 + a_1 \ln (V_e) , \tag{2.1}$$

where $a_0$ and $a_1$ are constants to be adjusted. In fact, the calibration curve $l - V_e$ is given by a logarithmic function. Then, by knowing the initial $l_0$ and final $l_f$ specimen lengths as well as respective electric potentials, $V_{e_0}$ and $V_{e_f}$, one can confirm or obtain specific calibration curve corresponding to each compression test. Since the sensor is assembled

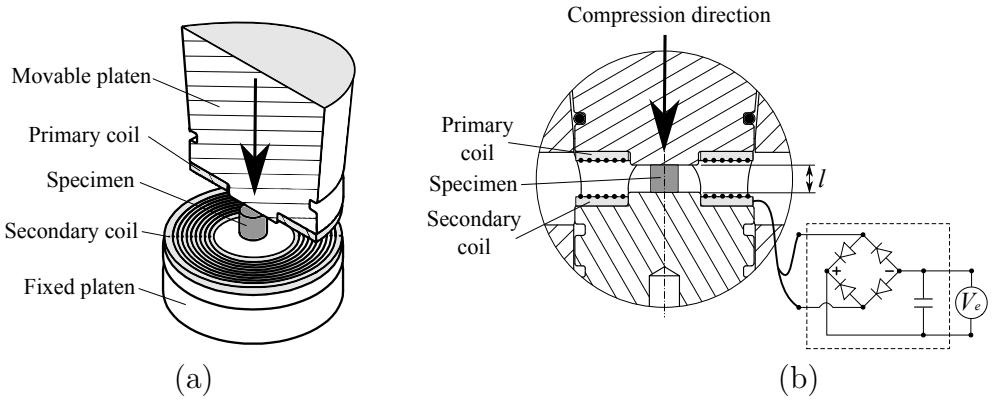


Figure 2.3: Schematic representation of (a) displacement sensor as well as (b) respective specimen height $l$ and acquired electric voltage $V_e$.

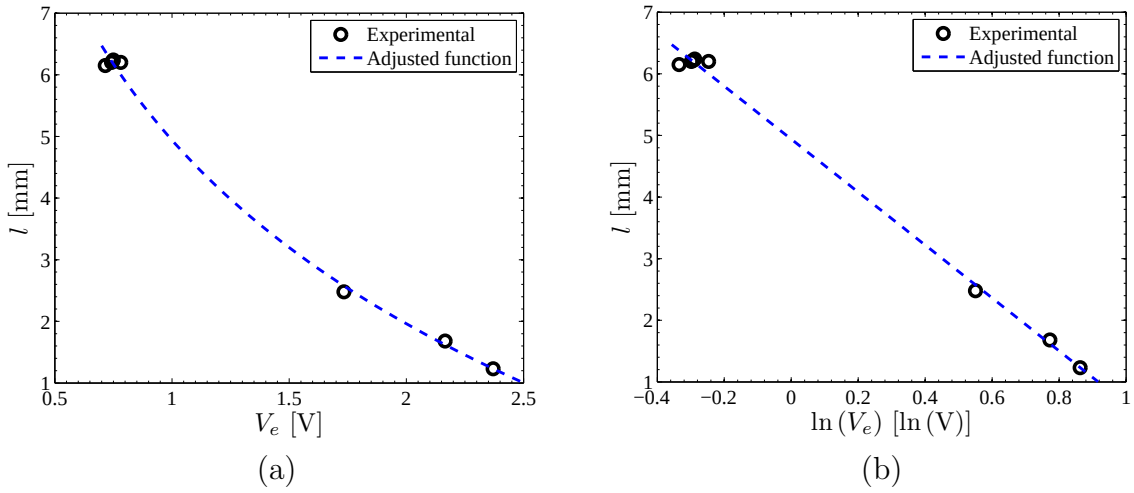


Figure 2.4: Calibration curve of the specimen height $l$ in terms of measured electric voltage $V_e$: (a) linear scale; (b) logarithmic scale.

directly on the compression platens, Figure 2.3(b), this apparatus is less sensible to elastic strain occurring in the tool or machine structures than in conventional equipments, what provides more precise measurements of the specimen height during compression.

Developed displacement sensor as well as respective data acquisition system is suitable to high strain-rate compressions, once this inductive sensor, combined with a high frequency function generation and an appropriate electric rectifier on the output, allows to obtain a high rate displacement data acquisition.

### 2.2.2 High velocity compression machine (gas gun machine)

The high velocity testing machine is composed of a metallic vessel, which is then pressurized. Figure 2.5(a) shows the machine with its trigger valve closed, and thus with the striker bar at rest. Testing is performed by manually actioning the trigger valve, allowing the passage of pressurized air from the vessel to the tube (Figure 2.5 (b)) where a brass striker bar (with $\oslash 25 \times 190\,\text{mm}$ and $\sim 800\,\text{g}$) is inside. The air pressure

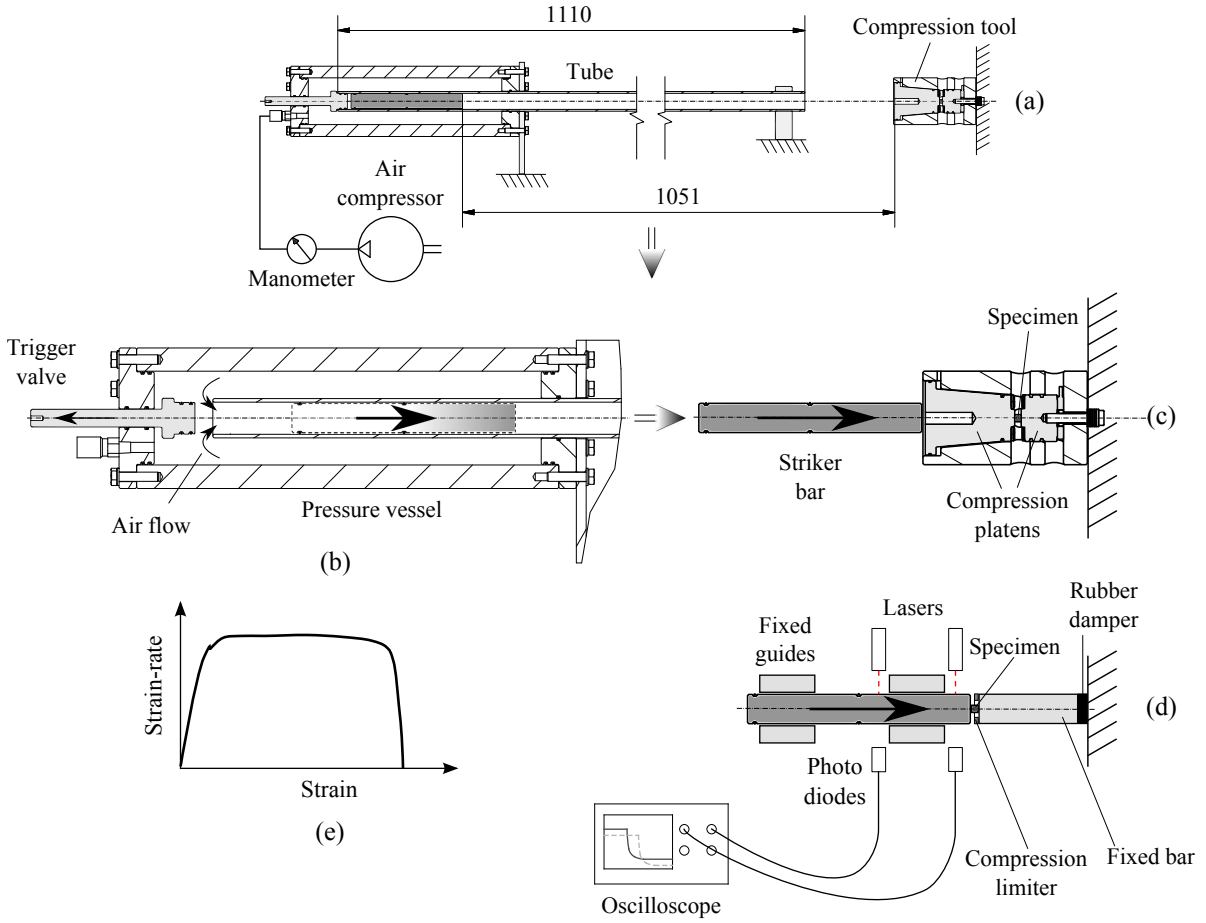


Figure 2.5: Schematic representation of high velocity compression machine: (a) Closed trigger valve, striker bar at rest; (b) Detail of open trigger valve, beginning of high velocity compression; (c) Detail of striker bar hitting the compression tool; (d) Detail of simplified assembling, striker bar hits directly the specimen; (e) Schematic representation of strain-rate vs. strain loading path.

drives the bar, which after traveling along the tube, hits the compression tool (described in Subsection 2.2.1), thus performing the specimen compression, as shown in detail in Figure 2.5(c). During the compression test, load and displacement data are acquired following data acquisition system described in Subsection 2.2.1. Both load (piezoelectric) and displacement (inductive) sensors can work under high frequency conditions, and the DAQ board PCI-6115 has four simultaneous analog inputs at 10 MHz per channel. As already pointed out, these features are suitable to adequately acquire force-displacement data during high velocity compressions.

As characteristic, at high velocity compressions, this apparatus can perform compressions at *quasi*-constant strain-rates. See Figure 2.5(e) for illustration.

Simplified assembling

The simplified high velocity compression machine combines the pneumatic actuator showed in Figure 2.5(b) and the compression tool displayed in Figure 2.5(d). In this

case, bar velocity right before impacting the specimen is measured by using two lighters and two photo diodes, which are connected to an oscilloscope. By knowing the distance between the two photo diodes, the bar velocity is calculated by the measured time interval between the interruption of lights by the traveling bar.

Straining of specimen is limited by high strength metallic rings. Limiter thickness ranges from 1.5 to 5.5 mm. However, it is clear that at these high strain-rate testing conditions the involved momentum and energies would be greatly enhanced by impact velocity. Indeed, after the compression test, the remaining energy is high enough to damage the testing machine components. Thus, the incident bar weight has been properly adjusted during the experimental research. In this simplified assembling, in which the bar impacts directly on the work piece, this is aimed to use adaptive incident bar based on metallic and polymeric parts. The velocity ranging from 6 to 60 $\frac{\mathrm{m}}{\mathrm{s}}$ corresponds to incident bar weights ranging from 800 to 25 g, respectively. Further, in order to reduce vibrations, propagation and reflection of elastic waves due to high velocity impact, a rubber damper is also used. Contact surfaces of both fixed and movable compression bars were also machined and polished, limiting the average roughness (Ra) in the range of $0.07-0.15\,\mu$m.

The machine configuration described above is going to be used to investigate strain-rate influence on material hardness evolution. As it can be seen, this compression machine is very simple, since, apart from lighters, photo diodes and oscilloscope, this equipment has no instrumentation for measuring displacements and forces. However, strains are calculated by measuring the initial and final specimen lengths. In addition, hardening tests are performed right after each incremental compression.

*Remark* 2.1. Observing Figure 2.2, one notes that the specimen is positioned on the superior part of the fixed platen. On the other hand, the load cell is assembled under this component. When using this tool considering *quasi*-static loadings, according to equilibrium conditions, the compression force employed on tested specimen is very close to that measured by the load cell. However, this fact can not be readily extended to high velocity compressions, in which dynamic effects due to impact and wave propagation are present. Thus, in order to qualitatively evaluate and compare the compression force applied to the work piece with that dynamically measured by the load cell, Appendix B.5 presents a finite element analysis on the compression apparatus, considering a high velocity compression. The finite element simulation is conducted in software Abaqus explicit. The analysis emphasizes the existent time delay between displacement and load data acquisition during high velocity tests. Numerical results show that oscillations observed on experimental flow stress (Figure 2.11(a)) would be due to dynamic behavior of the compression platen and load cell assembling. Furthermore, simulation results qualitatively demonstrate that, after performing appropriate corrections considering the time delay, in an average way the force imposed on the load cell is close to that applied on the compressed specimen. This would demonstrate numerically that the assembly composed by the fixed

platen and load cell does not present significant damping or dissipating effects.

### 2.2.3 Hardness measurements: microhardness test machine and samples preparation

Between each compression test, the material strength is determined by microhardness measurements using a *Struers* hardness tester model *Duramin* -1/-2 with a Vickers diamond, applying a load of 4.9 N during a loading time of 15 s. Before hardness measurements, specimens are progressively sanded down with 600, 800, 1200, 2500 and 4000 grit sandpapers using water. This procedure allows to remove the extra strained layer due friction at the contact interface between tested specimen and compression platens, to try and bring about a more realistic approach in respect to an idealized uniaxial compression testing. Each hardness measurement along this work is performed considering ten hardness points, five on each specimen end face. Concerning the annealed state, initial hardness measurements of all specimens resulted in an average value of approximately 220 MPa, with an standard deviation not exceeding 5 MPa. This initial hardness value will be used as a reference quantity in the experimental results to be presented hereafter.

## 2.3 Experimental results

This section presents the experimental results for the aluminum AA1050 starting from an annealed condition, using equipments described earlier. The experimental results to be presented herein evidence the corresponding material behavior and give support to subsequent constitutive development.

### 2.3.1 Preliminary experimental aspects

Although strain and stress measures have not been defined yet, to present the corresponding experimental results, at this moment the following logarithmic strain measure is adopted:

$$\varepsilon \coloneqq \ln\left(l_0/l\right), \tag{2.2}$$

being $l_0$ and $l$ the initial and current specimen lengths, respectively. In addition, flow stress values to be presented herein are calculated by the following equation:

$$\sigma_{flow} = \frac{F}{A_s}, \tag{2.3}$$

where $F$ is the current force applied to the specimen, and $A_s$ is its current cross section area, which is calculated as

$$A_s = \frac{\pi d_0^2 l_0}{4l}, \tag{2.4}$$

in which $d_0$ is the initial specimen diameter. Equation (2.4) is obtained by keeping in mind that in the present analysis large strains are imposed, thus the associated elastic

strain represents a small part, and by assuming that the plastic deformation does not induce significant volumetric changes.

Before each compression, a standard procedure to reduce friction between work pieces and compression platens is employed. For both hardness and stress analysis, the specimen contact surfaces are sanded down with 400, 600, 800, 1200, 2500 and 4000 grit sandpapers using water, and then lubricated with a thin grease film. Furthermore, it is worth mentioning that, in every case, the specimen initial length $l_0$ is measured after sanding processes, that is, right before the compression test. Furthermore, in high strain-rate experiments, in order to remove irregularities due to impact with work pieces, contact surfaces of compression tools are sanded down and polished after each three compression tests, thus guaranteeing compression surfaces with average values of roughness (Ra) in the range of $0.07 - 0.15\,\mu$m.

The preceding unidimensional and homogeneous stress definition infers that stress triaxialities induced by friction conditions during compression tests are disregard in the treatment of experimental results. Stress triaxialities, considering a low friction coefficient (due to appropriate lubrication) are evaluated by means of numerical simulations in Chapter 6, where the stress-strain fields and corresponding compression forces of frictional cases are compared with those associated with frictionless simulations.

### 2.3.2 Hardness-strain data

In order to investigate both strain and strain-rate effects on material hardness evolution *quasi*-static and high strain-rate compression are performed. Experiments have the aim of investigating the rate-dependent strain-hardening behavior of aluminum AA1050. *Quasi*-static experiments are conducted in a *Maquidral* CNC double effect hydraulic press with a maximum load of 500 kN. These tests are performed considering an average strain-rate in the order of $10^{-2}\,\mathrm{s}^{-1}$. High strain-rate compressions are performed using the simplified high strain-rate compression apparatus described in Subsection 2.2.2, see also Figures 2.5(b) and (d).

Experiments consist of compressing the specimens incrementally to a total strain of $\varepsilon \approx 1.5$ at different compression velocities. Incremental procedure considers deformation steps lower than 25% of the total applied strain ($\Delta\varepsilon \leq 0.4$). Specifically on dynamic compression, applied strain was limited by using high strength metallic rings. Furthermore, the incremental procedure was adopted in order to avoid significant thermal effects during high strain-rate compressions. This procedure justify the adoption of an idealized isothermal formulation to represent the obtained experimental data.

After each incremental deformation, both total strain ($\varepsilon$) and hardness ($H_V$) measurements are conducted. Hardness tests are performed according to the description given in Subsection 2.2.3. The surface preparation outlined is a useful procedure, since, in addition of preparing the specimens to perform the hardness measurements, the specimen

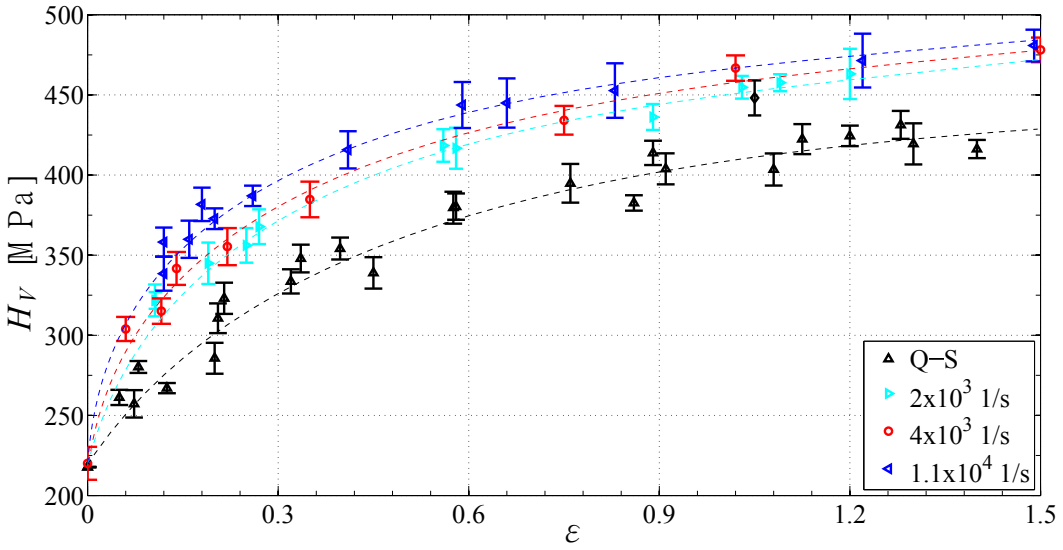


Figure 2.6: Hardness-strain experimental data obtained from constant strain-rate tests. Dashed lines are used only for visualization purposes.

end faces are then regularized (removing irregularities due to deformation and friction conditions) to the following compression step.

Compression tests are performed considering a wide strain-rate range, from *quasi*-static to high strain-rate conditions. The considered strain-rate values are: $10^{-2}$, $2\times10^3$, $4\times10^3$ and $1.1\times10^4\,\mathrm{s}^{-1}$. Incremental compressions provide hardness-strain data associated with employed strain-rates. These results are given in the sequel considering both constant strain-rate and sequential tests.

Constant strain-rate experiments

Constant strain-rate experimental results are displayed in Figure 2.6. In this figure, the initial hardness corresponds to the average value ($\approx 220\,\mathrm{MPa}$) of all annealed specimens. The other experimental data consist of an average of ten hardness measurements related to a given deformed specimen after each compression. Hardness points showed in Figure 2.6 present bars showing the corresponding standard deviation. Results of Figure 2.6 consist of four hardness-strain curves referring to a *quasi*-static testing ($\dot{\varepsilon} = 10^{-2}\,\mathrm{s}^{-1}$), and high velocity compressions performed at near constant strain-rates of $2\times10^3$, $4\times10^3$ and $1.1\times10^4\,\mathrm{s}^{-1}$. By analyzing the experimental results presented in Figure 2.6, one can realize the influence of imposed strain-rate on the material hardness evolution. This rate-dependence occurs in a manner that, for a given strain level, an increase in strain-rate increases the current material hardness. The strain-rate influence on material hardness is a macroscopic evidence of the material microscopic rate-sensitivity. As discussed in Section 1.4.3, the plastic deformation velocity has a significant influence on metallurgical features as the storage and arrangement of dislocations structures, which directly influence the formation of new sub/grains during dynamic recrystallization processes. Since the past

strain-rate-history has a major contribution on the current microstructural state [Zhang and Shim, 2010; Huang and Tao, 2011], it also does on the current material strength. The past rate-history influence on the macroscopic behavior of metals can be clearly realized by means of sequential strain-rate analyzes presented in the sequel.

Sequential strain-rate experiments

In order to investigate strain-rate-history effects on material hardness response, compressions involving decremental strain-rate and strain-rate jump tests are also performed. The specific sequential strain-rate experiments to be carried out are described in what follows:

- *Decremental strain-rate test*: Work piece is incrementally compressed to a given strain level at a high strain-rate. After this deformation, compression follows a low strain-rate loading, see schematic representations of Figures 1.7(a) and (c);

- *Strain-rate jump test*: In this case, the compression is started following a low strain-rate incremental loading. Then, from a given level of straining, deformation continues by imposing a high strain-rate deformation increments, see illustrations of Figures 1.7(b) and (d);

Experimental data concerning a decremental strain-rate test (test 1) is shown in Figure 2.7(a), in which at a given strain $\varepsilon_1 = 0.14$ the loading-rate is changed from a high strain-rate $\dot{\varepsilon} = 4 \times 10^3\,\mathrm{s}^{-1}$ regime to a *quasi*-static condition. Notice that in this case, the hardening state right before the decremental response is lower than the hardness saturation associated with the *quasi*-static monotonic loading. After a slight reduction in the hardness response is noticed, it restarts to increase. Analyzing the results given in Figure 2.7(a), one can realize that the decremental response tends asymptotically to the *quasi*-static curve. The difference between the decremental and *quasi*-static curves right after the change in strain-rate is due to an extra material strength induced by the previously imposed high strain-rate $\dot{\varepsilon} = 4 \times 10^3\,\mathrm{s}^{-1}$ until the strain of 0.14. As already commented, this behavior is a macroscopic evidence of strain-rate-dependent microstructural evolution. Figure 2.7(a) also shows a decremental strain-rate test, in which the hardness state right after the decremental response is greater than the *quasi*-static hardness saturation (test 2). In this case, at a given strain of $\varepsilon_1 = 0.43$, the strain-rate is changed from a high level of $\dot{\varepsilon} = 1.1 \times 10^4\,\mathrm{s}^{-1}$ to a *quasi*-static condition. Right after the strain-rate decrease, the hardness response shows a fast reduction and then a slight *quasi*-linear increasing, following a *quasi*-constant hardness-rate increasing similar to that associated with the *quasi*-static curve. In this case, the difference between the decremental and *quasi*-static responses is even higher than that of test 1, since imposed strain-rate and associated total strain are higher than those employed in the first test.

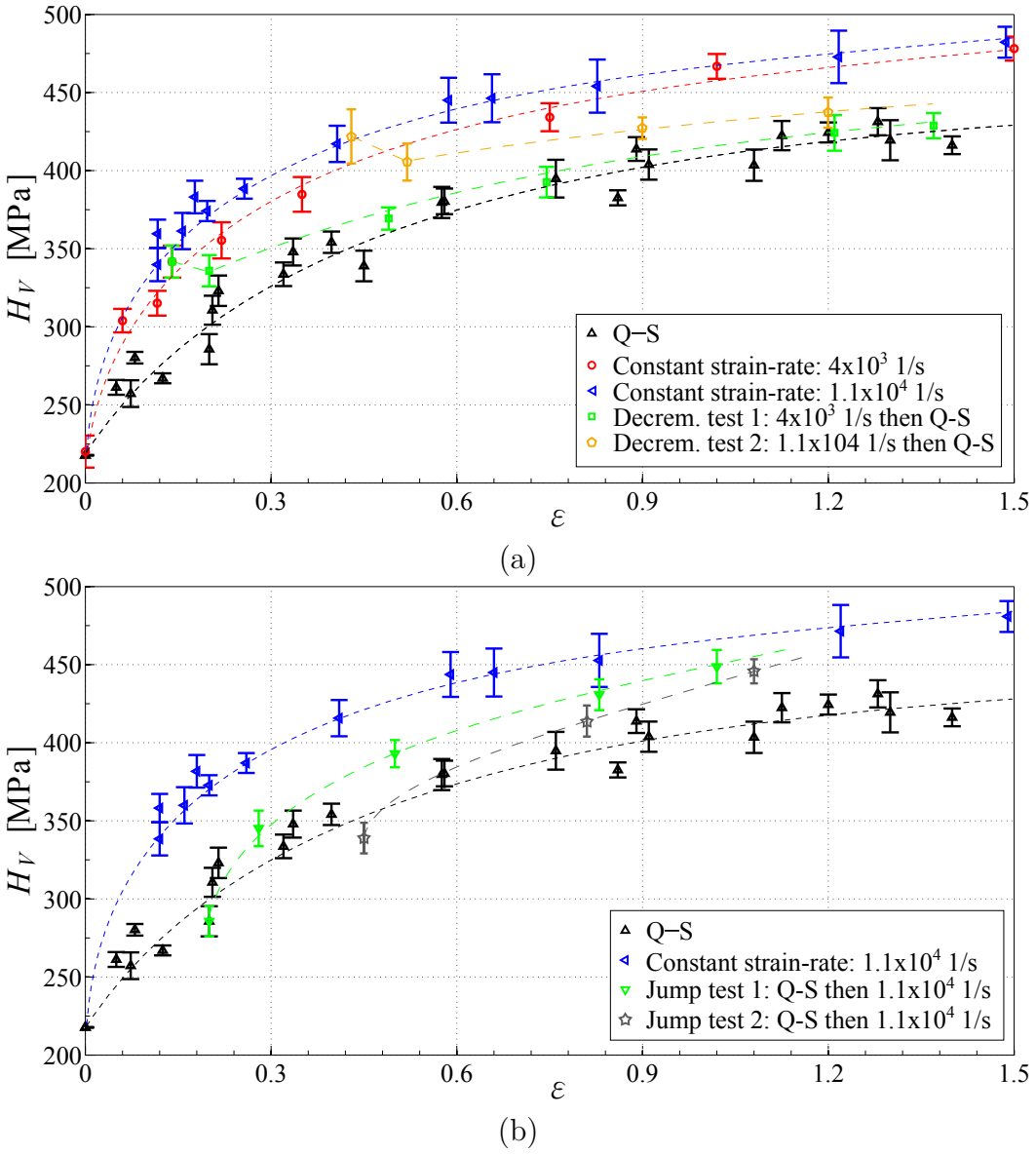


Figure 2.7: (a) Hardness-strain experimental data obtained from decremental strain-rate tests. Test 1: Change from a high strain-rate, $4 \times 10^3\,\mathrm{s}^{-1}$, to a *quasi*-static condition at a given strain of $\varepsilon_1 = 0.14$. Test 2: Change from a high strain-rate, $1.1 \times 10^4\,\mathrm{s}^{-1}$, to a *quasi*-static condition at a given strain of $\varepsilon_1 = 0.43$. (b) Hardness-strain experimental data obtained from strain-rate jump tests. Change from *quasi*-static to high strain-rate, $1.1 \times 10^4\,\mathrm{s}^{-1}$, conditions at given strains of $\varepsilon_1 = 0.2$ (test 1) and $\varepsilon_1 = 0.45$ (test 2). Dashed lines are used only for visualization purposes.

We also perform two strain-rate jump experiments. These simulations are performed by changing the loading-rate from a *quasi*-static condition to a high strain-rate $\dot{\varepsilon} = 1.1 \times 10^4\,\mathrm{s}^{-1}$ loading. Obtained results are shown in Figure 2.7(b). Strain-rate jumps were performed at strains of $\varepsilon_1 = 0.2$ (test 1) and $\varepsilon_1 = 0.45$ (test 2). For these high strain-rate regimes, the loading-rate influence on material hardness is also clear, in a manner that the strain-rate jump has strongly changed the hardness response. However, due to the known loading-history effects, the jumping response does not tend asymptotically to the

constant high strain-rate curve. In fact, the experiments show a certain resistance in approaching the monotonic high strain-rate response.

### 2.3.3 Stress-strain data

This subsection presents the stress-strain results referring to both *quasi*-static and high strain-rate experiments, considering constant strain-rate as well as sequential tests.

#### Constant strain-rate experiments

This topic outlines the results of constant strain-rate experiments. The results shall be used in order to characterize the strain-rate influence on specific material behaviors: *quasi*-static flow stress, rate-dependent yield stress (or non-viscous stress) and rate-dependent flow stress. Experimental results to be presented in this topic are obtained from incremental or continuous monotonic compressions.

*Quasi*-static compressions are performed using the compression tool presented in Subsection 2.2.1 and a Maquidral CNC double effect hydraulic press with a maximum load of 500 kN. *Quasi*-static tests employ an average strain-rate of approximately $10^{-2}\,\mathrm{s}^{-1}$. With the aim of avoiding significant friction effects, *quasi*-static compressions are performed incrementally. Following this procedure, the compressed specimens are lubricated between each incremental deformation. Incremental *quasi*-static stress-strain data are showed in Figure 2.8 (points). The *quasi*-static strain-hardening behavior associated with this material can be easily observed from this figure. Starting from an annealed state, the initial yield stress $\sigma_y$ of approximately 45 MPa increases to a value near to 140 MPa for total strain equal to 1. Figure 2.8 also shows the comparison between the results obtained from both incremental and continuous compressions. From this comparison, higher differences between the two curves are observed for strain levels greater than 0.6. This behavior is due to friction effects, which become more pronounced as the imposed strain (and thus the current contacting areas) increases. It is worth mentioning that incremental reloading of Figure 2.8 present variations on the curve slope related to elastic phase. These variations are due to corresponding displacement sensor sensitivity. Although it is adequate to measure the displacement during the plastic phase, it is not precise enough to accurately represent the elastic modulus.

In order to obtain the rate-dependent yield stress ($\sigma_y + A$, where $A$ is an isotropic hardening parameter), preceding experimental rate-dependent hardness data are considered. For this purpose, a correlation between the current material hardness and the yield stress,

$$\sigma_y + A = \varphi\left(H_V\right), \tag{2.5}$$

has therefore to be assessed. In the above equation, $\sigma_y + A$ is given as a function $\varphi$ of

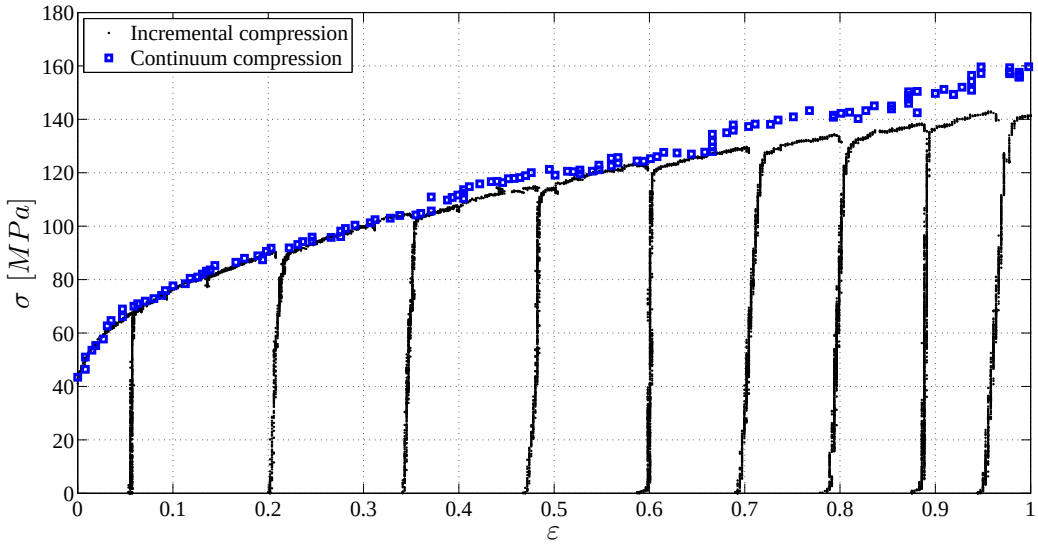


Figure 2.8: Comparison between incremental and continuum *quasi*-static stress-strain curves.

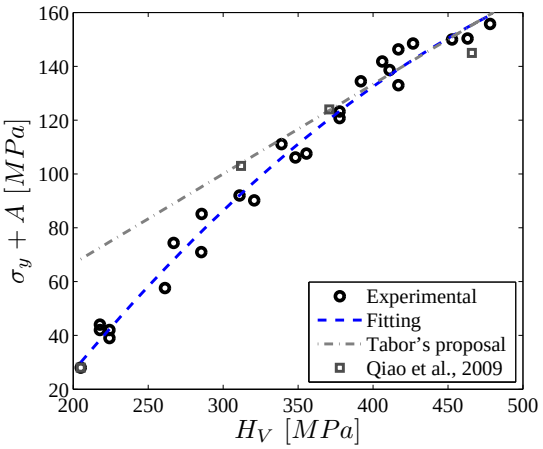


Figure 2.9: Experimental and analytical correlations between current yield stress $\sigma_y + A$ and material hardness $H_V$.

the current material hardness $H_V$. Although, there exist analytical correlations between the current strength and material hardness (e.g. those of Johnson, 1970, and Gao et al., 2006), some authors have shown that for metals such as steels [Busby et al., 2005; Pavlina and Van Tyne, 2008], magnesium [Cáceres et al., 2005], and aluminum [Tiryakioglu et al., 2015] a linear relationship between Vickers hardness and yield stress can be empirically employed. Qiao et al., 2009, proposed an exponential relationship between $\sigma_y + A$ and $H_V$ for the aluminum AA1050. However, our function $\varphi$ having a quadratic form,

$$\sigma_y + A = c_0 + c_1 H_V + c_2 H_V^2, \tag{2.6}$$

appears suitable for fitting experimental data.

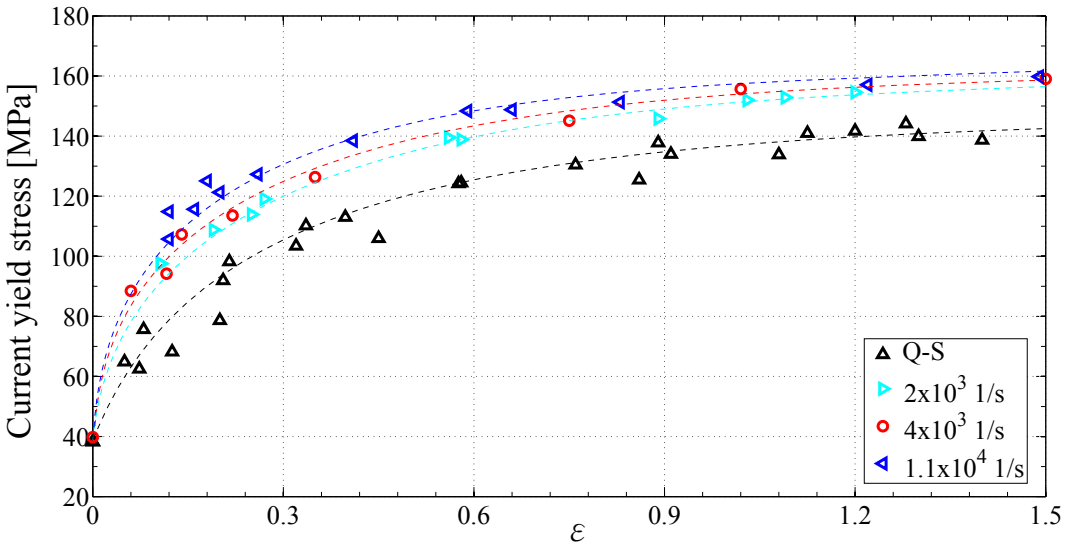


Figure 2.10: Strain-rate influence on current yield stress vs. strain curves. Current yield stress was estimated from hardness data of Figure 2.6 using empirical relation (2.6) and parameters given in Eqs. (2.7). Dashed lines are used only for visualization purposes.

Figure 2.9 shows an experimental correlation between the yield stress and corresponding material hardness. These experimental results are obtained considering hardness-strain and stress-strain data. Calibration of Eq. (2.6) considering data of Figure 2.9 results in the following constants:

$$c_0 = -133.5, \quad c_1 = 0.937, \quad \text{and} \quad c_2 = -6.801 \times 10^{-4}. \tag{2.7}$$

Figure 2.9 displays the adjusted equation (2.6) together with experimental results, showing a good correlation. For comparison purposes, experimental data presented by Qiao et al., 2009, are also shown. This figure has also plotted the *Tabor*'s relationship $\left(\sigma_y + A \approx \frac{H_V}{3}\right)$, which was deduced considering a perfectly-plastic material [Tabor, 2000]. *Tabor*'s relation fits well when local material hardening imposed by indentation process is not pronounced. In present case, *Tabor*'s relation seems to work for $\sigma_y + A > 130\,\text{MPa}$. In a regime in which strain-hardening is significant, i.e., for stresses close to the initial yield stress (associated with an annealed material) a greater difference between *Tabor*'s proposal and experimental data is observed. To solve this problem, an effective strain and corresponding stress hardening due to indentation-induced straining have been employed [Tabor, 2000]. Considering the empirical relation given in Eq. (2.6), this pronounced hardening associated with initial stages of deformation is accounted for by negative values of constant $c_0$ [Tiryakioglu et al., 2015].

Now, having Eq. (2.6) and constants given in Eqs. (2.7), the rate-dependent yield stress is estimated from rate-dependent hardness data presented in Figure 2.6. Obtained results are showed in Figure 2.10. Then, the next step is to characterize the instantaneous strain-rate-sensitivity.

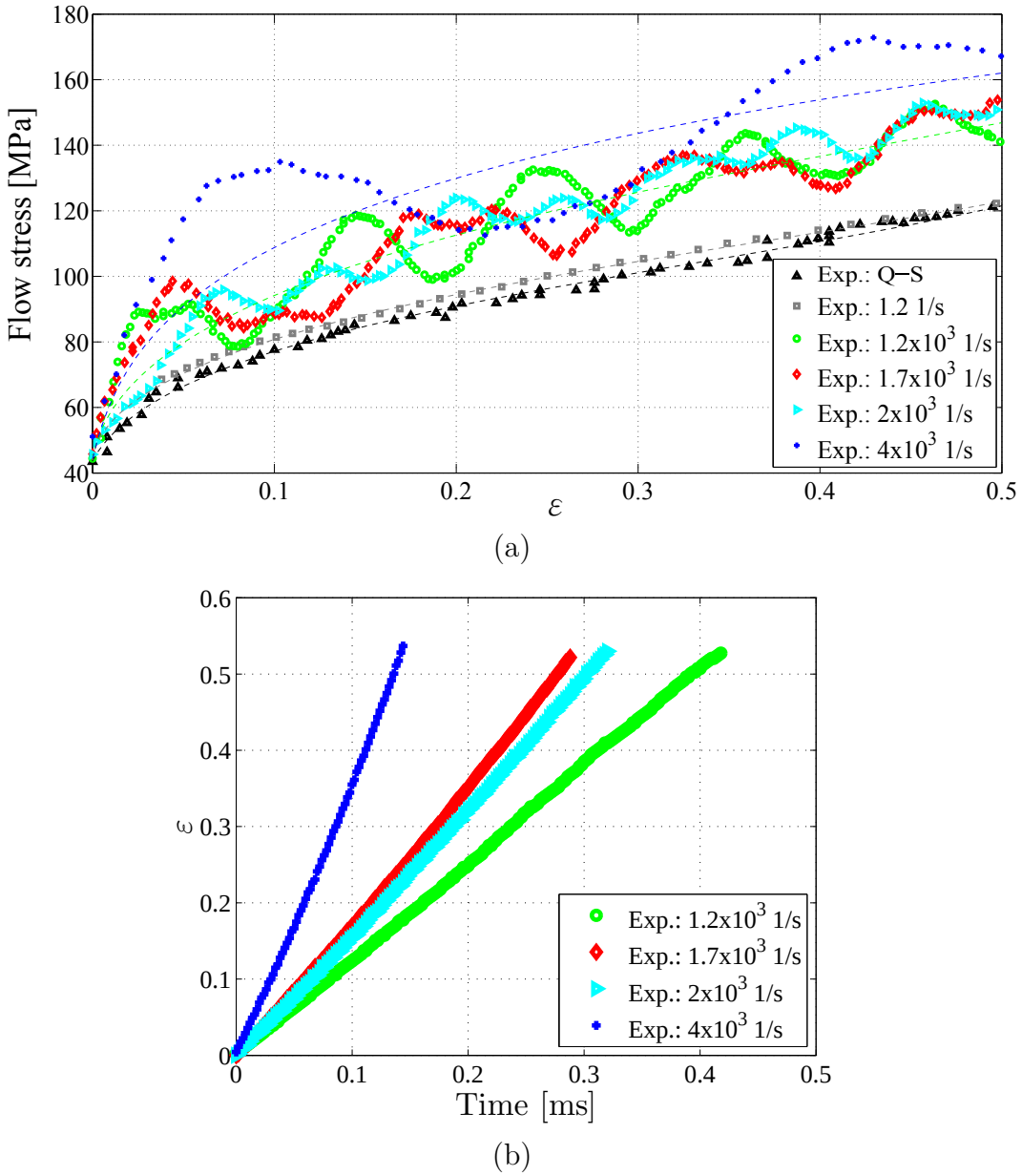


Figure 2.11: (a) Experimental flow stress-strain curves for different strain-rates; (b) Experimental time-histories of imposed strain corresponding to the high velocity compressions. In figure (a), thin dashed lines are not tendency lines, they were used only for easy visualization.

The remaining constitutive feature to be addressed is the instantaneous flow stress rate-sensitivity. To obtain suitable experimental data and perform this constitutive characterization, high strain-rate compressions are performed using the assemblage consisting of the pneumatic actuator described in Subsection 2.2.2 and the compression tool of Subsection 2.2.1, as showed in Figures 2.5(a)-(c). Experiments consist of performing high strain-rate continuous compressions employing different strain-rates. Chosen values are: $1.2 \times 10^3$, $1.7 \times 10^3$, $2.0 \times 10^3$ and $4.0 \times 10^3\,\mathrm{s}^{-1}$. Flow stress-strain curves obtained follow-

ing this procedure are showed in Figure 2.11.[1] Oscillations observed in flow stress-strain curves would be due to elastic wave propagation induced during high velocity compressions. As numerically evidenced in Appendix B.5, corresponding oscillations could be attributed to the dynamic behavior of the compression platen and load cell assembling and not to specimen inertia, since a minor stress (or force) oscillation is numerically predicted in the compressed specimen. See Figure B.2.

Since the whole compression is performed in a single step (i.e., a continuous test), the imposed strain is limited to a maximum value of $\varepsilon_{max} = 0.5$ in order to avoid significant thermal effects due to high velocity plastic deformation. Considering this strain level and assuming *quasi*-adiabatic conditions, the maximum temperature increase due to high velocity plastic deformation can be estimated. Reasoning on the energy conservation principle, the following expression for the temperature change is obtained:

$$\Delta\theta = \frac{\beta_{TQ}}{\rho_0 c_p} \int_0^{\varepsilon_{max}} \sigma d\varepsilon, \tag{2.8}$$

where $\beta_{TQ} \approx 0.9$ is the *Taylor-Quinney* coefficient assumed as constant[2], $\rho_0$ is the reference specific mass and $c_p$ is the specific heat at constant pressure. Then, employing this equation to the flow stress-strain curve associated with the strain-rate of $4.0 \times 10^3\,\mathrm{s}^{-1}$, and knowing the aluminum AA1050 proprieties, $\rho_0 = 2700\,\frac{\mathrm{kg}}{\mathrm{m}^3}$ and $c_p = 900\,\frac{\mathrm{J}}{\mathrm{kgK}}$, a maximum temperature increase of $\Delta\theta \approx 20^{\mathrm{o}}\mathrm{C}$ is estimated. Then, starting from a room temperature of approximately $25\,^{\mathrm{o}}\mathrm{C}$, a maximum temperature of $45\,^{\mathrm{o}}\mathrm{C}$ is reached during this high strain-rate compression. According to experimental results of Andrade-Campos et al., 2004, starting from room temperature, the thermal softening in the stress response of an aluminum AA1050 is approximately 10% for a temperature increase of $\approx 20^{\mathrm{o}}\mathrm{C}$. This fact can justify the simplifying assumption of considering isothermal conditions in future developments.

Sequential experiments

This topic focus on sequential strain-rate experiments, more specifically on decremental strain-rate tests. Experiments consists of high strain-rate compressions, until a given prestrain level, followed by a *quasi*-static deformation. Three decremental strain-rate tests (DT) are considered. Table 2.2 presents the prestrain level $\bar{\varepsilon}$ and strain-rate $\dot{\bar{\varepsilon}}$ associated with high velocity loading of each test. The specimen considered herein were incrementally compressed during the hardness-strain analysis presented in Subsection 2.2.3 employing constant strain-rate conditions, that is, by using the simplified high strain-rate

[1]We remark that to obtain adequate stress-strain results from force-displacement data, careful corrections, considering the time delay between displacement and load data acquisition during high velocity compressions, were performed. See analysis and discussion presented in Appendix B.5.

[2]Detailed considerations concerning a variable *Taylor-Quinney* coefficient are reported, e.g., by Macdougall, 2000, and Ristinmaa et al., 2007.

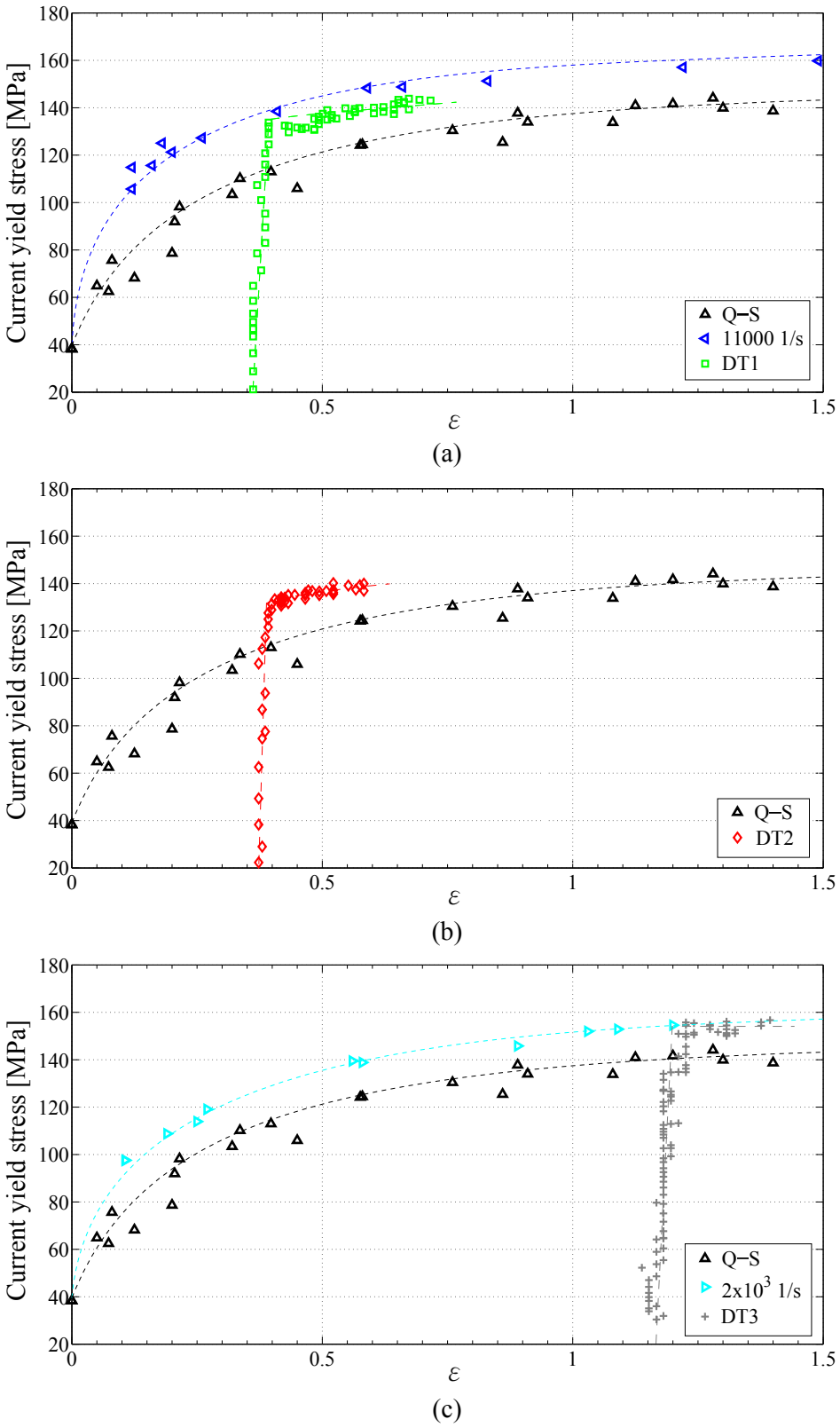


Figure 2.12: *Quasi*-static reload stress after high strain-rate loading: (a) DT1; (b) DT2; (c) DT3. Loading data are given in Table 2.2.

compression apparatus described in Subsection 2.2.2. Pre-deformed specimens, following conditions of Table 2.2, are then *quasi*-statically reloaded in the compression tool of

Subsection 2.2.1 and driven by a *Maquidral* CNC double effect hydraulic press with a maximum load of 500 kN.

Table 2.2: Prestrain $\bar{\varepsilon}$ and related strain-rate $\dot{\bar{\varepsilon}}$ associated with high velocity phase of decremental strain-rate testing.

| | DT1 | DT2 | DT3 |
|---|---|---|---|
| $\bar{\varepsilon}$ | 0.39 | 0.40 | 1.2 |
| $\dot{\bar{\varepsilon}}$ $[s^{-1}]$ | $1.1 \times 10^4$ | $6 \times 10^3$ | $2 \times 10^3$ |

Experimental reloading stress-strain curves associated with tests DT1, DT2, and DT3 are showed in Figures 2.12(a), (b), and (c), respectively. For comparison purposes, experimental data associated with high strain-rate and *quasi*-static monotonic loading of Figure 2.10 are also displayed. Even having a slight softening at the beginning, the material presents a small or *quasi*-null hardening during *quasi*-static reloading. When current reload yield stress is lower than corresponding *quasi*-static saturation stress, material presents a slight linear hardening during *quasi*-static reloading, Figures 2.12(a) and (b). However, when related reload strength is greater than respective *quasi*-static saturation, as shown in Figure 2.12(c), a nearly perfectly-plastic behavior is observed. In every case, the *quasi*-static reload stress is greater than that associated with the monotonic *quasi*-static flow stress-strain curve. As discussed in Subsection 2.2.3, this behavior evidences the strain-rate-history effects, reflecting in a macroscopic stress-strain response the strain-rate influence on the material microstructural evolution. These results are in agreement with experiments of Klepaczko, 1975, Chiem and Duffy, 1983, Rashid et al., 1992, and Tanner and McDowell, 1999, on stress analysis, and of Zhang and Shim, 2010, and Huang and Tao, 2011, on material hardness analysis.

# 3 ELASTIC-VISCOPLASTIC FORMULATION

The macroscopic constitutive framework to be developed here is intended to describe the mechanical behavior of a body $\mathcal{B}$ subjected to deformation process involving finite plastic strains associated to high strain-rates. Thereby, this chapter focus on describing continuum aspects related to a macroscopic viscoplastic formulation following a finite strain framework. As simplifying assumptions, $\mathcal{B}$ is assumed to be composed by a homogeneous material possessing both elastic and inelastic isotropy, and that these characteristics are not affected by imposed deformation. Furthermore, $\mathcal{B}$ is considered to behave as an elastic-viscoplastic medium: for equivalent stresses lower than a given threshold, the material presents an elastic (reversible) behavior, and for stresses exceeding that critical state, rate-dependent inelastic (irreversible) deformation occurs.

Within the present constitutive context, both phenomenological or physically-based viscoplastic models can be considered. The difference is given by the choice of internal variables to be employed as well as their evolution equations. Concerning the finite strain formulation, the following considerations are adopted:

- a Total *Lagrangian* description;
- the multiplicative decomposition of the deformation gradient;
- constitutive equations are given in terms of the (logarithmic) *Hencky* strain measure and its conjugate pair, the rotated *Kirchhoff* stress tensor (or *Mandel* stress tensor [Mandel, 1972]).

Both *Hencky* strain and rotated *Kirchhoff* stress measures were adopted by Eterovic and Bathe, 1990, and Weber and Anand, 1990, which combined with an implicit exponential integration scheme allowed for obtaining a return mapping algorithm similar to that obtained in a infinitesimal strain framework.

*Remark* 3.1. Key hypotheses concerning the present approach are the material homogeneity and the persistent elastic and inelastic isotropy. In general, real materials do not satisfy these conditions. As discussed in the introductory sections, metallic materials at underlying scales are strongly heterogeneous and anisotropic [Winther, 2005; Farbaniec et al., 2012; Hansen and Barlow, 2014]. However, when working in a macroscopic scale, at which the characteristic length of the structure is much grater than that corresponding to the microscopic heterogeneities, mainly when dealing with annealed materials, the hypothesis of homogeneity and isotropy provide reasonable results when analyzing metallic structures. However, as explained in Section 1.4, as the deformation proceeds, at least plastic anisotropy can be induced from formation of textures and lamellar structures. From a modeling point of view, anisotropic plastic behavior, as material texturing and

the *Bauschinger* effect developed during deformation, can not be represented nor by scalar internal variables representing an isotropic hardening behavior neither by a standard *von Mises* yield criterion. These effects become more important when significant changes in deformation direction occur. In these cases, the flow stress is considerably influenced by anisotropic hardening effects. On one hand, in a modeling task in which anisotropic effects are of great importance, non standard anisotropic yield criteria and tensor hardening behavior, resulting from crystallographic texturing, have to be adopted. Following a non exhaustive list, works of Hill, 1948, 1979a, Barlat, 1987, Barlat et al., 2003, Plunkett et al., 2006, Beyerlein and Tomé, 2007, Viatkina et al., 2008, Fajoui et al., 2009, Knezevic et al., 2013, Barlat et al., 2014, Mánik et al., 2015, Zhang et al., 2015, are referred to. On the other hand, due to experimental limitations and in order to provide a simplified finite strain model, the present approach, which adopts a *von Mises* yield criterion with isotropic hardening, is restricted to applications consisting of monotonic loadings.

## 3.1 Continuum mechanics fundamentals

Continuum mechanics fundamentals addressed in this section are: (i) finite strain kinematic description; (ii) corresponding boundary value problem formulation; (iii) statement of thermodynamic principles, as the first and second laws of thermodynamics, and the dissipation inequality; and finally (iv) an overview on the internal variable constitutive modeling. In particular, thermodynamic restrictions imposed by the first and second principles are further considered in order to evaluate the thermodynamic consistency of the proposed constitutive formulation.

Due to brevity of the following overview, more details on continuum mechanics theory can be found in standard textbooks, as those of Ciarlet, 1988, Marsden and Hughes, 1994, Haupt, 2000, Spencer, 2004, and Gurtin et al., 2010.

### 3.1.1 Deformation process description

Let $\bar{\Omega}_0 \in \mathcal{R}^3$ be a *reference configuration* of a body $\mathcal{B}$ at an initial time $t = t_0$. Actually, $\bar{\Omega}_0$ is the closure of a bounded, connected, subset $\bar{\Omega}_0$ of *Euclidean* space $\mathcal{R}^3$ with a sufficiently smooth boundary $\partial\Omega_0$, i.e., $\bar{\Omega}_0 = \Omega_0 \cup \partial\Omega_0$. A given material point $P_0 \in \bar{\Omega}_0$ is defined by a position vector $\boldsymbol{X} \in \mathcal{R}^3$ defined with respect to a given coordinate system with origin "$O$", as showed in Figure 3.1. Supposing that $\mathcal{B}$ is deformed during a time interval of interest $\mathcal{I} = (t_0, t_f] \subset \mathcal{R}_{\geq 0}$, the deformed configuration of $\mathcal{B}$, $\bar{\Omega} \in \mathcal{R}^3$, is given by a deformation function

$$\boldsymbol{\varphi} : \bar{\Omega}_0 \times \mathcal{I} \rightarrow \mathcal{R}^3, \tag{3.1}$$

in a manner that, at a given time instant $t \in \mathcal{I}$, associated current configuration is defined by $\bar{\Omega} = \boldsymbol{\varphi}_t\left(\bar{\Omega}_0\right)$, where $\boldsymbol{\varphi}_t(\boldsymbol{X}) = \boldsymbol{\varphi}(\boldsymbol{X}, t)$. Function $\boldsymbol{\varphi}$ is bijective, smooth, and orientation-preserving. This function maps each material point $P_0 \in \bar{\Omega}_0$ into a current

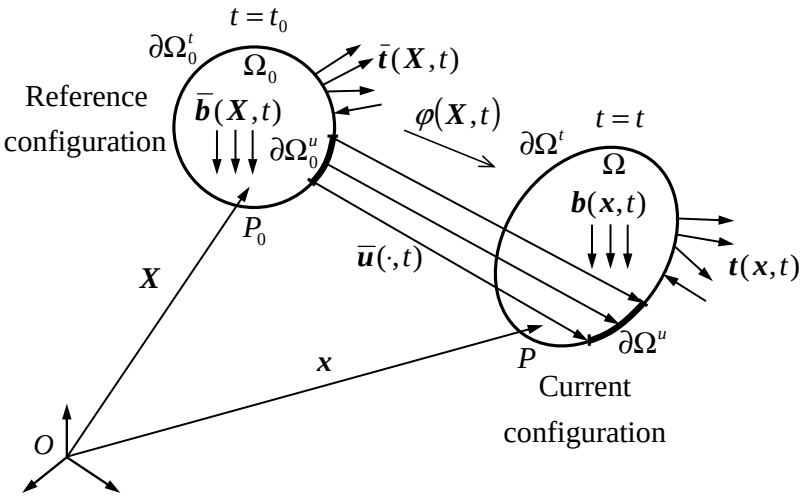


Figure 3.1: Schematic representation of corresponding initial boundary value problem.

one $P \in \bar{\Omega}$, which is then defined by a position vector $\boldsymbol{x} \in \mathcal{R}^3$ related to the same reference system. Knowing the reference position vector $\boldsymbol{X}$, the current position vector $\boldsymbol{x}$ can be obtained by means of function $\boldsymbol{\varphi}$:

$$\boldsymbol{x} = \boldsymbol{\varphi}\left(\boldsymbol{X}, t\right). \tag{3.2}$$

During the deformation motion, each point $P_0$ undergoes a displacement $\boldsymbol{u} : \bar{\Omega}_0 \times \mathcal{I} \rightarrow \mathcal{R}^3$ given by

$$\boldsymbol{x} = \boldsymbol{X} + \boldsymbol{u}. \tag{3.3}$$

A key quantity in deformation analysis is the deformation gradient $\boldsymbol{F} : \bar{\Omega}_0 \times \mathcal{I} \rightarrow \mathcal{M}^3_+$,[1] relating a material line before, $d\boldsymbol{X}$, and after, $d\boldsymbol{x}$, deformation: $d\boldsymbol{x} = \boldsymbol{F} d\boldsymbol{X}$. According to a Cartesian coordinate system, tensor $\boldsymbol{F}$ is defined as [Gurtin, 1981; Ciarlet, 1988; Marsden and Hughes, 1994; Spencer, 2004]

$$\boldsymbol{F} \coloneqq \nabla_{\boldsymbol{X}} \boldsymbol{\varphi}\left(\boldsymbol{X}, t\right) \;\text{ or }\; F_{ij} \coloneqq \frac{\partial \varphi_i}{\partial X_j}. \tag{3.4}$$

In terms of displacements, keeping in mind Eq. (3.3), Eq. (3.4) is rewritten as

$$\boldsymbol{F} = \boldsymbol{I} + \nabla_{\boldsymbol{X}} \boldsymbol{u} \;\text{ or }\; F_{ij} = \delta_{ij} + \frac{\partial u_i}{\partial X_j}, \tag{3.5}$$

where $\boldsymbol{I}$ is the identity matrix associated with set $\mathcal{M}^3$, and $\delta_{ij}$ is the *Kronecker*'s delta defined as:

$$\delta_{ij} \coloneqq \begin{cases} 0 \rightarrow & i \neq j \\ 1 \rightarrow & i = j \end{cases} \quad i, j = \{1, 2, 3\}. \tag{3.6}$$

[1] $\mathcal{M}^n \subset \mathcal{R}^n \times \mathcal{R}^n$ is the set of every second-order quadratic tensor with dimension $n$. $\mathcal{M}^n_+$ is the set of every orientation-preserving tensor belonging to $\mathcal{M}^n$. Thus, for $n = 3$ $\mathcal{M}^3_+ = \left\{\boldsymbol{M} \in \mathcal{M}^3 | \det\left(\boldsymbol{M}\right) > 0\right\}$.

### 3.1.2 Equilibrium equation and boundary conditions

Following a *Total Lagrangian* description, deformation experienced by $\mathcal{B}$ (Figure 3.1) is induced by an ordinary loading-history defined by a prescribed body force

$$\bar{\boldsymbol{b}} : \Omega_0 \times \mathcal{I} \to \mathcal{R}^3, \tag{3.7}$$

a prescribed surface traction $\bar{\boldsymbol{t}}$ acting on $\partial\Omega_0^t$,

$$\bar{\boldsymbol{t}} : \partial\Omega_0^t \times \mathcal{I} \to \mathcal{R}^3, \tag{3.8}$$

and a prescribed boundary displacement $\bar{\boldsymbol{u}} : \partial\Omega_0^u \times \mathcal{I} \to \mathcal{R}^3$, such that

$$\boldsymbol{u} = \bar{\boldsymbol{u}} \ \text{ on } \ \partial\Omega_0^u \times \mathcal{I}. \tag{3.9}$$

Thus, according to Eq. (3.1), in this boundary portion function $\bar{\boldsymbol{\varphi}}(\boldsymbol{X}, t) : \partial\Omega_0^u \times \mathcal{I} \to \mathcal{R}^3$ is then prescribed according to imposed displacement-history,

$$\bar{\boldsymbol{\varphi}}(\boldsymbol{X}, t) = \boldsymbol{X} + \bar{\boldsymbol{u}}(\boldsymbol{X}, t). \tag{3.10}$$

Both natural, $\partial\Omega_0^t$, and essential, $\partial\Omega_0^u$, boundaries are defined in order to comply with conditions

$$\partial\Omega_0^u \cup \partial\Omega_0^t = \partial\Omega_0 \ \text{ and } \ \partial\Omega_0^u \cap \partial\Omega_0^t = \emptyset. \tag{3.11}$$

The set of kinematically admissible displacements $\mathcal{K}$ is defined as the set of every sufficiently regular displacement function satisfying the imposed essential boundary conditions (3.9):

$$\mathcal{K} = \left\{ \boldsymbol{u} : \bar{\Omega}_0 \times \mathcal{I} \to \mathcal{R}^3 | \boldsymbol{u}(\boldsymbol{X}, t) = \bar{\boldsymbol{u}}(\boldsymbol{X}, t), \ t \in \mathcal{I}, \ \boldsymbol{X} \in \partial\Omega_0^u \right\}. \tag{3.12}$$

The equation describing the body motion is obtained from the *linear momentum conservation principle*[2], such that, considering a *quasi*-static problem, the following equilibrium equation is obtained:

$$\mathrm{div}_{\boldsymbol{X}}\left[\boldsymbol{P}(\boldsymbol{X}, t)\right] + \bar{\boldsymbol{b}}(\boldsymbol{X}, t) = 0 \ \text{ in } \ \Omega_0 \times \mathcal{I}, \tag{3.13}$$

where[3]

$$\boldsymbol{P} \coloneqq \det(\boldsymbol{F})\, \boldsymbol{\sigma} \boldsymbol{F}^{-T} \in \mathcal{M}^3 \tag{3.14}$$

[2]Linear momentum conservation principle, $\frac{D}{Dt}\int_\Omega \rho \boldsymbol{v} dv = \int_\Omega \boldsymbol{b} dv + \int_{\partial\Omega} \boldsymbol{t} da$, implies in the following equilibrium equations (considering $\frac{D\boldsymbol{v}}{Dt} = \boldsymbol{0}$): $\mathrm{div}_{\boldsymbol{x}}(\boldsymbol{\sigma}) + \boldsymbol{b} = \boldsymbol{0}$ in $\Omega$, subjected to $\boldsymbol{t} = \boldsymbol{\sigma n}$ on $\partial\Omega$, for an *Eulerian* description, and $\mathrm{div}_{\boldsymbol{X}}(\boldsymbol{P}) + \bar{\boldsymbol{b}} = \boldsymbol{0}$ in $\Omega_0$, subjected to $\bar{\boldsymbol{t}} = \boldsymbol{PN}$ on $\partial\Omega_0$, for a *Lagrangian* description [Gurtin, 1981; Spencer, 2004].

[3]Along this work single contractions between two second-order tensors, and between a second-order tensor and a vector are omitted, i.e., $\boldsymbol{S}\cdot\boldsymbol{T} = \boldsymbol{ST}$, in components $(\boldsymbol{ST})_{ij} = S_{ik}T_{kj}$, and $\boldsymbol{S}\cdot\boldsymbol{t} = \boldsymbol{St}$, in components $(\boldsymbol{St})_i = S_{ij}t_j$.

is the first *Piola-Kirchhoff* stress tensor, which is related to the *Cauchy* stress tensor $\boldsymbol{\sigma} \in \mathcal{S}^3$.[4] The boundary value problem consists of solving Eq. (3.13) for $\boldsymbol{u} \in \mathcal{K}$, such that the stress field $\boldsymbol{P}$ complies with the natural boundary condition:

$$\boldsymbol{P}(\boldsymbol{X}, t)\, \boldsymbol{N}(\boldsymbol{X}) = \bar{\boldsymbol{t}}(\boldsymbol{X}, t) \;\text{ on }\; \partial\Omega_0^t \times \mathcal{I}, \tag{3.15}$$

where $\boldsymbol{N}$ is the unit outward normal vector of $\partial\Omega_0$ at $\boldsymbol{X}$.

### 3.1.3 First law of thermodynamics

The first law of thermodynamics is an assertion on the conservation of energy. This law states that the rate of external work $W$ done on the system plus the heat $Q$ received by it is equal to the rate of kinetic energy $K$ plus the rate of internal energy $U$, i.e.,

$$\dot{U} + \dot{K} = \dot{W} + Q. \tag{3.16}$$

see, e.g., Truesdell, 1968. Knowing the relations

$$\dot{U} = \int_{\Omega_0} \rho_0 \dot{e} dV, \tag{3.17}$$

$$K = \frac{1}{2} \int_{\Omega_0} \rho_0 \dot{\boldsymbol{u}} \cdot \dot{\boldsymbol{u}} dV, \tag{3.18}$$

$$\dot{W} = \dot{K} + \int_{\Omega_0} \boldsymbol{P} : \dot{\boldsymbol{F}} dV, \tag{3.19}$$

$$Q = -\int_{\partial\Omega_0} \bar{\boldsymbol{q}} \cdot \boldsymbol{N} dA + \int_{\Omega_0} \rho_0 \bar{r} dV = \int_{\Omega_0} \left(-\mathrm{div}_{\boldsymbol{X}} \bar{\boldsymbol{q}} + \rho_0 \bar{r}\right) dV, \tag{3.20}$$

we arrive at the local form of the energy balance [Coleman and Gurtin, 1967], given in a *Lagrangian* form,

$$\rho_0 \dot{e} = \boldsymbol{P} : \dot{\boldsymbol{F}} - \mathrm{div}_{\boldsymbol{X}} \bar{\boldsymbol{q}} + \rho_0 \bar{r} \;\text{ in }\; \Omega_0 \times \mathcal{I}, \tag{3.21}$$

where $e : \Omega_0 \times \mathcal{I} \to \mathcal{R}$ is the specific internal energy, $\bar{\boldsymbol{q}} : \Omega_0 \times \mathcal{I} \to \mathcal{R}^n$ is the heat flow, $\bar{r} : \Omega_0 \times \mathcal{I} \to \mathcal{R}$ is the specific heat generation, and $\rho_0 : \Omega_0 \times \mathcal{I} \to \mathcal{R}_{>0}$ is the mass per unity of reference volume. Operator $\dot{(\cdot)} = \frac{D}{Dt}(\cdot)$ denotes a material time derivative of $(\cdot)$.

### 3.1.4 Second law of thermodynamics, and *Clausius-Duhem* inequality

The second law of thermodynamics is a restriction on the direction in which a thermodynamic process can occur. This law states that the entropy production rate $\dot{S}_i$ (irreversible part), given by the rate of internal entropy $S$ (state function) minus the rate of the entropy supplied $S_r$ (reversible part) to $\mathcal{B}$ from the environment, must be non-negative

[4] $\mathcal{S}^n$ is the set of every symmetric tensor belonging to $\mathcal{M}^n$. For $n = 3$: $\mathcal{S}^3 = \left\{\boldsymbol{M} \in \mathcal{M}^3 | \boldsymbol{M} = \boldsymbol{M}^T\right\}$.

[Coleman and Gurtin, 1967; Ziegler, 1977]:

$$\dot{S}_i = \dot{S} - \dot{S}_r \geq 0 \text{ in } \Omega_0 \times \mathcal{I}. \tag{3.22}$$

From the expressions

$$\dot{S}_i = \int_{\Omega_0} \rho_0 \dot{s}_i dV, \tag{3.23}$$

$$\dot{S} = \int_{\Omega_0} \rho_0 \dot{s} dV, \tag{3.24}$$

and assuming that $\dot{S}_r$ is given by[5]

$$\dot{S}_r = \int_{\Omega_0} \left( -\text{div}_{\boldsymbol{X}} \frac{\bar{\boldsymbol{q}}}{\theta} + \frac{\rho_0 \bar{r}}{\theta} \right) dV, \tag{3.25}$$

we obtain the local form of the second law

$$\rho_0 \dot{s}_i = \rho_0 \dot{s} + \text{div}_{\boldsymbol{X}} \frac{\bar{\boldsymbol{q}}}{\theta} - \frac{\rho_0 \bar{r}}{\theta} \geq 0 \text{ in } \Omega_0 \times \mathcal{I}, \tag{3.26}$$

where $\dot{s}_i : \Omega_0 \times \mathcal{I} \to \mathcal{R}_{\geq 0}$ is the specific entropy production rate, $\dot{s} : \Omega_0 \times \mathcal{I} \to \mathcal{R}$ is the specific internal entropy rate and $\theta : \Omega_0 \times \mathcal{I} \to \mathcal{R}_{>0}$ is the absolute temperature.

Isolating the specific heat generation $\bar{r}$ in Eq. (3.21) and substituting it into Eq. (3.26), after some algebraic manipulations, yields

$$\Phi_0 = \boldsymbol{P} : \dot{\boldsymbol{F}} - \rho_0 (\dot{e} - \theta \dot{s}) - \frac{1}{\theta} \bar{\boldsymbol{q}} \cdot \nabla_{\boldsymbol{X}} \theta \geq 0 \text{ in } \Omega_0 \times \mathcal{I}, \tag{3.27}$$

where $\nabla_{\boldsymbol{X}} \theta$ denotes the temperature gradient. In inequality (3.27) the dissipation per unit of reference volume is defined as $\Phi_0 \coloneqq \rho_0 \theta \dot{s}_i : \Omega_0 \times \mathcal{I} \to \mathcal{R}_{\geq 0}$. Introducing the specific *Helmholtz* free energy $\psi \coloneqq e - \theta s : \Omega_0 \times \mathcal{I} \to \mathcal{R}_{\geq 0}$, and inserting it into the dissipation inequality (3.27), the following expression is obtained:

$$\Phi_0 = \boldsymbol{P} : \dot{\boldsymbol{F}} - \rho_0 \left( \dot{\psi} + s \dot{\theta} \right) - \frac{1}{\theta} \bar{\boldsymbol{q}} \cdot \nabla_{\boldsymbol{X}} \theta \geq 0 \text{ in } \Omega_0 \times \mathcal{I}, \tag{3.28}$$

which is known as *Clausius-Duhem* inequality.

### 3.1.5 Thermodynamics with internal variables

According to the *principle of thermodynamic determinism*, calorodynamic quantities as $\boldsymbol{P}(t)$, $\psi(t)$, $s(t)$, and $\bar{\boldsymbol{q}}(t)$ of a given material point of a body subjected to given loading-history, supposing a *simple material* and following the *local action principle*, are determined from constitutive functionals given in terms of the histories of thermokinetic quantities, $\boldsymbol{F}$, $\theta$, and $\nabla_{\boldsymbol{X}} \theta$, given at this point [Coleman and Gurtin, 1967; Perzyna,

[5]That assumption was criticized by some authors, as Woods, 1981, 1982. However, this criticism does not apply to bodies in the context of this work, see Lubliner, 2008, p.47.

1971; Truesdell, 1984]. These constitutive functionals have to satisfy some constitutive axioms, as *material objectivity* and *symmetry*, and also to comply with the first and second laws of thermodynamics. However, it is hard do deal with a constitutive formulation given by these history functionals [Mandel, 1972, p. 43], since it should apply to the behavior of real materials subjected to real thermomechanical processes, thus requiring to introduce simplification at the constitutive theory level. An alternative approach to perform this simplification is the thermodynamic with internal variables (TIV) framework. This approach allows the description of a non-equilibrium thermodynamic process based on the existence of a set of $n_{int} \geq 1$ internal variables $\boldsymbol{\alpha} = \{\alpha_1, \alpha_2, ..., \alpha_{n_{int}}\} \in \mathcal{R}^{n_{int}}$. The internal variables $\alpha_i$ $(i = 1, 2, ..., n_{int})$, possessing scalar, vectorial and/or tensor natures, characterize dissipative mechanisms,[6] and substitute the preceding histories of $\boldsymbol{F}$, $\theta$, and $\nabla_{\boldsymbol{X}}\theta$ in the constitutive description [Coleman and Gurtin, 1967; Kestin and Rice, 1969; Rice, 1971; Lubliner, 1972]. In other words, the instantaneous material response, which is the product of the entire past deformation-history undergone by the material, may be assumed to be representable by a small number of macroscopic internal variables, whose evolution is represented by rate equations [Rice, 1971; Brown et al., 1989]. Thereby, following the TIV approach, one assumes that the current local thermodynamic state of a given material point is uniquely determined by the instantaneous values of the following state variables:[7]

$$(\boldsymbol{F}, \theta, \boldsymbol{\alpha})\,. \tag{3.29}$$

It is worth mentioning that, according to the TIV theory, variables as temperature and entropy, which are fundamentally associated with equilibrium states, are defined at a non-equilibrium state by associating with this a fictitious "*accompanying equilibrium state*", which is then obtained by fixing the internal variables at the values of the current non-equilibrium state, and allowing the system to reach a *constrained equilibrium* [Kestin and Rice, 1969; Rice, 1971]. This concept is discussed by several authors, such as Lubliner, 1972, Bataille and Kestin, 1976, 1979, Germain et al., 1983, and Horstemeyer and Bammann, 2010.

The following sections specify corresponding kinematic description and associated internal variable constitutive formulation to an elastic-viscoplastic material.

## 3.2 Finite strain kinematics for an elastic-viscoplastic material

This section provides the main features of the macroscopic formulation adopted for modeling an elastic-viscoplastic material at finite strains. The starting point is the clas-

[6] In order to properly describe a given constitutive behavior, the choice of corresponding internal variables, intended to phenomenologically represent given microscopic dissipative mechanisms, have to be guided by means of a model in which those variables have physical interpretation [Muschik, 1990].

[7] Coleman and Gurtin, 1967, have demonstrated that, in order to satisfy the *Clausius-Duhem* inequality (3.28), the specific free energy $\psi$ can not depends on the temperature gradient $\nabla_{\boldsymbol{X}}\theta$, i.e., $\frac{\partial \psi}{\partial \nabla_{\boldsymbol{X}}\theta} = \boldsymbol{0}$.

sical multiplicative decomposition of the deformation gradient

$$\boldsymbol{F} = \boldsymbol{F}^{e}\boldsymbol{F}^{vp}, \tag{3.30}$$

where $\boldsymbol{F}^{e}$ and $\boldsymbol{F}^{vp} \in \mathcal{M}^{3}_{+}$ are the elastic and viscoplastic parts of $\boldsymbol{F}$. This decomposition was introduced by Lee and Liu, 1967, Lee, 1969, and Mandel, 1972, and was also investigated by Lubliner, 1984, 1986, exploring the maximum dissipation principle and normality rules. Furthermore, the multiplicative decomposition of $\boldsymbol{F}$ can find physical justification on the crystal plasticity theory, which assumes that the plastic deformation is induced by relative sliding between material portions occurring in specific crystallographic planes and directions [Rice, 1971; Mandel, 1972; Asaro, 1983]. Decomposition given in Eq. (3.30) supposes the existence of a stress-free local state $O_{\xi}$, which defines an intermediate configuration. The stress-free local state is mapped from reference configuration $\bar{\Omega}_0$ by $\boldsymbol{F}^{vp}$ and from current configuration $\bar{\Omega}$ by $\boldsymbol{F}^{e^{-1}}$, see Figure 3.2.

*Remark* 3.2. We remark that, in general, the stress-free local state is not unique, once even imposing arbitrary rigid rotations on $O_{\xi}$, a stress-free state is maintained. However, in specific applications the decomposition (3.30) can be performed uniquely by means of additional specifications dictated by the material model. In the present case such an additional restriction is imposed by assuming a irrotational viscoplastic (null viscoplastic spin: Eq. (3.60)) deformation in intermediate configuration. For detailed discussion on that hypothesis, see, e.g., work of Gurtin et al., 2010, p. 567.

Adopting the multiplicative decomposition of $\boldsymbol{F}$ leads to some important kinematic aspects related to the deformation analysis of $\mathcal{B}$. These aspects are addressed in the following. By inserting Eq. (3.30) into the definition of the velocity gradient tensor

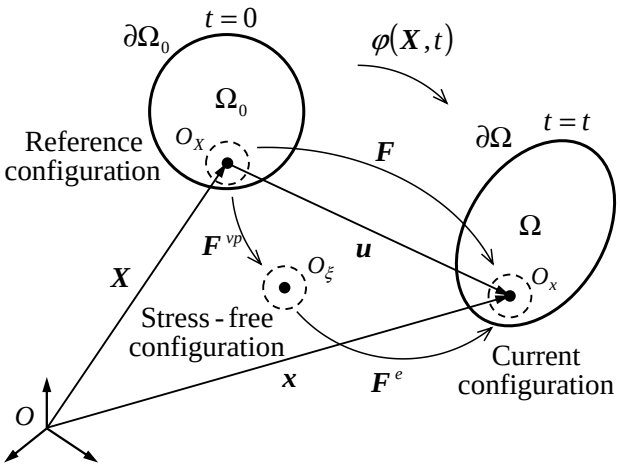


Figure 3.2: Schematic representation of multiplicative decomposition of $\boldsymbol{F}$.

$\boldsymbol{L} \in \mathcal{M}^3$,[8]

$$\boldsymbol{L} \coloneqq \nabla_{\boldsymbol{x}} \mathbf{v} = \dot{\boldsymbol{F}} \boldsymbol{F}^{-1}, \tag{3.31}$$

we obtain

$$\boldsymbol{L} = \boldsymbol{L}^e + \boldsymbol{L}^{vp}, \tag{3.32}$$

where the elastic and inelastic parts of $\boldsymbol{L}$, are defined respectively as

$$\boldsymbol{L}^e \coloneqq \dot{\boldsymbol{F}}^e \boldsymbol{F}^{e^{-1}} \text{ and } \boldsymbol{L}^{vp} \coloneqq \boldsymbol{F}^e \dot{\boldsymbol{F}}^{vp} \boldsymbol{F}^{vp^{-1}} \boldsymbol{F}^{e^{-1}}, \tag{3.33}$$

both related to the current configuration $\bar{\Omega}$. The strain-rate tensor $\boldsymbol{D} \in \mathcal{S}^3$, symmetrical part of $\boldsymbol{L}$, then also follows an additive decomposition,

$$\boldsymbol{D} = \boldsymbol{D}^e + \boldsymbol{D}^{vp}, \tag{3.34}$$

with

$$\boldsymbol{D}^e \coloneqq \frac{1}{2}\left(\boldsymbol{L}^e + \boldsymbol{L}^{e^T}\right) \text{ and } \boldsymbol{D}^{vp} \coloneqq \frac{1}{2}\left(\boldsymbol{L}^{vp} + \boldsymbol{L}^{vp^T}\right). \tag{3.35}$$

As already stated $\boldsymbol{F} \in \mathcal{M}^3_+$, what yields the *Jacobian*

$$J \coloneqq \det(\boldsymbol{F}) > 0. \tag{3.36}$$

Assuming dislocation mediated plasticity, results in a volume-preserving inelastic evolution, what yields

$$J^{vp} \coloneqq \det(\boldsymbol{F}^{vp}) = 1, \tag{3.37}$$

and consequently

$$J^e \coloneqq \det(\boldsymbol{F}^e) = \det(\boldsymbol{F}) > 0. \tag{3.38}$$

This fact guarantees that both $\boldsymbol{F}^e$ and $\boldsymbol{F}^{vp}$ are non-singular tensors. By satisfying the last two conditions, one can apply the polar decomposition of both $\boldsymbol{F}^e$ and $\boldsymbol{F}^{vp}$, respectively as [Eterovic and Bathe, 1990; Weber and Anand, 1990]

$$\boldsymbol{F}^e = \boldsymbol{R}^e \boldsymbol{U}^e \text{ and } \boldsymbol{F}^{vp} = \boldsymbol{R}^{vp} \boldsymbol{U}^{vp}, \tag{3.39}$$

where[9] $\boldsymbol{R}^e \in \mathcal{O}^3_+$ $\left(\boldsymbol{R}^{vp} \in \mathcal{O}^3_+\right)$ is the elastic (inelastic) rotation tensor, and[10] $\boldsymbol{U}^e \in \mathcal{S}^3_>$ $(\boldsymbol{U}^{vp} \in \mathcal{S}^3_>)$ is the elastic (inelastic) right-stretch tensor. In addition, concerning the elastic deformation, tensor $\boldsymbol{U}^e$ correlates with the elastic right *Cauchy-Green* strain tensor,

[8] It is worth mentioning that $\boldsymbol{L}$ is an *Eulerian* measure.

[9] $\mathcal{O}^n_+$ is the set of every proper orthogonal tensor belonging to $\mathcal{M}^n$. Therefore, considering $n = 3$ one has $\mathcal{O}^3_+ = \left\{\boldsymbol{M} \in \mathcal{M}^3 | \boldsymbol{M}^T\boldsymbol{M} = \boldsymbol{M}\boldsymbol{M}^T = \boldsymbol{I} \text{ and } \det\boldsymbol{M} = 1\right\}$.

[10] $\mathcal{S}^n_>$ is the set of every symmetric, positive, definite tensor belonging to $\mathcal{M}^n$. Therefore, for $n = 3$ one has $\mathcal{S}^3_> = \left\{\boldsymbol{M} \in \mathcal{S}^3 | \boldsymbol{a}^T\boldsymbol{M}\boldsymbol{a} > 0, \ \forall \boldsymbol{a} \in \mathcal{R}^3 \neq \boldsymbol{0}\right\}$.

$\boldsymbol{C}^e \coloneqq \boldsymbol{F}^{e^T}\boldsymbol{F}^e \in \mathcal{S}^3_>$, by

$$(\boldsymbol{U}^e)^2 = \boldsymbol{C}^e. \tag{3.40}$$

The present development adopts the *Hencky* (or logarithmic) strain measure:[11]

$$(\boldsymbol{E}^e)^{(0)} = \ln(\boldsymbol{U}^e). \tag{3.41}$$

For sake of simplicity, in what follows the notation

$$\boldsymbol{E} = \boldsymbol{E}^{(0)} \in \mathcal{S}^3_> \tag{3.42}$$

is adopted. The work conjugate of $\boldsymbol{E}$ is the rotated *Kirchhoff* stress tensor, $\bar{\boldsymbol{\tau}} \in \mathcal{S}^3$, defined as

$$\bar{\boldsymbol{\tau}} = \boldsymbol{R}^{e^T}\boldsymbol{\tau}\boldsymbol{R}^e = J\boldsymbol{R}^{e^T}\boldsymbol{\sigma}\boldsymbol{R}^e. \tag{3.43}$$

The scalar product $\bar{\boldsymbol{\tau}} : \dot{\boldsymbol{E}}$ satisfies the invariance related to the rate of work per unit of volume ($\dot{w}_0 : \Omega_0 \times \mathcal{I} \to \mathcal{R}_{\geq 0}$) [Hill, 1979b]:

$$\dot{w}_0 = J\boldsymbol{\sigma} : \boldsymbol{D} = \boldsymbol{\tau} : \boldsymbol{D} = \boldsymbol{P} : \dot{\boldsymbol{F}} = \frac{1}{2}\boldsymbol{P}^S : \dot{\boldsymbol{C}} = \bar{\boldsymbol{\tau}} : \dot{\boldsymbol{E}}, \tag{3.44}$$

where the second *Piola-Kirchhoff* $\left(\boldsymbol{P}^S \in \mathcal{S}^3\right)$ and *Kirchhoff* stress tensors ($\boldsymbol{\tau} \in \mathcal{S}^3$) are given respectively by (see also Eq. (3.14))

$$\boldsymbol{P}^S \coloneqq \boldsymbol{F}^{-1}\boldsymbol{P} = J\boldsymbol{F}^{-1}\boldsymbol{\sigma}\boldsymbol{F}^{-T} \text{ and } \boldsymbol{\tau} = \boldsymbol{P}\boldsymbol{F}^T = J\boldsymbol{\sigma} \tag{3.45}$$

The symmetry associated with tensors $\boldsymbol{C}^e$, $\boldsymbol{U}^e$, and $\boldsymbol{E}^e$ allows to perform the following spectral decompositions [Weber and Anand, 1990; de Souza Neto et al., 2008]:

$$\boldsymbol{C}^e = \sum_{i=1}^{3} (\lambda_i^e)^2\, \boldsymbol{l}_i \otimes \boldsymbol{l}_i, \quad \boldsymbol{U}^e = \sum_{i=1}^{3} \lambda_i^e \boldsymbol{l}_i \otimes \boldsymbol{l}_i, \quad \text{and} \quad \boldsymbol{E}^e = \sum_{i=1}^{3} \ln(\lambda_i^e)\, \boldsymbol{l}_i \otimes \boldsymbol{l}_i, \tag{3.46}$$

where $(\lambda_i^e)^2$ are the eigenvalues and $\boldsymbol{l}_i$ the eigenvectors of tensor $\boldsymbol{C}^e$. One notes that tensors $\boldsymbol{C}^e$, $\boldsymbol{U}^e$, and $\boldsymbol{E}^e$ have the same principal directions. Once $\ln(\boldsymbol{U}^e)$ is an isotropic function, the spectral decomposition of $\boldsymbol{E}^e$ can be given according to Eq. $(3.46)_3$. For more details, see de Souza Neto et al., 2008, for example.

### 3.3 *Helmholtz* free-energy and reduced dissipation inequality

As discussed previously in Subsection 3.1.5, the TIV approach assumes that the local thermodynamic state can be uniquely determined by the instantaneous values of a given

[11] That strain measure is a special case of a *Lagrangian* family: $\boldsymbol{E}^{(m)} = \begin{cases} \frac{1}{m}(\boldsymbol{U}^m - \boldsymbol{I}) & \text{for } m \neq 0 \\ \ln(\boldsymbol{U}) & \text{for } m = 0 \end{cases}$ [Hill, 1979b; Ogden, 1997; Seth, 1964].

set of state variables, in this case $(\boldsymbol{F}, \theta, \boldsymbol{\alpha})$. However, a set composed by $(\theta, \boldsymbol{\alpha})$ and a given strain measure in terms of $\boldsymbol{F}$ is not suitable for a plastic material, once the total deformation gradient describes the whole deformation process, from the initial state to the current one. Consequently, if there is no hardening, the state will be the same at every stress-free configurations. For example, supposing a cylindrical specimen, which was subjected to a finite plastic strain, its local thermodynamic state is independent on the total stretching, that is, it depends on $\boldsymbol{F}^e$ and not on $\boldsymbol{F}$ [Mandel, 1972, p. 43-44]. In summary, to achieve invariance with respect to previous plastic deformations the set of state variables, instead of depending on $\boldsymbol{F}$, has to depend on a strain measure given in terms of the elastic part $\boldsymbol{F}^e$. See also the discussion of Miehe and Schotte, 2004.

In a first moment, two scalar internal variables are introduced. Therefore, $n_{int} = 2$, and the set of internal variables becomes $\boldsymbol{\alpha} = \{\alpha_1, \alpha_2\}$, where both $\alpha_1, \alpha_2 \in \mathcal{R}_{\geq 0}$ are macroscopic inelastic variables associated with the isotropic hardening. On one hand, variable $\alpha_1$ is intended to represent the hardening behavior during Stages II and III, and on the other hand, variable $\alpha_2$ features the *quasi*-linear hardening observed during deformation Stage IV (see discussions provided in Subsections 1.4.1 and 1.4.4).

As a consequence of previous discussion, the current local thermodynamic state of a given material point is uniquely determined by the instantaneous values of variables

$$(\boldsymbol{E}^e, \theta, \boldsymbol{\alpha}), \tag{3.47}$$

given in a stress-free configuration. Therefore, considering isothermal processes $\left(\dot{\theta} = 0\right)$, the *Helmholtz* free energy $\psi : \mathcal{S}^3_> \times \mathcal{R}^2_{\geq 0} \to \mathcal{R}_{\geq 0}$ can be given by the following additive decomposition [Lubliner, 1984]:

$$\psi(\boldsymbol{E}^e, \boldsymbol{\alpha}) = \psi^e(\boldsymbol{E}^e) + \psi^{vp}(\boldsymbol{\alpha}), \tag{3.48}$$

where the elastic part $\psi^e : \mathcal{S}^3_> \to \mathcal{R}_{\geq 0}$ is given in terms of $\boldsymbol{E}^e$, and the inelastic part $\psi^{vp} : \mathcal{R}^2_{\geq 0} \to \mathcal{R}_{\geq 0}$ as a function of the internal variables $\alpha_1$ and $\alpha_2$. Thus, supposing that function $\psi(\boldsymbol{E}^e, \boldsymbol{\alpha})$ is sufficiently smooth its rate is given by (summation over repeated indices is not applied)

$$\dot{\psi}(\boldsymbol{E}^e, \boldsymbol{\alpha}) = \frac{\partial \psi^e}{\partial \boldsymbol{E}^e} : \dot{\boldsymbol{E}}^e + \sum_{k=1}^{2} \frac{\partial \psi^{vp}}{\partial \alpha_k} \dot{\alpha}_k. \tag{3.49}$$

Using the decomposition of Eq. (3.34) and knowing the work conjugates of Eq. (3.44), the *Clausius-Duhem* inequality(3.28) is rewritten as

$$\Phi_0 = \left( \bar{\boldsymbol{\tau}} - \rho_0 \frac{\partial \psi^e}{\partial \boldsymbol{E}^e} \right) : \dot{\boldsymbol{E}}^e + \boldsymbol{\tau} : \boldsymbol{D}^{vp} - \sum_{k=1}^{2} \rho_0 \frac{\partial \psi^{vp}}{\partial \alpha_k} \dot{\alpha}_k \geq 0. \tag{3.50}$$

Once condition (3.50) holds for every thermodynamic processes, the constitutive relation [Coleman and Gurtin, 1967; Lubliner, 1984; Rice, 1971]

$$\bar{\boldsymbol{\tau}} = \rho_0 \frac{\partial \psi^e}{\partial \boldsymbol{E}^e}, \tag{3.51}$$

and the dissipation inequality

$$\Phi_0 = \boldsymbol{\tau} : \boldsymbol{D}^{vp} - \sum_{k=1}^{2} A_k \dot{\alpha}_k \geq 0, \tag{3.52}$$

are then obtained. In the last expression, the thermodynamic forces $A_1, A_2 \in \mathcal{R}_{\geq 0}$, which are the respective work conjugate of internal variables $\alpha_1, \alpha_2$, were defined as:

$$A_k \coloneqq \rho_0 \frac{\partial \psi^{vp}}{\partial \alpha_k},\ k = \{1, 2\}\,. \tag{3.53}$$

Since isothermal processes are assumed, only the intrinsic dissipation is accounted for by potential $\Phi_0$.

In the subsequent development, the free-energy is assumed to be given by the standard quadratic forms:

$$\rho_0 \psi^e = \frac{1}{2} \boldsymbol{E}^e : \mathbb{D}^e : \boldsymbol{E}^e \ \text{ and } \ \rho_0 \psi^{vp} = \frac{1}{2} \left( \bar{H} \alpha_1^2 + \tilde{H} \alpha_2^2 \right), \tag{3.54}$$

where $\mathbb{D}^e \coloneqq \rho_0 \frac{\partial^2 \psi^e}{\partial \boldsymbol{E}^e \otimes \partial \boldsymbol{E}^e}$ is a hyperelastic forth-order tensor, which is assumed to be symmetric, positive-definite, and constant. Parameter $\bar{H}, \tilde{H} \in \mathcal{R}_{\geq 0}$ are model constants, which in a formal way respectively read $\bar{H} \coloneqq \rho_0 \frac{\partial^2 \psi^{vp}}{\partial \alpha_1^2}$ and $\tilde{H} \coloneqq \rho_0 \frac{\partial^2 \psi^{vp}}{\partial \alpha_2^2}$. Due to the use of two internal variables, definition of viscoplastic free-energy $\rho_0 \psi^{vp}$ stated in Eq. (3.54) is different to that presented in [dos Santos et al., 2016], where a single internal variable was employed.

In view of Eqs. (3.51) and $(3.54)_1$, (3.53) and $(3.54)_2$, the following constitutive relations are therefore obtained:

$$\bar{\boldsymbol{\tau}} = \rho_0 \frac{\partial \psi^e}{\partial \boldsymbol{E}^e} = \mathbb{D}^e : \boldsymbol{E}^e,\ A_1 = \rho_0 \frac{\partial \psi^{vp}}{\partial \alpha_1} = \bar{H} \alpha_1, \text{ and } A_2 = \rho_0 \frac{\partial \psi^{vp}}{\partial \alpha_2} = \tilde{H} \alpha_2. \tag{3.55}$$

Equations $(3.55)_2$ and $(3.55)_3$ are particularizations of general relations given in Eqs. (1.6) and (1.7), respectively. Complying with assumed elastic isotropy hypothesis, elastic tensor is given by

$$\mathbb{D}^e = 2\mu \mathbb{I} + \left( \kappa - \frac{2}{3} \mu \right) \boldsymbol{I} \otimes \boldsymbol{I}, \tag{3.56}$$

being $\mathbb{I}$, $\boldsymbol{I}$, $\mu \in \mathcal{R}_{>0}$, and $\kappa \in \mathcal{R}_{>0}$ the fourth-order and the second-order identity tensors, the shear and bulk modulus, respectively. Components of $\mathbb{I}$ are $I_{ijkl} = \frac{1}{2} \left( \delta_{ik} \delta_{jl} + \delta_{il} \delta_{jk} \right)$.

By hypothesis, every hyperelastic characteristic highlighted earlier does not change with imposed deformation.

As was discussed previously, the velocity gradient tensor $\boldsymbol{L}$, Eq. (3.31), and its elastic and inelastic parts, given respectively by Eqs. (3.32) and (3.33), are quantities defined on the current configuration. Thus, in order to be coherent with the present approach, those variables, specifically the inelastic strain-rate tensor $\boldsymbol{D}^{vp}$, Eq. $(3.34)_2$, have to be accounted for in the stress-free configuration. Thus, tensor $\boldsymbol{L}^{vp}$ in Eq. $(3.33)_2$ is pulled back to the intermediate configuration by performing the product

$$\bar{\boldsymbol{L}}^{vp} := \boldsymbol{F}^{e^{-1}} \boldsymbol{L}^{vp} \boldsymbol{F}^{e},$$

which yields

$$\bar{\boldsymbol{L}}^{vp} := \dot{\boldsymbol{F}}^{vp} \boldsymbol{F}^{vp^{-1}}, \tag{3.57}$$

where $\bar{\boldsymbol{L}}^{vp}$ is the inelastic part of $\boldsymbol{L}$ given in the intermediate configuration. Tensor $\bar{\boldsymbol{L}}^{vp}$ can be decomposed into its symmetric $\bar{\boldsymbol{D}}^{vp}$ (inelastic strain-rate tensor) and antisymmetric $\bar{\boldsymbol{W}}^{vp}$ (inelastic spin tensor) parts:

$$\bar{\boldsymbol{L}}^{vp} = \bar{\boldsymbol{D}}^{vp} + \bar{\boldsymbol{W}}^{vp}, \tag{3.58}$$

where

$$\bar{\boldsymbol{D}}^{vp} = \frac{1}{2}\left(\bar{\boldsymbol{L}}^{vp} + \bar{\boldsymbol{L}}^{vp^T}\right) \text{ and } \bar{\boldsymbol{W}}^{vp} = \frac{1}{2}\left(\bar{\boldsymbol{L}}^{vp} - \bar{\boldsymbol{L}}^{vp^T}\right). \tag{3.59}$$

However, considering the hypothesis of isotropic plasticity adopted in the present formulation, without loss in generality, a irrotational plastic flow may be assumed [Weber and Anand, 1990; de Souza Neto et al., 2008; Gurtin et al., 2010]:

$$\bar{\boldsymbol{W}}^{vp} = \boldsymbol{0}. \tag{3.60}$$

This fact allows rewriting the dissipation inequality (3.52) as

$$\Phi_0 = \boldsymbol{\tau} : \boldsymbol{F}^{e} \bar{\boldsymbol{D}}^{vp} \boldsymbol{F}^{e^{-1}} - \sum_{k=1}^{2} A_k \dot{\alpha}_k \geq 0. \tag{3.61}$$

After an algebraic manipulation, considering the isotropy associated with tensor $\mathbb{D}^e$ of Eq. (3.56), the reduced dissipation inequality reads [Eterovic and Bathe, 1990]:

$$\Phi_0 = \bar{\boldsymbol{\tau}} : \bar{\boldsymbol{D}}^{vp} - \sum_{k=1}^{2} A_k \dot{\alpha}_k \geq 0. \tag{3.62}$$

### 3.4 Elastic domain and yield function

In the present approach, the isotropic hardening is represented by a variable $A \in \mathcal{R}_{\geq 0}$ given by the sum of the two thermodynamic forces $A_1$ and $A_2$:

$$A = A_1 + A_2. \tag{3.63}$$

Accordingly, the isotropic hardening results strengthening mechanisms associated with earlier (Stages II and III) as well as latter (Stage IV) deformation stages. See discussion provided in Subsection 1.4.4. Hardening variable $A$ dictates the current elastic domain size. In a formal way, the transition between a purely elastic state and an elastic-viscoplastic one is defined by a closed convex set $\left(\bar{\mathcal{Y}} \subset \mathcal{S}^3_{>} \times \mathcal{R}_{\geq 0}\right)$ given by

$$\bar{\mathcal{Y}} = \left\{(\bar{\boldsymbol{\tau}}, A) \,|f\,(\bar{\boldsymbol{\tau}}, A) \leq 0\right\}, \tag{3.64}$$

where the yield function $(f : \mathcal{S}^3_{>} \times \mathcal{R}_{\geq 0} \to \mathcal{R})$

$$f = f\,(\bar{\boldsymbol{\tau}}, A) \tag{3.65}$$

depends on both $\bar{\boldsymbol{\tau}}$ and $A$. Condition $f = 0$ defines the yield surface $\partial\mathcal{Y} \subset \bar{\mathcal{Y}}$, which is the boundary of set $\bar{\mathcal{Y}}$:

$$\partial\mathcal{Y} = \left\{(\bar{\boldsymbol{\tau}}, A) \,|f\,(\bar{\boldsymbol{\tau}}, A) = 0\right\}. \tag{3.66}$$

In the rate-independent plasticity theories, set $\bar{\mathcal{Y}}$ stands for the admissible stress space. Accordingly, all stress states $(\bar{\boldsymbol{\tau}}, A)$ must lie into the domain $\bar{\mathcal{Y}}$. In contrast, condition $(\bar{\boldsymbol{\tau}}, A) \notin \bar{\mathcal{Y}}$ is physically possible in viscoplastic approaches.

For sake of simplicity, a *von Mises* yield criterion with an isotropic hardening is adopted in subsequent analysis:

$$f\,(\bar{\boldsymbol{\tau}}, A) = \left\|\bar{\boldsymbol{\tau}}^D\right\| - \sqrt{\frac{2}{3}}\,(\sigma_y + A), \tag{3.67}$$

where $\left\|\bar{\boldsymbol{\tau}}^D\right\| = \sqrt{\bar{\tau}^D_{ij}\bar{\tau}^D_{ij}}$, $\bar{\boldsymbol{\tau}}^D = \bar{\boldsymbol{\tau}} - \frac{1}{3}\mathrm{tr}\,(\bar{\boldsymbol{\tau}})\,\boldsymbol{I}$ is the deviatoric part of $\bar{\boldsymbol{\tau}}$ and $\sigma_y \in \mathcal{R}_{>0}$ is the initial yield stress, which in this work corresponds to an annealed condition. The initial yield stress (related to an annealed state) of FCC metals can be considered as a rate-independent quantity [Voyiadjis and Abed, 2005; Rusinek et al., 2010; Rusinek and Jankowiak, 2014]. In this type of metals, the *Peierls-Nabarro* stress (which is strongly temperature and rate-dependent) has a minor contribution on the strength, thus the initial plastic flow is governed by short range barriers, as dislocations forests [Dieter, 1986], which in their turn depend on the current microstructural state and not on the instantaneous strain-rate. Thus, following this discussion, a constant initial yield stress $\sigma_y$ is going to be considered in this work.

### 3.5 Flow potential and inelastic evolution equations

In addition to defining the yield criterion as well as specific internal variables, kinetic and structure evolution equations have to be addressed. The kinetic equation represents the kinetics of plastic flow at constant structure. In other words, kinetic equation correlates an equivalent plastic strain-rate with applied stress considering a *fixed microstructure* [Kocks et al., 1975; Estrin and Mecking, 1984; Tjøtta and Mo, 1993]. In contrast, the structure evolution equation describes structure changes due to imposed deformation at a *given strain-rate* (and temperature) [Kocks et al., 1975; Estrin and Mecking, 1984]. Selecting suitable internal variables and defining their evolution equations are most cumbersome task in developing a suitable viscoplastic model, since the microstructure evolves in a very complicated manner. According to Brown et al., 1989, this task becomes even harder because the different mechanisms governing plastic deformation are still incompletely known, and also the actual mechanisms are associated with complex structures and processes certainly not totally representable by a few internal variables. In what follows, proposed functional forms are based upon previous constitutive developments, relevant metallurgical evidences described in the literature, and also on the experimental results presented in Section 2.3.

Following a formal constitutive framework, inelastic evolution can be given by general constitutive equations,[12]

$$\bar{\boldsymbol{D}}^{vp} = \dot{\lambda}\frac{\partial \phi}{\partial \bar{\boldsymbol{\tau}}}, \;\; \dot{\alpha}_1 = -\dot{\lambda}\frac{\partial \phi}{\partial A_1}, \;\; \text{and} \;\; \dot{\alpha}_2 = -\dot{\lambda}\frac{\partial \phi}{\partial A_2}, \tag{3.68}$$

in which $\phi = \phi\left(\bar{\boldsymbol{\tau}}, \boldsymbol{A}\right)$ is a flow potential. In order to comply with thermodynamic restrictions imposed by the dissipation inequality (3.62), potential $\phi$ is required to be a convex non-negative function of both $\bar{\boldsymbol{\tau}}$ and $\boldsymbol{A} = \{A_1, A_2\}$, and zero-valued at origin, i.e., $\phi\left(\boldsymbol{0}, \boldsymbol{0}\right) = 0$ [Rice, 1971; Halphen and Son Nguyen, 1975; Chaboche, 1989; Nemat-Nasser, 2009].

In the inelastic evolution equations given in Eq. (3.68), $\dot{\lambda} \in \mathcal{R}_{\geq 0}$ is a viscoplastic multiplier which, differently from a rate-independent model, instead of satisfying the *Karush-Kuhn-Tucker* and consistency conditions, must satisfy a given kinetic equation. In the present development, following a phenomenological approach, the viscoplastic framework proposed by Perzyna, 1966, 1971 is chosen. Therefore, the kinetic equation is given by an overstress function:

$$\dot{\lambda} = \Theta\left(\langle f \rangle, A\right), \tag{3.69}$$

where $\langle x \rangle := \frac{1}{2}\left(x + |x|\right)$ denotes the *Macaulay* brackets and $\Theta : \mathcal{R}^2_{\geq 0} \rightarrow \mathcal{R}_{\geq 0}$ is the overstress function which should be convex. Usually, function $\Theta$ is given only in terms of

[12] If $\phi\left(\bar{\boldsymbol{\tau}}, \boldsymbol{A}\right)$ is a non-smooth function, a more general formulation can be obtained inside the convex analysis framework employing sub-gradient concepts [Eve et al., 1990b,a; de Angelis, 2000].

positive values of yield function $f$. However, subsequent analysis conveniently assumes that $\Theta$ depends explicitly on both $f$ and hardening parameter $A$, and as usual, complies with condition $\Theta(0, A) = 0$. For values of yield function satisfying $f \geq 0$, $\Theta$ admits an inverse in terms of $f$ and $\dot{\lambda}$:

$$f = \Theta^{-1}\left(\dot{\lambda}, A\right). \tag{3.70}$$

The following step consists now of choosing the proper flow potential $\phi$, which will define the functional forms associated with material inelastic evolution. In a first moment, this potential assumes a simple additive decomposition:

$$\phi\left(\bar{\boldsymbol{\tau}}, A_1, A_2\right) = \phi_{\bar{\tau}}\left(\bar{\boldsymbol{\tau}}\right) + \phi_1\left(A_1\right) + \phi_2\left(A_2\right). \tag{3.71}$$

The following flow potentials are going to be assumed:

$$\phi_{\bar{\tau}} = \left\|\bar{\boldsymbol{\tau}}^D\right\|, \;\; \phi_1 = -\sqrt{\frac{2}{3}} h_1 \left(1 - \frac{A_1}{2A_\infty}\right) A_1, \;\; \text{and} \;\; \phi_2 = -\sqrt{\frac{2}{3}} h_2 A_2, \tag{3.72}$$

where $A_\infty \geq 0$, $h_1 \geq 0$, and $h_2 \geq 0$ are parameters which can depend on the imposed strain-rate, through the accumulated viscoplastic strain $\varepsilon$, whose rate is defined as

$$\dot{\varepsilon} := \sqrt{\frac{2}{3}} \left\|\bar{\boldsymbol{D}}^{vp}\right\| \geq 0. \tag{3.73}$$

We highlight that, since structure evolution equations are taken at a given viscoplastic strain-rate [Kocks et al., 1975; Estrin and Mecking, 1984], consequently in potentials $\phi_1$ and $\phi_2$ corresponding parameters $A_\infty$, $h_1$, and $h_2$ are fixed. Furthermore, potentials defined in Eqs. (3.72) were set *a priori* in order to comply with the evolution equations to be presented in the sequel.

Flow potential $\phi_{\bar{\tau}}$ assumed in Eq. $(3.72)_1$ complies with the *von Mises* yield criterion and with an associative flow rule. Then the following flow rule is obtained for the viscoplastic strain-rate:

$$\bar{\boldsymbol{D}}^{vp} = \dot{\lambda} \boldsymbol{N}_{\bar{\tau}}, \tag{3.74}$$

where $\boldsymbol{N}_{\bar{\tau}} := \frac{\bar{\tau}^D}{\left\|\bar{\tau}^D\right\|}$ is an unity tensor: $\left\|\boldsymbol{N}_{\bar{\tau}}\right\| = 1$. Consequently, the rate given in Eq. (3.73) becomes

$$\dot{\varepsilon} = \sqrt{\frac{2}{3}} \dot{\lambda} \geq 0. \tag{3.75}$$

The other two potentials of Eq. (3.72) are set in order to comply with the following observations.

There are many phenomenological works [Perzyna, 1966, 1971; Perić, 1993; Ristinmaa and Ottosen, 1998; Alfano et al., 2001] in which the accumulated viscoplastic strain $\varepsilon$ is taken as an internal variable, which is related to the hardening variable by means of

constant parameters. However, as discussed by Nemat-Nasser, 2009, p.212, these constitutive proposals have limited predictive capabilities in accounting for loading-history effects. Then, with the aim of incorporating strain-rate effects into hardening mechanisms, instead of Eq. (3.73), an alternative evolution law for internal variables $\alpha_1$ and $\alpha_2$ shall be adopted. In the present development, the internal variables $\alpha_1$ and $\alpha_2$ do not have physical meaning as in physically-based models, which are based on rational analysis of the underlying inelastic mechanisms. However, as a simple macroscopic proposal still falling into a phenomenological approach, the present model has qualitative micromechanical basis, relying on mechanisms as accumulation and organization of dislocation cells, and formation of new sub/grains. Some authors as Rusinek and Jankowiak, 2014, classify this type of constitutive formulation as semi-physical models, in which, similarly to physically-based formulations, the accumulated plastic strain serves only as a *load parameter*, and not as a proper state variable [Nemat-Nasser, 2009, p.213].

From a physical point of view, it is commonly accepted that the overall strain-rate-sensitivity on stress response of metals is composed by two main contributions: (i) the instantaneous rate-sensitivity, which is related to the waiting-time of thermally activated dislocation motion and to viscous drag resistance (this effect can be accounted for by function $\Theta$); and (ii) the microstructural rate-dependence, associated with the evolution of metallurgical features, such as dislocation storage and grain/subgrain sizes. Those two rate-dependent mechanisms can be strongly influenced by both the strain and strain-rate-histories [Klepaczko and Chiem, 1986; Rashid et al., 1992].

Considering the present constitutive approach, microstructural aspects are macroscopically accounted for by the hardening variable $A = A_1 + A_2$, which contribute to the current material strength $\sigma_y + A\left(\alpha_1, \alpha_2, \ldots\right)$. Since the model is intended to describe finite strain deformation processes, the present isotropic hardening is proposed be the result of two contributions covering deformation Stages II, III, and IV. The first hardening variable $\alpha_1$ corresponds to accumulation and arrangement of dislocation cells. These features govern the material hardening response observed in deformation Stages II and III [Nes, 1997; Kocks and Mecking, 2003]. The second contribution, featured by $\alpha_2$, relates to material hardening observed at later stages of straining: Stage IV. This deformation stage is characterized by a significant reduction in the hardening-rate at the Stage III saturation [Rollett et al., 1989; Nes, 1997; Kocks and Mecking, 2003]. See for instance explanation given in Subsection 1.4.1.

According to Eq. $(3.68)_2$, flow potential of Eq. $(3.72)_2$, and considering Eq. $(3.55)_2$ and (3.75), variable $\alpha_1$ related to dislocation storage has its evolution given by

$$\dot{\alpha}_1 = h_1 \left(1 - \frac{\alpha_1}{\alpha_\infty}\right) \dot{\varepsilon}, \tag{3.76}$$

in which $\alpha_\infty$ is the saturation parameter related to $\alpha_1$. Parameter $h_1$ stands for the

rate at which $\alpha_1$ approaches the saturation. The last evolution equation is a simple empirical expression based upon dislocation generation and annihilation processes, which disregards static recovery mechanisms[13] [Kocks, 1976; Brown et al., 1989; Tjøtta and Mo, 1993]. Moreover, in view of Eq. $(3.55)_2$ one obtains

$$\dot{A}_1 = H_1 \left(1 - \frac{A_1}{A_\infty}\right) \dot{\varepsilon}, \tag{3.77}$$

where $H_1 \coloneqq \bar{H} h_1$ is the hardening-rate and $A_\infty \coloneqq \bar{H} \alpha_\infty$ is the saturation hardening to be defined latter. In order to account for monotonic loading applications, one can readily integrate evolution equation (3.77) for a constant strain-rate $\dot{\varepsilon}$, what results in the following *Voce* hardening rule [Voce, 1948]:

$$\frac{A_1 - A_\infty}{A_{1_i} - A_\infty} = \exp\left[-\delta \left(\varepsilon - \varepsilon_i\right)\right]. \tag{3.78}$$

Parameters $A_{1_i}$ and $\varepsilon_i$ stand for the initial values of $A_1$ and $\varepsilon$, respectively. In the present formulation, ratio $\delta \coloneqq \frac{H_1}{A_\infty}$ and parameter $A_\infty$ are assumed to be rate-dependent quantities.

The second hardening variable $\alpha_2$ is linked to hardening behavior observed during deformation Stage IV, which is not as well understood as are the other stages (I, II and III). See discussion in Subsection 1.4.1. Based upon monotonic loading applications, a simple form of potential $\phi_2$ (Eq. $(3.72)_3$) was assumed, thus yielding a linear relationship between $\dot{\alpha}_2$ and the loading rate $\dot{\varepsilon}$,

$$\dot{\alpha}_2 = h_2 \dot{\varepsilon}, \tag{3.79}$$

which is evidenced to be in accordance with experimentally observed *quasi*-linear hardening featuring deformation Stage IV. From Eqs. $(3.55)_3$ and (3.79) the rate of $A_2$ can be given in terms of the accumulated viscoplastic strain-rate $\dot{\varepsilon}$:

$$\dot{A}_2 = H_2 \dot{\varepsilon}, \tag{3.80}$$

where $H_2 \coloneqq \tilde{H} h_2$ is the linear hardening-rate related to Stage IV. Even approximately, it is possible to write a scaling law between $H_2$ and saturation parameter $A_\infty$, $H_2 = c A_\infty$ [Rollett et al., 1989; Kocks and Mecking, 2003], which yields

$$\dot{A}_2 = c A_\infty \dot{\varepsilon}, \tag{3.81}$$

[13] Law (3.77) is a particular case of the *Bailey-Orowan* equation [Bailey, 1926; Orowan, 1945], without the static recovery term. A more general model was employed by Brown et al., 1989, for hot working of metals, where they assume the evolution $\dot{\alpha}_1 = h_1 \left|\left(1 - \frac{\alpha_1}{\alpha_\infty}\right)\right|^a \operatorname{sign}\left(1 - \frac{\alpha_1}{\alpha_\infty}\right) \dot{\varepsilon} - \dot{r}$, in which $a \geq 1$ and $\dot{r}$ is the static recovery evolution.

where $c \geq 0$ is a small constant. Integrating this equation for a constant rate $\dot{\varepsilon}$, one has

$$A_2 = A_{2_i} + cA_\infty \left(\varepsilon - \varepsilon_i\right). \tag{3.82}$$

Observing Eq. (3.82), one observes that the hardening-rate at large strains is given by term $cA_\infty$, which is dependent on strain-rate since $A_\infty$ is a rate-dependent parameter. In fact, $A_\infty$ increases with imposed strain-rate. However, within the strain-rate range considered here, as $c$ has a small value, the difference between stress values $cA_\infty\varepsilon$ obtained for both *quasi*-static and high strain-rate loading is small when compared with the total stress for a given strain level $\varepsilon$. Thus, approximation $cA_\infty \approx$ cte can be considered. Then, assuming $A_{2_i} = \varepsilon_i = 0$, even for a varying strain-rate loading, one has

$$A_2 \approx cA_\infty\varepsilon. \tag{3.83}$$

The last equation gives the hardening $A_2$ as a state function of $\varepsilon$. However, since in general case the accumulated viscoplastic strain $\varepsilon$ is not a suitable internal variable, this state equation is based upon monotonic loading conditions. This simplification was taken in order to work in terms of only one hardening variable: $A$. Then, combination of Eqs. (3.78) and (3.83), in view of Eq. (3.63), results

$$A = A_i + A_\infty c\left(\varepsilon - \varepsilon_i\right) + \left[A_\infty\left(1 + c\varepsilon_i\right) - A_i\right]\left\{1 - \exp\left[-\delta\left(\varepsilon - \varepsilon_i\right)\right]\right\}, \tag{3.84}$$

where $A_i$ is the initial value of $A$. Further, for $A_i = \varepsilon_i = 0$, Eq. (3.84) reduces to

$$A = A_\infty\left[1 + c\varepsilon - \exp\left(-\delta\varepsilon\right)\right], \tag{3.85}$$

which can be seen as a modified *Voce* hardening rule appended with a linear term. This relationship, which was qualitatively based upon metallurgical aspects, is slightly different from those proposed by Tome et al., 1984, or Simo and Armero, 1992. The latter is recovered when both $\delta$ and $A_\infty$ are constant.

However, here the hardening rule (3.85) should account for rate effects on hardening response by letting parameters $\delta$ and $A_\infty$ to be rate-dependent. Therefore, the following *a priori* rate-dependent forms are postulated for both $\delta$ and $A_\infty$, respectively:[14]

$$\delta = \left[1 - \beta_1\left(\dot{\varepsilon}\right)\right]\delta^{lwr} + \beta_1\left(\dot{\varepsilon}\right)\delta^{up} \tag{3.86}$$

[14]The present constitutive proposal was first published in a previous article [dos Santos et al., 2016]. However, in that work, in order to represent experimental results associated with an annealed high purity copper available in the literature [Nemat-Nasser and Li, 1998; Tanner and McDowell, 1999; Jordan et al., 2013], parameter $\delta$ was considered to be constant and $A_\infty$ rate-dependent. In the present development, with the aim of providing a more general approach, and also of representing experimental data presented in Section 2.3, both parameters $\delta$ and $A_\infty$ are assumed to be rate-dependent.

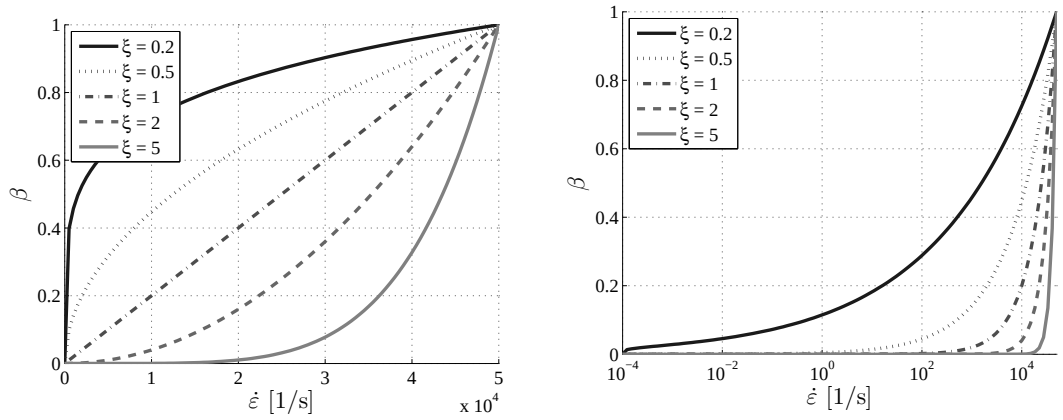


Figure 3.3: Influence of parameter $\xi$ on function $\beta\left(\dot{\varepsilon}\right)$ for $\dot{\varepsilon}_{lwr} = 10^{-4}\,\mathrm{s}^{-1}$ and $\dot{\varepsilon}_{up} = 5 \times 10^{4}\,\mathrm{s}^{-1}$: (a) linear scale; (b) logarithm scale. Source: dos Santos et al., 2016.

and

$$A_{\infty} = \left[1 - \beta_2\left(\dot{\varepsilon}\right)\right] A_{\infty}^{lwr} + \beta_2\left(\dot{\varepsilon}\right) A_{\infty}^{up}, \tag{3.87}$$

where $\delta^{lwr}$ and $A_{\infty}^{lwr}$ are the respective values of both $\delta$ and $A_{\infty}$ measured at a lower reference rate $\dot{\varepsilon}_{lwr} \ll 1$, $\delta^{up}$ and $A_{\infty}^{up}$ are the values associated with an upper reference strain-rate $\dot{\varepsilon}_{up} \gg 1$. In Eqs. (3.86) and (3.87), based on the previous work [dos Santos et al., 2016], functions $\beta_i,\ i = \{1, 2\}$, are given by

$$\beta_i\left(\dot{\varepsilon}\right) = \left(\frac{\dot{\varepsilon} - \dot{\varepsilon}_{lwr}}{\dot{\varepsilon}_{up} - \dot{\varepsilon}_{lwr}}\right)^{\xi_i}, \tag{3.88}$$

satisfying $\beta_i\left(\dot{\varepsilon}_{lwr}\right) = 0$ and $\beta_i\left(\dot{\varepsilon}_{up}\right) = 1$. Parameters $\xi_i > 0,\ i = \{1, 2\}$, are model constants. Function $\beta$ versus inelastic strain-rate $\dot{\varepsilon}$ is displayed in Figures 3.3 for different values of $\xi$ , with $\dot{\varepsilon}_{lwr} = 10^{-4}\,\mathrm{s}^{-1}$ and $\dot{\varepsilon}_{up} = 5 \times 10^{4}\,\mathrm{s}^{-1}$. Increasing parameter $\xi$ causes a more sudden increase in function $\beta$ as $\dot{\varepsilon}$ approaches $\dot{\varepsilon}_{up}$. Functions $\beta_i,\ i = \{1, 2\}$, are empirical relations intended to represent experimental results showing that both nonlinear hardening-rate and saturation hardening are increased by increasing the imposed strain-rate (see 2.10). In addition, these features change their rate-sensitivity for higher strain-rates [Follansbee and Kocks, 1988].

*Remark* 3.3. A discussion on the strain-rate validity of the constitutive assumptions associated with the preceding proposal have to be addressed. Some authors, as Qi et al., 2009, and Yu et al., 2013, advocate that the strain-rate-induced strengthening of engineering materials tends to a saturation limit. On one hand, the functional form of Eq. (3.88) presented in this work does not express the saturation of parameters $\delta$ and $A_{\infty}$ in terms of strain-rate. Such an assumption becomes reasonable into the strain-rate regime adopted in this work, since authors such as Armstrong et al., 2007, and Meyers et al., 2003, have shown that the flow stress (controlled by dislocation generation at the shock

front) of ductile FCC metals as pure copper still increases with strain-rate for values exceeding $10^7\,\mathrm{s}^{-1}$. See also discussion of Huang et al., 2009, and references cited therein. In fact, there are few works (see Borodin et al., 2014) pointing towards a saturation in the strain-rate effect on the dynamic yielding strength of metals at ultra-high strain-rates ($> 10^7\,\mathrm{s}^{-1}$). On the other hand, for material modeling purpose, in which the strain-rate effect saturation becomes a significant constitutive feature within the desired strain-rate regime, this saturation behavior can be accounted for by adopting a *S-shaped* functional form for parameter $\beta_i\left(\dot{\varepsilon}\right)$ instead of functional form proposed in Eq. (3.88). However, the model presented in this work is not intended to model very high strain-rate (much higher than $10^4\,\mathrm{s}^{-1}$) processes, where the the plastic deformation and the hardening behavior can be controlled by shock wave propagation [Meyers, 1994].

For a graphical illustration, keeping $\delta$ constant and setting $c = 0$, a schematic representation of the strain-rate influence on saturation hardening $A_\infty$, and thus on the stress-strain response, is showed in Figure 3.4(a). In this figure a high strain-rate loading (at a finite inelastic strain-rate $\dot{\varepsilon}$) followed by an unloading and subsequent *quasi*-static-reloading is shown. This curve (solid-line) is compared with a *quasi*-static loading (dashed-line). From this comparison one can note the previous strain-rate influence on the saturation hardening $A_\infty$, where $A_\infty\left(\dot{\varepsilon}\right)$ is greater than the associated *quasi*-static value $A_\infty^{lwr}$, such that the *quasi*-static loading curve is not recovered by the *quasi*-static-reloading. Furthermore, since $\dot{\varepsilon} < \dot{\varepsilon}_{up}$, then $A_\infty\left(\dot{\varepsilon}\right) < A_\infty^{up}$. In contrast, considering $A_\infty$ constant and $c = 0$, Figure 3.4(b) shows the role played by the rate-dependent parameter $\delta\left(\dot{\varepsilon}\right)$ on hardening evolution. In summary, by increasing the imposed strain-rate the nonlinear hardening behavior approaches faster its saturation.

Based upon preliminary experimental investigations on the high strain-rate material behavior, the saturation hardening $A_\infty$ was observed to be influenced by previous strain-rate-history experienced by the material. As a result, instead of being a state function in terms of the current strain-rate $\dot{\varepsilon}$ (Eq. (3.87)), saturation $A_\infty$ has to depend on the past deformation-history. In this sense, an effective saturation hardening $\bar{A}_\infty$ is introduced:

$$\bar{A}_\infty \coloneqq \frac{1}{\bar{\varepsilon}} \int_0^{\bar{\varepsilon}} A_\infty\left(\dot{\varepsilon}\right) d\varepsilon, \tag{3.89}$$

where $\bar{\varepsilon}$ is the current accumulated viscoplastic strain and $A_\infty\left(\dot{\varepsilon}\right)$ is computed by Eq. (3.87). Adopted rule (3.89) is a weighted averaging, and is employed to calculate the effective parameter $\bar{A}_\infty$, where the weights are given in terms of the accumulated viscoplastic strain increment $d\varepsilon$ associated with a corresponding value $A_\infty\left(\dot{\varepsilon}\right)$. Actually, Eq. (3.89) stands for memory effects, which in fact violates hypothesis inherent in the TIV theory, but it is necessary in order to represent observed experimental response. Thereby, henceforth the effective saturation hardening $\bar{A}_\infty$ will be employed, keeping in mind that when the whole loading is performed according to a constant strain-rate it reduces to

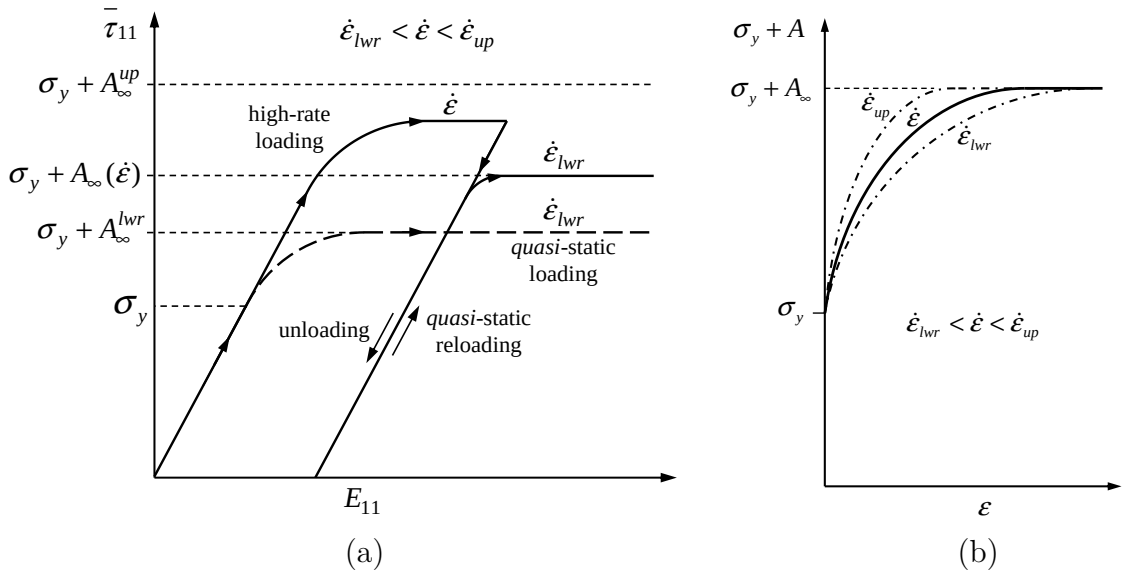


Figure 3.4: Schematic representation of the strain-rate influence on (a) saturation hardening ($A_\infty$) and (b) nonlinear hardening-rate ($\delta$) parameters. Source of figure (a): dos Santos et al., 2016.

$\bar{A}_\infty = A_\infty(\dot{\varepsilon})$.

Considering a loading case in which $N$ distinct constant strain-rate steps are imposed, within the $(n+1)$-th step the current effective saturation hardening of Eq. (3.89) becomes

$$\bar{A}_{\infty_{n+1}} = \frac{1}{\bar{\varepsilon}}\left[\sum_{i=1}^{n} A_{\infty_i}\Delta\varepsilon_i + A_{\infty_{n+1}}(\bar{\varepsilon} - \varepsilon_n)\right], \tag{3.90}$$

where $A_{\infty_i} = A_\infty(\dot{\varepsilon}_i)$, $\Delta\varepsilon_i = \varepsilon_i - \varepsilon_{i-1}$, $\varepsilon_n$ is the total accumulated viscoplastic strain at the end of the $n-$th constant strain-rate step. In the last equation, the weights are given by $\frac{\Delta\varepsilon_i}{\bar{\varepsilon}}$. Therefore, Eq. (3.90) can be rewritten as

$$\bar{A}_{\infty_{n+1}} = \frac{\varepsilon_n}{\bar{\varepsilon}}\bar{A}_{\infty_n} + \left(1 - \frac{\varepsilon_n}{\bar{\varepsilon}}\right)A_{\infty_{n+1}}, \tag{3.91}$$

where $\bar{A}_{\infty_n} := \frac{1}{\varepsilon_n}\sum_{i=1}^{n} A_{\infty_i}\Delta\varepsilon_i$. Considering a case with two constant strain-rate steps $(n+1=2)$, Eq. (3.91) becomes

$$\bar{A}_{\infty_1} = A_\infty(\dot{\varepsilon}_1), \tag{3.92}$$

within the first step, and

$$\bar{A}_{\infty_2} = \frac{\varepsilon_1}{\bar{\varepsilon}}\bar{A}_{\infty_1} + \left(1 - \frac{\varepsilon_1}{\bar{\varepsilon}}\right)A_\infty(\dot{\varepsilon}_2), \tag{3.93}$$

for the second step, where $\varepsilon_1$ is the accumulated viscoplastic strain at the end of step 1. Equations (3.92) and (3.93) will be used to demonstrate the constitutive capabilities

associated with the present formulation in capturing strain-rate changing effects observed during decremental strain-rate tests.

Having obtained the corresponding inelastic evolution equations, namely Eqs. (3.74), (3.76), and (3.79), a relevant discussion refers to the conditions imposed by the non-negative dissipation stated by inequality (3.62). Accordingly, intrinsic dissipation reads

$$\Phi_0 = \dot{\lambda}\left[\left\|\bar{\boldsymbol{\tau}}^D\right\| - \sqrt{\frac{2}{3}}h_1\left(1-\frac{A_1}{A_\infty}\right)A_1 - \sqrt{\frac{2}{3}}h_2 A_2\right] \geq 0, \tag{3.94}$$

making use of Eqs. (3.67) and (3.70),

$$\Phi_0 = \dot{\lambda}\left[\sqrt{\frac{2}{3}}\left(\sigma_y + A_1 + A_2\right) + \Theta^{-1} - \sqrt{\frac{2}{3}}h_1\left(1-\frac{A_1}{A_\infty}\right)A_1 - \sqrt{\frac{2}{3}}h_2 A_2\right] \geq 0. \tag{3.95}$$

Since $\dot{\lambda} \geq 0$, positivity of $\Phi_0$ is equivalent to the following condition:

$$\sigma_y + \sqrt{\frac{3}{2}}\Theta^{-1} + \left[1 - h_1\left(1-\frac{A_1}{A_\infty}\right)\right]A_1 + \left(1-h_2\right)A_2 \geq 0. \tag{3.96}$$

Keeping in mind that $\sigma_y \geq 0$, $\frac{A_1}{A_\infty} \leq 1$, $A_1 \geq 0$, and $A_2 \geq 0$, positivity of each separate term above is ensured provided that $h_1 \leq 1$ and $h_2 \leq 1$, thus implying that inequality (3.62) is always fulfilled. Furthermore, knowing that $h_1 = \frac{H_1}{\bar{H}} = \frac{A_\infty \delta}{\bar{H}}$ and $h_2 = \frac{H_2}{\tilde{H}} = \frac{A_\infty c}{\tilde{H}}$, previous conditions indicate that $A_\infty \delta \leq \bar{H}$ and $A_\infty c \leq \tilde{H}$, respectively. Notice that parameters $A_\infty$, $\delta$, and $c$ related to hardening response are quantified in this work. However, moduli $\bar{H}$ and $\tilde{H}$ for the plastically stored energy have to be adjusted from suitable experiments, for example, from calorimetry [Godfrey et al., 2005], what is beyond the present scope.

### 3.5.1 Overstress function

In order to complete the present constitutive formulation, specific functional forms for the overstress function $\Theta\left(\langle f \rangle, A\right)$, Eq. (3.69), must be introduced. Functional forms of $\Theta\left(\langle f \rangle, A\right)$ should incorporate material physical aspects as the instantaneous rate-dependence, while keeping it simple enough to be mathematically tractable. For this purpose, phenomenological proposals of function $\Theta\left(\langle f \rangle, A\right)$ will be employed. Reasoning on this way, two widely employed viscoplastic models are those of Perzyna, 1966, 1971, and Perić, 1993, which are described briefly in what follows. For more details, works of Alfano et al., 2001, and dos Santos, 2012, are also referred to.

Perzyna-based model

Constitutive function $\Theta\left(\langle f\rangle, A\right)$ is given by [Perzyna, 1966, 1971]

$$\dot{\lambda} = \Theta\left(\langle f\rangle, A\right) = \frac{1}{\vartheta}\left[\frac{\langle f\rangle}{R\left(A\right)}\right]^{m}, \tag{3.97}$$

where $\vartheta \in \mathcal{R}_{>0}$ is a viscosity parameter, $\frac{1}{m} \in \mathcal{R}_{>0}$ is the rate-sensitivity, and $R$ is a characteristic size associated with the yield locus given in terms of the hardening variable $A$. In the context of *von Mises* criterion, Eq. (3.67), one has

$$R\left(A\right) = \sqrt{\frac{2}{3}}\left(\sigma_y + A\right). \tag{3.98}$$

For $f \geq 0$, the inverse function $\Theta^{-1}\left(\dot{\lambda}, A\right)$ is given by

$$f = \Theta^{-1}\left(\dot{\lambda}, A\right) = R\left(A\right)\left[\vartheta\dot{\lambda}\right]^{\frac{1}{m}}. \tag{3.99}$$

Perić-based model

Viscoplastic models should recover the rate-independent behavior as $\vartheta \to 0$ or as $m \to \infty$. Unfortunately, the rate-independent feature is not recovered when $m \to \infty$ by the *Perzyna* nonlinear model. To overcome this problem, Perić, 1993, proposed a viscoplastic model which retrieves the inviscid behavior in both limit cases. In this model, function $\Theta\left(\langle f\rangle, A\right)$ is expressed as

$$\dot{\lambda} = \Theta\left(\langle f\rangle, A\right) = \frac{1}{\vartheta}\left\{\left[\frac{\langle f\rangle + R\left(A\right)}{R\left(A\right)}\right]^{m} - 1\right\}, \tag{3.100}$$

and its inverse function $\Theta^{-1}\left(\dot{\lambda}, A\right)$, for $f \geq 0$, reads

$$f = \Theta^{-1}\left(\dot{\lambda}, A\right) = R\left(A\right)\left[\left(1 + \vartheta\dot{\lambda}\right)^{\frac{1}{m}} - 1\right]. \tag{3.101}$$

Modified Perić model

Both viscoplastic models described earlier (Eqs. (3.97) and (3.100)) can be seen as phenomenological simplifications of an *Arrhenius* evolution equation [Perzyna, 1986], which is employed in physically-based models to describe thermally-activated dislocation motion [Kocks et al., 1975; Follansbee and Kocks, 1988]. However, there are researchers pointing out that the thermal activation mechanism does not control the dislocation glide for strain-rates in the order of $10^4\,\mathrm{s}^{-1}$. For this strain-rate range, the most important role is played by viscous drag mechanisms [Regazzoni et al., 1987; Rodríguez-Martínez et al., 2011], which provides a major resistance to the motion of dislocations under these

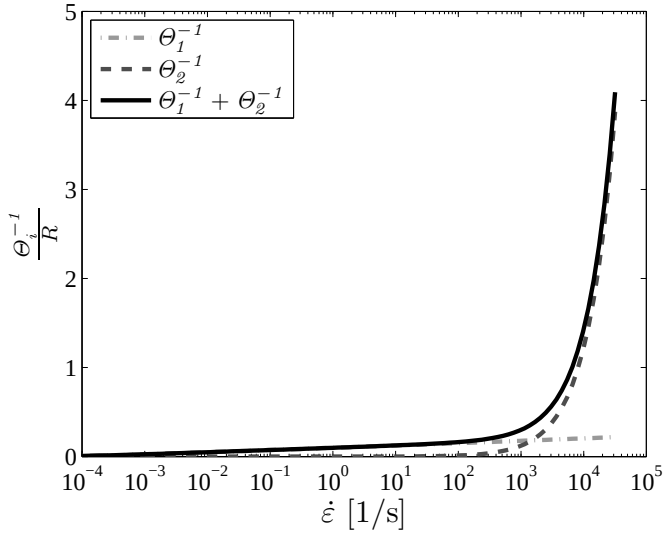


Figure 3.5: Evaluation of functions $\Theta_1^{-1} \coloneqq \left(1 + \vartheta_1 \dot{\lambda}\right)^{\frac{1}{m}} - 1$, $\Theta_2^{-1} \coloneqq \vartheta_2 \dot{\lambda}$ and the sum $\Theta^{-1} = \Theta_1^{-1} + \Theta_2^{-1}$ (normalized by parameter $R$) in terms of $\dot{\varepsilon} = \sqrt{\frac{2}{3}}\dot{\lambda}$, for $\vartheta_1 = 1 \times 10^4\,\mathrm{s}$, $m = 100$ and $\vartheta_2 = 1 \times 10^{-4}\,\mathrm{s}$.

deformation conditions (see also discussion of Subsection 1.4.5). The great majority of empirical and phenomenological viscoplastic models does not identify the different rate-dependent features responsible for observed viscous effects [Perzyna, 1966, 1971; Johnson and Cook, 1983; Perić, 1993; Simo et al., 1988; Ristinmaa and Ottosen, 1998; Alfano et al., 2001]. Thus, aiming at improving the strain-rate range of applicability of phenomenological approaches, following a simplifying procedure, the drag resistance is proposed to be modeled by a linear relationship between stress level and current strain-rate. Accordingly, phenomenologically accounting for both thermally-activated and viscous drag mechanisms, a modified version of *Perić*'s model is proposed. The modification consists of introducing the linear term $\vartheta_2 \dot{\lambda}$ in Eq. (3.101):

$$f = \Theta^{-1}\left(\dot{\lambda}, A\right) = R\left[\left(1 + \vartheta_1 \dot{\lambda}\right)^{\frac{1}{m}} + \vartheta_2 \dot{\lambda} - 1\right]. \tag{3.102}$$

In the proposed viscoplastic equation, constants $\vartheta_1 \in \mathcal{R}_{>0}$ and $\frac{1}{m} \in \mathcal{R}_{>0}$ are respectively the viscosity and rate-sensitivity parameters associated with thermally-activated mechanisms, and $\vartheta_2 \in \mathcal{R}_{>0}$ is the viscosity parameter related to viscous drag resistance.

For metallic materials, as it will be verified in Chapter 4, parameter $\frac{1}{\vartheta_1}$ can be seen as a lower reference strain-rate, and $\vartheta_1$ assumes high values in the order of $10^3\,\mathrm{s}$ or even higher. In turn, constant $m$ has values in the order of $10^2$ [dos Santos et al., 2016]. Parameter $\frac{1}{\vartheta_2}$ is seen as a higher reference strain-rate, then $\vartheta_2$ has values much lower than the unity, in the order of $10^{-3}\,\mathrm{s}$ or lower. Thus, in order to illustrate the features associated with the proposed viscoplastic function, functions $\Theta_1^{-1} \coloneqq \left(1 + \vartheta_1 \dot{\lambda}\right)^{\frac{1}{m}} - 1$, $\Theta_2^{-1} \coloneqq \vartheta_2 \dot{\lambda}$, and the sum $\Theta_1^{-1} + \Theta_2^{-1}$ (normalized by parameter $R$) are qualitatively evaluated in Figure 3.5 in

terms of strain-rate $\dot{\varepsilon} = \sqrt{\frac{2}{3}}\dot{\lambda}$, considering $\vartheta_1 = 1 \times 10^4\,\mathrm{s}$, $m = 100$ and $\vartheta_2 = 1 \times 10^{-4}\,\mathrm{s}$. Results of Figure 3.5 show that a critical strain-rate between $10^2$ and $10^3\,\mathrm{s}^{-1}$ delimits the transition from the low strain-rate-sensitivity to the high strain-rate regime. On one hand, from low to moderate strain-rates the viscous behavior is governed by term $\Theta_1^{-1}$, which in our approach is linked to thermal activation mechanisms and is the model of Perić, 1993 itself, defined in Eq. (3.101). On the other hand, at high strain-rates, function $\Theta_2^{-1}$ related to viscous drag resistance controls the instantaneous rate-sensitivity.

### 3.5.2 Constitutive formulation highlights

Before further theoretical developments, a series of comments related to proposed constitutive modeling deserve to be stated. In this respect, some main features of the model are emphasized below:

- Starting from additive decomposition of hardening into two contributions, respectively associated with dislocation storage and geometry changes at microscale level, a hardening law given in Eq. (3.85) has been obtained. Referred to as "modified *Voce* hardening law", it allows to account for nonlinear hardening until corresponding saturation $\left(A \leq \bar{A}_\infty\right)$, and for *quasi*-linear hardening observed at subsequent stages of straining. Interestingly, the linear component in the hardening law is also rate-dependent since the saturation hardening $\bar{A}_\infty$ is a rate-dependent parameter;

- The model ability to account for rate-dependent material hardening behavior stems directly from the rate-dependence of parameters $\delta$ and $A_\infty$, as clearly expressed by Eqs. (3.87) and (3.86) through functions $\beta_i\left(\dot{\varepsilon}\right)$. The specific expression (3.88) seems suitable for capturing significant hardening rate-sensitivity observed at high strain-rates, as illustrated in Figure 3.3(b);

- The proposed overstress function, Eq. (3.102), is expected to improve the well established phenomenological models as those of Perzyna, 1966, 1971, and Perić, 1993, in the sense that it increases the strain-rate range of applicability related to this kind of approach. The modification is achieved by an additional linear contribution intended to phenomenologically represent viscous drag effects on the instantaneous rate-sensitivity;

- Apart from elastic constants, the whole proposed constitutive model depends on eleven independent scalar parameters whose phenomenological interpretation is clear. This feature allows to identify corresponding model constants from experimental data by means of subsequent steps. Actually, the model calibration is rather simple and can be achieved considering four separate constitutive aspects (as detailed in Chapter 4): (i) *quasi*-static strain-hardening; (ii) strain-rate-hardening; (iii) low to intermediate strain-rate; and (iv) high strain-rate viscous behavior.

- The model proposed in this work is a generalization of the formulation provided by dos Santos et al. [2016], so that, the last one is retrieved by setting $\delta^{lwr} = \delta^{up} = \delta$, $\vartheta_2 = 0$, and the saturation hardening being computed directly from Eq. (3.87).

While presenting relevant constitutive capabilities, limitations related to the proposed model have to be addressed. In general finite strain applications, temperature dependence of polycrystalline FCC metals becomes important at high strain-rates. However, the present model does not explicitly account for the heat generated during high velocity plastic deformations. The present proposal aims at providing a simple constitutive tool focused mainly on rate-dependent constitutive features considering idealized isothermal conditions. Under high strain-rate conditions, the present model should be adjusted from incremental deformation tests, in order to minimize thermal effects in experimental results (see for instance Follansbee and Kocks, 1988, and Nemat-Nasser and Isaacs, 1997). In its current form, proposed model can be employed for predicting high strain-rate plastic deformations restricted to moderate continuous strain increments: $\Delta\varepsilon < 0.5$. Simulations performed considering adiabatic and isothermal settings at high strain-rates have shown the difference between adiabatic and isothermal conditions for copper is not significant as long as moderate strain increments are respected [Follansbee and Kocks, 1988; Molinari and Ravichandran, 2005]. Moreover, isothermal viscoplastic models can be used in high strain-rate conditions when the desired loading-history corresponding to a given application can be reproduced in laboratory material characterization [Silva et al., 2014]. In this situation, thermal effects are implicitly accounted for through adjusted model parameters. Otherwise, in cases where thermal effects have to be explicitly accounted for, within the present framework temperature influence shall be considered by adopting adiabatic conditions at high strain-rates, and assuming temperature-dependences on parameters $\sigma_y$, $\vartheta_1$, $\vartheta_2$, $m$, and on evolution of hardening variables $A_1$, $A_2$ through parameters $\delta$ and $A_\infty$, which are somehow related to temperature-dependent dynamic recovery mechanisms.

## 3.6 Model summary

For easier reading and future discussion, the present constitutive development is summarized in what follows:

- Deformation gradient decomposition:

$$\boldsymbol{F} = \boldsymbol{F}^e \boldsymbol{F}^{vp}; \tag{3.103}$$

- *Helmholtz* free-energy:

$$\psi\left(\boldsymbol{E}^e, \alpha_1, \alpha_2\right) = \frac{1}{2}\boldsymbol{E}^e : \mathbb{D}^e : \boldsymbol{E}^e + \frac{1}{2}H\left(\alpha_1^2 + \alpha_2^2\right); \tag{3.104}$$

- Constitutive relationships:

$$\bar{\boldsymbol{\tau}} = \mathbb{D}^e : \boldsymbol{E}^e, \;\; A_1 = H\alpha_1, \;\; \text{and} \;\; A_2 = H\alpha_2; \tag{3.105}$$

- Yield function:

$$f\left(\bar{\boldsymbol{\tau}}, A\right) = \left\|\bar{\boldsymbol{\tau}}^D\right\| - \sqrt{\frac{2}{3}}\left(\sigma_y + A\right), \tag{3.106}$$

  with $A = A_1 + A_2$;

- Inelastic evolution:

$$\bar{\boldsymbol{D}}^{vp} = \dot{\lambda}\boldsymbol{N}_{\bar{\boldsymbol{\tau}}}, \tag{3.107}$$

$$\dot{\varepsilon} = \sqrt{\frac{2}{3}}\dot{\lambda}, \tag{3.108}$$

$$f = \Theta^{-1}\left(\dot{\lambda}, A\right) = R\left[\left(1 + \vartheta_1\dot{\lambda}\right)^{\frac{1}{m}} + \vartheta_2\dot{\lambda} - 1\right], \tag{3.109}$$

$$\dot{A}_1 = H_1\left(1 - \frac{A_1}{\bar{A}_\infty}\right)\dot{\varepsilon}, \tag{3.110}$$

$$A_2 = c\bar{A}_\infty\varepsilon, \tag{3.111}$$

  where

$$\delta = \left[1 - \beta_1\left(\dot{\varepsilon}\right)\right]\delta^{lwr} + \beta_1\left(\dot{\varepsilon}\right)\delta^{up} \tag{3.112}$$

$$\bar{A}_\infty = \frac{1}{\bar{\varepsilon}}\int_0^{\bar{\varepsilon}} A_\infty\left(\dot{\varepsilon}\right)d\varepsilon \tag{3.113}$$

  with

$$A_\infty = \left[1 - \beta_2\left(\dot{\varepsilon}\right)\right]A_\infty^{lwr} + \beta_2\left(\dot{\varepsilon}\right)A_\infty^{up}, \tag{3.114}$$

$$\beta_i\left(\dot{\varepsilon}\right) = \left(\frac{\dot{\varepsilon} - \dot{\varepsilon}_{lwr}}{\dot{\varepsilon}_{up} - \dot{\varepsilon}_{lwr}}\right)^{\xi_i}, \;\; i = \{1, 2\}, \tag{3.115}$$

  being $\bar{\varepsilon}$ the current accumulated viscoplastic strain and $\delta = \frac{H_1}{\bar{A}_\infty}$;

- Hardening rule for constant strain-rate loading. For $\dot{\varepsilon}$-cte, in view of relationship $A = A_1 + A_2$, evolution equations (3.110) and (3.111) yield:

$$A = A_\infty\left[1 + c\varepsilon - \exp\left(-\delta\varepsilon\right)\right]. \tag{3.116}$$

## 3.7 Modeling the material hardness evolution

So far, the constitutive model considering stress-strain response has been formulated. However, in some engineering applications, there is a need to directly control and predict the material hardness evolution. With the goal of handling this issue, this section provides a constitutive alternative to model the corresponding material hardness response in terms

of strain and strain-rate histories. The approach follows from analogy with the formulation of hardening equations given in Section 3.5. Therefore, the hardness variable is assumed to be given by

$$H_V = H_0 + H_\varepsilon, \tag{3.117}$$

where $H_0$ is the hardness associated with an annealed state and $H_\varepsilon$ depends on the plastic deformation and strain-rate histories. Thereby, based on Eqs. (3.63) and (3.83) variable $H_\varepsilon$ is written as

$$H_\varepsilon = H_d + c_h H_\infty \varepsilon, \tag{3.118}$$

where $c_h \geq 0$ is a material parameter, $H_\infty$ is the saturation hardness, $H_d$ is associated with strengthening due dislocation storage, and $c_h H_\infty \varepsilon$ is related to hardening mechanisms of Stage IV. Motivated by Eq. (3.77), evolution of $H_d$ assumes the form

$$\dot{H}_d = H_h \left(1 - \frac{H_d}{H_\infty}\right) \dot{\varepsilon}, \tag{3.119}$$

where $H_h > 0$ is a parameter. Integrating the last equation for $\dot{\varepsilon}$ constant, reads

$$\frac{H_d - H_\infty}{H_{d_i} - H_\infty} = \exp\left[-\delta_h \left(\varepsilon - \varepsilon_i\right)\right]. \tag{3.120}$$

Parameters $H_{d_i}$ and $\varepsilon_i$ stand for respectively initial values of $H_d$ and $\varepsilon$, and $\delta_h = \frac{H_h}{H_\infty}$. Combining Eqs. (3.118) and (3.120) provides

$$H_\varepsilon = H_{\varepsilon_i} + H_\infty c_h \left(\varepsilon - \varepsilon_i\right) + \left[H_\infty \left(1 + c_h \varepsilon_i\right) - H_{\varepsilon_i}\right] \left\{1 - \exp\left[-\delta_h \left(\varepsilon - \varepsilon_i\right)\right]\right\}, \tag{3.121}$$

where $H_{\varepsilon_i}$ is the initial value of $H_\varepsilon$. Considering that $H_{\varepsilon_i} = \varepsilon_i = 0$, Eq. (3.121) reduces to

$$H_\varepsilon = H_\infty \left[1 + c_h \varepsilon - \exp\left(-\delta_h \varepsilon\right)\right], \tag{3.122}$$

which is analogous to Eq. (3.85). In summary, in a constant strain-rate loading, considering Eqs. (3.117) and (3.122), current material hardness can be calculated by

$$H_V = H_0 + H_\infty \left[1 + c_h \varepsilon - \exp\left(-\delta_h \varepsilon\right)\right]. \tag{3.123}$$

Strain-rate-history effects on hardness response can be accounted for by applying the same procedure employed previously. That is, by letting parameters $\delta_h$ and $H_\infty$ to be rate-dependent. Based upon relationships given in Eqs. (3.86) and (3.87), the respective rate-dependent forms are then assumed for both $\delta_h$ and $H_\infty$:

$$\delta_h = \left[1 - \beta_{h_1}\left(\dot{\varepsilon}\right)\right] \delta_h^{lwr} + \beta_{h_1}\left(\dot{\varepsilon}\right) \delta_h^{up} \tag{3.124}$$

and

$$H_{\infty} = \left[1 - \beta_{h_2}\left(\dot{\varepsilon}\right)\right] H_{\infty}^{lwr} + \beta_{h_2}\left(\dot{\varepsilon}\right) H_{\infty}^{up}, \tag{3.125}$$

where $\delta_h^{lwr}$ and $H_{\infty}^{lwr}$ are respectively the *quasi*-static values of $\delta_h$ and $H_{\infty}$ measured at a lower reference rate $\dot{\varepsilon}_{lwr} \ll 1$, $\delta_h^{up}$ and $H_{\infty}^{up}$ are the values associated with upper reference strain-rate $\dot{\varepsilon}_{up} \gg 1$. Functions $\beta_{h_i},\ i = \{1, 2\}$, follow the form presented in Eq. (3.88):

$$\beta_{h_i}\left(\dot{\varepsilon}\right) = \left(\frac{\dot{\varepsilon} - \dot{\varepsilon}_{lwr}}{\dot{\varepsilon}_{up} - \dot{\varepsilon}_{lwr}}\right)^{\xi_{h_i}}, \tag{3.126}$$

where $\xi_{h_i} > 0,\ \ i = \{1, 2\}$, are constants.

Analogously to the stress-strain modeling, referring specifically to Eq. (3.90), an effective saturation hardness $\bar{H}_{\infty}$ is also introduced to account for strain-rate influence on hardness evolution:

$$\bar{H}_{\infty} \coloneqq \frac{1}{\bar{\varepsilon}} \int_0^{\bar{\varepsilon}} H_{\infty}\left(\dot{\varepsilon}\right) d\varepsilon, \tag{3.127}$$

where $\bar{\varepsilon}$ is the current accumulated viscoplastic strain and $H_{\infty}\left(\dot{\varepsilon}\right)$ is the saturation hardness associated with strain-rate $\dot{\varepsilon}$. Following the integration procedure previously described, in which two constant strain-rate steps $(n + 1 = 2)$ are considered, Eq. (3.127) yields

$$\bar{H}_{\infty_1} = H_{\infty}\left(\dot{\varepsilon}_1\right), \tag{3.128}$$

for the first step, and

$$\bar{H}_{\infty_2} = \frac{\varepsilon_1}{\bar{\varepsilon}} \bar{H}_{\infty_1} + \left(1 - \frac{\varepsilon_1}{\bar{\varepsilon}}\right) H_{\infty}\left(\dot{\varepsilon}_2\right), \tag{3.129}$$

for the second step. Equations (3.128) and (3.129) are used to asses the constitutive capabilities associated with the present formulation in capturing the hardness-strain response obtained in sequential strain-rate tests described in Subsection 2.3.2 and showed in Figure 2.7.

# 4 CONSTITUTIVE MODEL CALIBRATION AND VALIDATION: ALUMINUM AA1050

The objective of this chapter is to describe the calibration strategy employed to determine the adjustable parameters associated with the proposed model. In fact, the model has three constitutive features to be calibrated: (i) strain-hardening; (ii) strain-rate-hardening; and (iii) instantaneous rate-sensitivity. The last one is subdivided into two contributions due to low and to high strain-rate effects. The first one is related to thermally-activated mechanisms, and the second one with viscous drag resistance.

The model calibration considers the experimental results presented in Section 2.3. With the aim of performing the model calibration considering the finite strain kinematic framework previously described, as a first task, in the following section the stress-strain formulation is therefore particularized to an unidimensional tensile/compression application.

## 4.1 Simulation of unidimensional compression test

Let us considering a homogeneous cylindrical specimen, geometrically defined in reference configuration by its diameter $d_0$ and length $l_0$, with symmetry axis coinciding with $X_1$, i.e., $0 \leq X_1 \leq l_0$ and $0 \leq \sqrt{X_2^2 + X_3^2} \leq \frac{d_0}{2}$ (Figure 4.1). The specimen is placed between two rigid and smooth platens subjected to respective vertical displacements $u_1 = 0$ at $X_1 = 0$ and $u_1 = \bar{u}_1$ at $X_1 = l_0$. For simple problem, the constitutively homogeneous material is considered as rigid-viscoplastic, that is $\bar{\boldsymbol{D}} = \bar{\boldsymbol{D}}^{vp}$.

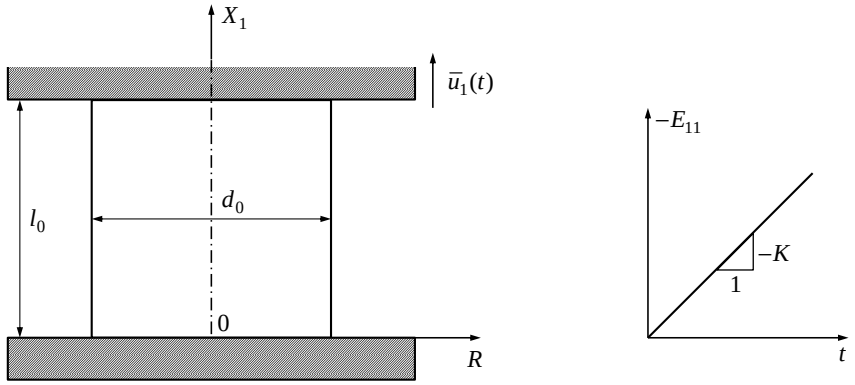


Figure 4.1: Schematic representation of unidimensional boundary value problem. Source: dos Santos et al., 2016.

The displacement vector $\boldsymbol{u}$ and deformation gradient $\boldsymbol{F}$ are considered to be given by

$$\boldsymbol{u} = \left\{ \begin{array}{c} (a_1 - 1)\, X_1 \\ (a_2 - 1)\, X_2 \\ (a_2 - 1)\, X_3 \end{array} \right\} \text{ and } \boldsymbol{F} = \left[ \begin{array}{ccc} a_1 & 0 & 0 \\ 0 & a_2 & 0 \\ 0 & 0 & a_2 \end{array} \right]. \tag{4.1}$$

Accordingly, the right stretch tensor $\boldsymbol{U} = \sqrt{\boldsymbol{F}^T \boldsymbol{F}}$ and the logarithmic strain measure $\boldsymbol{E} = \ln(\boldsymbol{U})$ are

$$\boldsymbol{U} = \begin{bmatrix} a_1 & 0 & 0 \\ 0 & a_2 & 0 \\ 0 & 0 & a_2 \end{bmatrix} \text{ and } \boldsymbol{E} = \begin{bmatrix} \ln(a_1) & 0 & 0 \\ 0 & \ln(a_2) & 0 \\ 0 & 0 & \ln(a_2) \end{bmatrix}, \tag{4.2}$$

where the principal stretches must complies with $a_1 \leq 1$ and $a_2 \geq 1$ in the compression case. Furthermore, $a_1$ is determined from boundary condition $u_1 = \bar{u}_1$ at $X_1 = l_0$,

$$a_1 = 1 + \frac{\bar{u}_1}{l_0} = \frac{l}{l_0}. \tag{4.3}$$

The rate of axial strain is

$$\dot{E}_{11} = \frac{\dot{a}_1}{a_1} = \frac{\dot{\bar{u}}_1}{l_0 + \bar{u}_1}. \tag{4.4}$$

Notice that for the specific case considered herein, the strain-rate $\bar{\boldsymbol{D}} = \text{sym}\left(\dot{\boldsymbol{F}}\boldsymbol{F}^{-1}\right)$ and the rate of strain $\dot{\boldsymbol{E}}$ are coincident. The analysis will be restricted to a constant rate of strain:

$$\dot{E}_{11} = \bar{D}_{11} = K < 0 \;\; (\text{compression}). \tag{4.5}$$

The prescribed displacement $\bar{u}_1(t)$ of upper cylinder face is actually controlled through the value of axial strain $E_{11}$ applied at a constant rate $K$. Thus, starting from $\bar{u}_1(t = 0) = 0$, the prescribed displacement takes the form

$$\bar{u}_1(t) = l_0 \left[\exp(Kt) - 1\right]. \tag{4.6}$$

For this simple compression case, the uniaxial stress state reads

$$\bar{\boldsymbol{\tau}} = \begin{bmatrix} \bar{\tau}_{11} & 0 & 0 \\ 0 & 0 & 0 \\ 0 & 0 & 0 \end{bmatrix}, \;\; \bar{\boldsymbol{\tau}}^D = \begin{bmatrix} \frac{2}{3}\bar{\tau}_{11} & 0 & 0 \\ 0 & -\frac{1}{3}\bar{\tau}_{11} & 0 \\ 0 & 0 & -\frac{1}{3}\bar{\tau}_{11} \end{bmatrix}, \tag{4.7}$$

and

$$\left\|\bar{\boldsymbol{\tau}}^D\right\| = \sqrt{\frac{2}{3}}\left|\bar{\tau}_{11}\right|, \tag{4.8}$$

where $|\bar{\tau}_{11}|$ denotes the absolute value of $\bar{\tau}_{11}$. Considering a rigid-viscoplastic material and assuming an associative evolution, it comes from Eqs. $(3.68)_1$ and $(3.72)_1$:

$$\bar{\boldsymbol{D}} = \sqrt{\frac{3}{2}}\dot{\lambda}\frac{\bar{\boldsymbol{\tau}}^D}{|\bar{\tau}_{11}|} = \sqrt{\frac{2}{3}}\dot{\lambda}\begin{bmatrix} 1 & 0 & 0 \\ 0 & -\frac{1}{2} & 0 \\ 0 & 0 & -\frac{1}{2} \end{bmatrix}\text{sign}(\bar{\tau}_{11}). \tag{4.9}$$

It follows that

$$\bar{D}_{11} = \sqrt{\frac{2}{3}}\dot{\lambda}\text{sign}\left(\bar{\tau}_{11}\right), \tag{4.10}$$

where $\dot{\lambda} = \frac{1}{\vartheta}\Theta\left(\langle f\rangle, A\right)$ and $\text{sign}\left(\bar{\tau}_{11}\right)$ denotes the signal of $\bar{\tau}_{11}$. Moreover, in view of Eqs. (3.73) and (4.10), the accumulated viscoplastic strain-rate becomes

$$\dot{\varepsilon} = \left|\bar{D}_{11}\right| = |K| \;\text{ and }\; \varepsilon = \int_0^t \left|\bar{D}_{11}\right| dt = |K|\, t, \tag{4.11}$$

since $\dot{\varepsilon}$ is constant and $\varepsilon\left(t=0\right) = 0$. Remember from Eq. (4.5) that

$$\dot{E}_{11} = \bar{D}_{11} \tag{4.12}$$

and thus $\varepsilon = |E_{11}| = |K|\, t$. The hardening variable can be calculated from Eq. (3.85),

$$A = \bar{A}_\infty \left[1 + c\varepsilon - \exp\left(-\delta\varepsilon\right)\right], \tag{4.13}$$

where $\delta$ is calculated from Eqs. (3.86) and (3.88) with $i = 1$, and $\bar{A}_\infty = A_\infty$ from Eqs. (3.87) and (3.88) with $i = 2$.

It is worth noting that, when considering this specific rigid-viscoplastic application with monotonic loading, the accumulated viscoplastic strain defined in Eq. (3.73), and specialized in Eq. (4.11) for a simple compression test, coincides with the logarithmic strain measure defined previously in Eq. (2.2) when the experimental results were first presented.

For this rigid-viscoplastic uniaxial test, the overstress function proposed in Subsection 3.5.1 is employed. In the case of inelastic flow, the current yield function must obey $f = \Theta^{-1}$, where function $\Theta^{-1}\left(\dot{\lambda}, A\right)$ is given in Eq. (3.102). Combination of Eqs. (3.67), (3.75), (3.102), (4.8), and (4.10) leads to the following expression for the axial stress

$$|\bar{\tau}_{11}| = \left(\sigma_y + A\right)\left[\left(1 + \sqrt{\frac{3}{2}}\vartheta_1\dot{\varepsilon}\right)^{\frac{1}{m}} + \sqrt{\frac{3}{2}}\vartheta_2\dot{\varepsilon}\right]. \tag{4.14}$$

Equation (4.14) shows how the current yield stress $\sigma_y + A$ is intensified by the rate-dependent term $\left[\left(1 + \sqrt{\frac{3}{2}}\vartheta_1\dot{\varepsilon}\right)^{\frac{1}{m}} + \sqrt{\frac{3}{2}}\vartheta_2\dot{\varepsilon}\right]$ in order to obtain the instantaneous flow stress response, $\bar{\tau}_{11}$, in terms of the current strain-rate $\dot{\varepsilon}$.

## 4.2 Model calibration

Model calibration is performed reasoning on the rigid-viscoplastic analytical solution given in Eq. (4.14), and the hardening variable $A$ is computed from Eq. (4.13), for which $\delta$ is calculated from Eqs. (3.86) and (3.88) with $i = 1$, and $\bar{A}_\infty = A_\infty$ from Eqs. (3.87)

and (3.88) with $i = 2$. Therefore, the set of model constants to be adjusted is:

$$\left\{\sigma_y, c, \delta^{lwr}, \delta^{up}, \xi_1, A_\infty^{lwr}, A_\infty^{up}, \xi_2, \vartheta_1, m, \vartheta_2\right\}. \tag{4.15}$$

The reference strain-rates $\dot{\varepsilon}_{lwr}$ and $\dot{\varepsilon}_{up}$ are defined *a priori*:

$$\dot{\varepsilon}_{lwr} = 1 \times 10^{-4}\,\mathrm{s}^{-1} \text{ and } \dot{\varepsilon}_{up} = 1.5 \times 10^{4}\,\mathrm{s}^{-1}. \tag{4.16}$$

These reference values define the strain-rate range of applicability associated with the present model calibration. The upper value $\dot{\varepsilon}_{up} = 1.5 \times 10^4\,\mathrm{s}^{-1}$ was set in order cover a wide strain-rate range while being close to the highest experimental strain-rate: $\dot{\varepsilon} = 1.1 \times 10^4\,\mathrm{s}^{-1}$.

Calibration procedure is carried out by means of a nonlinear least-square method. Although, the present model has 11 parameters (related to the inelastic response) to be adjusted, using this simple gradient-based procedure is possible, once the proposed constitutive model enables to perform the calibration in subsequent steps, what allows identifying separately each constitutive contribution, and thus verifying graphically the value of each model constant. Calibration steps are summarized in the following:

- (i) *Quasi-static strain-hardening*. Four parameters are adjusted:

$$|\bar{\tau}_{11}| = \sigma_y + A_\infty^{qs}\left[1 + c\varepsilon - \exp\left(-\delta^{qs}\varepsilon\right)\right] \rightarrow \left\{\sigma_y, c, \delta^{qs}, A_\infty^{qs}\right\}, \tag{4.17}$$

- (ii) *Strain-rate-hardening*. Six parameters are adjusted:

$$\delta = \delta^{lwr} + \left(\frac{\dot{\varepsilon} - \dot{\varepsilon}_{lwr}}{\dot{\varepsilon}_{up} - \dot{\varepsilon}_{lwr}}\right)^{\xi_1}\left(\delta^{up} - \delta^{lwr}\right) \rightarrow \left\{\delta^{lwr}, \delta^{up}, \xi_1\right\}, \tag{4.18}$$

$$A_\infty = A_\infty^{lwr} + \left(\frac{\dot{\varepsilon} - \dot{\varepsilon}_{lwr}}{\dot{\varepsilon}_{up} - \dot{\varepsilon}_{lwr}}\right)^{\xi}\left(A_\infty^{up} - A_\infty^{lwr}\right) \rightarrow \left\{A_\infty^{lwr}, A_\infty^{up}, \xi_2\right\}, \tag{4.19}$$

(iii) *Instantaneous rate-sensitivity*:

1. From *quasi*-static to moderate strain-rate regimes. Two parameters are adjusted:

$$|\bar{\tau}_{11}| = (\sigma_y + A)\left(1 + \sqrt{\frac{3}{2}}\vartheta_1\dot{\varepsilon}\right)^{\frac{1}{m}} \rightarrow \left\{\vartheta_1, m\right\}, \tag{4.20}$$

2. At high strain-rate regimes. One parameter is adjusted:

$$|\bar{\tau}_{11}| = (\sigma_y + A)\left[\left(1 + \sqrt{\frac{3}{2}}\vartheta_1\dot{\varepsilon}\right)^{\frac{1}{m}} + \sqrt{\frac{3}{2}}\vartheta_2\dot{\varepsilon}\right] \rightarrow \left\{\vartheta_2\right\}. \tag{4.21}$$

Detailed descriptions on each calibration step are provided in the subsequent topics.

### 4.2.1 Rate-dependent yield stress

The rate-dependent yield stress associated with the present model is given by the sum of the initial yield stress and hardening variable: $\sigma_y + A$. This quantity accounts for both the strain and strain-rate-hardening responses. Reasoning on the preceding uniaxial compression solution, Eqs. (4.13) and (4.14), the current yield stress reads

$$|\bar{\tau}_{11}| = \sigma_y + A_\infty \left[1 + c\varepsilon - \exp\left(-\delta\varepsilon\right)\right], \tag{4.22}$$

in which instantaneous rate effects are disregarded, that is, $\left[\left(1 + \sqrt{\frac{3}{2}}\vartheta_1\dot{\varepsilon}\right)^{\frac{1}{m}} + \sqrt{\frac{3}{2}}\vartheta_2\dot{\varepsilon}\right] = 1$. The model calibration considers the rate-dependent yield stress-strain curves presented in Figure 2.10 of Subsection 2.3.3.

In a first step, parameters $\sigma_y$, $c$, $A_\infty^{qs}$, and $\delta^{qs}$ (of Eq. (4.22)) are adjusted considering the *quasi*-static curve. Then, by keeping $\sigma_y$ and $c$ fixed, other values of parameters $A_\infty$ and $\delta$ associated with higher strain-rate curves are obtained. Adjusted values of $\sigma_y$ and $c$, as well as of $A_\infty$ and $\delta$ corresponding to each strain-rate are given in Table 4.1. Considering data of this table 4.1 and reference strain-rates given in Eq. (4.16), functions $\delta\left(\dot{\varepsilon}\right)$ (parameters $\delta^{lwr}$, $\delta^{up}$, $\xi_1$ of Eqs. (3.86) and (3.88)) and $A_\infty\left(\dot{\varepsilon}\right)$ (parameters $A_\infty^{lwr}$, $A_\infty^{up}$, $\xi_2$ of Eqs. (3.87) and (3.88)) are therefore adjusted. Achieved results are described in Table 4.2, and adjusted functions $\delta\left(\dot{\varepsilon}\right)$ and $A_\infty\left(\dot{\varepsilon}\right)$ are displayed respectively in Figures 4.2(a) and (b). In these figures, good agreement between adopted functions and reference data are observed. While Figure 4.2(a) shows a pronounced rate-sensitivity associated with parameter $\delta$, in Figure 4.2(b) a smooth transition in the rate-sensitivity of parameter $A_\infty$ is observed. Furthermore, Figure 4.2(c) displays how the athermal hardening-rate $H_1 = A_\infty\delta$ of Eq. (3.77) varies in terms of strain-rate changes. In accordance with previous works on FCC metals (for instance that of Follansbee and Kocks, 1988) the athermal hardening-rate has a less pronounced rate-sensitivity in a low-strain-rate range ($\dot{\varepsilon} < 10^3\,\mathrm{s}^{-1}$), and when

Table 4.1: Saturation hardening $A_\infty$, hardening-rates $\delta$, $c$, and initial yield stress $\sigma_y$ obtained by calibration.

| | $\dot{\varepsilon}$ [$\mathrm{s}^{-1}$] | | | |
|---|---|---|---|---|
| | $Q-S$ | $2\times10^3$ | $4\times10^3$ | $1.1\times10^4$ |
| $A_\infty$ [MPa] | 83.43 | 93.65 | 94.54 | 96.92 |
| $\delta$ [−] | 3.917 | 6.767 | 7.409 | 9.074 |
| $\sigma_y$ [MPa] | 41.17 | – | – | – |
| $c$ [−] | 0.15 | – | – | – |

Table 4.2: Parameters $\delta^{lwr}$, $\delta^{up}$, $\xi_1$, $A_\infty^{lwr}$, $A_\infty^{up}$, and $\xi_2$ obtained by calibration, for $\dot{\varepsilon}_{lwr} = 10^{-4}\,\mathrm{s}^{-1}$ and $\dot{\varepsilon}_{up} = 1.5 \times 10^{4}\,\mathrm{s}^{-1}$.

| $\delta^{lwr}$ [−] | $\delta^{up}$ [−] | $\xi_1$ [−] | $A_\infty^{lwr}$ [MPa] | $A_\infty^{up}$ [MPa] | $\xi_2$ [−] |
|---|---|---|---|---|---|
| 3.884 | 9.653 | 0.3553 | 81.28 | 97.55 | 0.1421 |

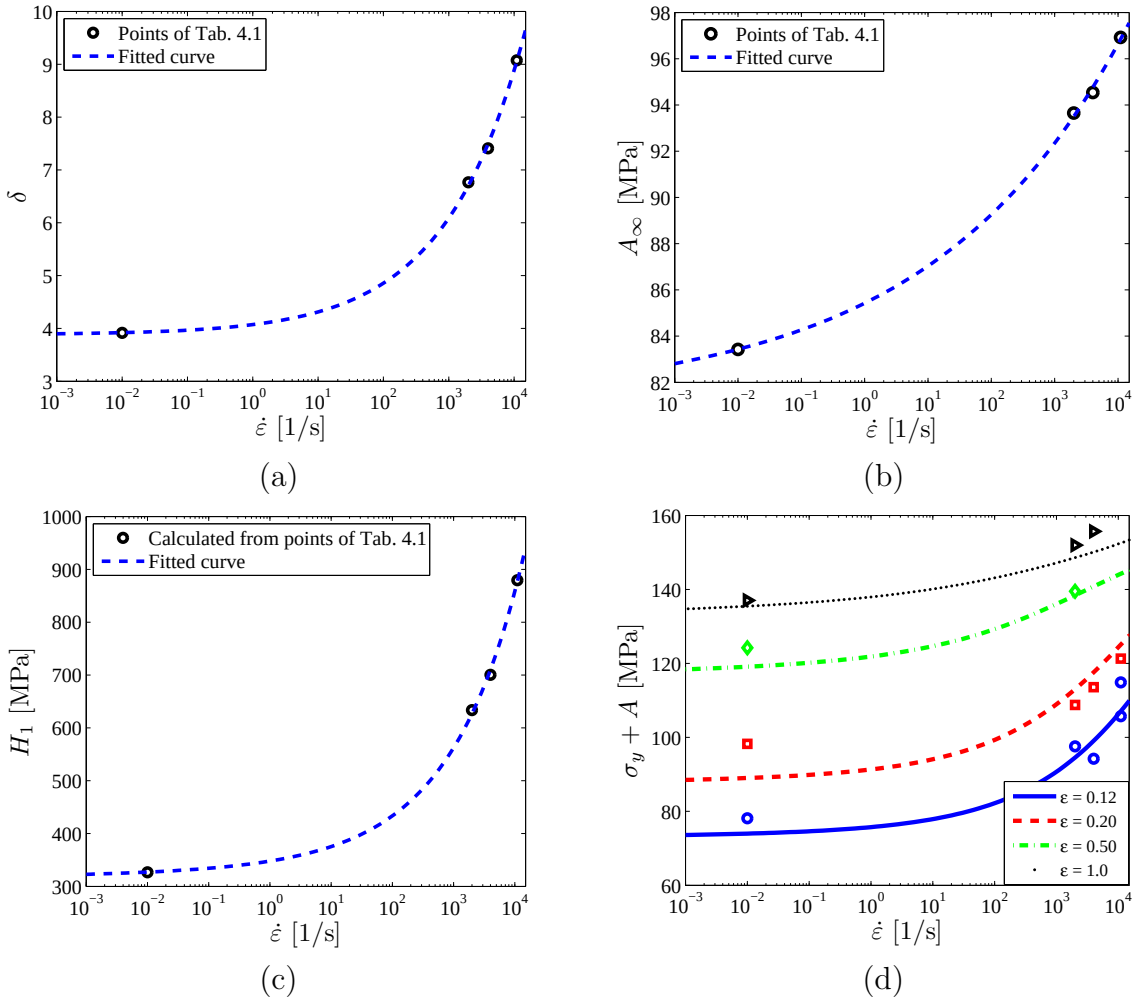


Figure 4.2: Comparison of adjusted constitutive functions with values of Table 4.2: (a) Equations (3.86) and (3.88) with $i = 1$; and (b) Equations (3.87) and (3.88) with $i = 2$; (c) Parameter $H_1 = A_\infty \delta$. Reference strain-rates are $\dot{\varepsilon}_{lwr} = 10^{-4}\,\mathrm{s}^{-1}$ and $\dot{\varepsilon}_{up} = 1.5 \times 10^{4}\,\mathrm{s}^{-1}$. (d) Rate-sensitivity associated with the current yield stress for different strain levels (Equations (4.22), (3.86), (3.87), and (3.88), as well as parameters of Table 4.2 are employed).

higher strain-rates ($\dot{\varepsilon} > 10^{3}\,\mathrm{s}^{-1}$) are reached, a strong rate-dependence is evidenced.

Figures 4.2(d) and 4.3 show respectively the adjusted curves for the evolution of yield stress as function of $\dot{\varepsilon}$ considering different strain levels, and the yield stress-strain curves for different values of $\dot{\varepsilon}$, in which the experimental results are also depicted in order to allow a graphical comparison. Results of Figure 4.2(d) present a small rate-influence on $\sigma_y + A$ at low strain-rates, and a pronounced rate-sensitivity at high strain-rates ($\dot{\varepsilon} > 10^{3}\,\mathrm{s}^{-1}$)

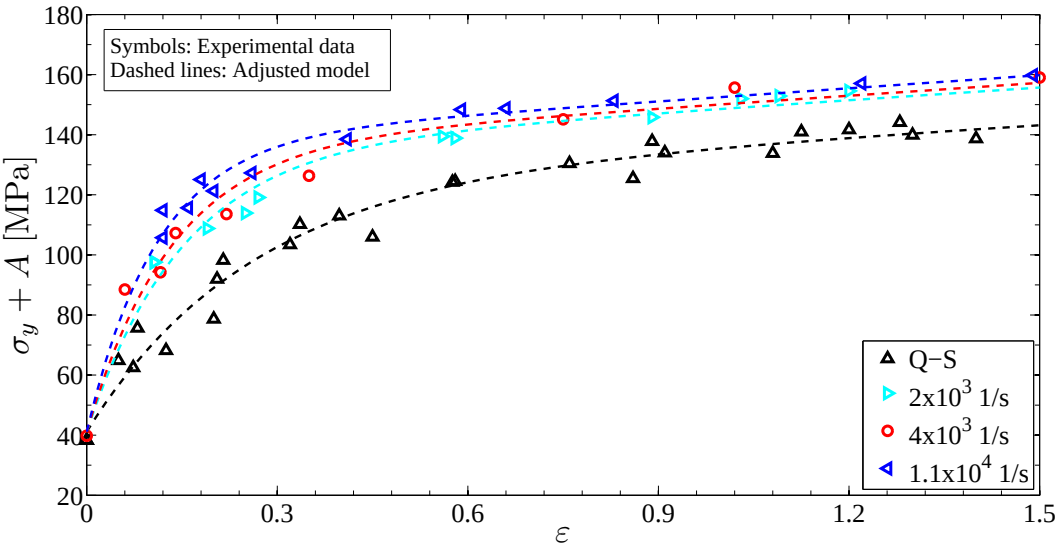


Figure 4.3: Yield stress vs. accumulated viscoplastic strain: Comparison of reference data and adjusted constitutive model, using Eqs. (4.22), (3.86), (3.87), and (3.88), as well as parameters of Table 4.2.

are evidenced. However, observed rate-sensitivity decreases as the strain level increases. In Figure 4.3, as expected based on results of Figures 4.2(a) and (b), higher strain-rates increase both the nonlinear $\delta$ and linear $A_\infty c$ hardening-rates. Both Figures 4.2(d) and 4.3 show that the adjusted model responses are in good agreement with corresponding reference data.

Preceding calibration was performed in order to characterize both strain-hardening and strain-rate-hardening responses of the proposed model. In the following subsection the instantaneous flow stress rate-sensitivity is considered.

### 4.2.2 Instantaneous flow stress

At this stage, the model parameters related to strain-, strain-rate-hardening behavior have been adjusted. In what follows, parameters $\vartheta_1$, $\vartheta_2$, and $m$ associated with instantaneous rate-sensitivity of Eq. (4.14) have to be adjusted. For this purpose, flow stress-strain curves presented in Figure 2.11(a) are now considered.

As previously discussed (see Figure 3.5 and comments of Subsection 3.5.1), the term containing parameters $\vartheta_1$ and $m$ in Eqs. 3.102 and 4.14 is intended to model viscous effects from low to moderate strain-rates, i.e., within the strain-rate range in which thermal-activated dislocation glide dominate the plastic deformation process [Regazzoni et al., 1987; Nemat-Nasser and Li, 1998]. Then, for adjusting constants $\vartheta_1$ and $m$, the flow stress-strain curves related to strain-rates of $1.0 \times 10^{-2}$ (Q-S), 1.2, and $1.2 \times 10^3$ are considered. Employing this procedure, the following model parameters are then obtained:

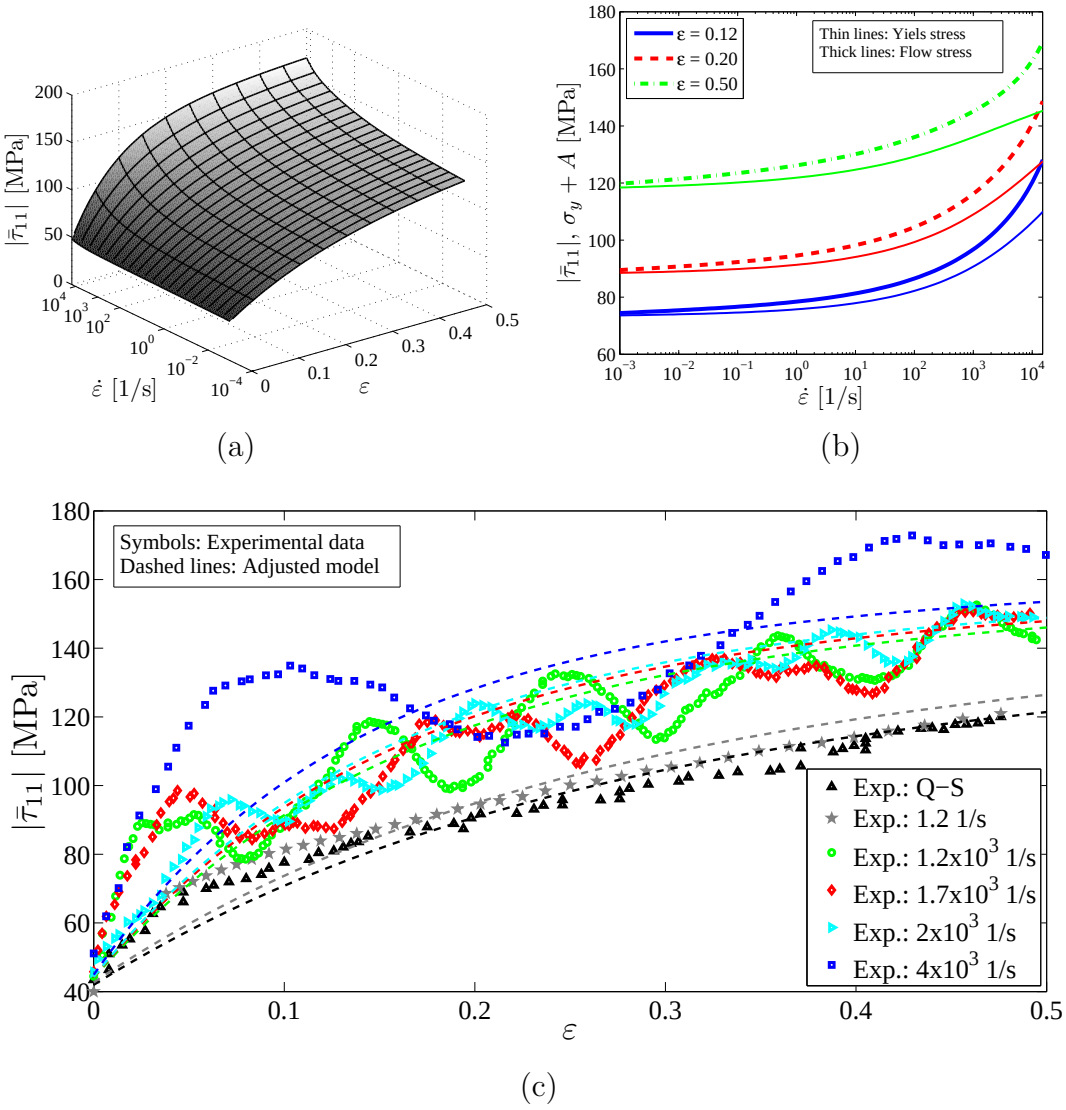


Figure 4.4: (a) Theoretical flow stress surface in terms of strain and strain-rate; (b) Flow stress rate-sensitivity of adjusted model for different strain levels (for comparison, yield stresses of Figure 4.2(d) are also represented by thin lines); (c) Comparison of theoretical flow stress and experimental data. Theoretical description considers Eqs. (4.14), (3.86), (3.87), and (3.88), as well as parameters of Table 4.3.

$$\vartheta_1 = 2.14 \times 10^4\,\mathrm{s} \;\text{ and }\; m = 291.55. \tag{4.23}$$

In a subsequent step, to adjust constant $\vartheta_2$, all flow stress-strain curves of Figure 2.11(a) are considered, including those associated with strain-rates of $1.7 \times 10^3$, $2.0 \times 10^3\,\mathrm{s}^{-1}$, and $4.0 \times 10^3\,\mathrm{s}^{-1}$. The resulting value is

$$\vartheta_2 = 5.15 \times 10^{-6}\,\mathrm{s}.$$

Corresponding fitted flow stress curves are showed in Figures 4.4(a)-(c). Figure 4.4(a) shows the overall model response, that is, this figure displays the flow stress response in

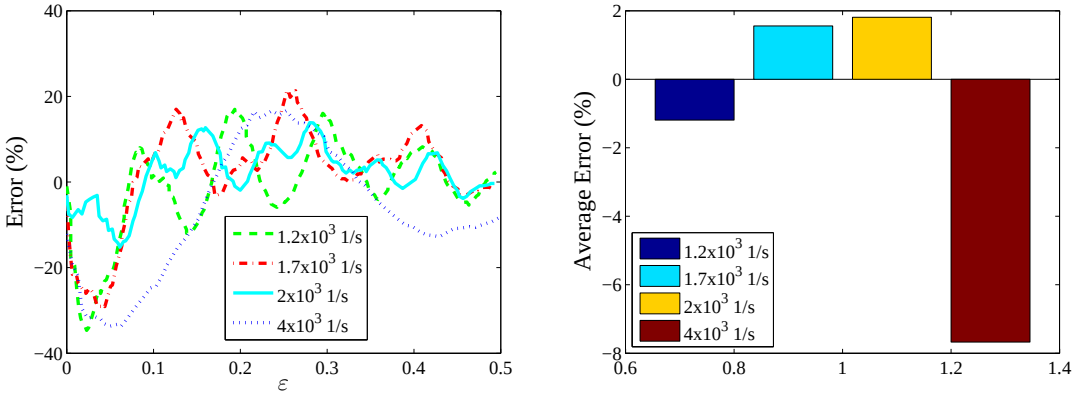


(a) (b)

Figure 4.5: (a) Relative error between adjusted model response and experimental flow stress considering high strain-rates: $1.2 \times 10^3$, $1.7 \times 10^3$, $2.0 \times 10^3\,s^{-1}$, and $4.0 \times 10^3\,s^{-1}$; (b) Average error (Error per number of experimental points) between adjusted model response and experimental flow stress considering high strain-rates: $1.2 \times 10^3$, $1.7 \times 10^3$, $2.0 \times 10^3\,s^{-1}$, and $4.0 \times 10^3\,s^{-1}$.

terms of imposed strain $\varepsilon$ and associated strain-rate $\dot{\varepsilon}$. In a general way, considering the strain-rate influence on material or model responses, a significant increase in instantaneous rate-sensitivity is observed for strain-rates higher than $10^3\,s^{-1}$. From a physical point of view, this behavior can be attributed to strong microstructural rate-sensitivity and also to viscous drag effects verified in a high strain-rate regime [Regazzoni et al., 1987; Rusinek and Rodríguez-Martínez, 2009; Gao and Zhang, 2012]. Considering the present constitutive model, associated rate-sensitivities are shown in Figure 4.4(b) for different strain levels. A slight increase in strain-rate-sensitivity is induced by increasing the straining level. In addition, for comparison purposes, rate-sensitivities (associated with the current yield stress) showed in Figure 4.2(d) are also displayed in Figure 4.4(b). From this comparison, it is clear for the present constitutive approach that viscous effects become pronounced only when the imposed strain-rate approaches $10^3\,s^{-1}$. This behavior can be phenomenologically related to viscous drag effects occurring at high strain-rates.

Figure 4.4(c) compares the adjusted model with corresponding reference experimental flow stress-strain curves. As it would be expected, based on preceding results, the flow stress increases by increasing the imposed strain-rate. Results of Figure 4.4(c) show significant differences between model response and experimental results, where relative errors of almost -35% are reached (Figure 4.5(a)) for the highest strain-rate curve. However, from analysis of Appendix B.5, one notices that this significant discrepancy could be due to oscillating experimental response due to dynamic behavior of compression platen and load cell assembling, and not due to intrinsic material response. Due to oscillating character, taking the average relative error per number of experimental points (Figure 4.5(b)), absolute average errors lower than 8% are verified. Thus, in an average way,

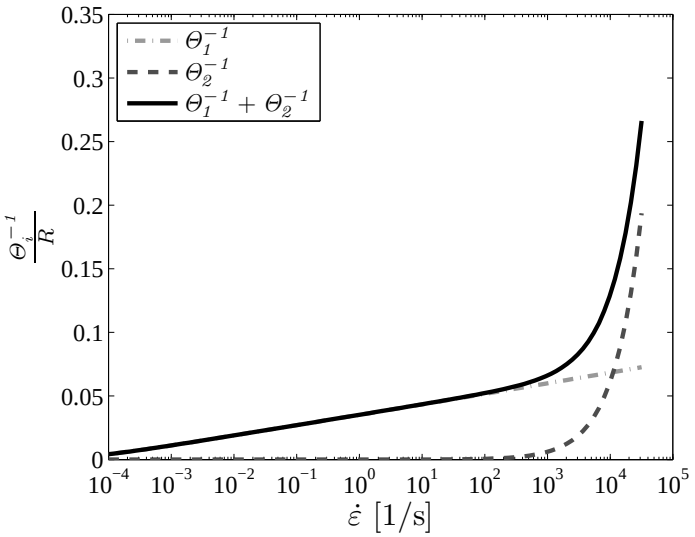


Figure 4.6: Evaluation of functions $\Theta_1^{-1} \coloneqq \left(1 + \vartheta_1 \dot{\lambda}\right)^{\frac{1}{m}} - 1$, $\Theta_2^{-1} \coloneqq \vartheta_2 \dot{\lambda}$ and the sum $\Theta^{-1} = \Theta_1^{-1} + \Theta_2^{-1}$ (normalized by parameter $R$) in terms of $\dot{\varepsilon} = \sqrt{\frac{2}{3}}\dot{\lambda}$ considering parameters of Table 4.3.

the model flow stress response, within the strain and strain-rate ranges considered, have provided a reasonable agreement with experimental data.

In order to demonstrate how each rate-sensitivity of term $\left[\left(1 + \sqrt{\frac{3}{2}}\vartheta_1 \dot{\varepsilon}\right)^{\frac{1}{m}} + \sqrt{\frac{3}{2}}\vartheta_2 \dot{\varepsilon}\right]$ influences the theoretical constitutive response associated with the aluminum AA1050, similarly to what was done in Figure 3.5, corresponding strain-rate evolutions of terms $\Theta_1^{-1} \coloneqq \left(1 + \vartheta_1 \dot{\lambda}\right)^{\frac{1}{m}} - 1$ and $\Theta_2^{-1} \coloneqq \vartheta_2 \dot{\lambda}$ are displayed in Figure 4.6, considering the model parameters of Table 4.3. From this Figure, one can readily observe that term $\Theta_1^{-1}$ plays a major role for strain-rates lower than $10^3\,\mathrm{s}^{-1}$, in a manner that the original *Perić* model given in Eq. (3.101) could be used within this this strain-rate range. In contrast, for strain-rates exceeding $10^3\,\mathrm{s}^{-1}$, term $\Theta_2^{-1}$ becomes important, thus demonstrating that a linear-like relationship between viscous stress and imposed strain-rate prevails at high strain-rate conditions, and justifying the need to employ the modified model given in Eq. (3.102).

Up to now, the model calibration considering constant strain-rate experiments was carried out, and corresponding adjusted model responses were compared with respective experimental data. Adjusted constants are shown in Table 4.3. In a general way, good agreement between model and experimental results have been observed. In the next sections model predictions are validated against sequential strain-rate tests concerning the reload stress response. Aiming at carrying out the corresponding validation, model predictions are compared with experimental sequential strain-rate tests reasoning on the reload stress response.

Table 4.3: Adjusted model parameters for annealed aluminum AA1050, with $\dot{\varepsilon}_{lwr} = 10^{-4}\,\mathrm{s}^{-1}$ and $\dot{\varepsilon}_{up} = 1.5 \times 10^{4}\,\mathrm{s}^{-1}$.

| $\sigma_y$ [MPa] | $c$ [–] | $\delta^{lwr}$ [–] | $\delta^{up}$ [–] | $\xi_1$ [–] | $A_\infty^{lwr}$ [MPa] | $A_\infty^{up}$ [MPa] | $\xi_2$ [–] | $\vartheta_1$ [s] | $\vartheta_2$ [s] | $m$ [–] |
|---|---|---|---|---|---|---|---|---|---|---|
| 41.2 | 0.15 | 3.9 | 9.7 | 0.36 | 81.3 | 97.6 | 0.14 | $2 \times 10^4$ | $5 \times 10^{-6}$ | 292 |

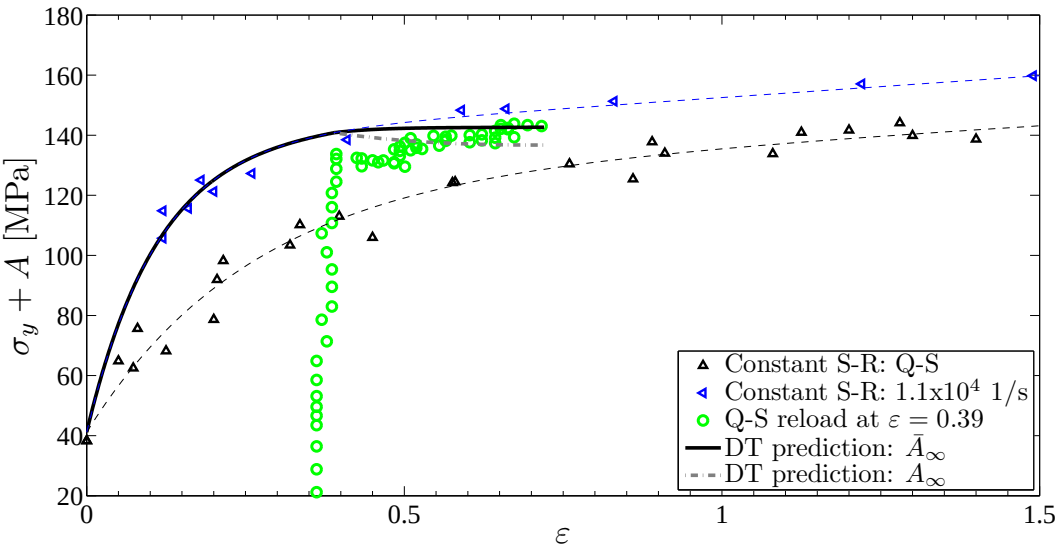


Figure 4.7: Model validation: *Quasi*-static reload stress after a high strain-rate ($\dot{\varepsilon} = 1.1 \times 10^4\,\mathrm{s}^{-1}$) prestraining of $\varepsilon = 0.39$. Comparison of model predictions and experimental data (squares). Experimental and analytical (thin dashed lines) constant strain-rate curves are also plotted.

## 4.3 Model validation considering stress-strain sequential tests

Model calibration considering constant strain-rate experiments resulted in parameters given in Table 4.3. Therefore, the adjusted model is going to be used for predicting the corresponding material behavior observed in the decremental strain-rate tests described in Subsection 2.3.3. Experiments consists of imposing a given strain level following a high strain-rate loading. The loading data are described in Table 2.2, in which prescribed pre-strain and related strain-rate are given. After the loading phase, the material is unloaded and subsequently reloaded following a *quasi*-static deformation.

Comparison of constitutive predictions and experimental data associated with tests DT1, DT2, and DT3 (of Table 2.2) are showed in Figures 4.7, 4.8, and 4.9, respectively. In theses figures, predictions considering the effective saturation hardening $\bar{A}_\infty$, Eqs. (3.91) and (3.87), and considering the instantaneous saturation hardening $A_\infty$, Eq. (3.87), are compared with experimental results obtained from *quasi*-static reloading performed after high velocity preloading. In addition, reference data associated with high strain-rate and *quasi*-static monotonic loading are also displayed.

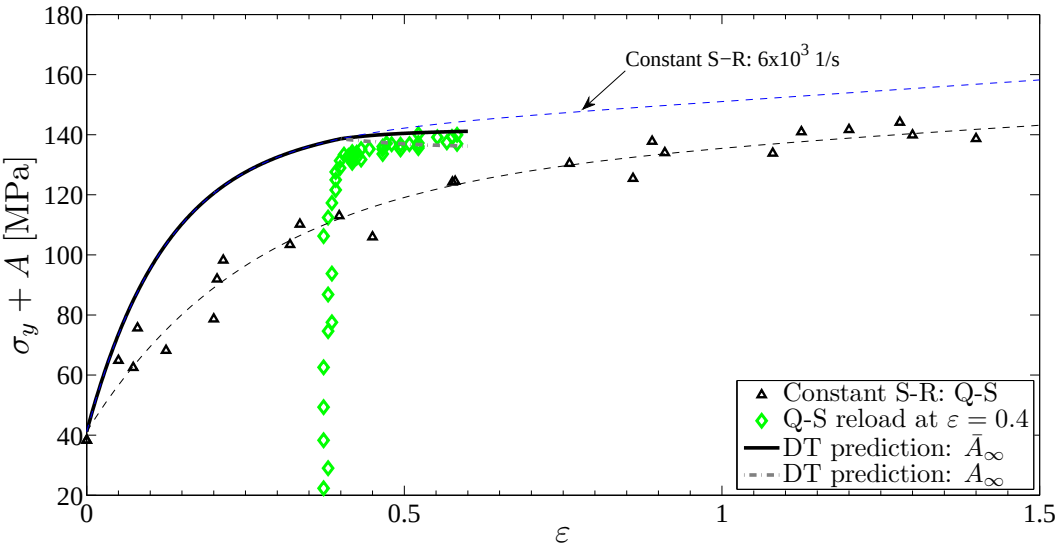


Figure 4.8: Model validation: *Quasi*-static reload stress after a high strain-rate ($\dot{\varepsilon} = 6 \times 10^3\,\mathrm{s}^{-1}$) prestraining of $\varepsilon = 0.40$. Comparison of model predictions and experimental data (diamonds). Experimental and analytical (thin dashed lines) constant strain-rate curves are also plotted.

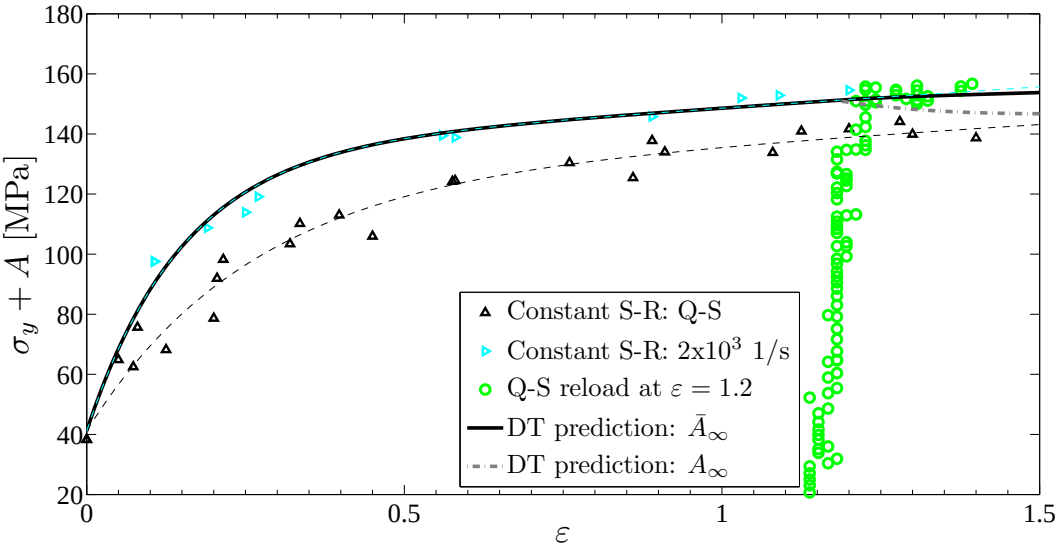


Figure 4.9: Model validation: *Quasi*-static reload stress after a high strain-rate ($\dot{\varepsilon} = 2 \times 10^3\,\mathrm{s}^{-1}$) prestraining of $\varepsilon = 1.2$. Comparison of model predictions and experimental data (circles). Experimental and analytical (thin dashed lines) constant strain-rate curves are also plotted.

On one hand, in all cases curves directly employing the instantaneous saturation hardening $A_\infty$ predict a rapid tendency toward the associated *quasi*-static response, then these descriptions quickly deviate from experimental data. On the other hand, although having a small deviation at the beginning, predictions considering the effective saturation hardening $\bar{A}_\infty$ present better agreement with observed experimental behavior. According

to discussion provided in Subsection 2.3.3, specifically on Figure 2.12, when the reload stress is lower than its respective *quasi*-static saturation stress, a slight linear hardening during the reloading phase is observed, Figures 4.7 and 4.8. In contrast, when the reload stress is higher than the corresponding *quasi*-static saturation, an almost perfectly-plastic behavior is evidenced. Furthermore, as expected, in Figure 4.9 where a higher prestrain was imposed, higher differences between predictions employing the effective $\bar{A}_\infty$ and the instantaneous one $A_\infty$ are observed.

## 4.4 Calibration of hardness model

This section aims at providing the model constants related to the constitutive formulation presented in Section 3.7 related to modeling of material hardness response in terms of imposed strain and strain-rate-histories. Calibration of hardness constants follows the procedure outlined in Subsection 4.2.1 corresponding to the rate-dependent yield stress. Constitutive equation to be calibrated is that given in Eq. (3.123), i.e.,

$$H_V = H_0 + H_\infty \left[1 + c_h \varepsilon - \exp\left(-\delta_h \varepsilon\right)\right], \tag{4.24}$$

where parameters $\delta_h$ and $H_\infty$ are given respectively by Eqs. (3.124) and (3.125), as well as Eq. (3.126). The first step consists of adjusting parameters $H_0$, $H_\infty$, $\delta_h$, and $c_h$ of Eq. (4.24), considering distinct strain-rates. Knowing the average initial hardness of annealed samples, corresponding quantity is set: $H_0 = 220\,\text{MPa}$. Subsequently, remaining parameters are adjusted considering constant strain-rate experimental hardness data of Figure 2.6. This procedure provides the adjusted parameters given in Table 4.4, associated with each strain-rate. Constant $c_h$ is calibrated only for the *quasi*-static curve, and then maintained fixed for the other cases.

Parameters $\delta_h$ and $H_\infty$ are plotted in terms of strain-rate $\dot{\varepsilon}$ in Figures 4.10(a) and (b), respectively. Calibration of function $\delta_h\left(\dot{\varepsilon}\right)$, Eqs. (3.124) and (3.126), in terms of constants $\delta_h^{lwr}$, $\delta_h^{up}$ and $\xi_{h_1}$ is performed considering results of Figure 4.10(a). In a similar way, considering function $H_\infty\left(\dot{\varepsilon}\right)$, parameters $H_\infty^{lwr}$, $H_\infty^{up}$ and $\xi_{h_2}$ of Eq. (3.125) are also

Table 4.4: Parameters $H_\infty$, $\delta_h$, $H_0$, and $c_h$ obtained by calibration.

| | $\dot{\varepsilon}\ [\text{s}^{-1}]$ | | | |
|---|---|---|---|---|
| | Q − S | $2 \times 10^3$ | $4 \times 10^3$ | $1.1 \times 10^4$ |
| $H_\infty$ [MPa] | 161.7 | 190.5 | 195.3 | 199.2 |
| $\delta_h$ [−] | 3.326 | 5.304 | 5.592 | 7.277 |
| $H_0$ [MPa] | 220 | – | – | – |
| $c_h$ [−] | 0.20 | – | – | – |

Table 4.5: Parameters $\delta_h^{lwr}$, $\delta_h^{up}$, $\xi_{h_1}$, $H_\infty^{lwr}$, $H_\infty^{up}$ and $\xi_{h_2}$ obtained by calibration, for $\dot{\varepsilon}_{lwr} = 10^{-4}\,\mathrm{s}^{-1}$ and $\dot{\varepsilon}_{up} = 1.5 \times 10^{4}\,\mathrm{s}^{-1}$.

| $\delta_h^{lwr}$ $[-]$ | $\delta_h^{up}$ $[-]$ | $\xi_{h_1}$ $[-]$ | $H_\infty^{lwr}$ $[MPa]$ | $H_\infty^{up}$ $[MPa]$ | $\xi_{h_2}$ $[-]$ |
|---|---|---|---|---|---|
| 3.333 | 7.809 | 0.4512 | 151.9 | 201.2 | 0.1139 |

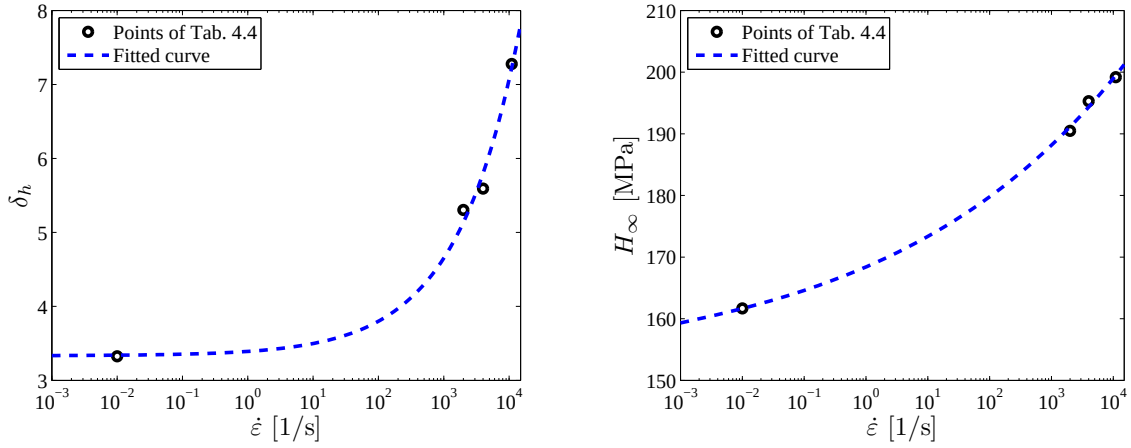


(a) (b)

Figure 4.10: Comparison of adjusted constitutive functions with values of Table 4.4: (a) Equations (3.124) and (3.126) with $i = 1$; and (b) Equations (3.125) and (3.126) with $i = 2$.

adjusted concerning data of Figure 4.10(b). Strain-rates were also set: $\dot{\varepsilon}_{lwr} = 10^{-4}\,\mathrm{s}^{-1}$ and $\dot{\varepsilon}_{up} = 1.5 \times 10^{4}\,\mathrm{s}^{-1}$. Obtained constants are given in Table 4.5.

Using those parameters given in Table 4.5, as well as $H_0 = 220\,\mathrm{MPa}$ and $c_h = 0.2$, considering $\dot{\varepsilon}_{lwr} = 10^{-4}\,\mathrm{s}^{-1}$ and $\dot{\varepsilon}_{up} = 1.5 \times 10^{4}\,\mathrm{s}^{-1}$, theoretical hardness-strain curves for distinct strain-rates are compared with experiments in Figure 4.11, showing good agreement.

In order to assess the hardness strain-rate dependence associated with the present model, the hardness surface as a function of strain $\varepsilon$ and its rate $\dot{\varepsilon}$ is displayed in Figure 4.12(a), where model description is compared with experiments. Regarding specifically on the hardness rate-sensitivity, Figure 4.12(b) shows the model hardness as a function of strain-rate for different strain levels. Within the strain and strain-rate ranges analyzed, these figures show that the observed hardness rate-sensitivity is more pronounced at lower strain levels and at high strain-rates ($\dot{\varepsilon} > 10^{3}\,\mathrm{s}^{-1}$). At large strains, a significant reduction in the strain-rate influence over theoretical material hardness is observed.

## 4.5 Model validation considering hardness-strain sequential tests

We have performed the model calibration considering constant strain-rate experiments, and as results parameters given in Table 4.5, $H_0 = 220\,\mathrm{MPa}$ and $c_h = 0.2$ were obtained.

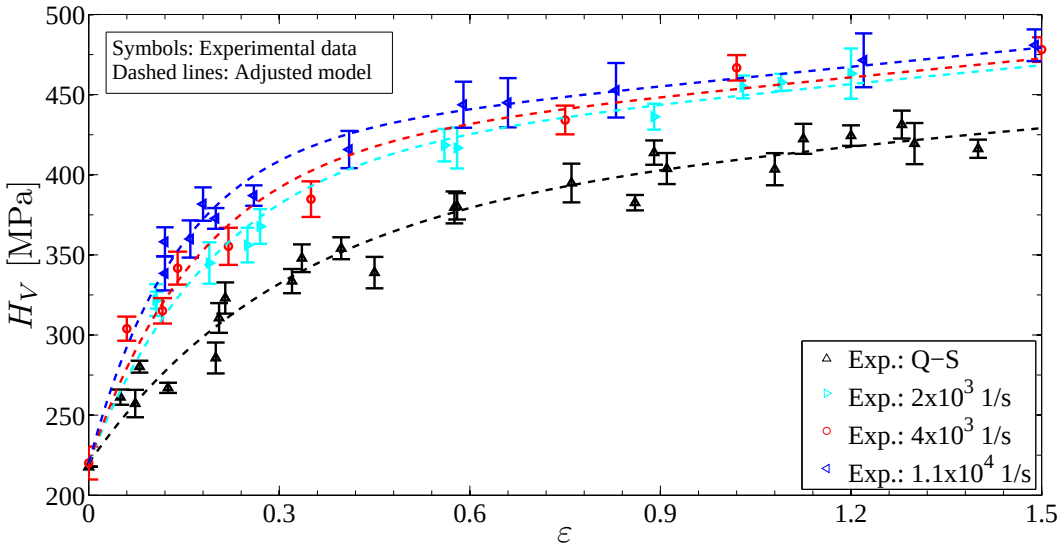


Figure 4.11: Hardness vs. accumulated viscoplastic strain: Comparison of experimental data and adjusted constitutive model, using Eqs. (3.123), (3.124) and (3.125), as well as parameters of Table 4.5, $H_0 = 220\,\mathrm{MPa}$ and $c_h = 0.2$, considering $\dot{\varepsilon}_{lwr} = 10^{-4}\,\mathrm{s}^{-1}$ and $\dot{\varepsilon}_{up} = 1.5 \times 10^{4}\,\mathrm{s}^{-1}$.

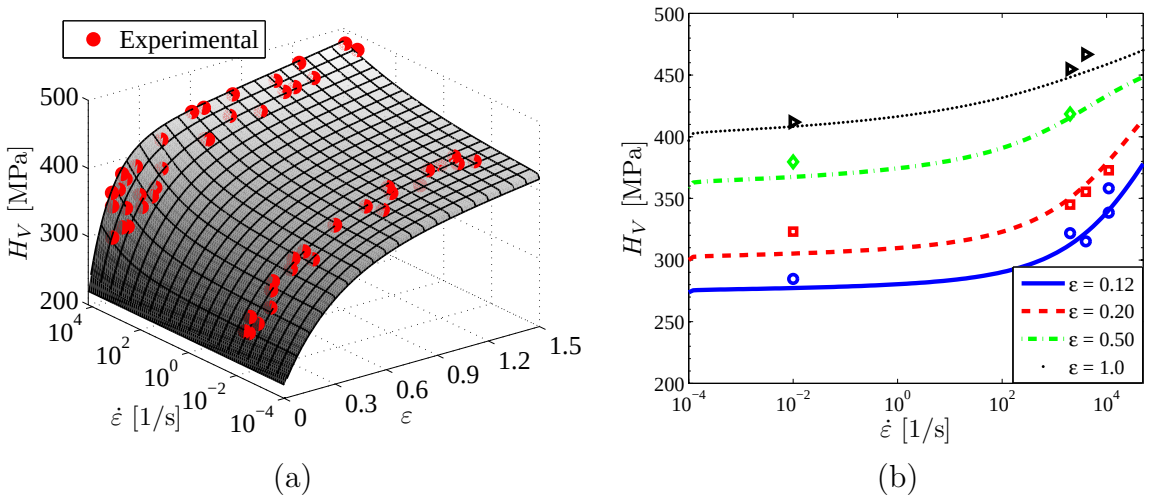


(a) (b)

Figure 4.12: Comparison of strain-rate-dependence of predicted material hardness with experiments (discrete points): (a) Model hardness surface; (b) Adjusted model rate-sensitivity for different strain levels. Adjusted model consists of Eqs. (3.123), (3.124) and (3.125), together with parameters of Table 4.3, $H_0 = 220\,\mathrm{MPa}$ and $c_h = 0.2$, with $\dot{\varepsilon}_{lwr} = 10^{-4}\,\mathrm{s}^{-1}$ and $\dot{\varepsilon}_{up} = 1.5 \times 10^{4}\,\mathrm{s}^{-1}$.

Now, considering those adjusted parameters, the model capabilities in capturing the effects of strain-rate changing on material hardness evolution will be evaluated.

Concerning decremental strain-rate simulation, in which at a given strain $\varepsilon_1 = 0.14$ the loading-rate is changed from a high strain-rate $\dot{\varepsilon} = 4 \times 10^{3}\,\mathrm{s}^{-1}$ regime to a *quasi*-static condition, comparison of model predictions against experimental data are shown in Figure 4.13. In this case, the hardening state right before the decremental response is lower

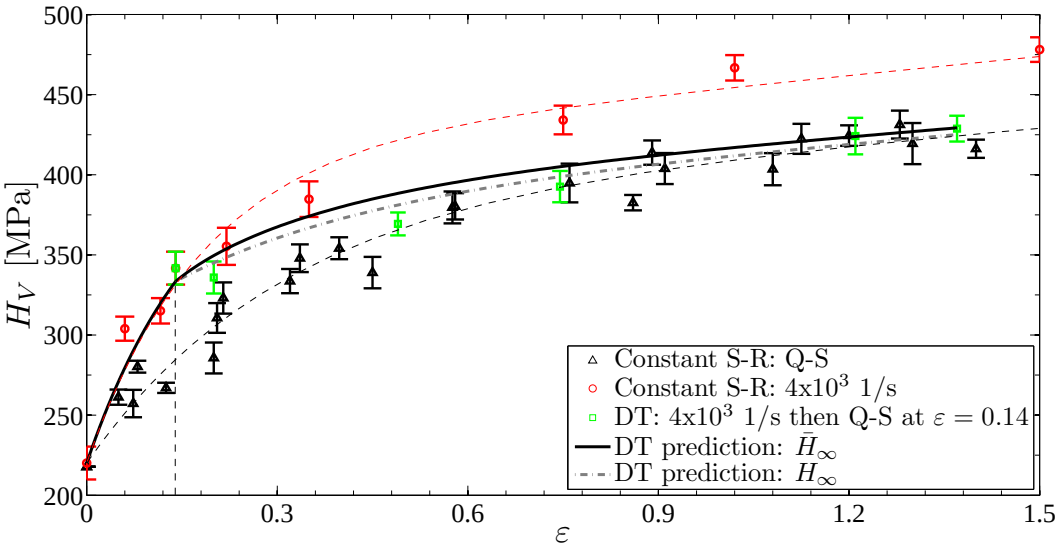


Figure 4.13: Decremental strain-rate test: $4 \times 10^3\,\mathrm{s}^{-1}$ then Q-S at $\varepsilon_1 = 0.14$. Comparison of model predictions and experimental data (squares). Experimental and analytical (thin dashed lines) constant strain-rate curves are also plotted.

than the hardness saturation associated with the *quasi*-static monotonic loading. Thus, even decreasing the hardness-rate associated with $\dot{\varepsilon} = 4 \times 10^3\,\mathrm{s}^{-1}$, in this case, after a slight reduction, the hardness response continues to increase. Concerning modeling aspects, Figure 4.13 shows that the decremental response, in which instantaneous saturation hardness $H_\infty$ (Eq. (3.125)) is employed, tends quickly to the *quasi*-static loading curve. In contrast, the prediction considering the effective saturation $\bar{H}_\infty$, Eq. (3.127), shows the past history influence on the hardness evolution, in manner that, from a high strain-rate condition, associated decremental response presents a resistance in approaching the monotonic *quasi*-static curve, and thus a better agreement with experiments is observed.

Figure 4.14 shows a decremental strain-rate test, in which the hardening state before the decremental response is greater than the *quasi*-static hardness saturation. In this case, at a given strain of $\varepsilon_1 = 0.43$, the strain-rate was changed from a high value of $\dot{\varepsilon} = 1.1 \times 10^4\,\mathrm{s}^{-1}$ to a *quasi*-static condition. Right after the strain-rate decrease, experiments shows a fast reduction and then a slight *quasi*-linear hardness increasing, following a rate similar to that showed by the corresponding *quasi*-static curve. Reasoning on adjusted model predictions, one observes, on one hand, that the model considering $\bar{H}_\infty$ (Eq. (3.127)) is not able to predict the fast hardness decreasing right after the strain-rate dropping, on the other hand, it adequately predicts the hardness response as the strain level increases. In contrast, model response employing $H_\infty$ (Eq. (3.125)) can describe fast hardness decreasing after strain-rate dropping, but it is not capable of predicting low strain-rate hardness evolution. In other words, model prediction considering $H_\infty$ tends to quickly recover the *quasi*-static response, what is not verified in experimental results. In a general

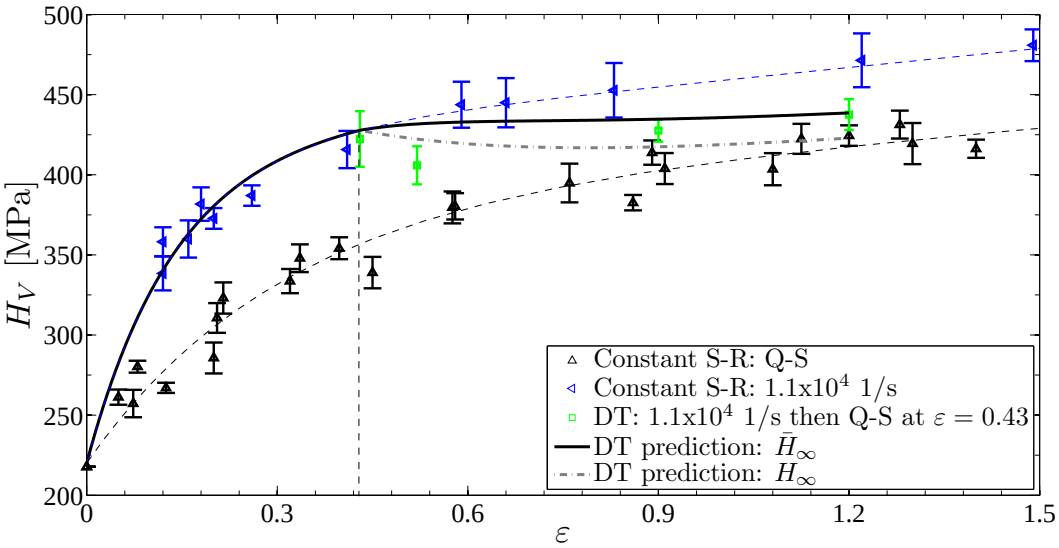


Figure 4.14: Decremental strain-rate test: $1.1 \times 10^4\,\mathrm{s}^{-1}$ then Q-S at $\varepsilon_1 = 0.43$. Comparison of model predictions and experimental data (squares). Experimental and analytical (thin dashed lines) constant strain-rate curves are also plotted.

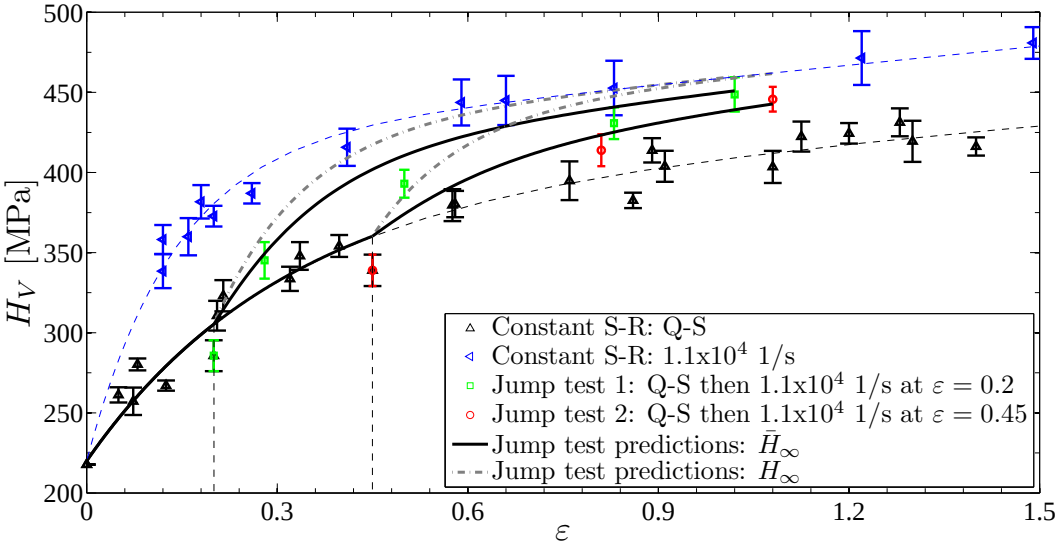


Figure 4.15: Strain-rate jump tests: Q-S then $1.1 \times 10^4\,\mathrm{s}^{-1}$ at $\varepsilon_1 = 0.2$ (test 1) and $\varepsilon_1 = 0.45$ (test 2). Comparison of model predictions and experimental data (squares for test 1 and circles for test 2). Experimental and analytical (thin dashed lines) constant strain-rate curves are also plotted.

way, one can conclude that the strain-rate-history dependence associated with the effective saturation hardness $\bar{H}_\infty$ is reasonable in order to represent observed experimental results.

We have also performed two strain-rate jump experiments. These simulations were performed by changing the loading-rate from a *quasi*-static condition to high strain-rate $\dot{\varepsilon} = 1.1 \times 10^4\,\mathrm{s}^{-1}$ loading. Strain-rate jumps were performed at strains of $\varepsilon_1 = 0.2$ (test 1) and $\varepsilon_1 = 0.45$ (test 2). Considering these simulations, comparison of experimental

data and model predictions are showed in Figure 4.15. For these high strain-rate regimes, an evident loading-rate influence on material hardness is noticed, in a manner that the strain-rate jump has strongly changed the hardness response. However, due to history effects the jumping response does not reach the constant high strain-rate curve in a fast manner as could predict the model employing the instantaneous saturation $H_\infty$. Rather, the experiments show a certain resistance in approaching the monotonic high strain-rate curve. In this sense, the model prediction employing the effective parameter $\bar{H}_\infty$presents minor deviations from experimental results.

# 5 NUMERICAL FORMULATION

Reasoning on large scale simulations, accurate, efficient, and robust numerical tools are mandatory in order to guarantee appropriate predictions and to save computational time. Generally speaking, the finite element (FE) method has proved to be a suitable tool in solving nonlinear initial boundary value problems [Simo and Hughes, 1998; de Souza Neto et al., 2008]. The whole numerical framework must integrate the set of nonlinear constitutive equations into a FE context, requiring the fulfillment of two main tasks at the material level: (i) the update of stress and state variables from a given strain increment, and (ii) the calculation of consistent tangent modulus to be used in the global implicit FE scheme, thus preserving quadratic convergence rate of *Newton*-type solution algorithms [Simo and Hughes, 1998; de Souza Neto et al., 2008]. Aiming at accomplishing these tasks and improving the computational efficiency, several viscoplastic implicit integration algorithms for large strain problems have been proposed [Lush et al., 1989; Weber and Anand, 1990; Zaera and Fernández-Sáez, 2006; Mourad et al., 2014]. Specifically, Lush et al., 1989, proposed a time-integration procedure for implementing the model of Anand, 1985, into a displacement-based FE context. In this sense, Zaera and Fernández-Sáez, 2006, implemented the constitutive model of Rusinek and Klepaczko, 2001, exploring both overstress [Perzyna, 1966, 1971] and consistency [Wang et al., 1997] viscoplastic models, and recently Mourad et al., 2014, proposed an integration scheme in order to incorporate the *MTS* model of Follansbee and Kocks, 1988, into a FE framework. Most of the large strain formulations are based on the well-known multiplicative decomposition of the deformation gradient [Lee, 1969; Mandel, 1972], and generally the corresponding algorithmic formulations preserve material objectivity.

This chapter has the aim of providing both the global and local numerical strategies for solving a large strain equilibrium problem considering the elastic-viscoplastic model developed earlier.[1] Section 5.1 first describes the global solution strategy to solve the whole equilibrium problem. The global solution strategy includes the statement of the continuum and incremental global weak formulation, associated with the whole boundary value problem stated in Section 3.1. The nonlinear equilibrium equation is then linearized in order to solve this problem following an iterative scheme, which therefore provides the displacement increment within a given time step. The spatial integration of the iterative displacement equation is performed by means of the Finite Element Method (FEM), which then provides a nodal displacement increment computed from the knowledge of the residual and the tangent matrix corresponding to the preceding iteration. Determination of the current stress field and calculation of the tangent matrix required for solving the incremental equilibrium equation relies upon the local constitutive equations formulated

[1]The present numerical framework was implemented in a proper finite element code programed in FORTRAN.

in Chapter 3. The numerical integration scheme employed to solve the local constitutive model, and analytical derivation of corresponding consistent tangent modulus required for computing the tangent matrix are outlined in Section 5.2.

## 5.1 Global solution strategy

As a first step, the weak form associated with the global boundary value problem stated in Subsection 3.1.2 is formulated. For this purpose, the Virtual Work Principle is employed. This variational formulation is widely employed for solving equilibrium problems considering both elastic and inelastic media. It is recalled that the finite strain framework adopted here follows a Total Lagrangian description, in which associated integral formulation have to be satisfied in the reference configuration $\bar{\Omega}_0$.

### 5.1.1 Weak formulation - Virtual Work Principle

Analytical solutions for the boundary value problem described in Subsection 3.1.2 are possible only when very simple specific conditions, concerning geometry, material, loading-histories, and boundary conditions, are complied with. This is not the case when dealing with general engineering applications. Thus, in order to deal with more complex cases, numerical methods are thereby required. Aiming at using the FEM, the virtual work formulation[2] associated with the strong form of equilibrium problem described in Subsection 3.1.2 is stated as follows. The problems consists of finding a kinematically admissible displacement field $\boldsymbol{u}(\boldsymbol{X}, t) \in \mathcal{K}$ (see Eq. (3.12)), such that for every $t \in (t_0, t_f]$, the following integral equation is satisfied:[3]

$$\mathscr{R}(\boldsymbol{u}, \boldsymbol{\eta}) = \int_{\Omega_0} \boldsymbol{P}(\boldsymbol{u}) : \nabla_{\boldsymbol{X}} \boldsymbol{\eta} dV - \int_{\Omega_0} \rho_0 \bar{\boldsymbol{b}} \cdot \boldsymbol{\eta} dV - \int_{\partial\Omega_0^t} \bar{\boldsymbol{t}} \cdot \boldsymbol{\eta} dA = 0, \ \ \forall \boldsymbol{\eta} \in \mathcal{V}. \tag{5.1}$$

$\mathscr{R}(\boldsymbol{u}, \boldsymbol{\eta})$ is the virtual work functional and can be seen as a residual quantity when the weak equilibrium equation (5.1) is not satisfied. Set[4]

$$\mathcal{V} = \left\{ \boldsymbol{\eta} : \bar{\Omega}_0 \to \mathcal{R}^3 | \boldsymbol{\eta}(\boldsymbol{X}) = 0, \ \boldsymbol{X} \in \partial\Omega_0^u \right\}, \tag{5.2}$$

[2]When compared with the original strong form solution, a lower regularity degree is required to the solution function associated with the weak formulation. For a greater discussion on this assertion, see, e.g., Hughes, 2000, Reddy, 1986, 2002, and Zienkiewicz and Taylor, 2000a. The equivalence between both weak and strong formulations can be found in many standard textbooks. Concerning inelastic problems, works of de Souza Neto et al., 2008, p.77, and Simo and Hughes, 1998, p.25, are referenced.

[3]In general, traction vector $\bar{\boldsymbol{t}}$ is not always known *a priori*. In fact, notice that the current traction vector $\boldsymbol{t} = \boldsymbol{\sigma}\boldsymbol{n}$ is given in terms of the *Cauchy* stress tensor $\boldsymbol{\sigma}$ and the current unit outward normal vector $\boldsymbol{n}$. Accordingly, the reference traction vector $\bar{\boldsymbol{t}}$ depends on the current deformation by $\bar{\boldsymbol{t}} = \det \boldsymbol{F}\boldsymbol{\sigma}\boldsymbol{F}^{-T}\boldsymbol{N}$, where $\boldsymbol{N}$ is the reference unit outward normal vector.

[4]For hardening viscoplastic materials, with $t-$fix, one has $\mathcal{K} \subset \mathcal{H}^1(\Omega_0)$ and $\mathcal{V} \subset \mathcal{H}^1(\Omega_0)$, where $\mathcal{H}^1(\Omega_0)$ represents the *Sobolev* space, which contains functions with square-integrable derivatives, see, e.g., the works of Simo and Hughes, 1998, and Hughes, 2000.

is the space of kinematically admissible virtual displacements $\boldsymbol{\eta}$ satisfying the essential boundary condition of Eq. (3.9).

It is emphasized that, although stating the Virtual Work Principle does not require specifying the constitutive relationship between both stress $\boldsymbol{P}$ and displacement $\boldsymbol{u}$ fields [Dym and Shames, 1973; Reddy, 1986, 2002], solving the whole problem requires relating $\boldsymbol{P}$ to $\boldsymbol{u}$, which is achieved by adopting a specific constitutive model. The present approach deals with a path-dependent material, whose constitutive behavior is described according to the elastic-viscoplastic model formulated in Chapter 3. In this class of materials, the stress tensor $\boldsymbol{P}$ is not only a function of the instantaneous value of $\boldsymbol{F}$. The current stress state depends on the past deformation history to which the material has been subjected [Coleman and Gurtin, 1967; Perzyna, 1971]. Within the present context, adopting the TIV approach (Subsection 3.1.5), the stress tensor $\boldsymbol{P}$ is the solution of the constitutive initial value problem, Eqs. (3.107)-(3.115) and corresponding initial conditions, by knowing the history of $\boldsymbol{F}(t)$, $\forall t \in \mathcal{I}$. Using a numerical procedure for integrating the corresponding rate constitutive equations is therefore an essential requirement for solving the whole equilibrium problem. In the present case, the strategy used to integrate the rate equations involves a time discretization. In what follows an incremental strategy is thus described to solve Eq. (5.1) incrementally.

### 5.1.2 Incremental Boundary Value Problem

The incremental strategy adopted herein consists of subdividing the whole time interval $(t_0, t_f]$ into $N > 0$ subintervals $(t_n, t_{n+1}]$, such that

$$(t_0, t_f] = \bigcup_{n=1}^{N} (t_n, t_{n+1}], \tag{5.3}$$

where $t_n$ and $t_{n+1}$ are the initial and final instants associated to the $n-$th time interval. Adopting an implicit solution scheme, for a time subinterval $(t_n, t_{n+1}]$ equation (5.1) have to be satisfied at $t_{n+1}$, and the increment associated with a given quantity $(\cdot)$ is given by

$$\Delta(\cdot) \coloneqq (\cdot)_{n+1} - (\cdot)_n, \tag{5.4}$$

being $(\cdot)_{n+1}$ and $(\cdot)_n$ the values at instants $t_{n+1}$ and $t_n$, respectively.

Within the context of an implicit strategy, the internal variables $\boldsymbol{\alpha}_n(\boldsymbol{X})$, the displacement $\boldsymbol{u}_n(\boldsymbol{X})$, as well as the stress $\boldsymbol{P}_n(\boldsymbol{X})$ fields are assumed to be known at the initial time instant $t_n$ and complying with Eq. (5.1). The incremental equilibrium problem corresponding to a time subinterval $(t_n, t_{n+1}]$ consists therefore of finding the current displacement field $\boldsymbol{u}_{n+1}(\boldsymbol{X}) \in \mathcal{K}_{n+1}$, such that

$$\mathscr{R}(\boldsymbol{u}_{n+1}, \boldsymbol{\eta}) = \int_{\Omega_0} \boldsymbol{P}_{n+1} : \nabla_{\boldsymbol{X}} \boldsymbol{\eta} dV - \int_{\Omega_0} \rho_0 \bar{\boldsymbol{b}}_{n+1} \cdot \boldsymbol{\eta} dV - \int_{\partial\Omega_0^t} \bar{\boldsymbol{t}}_{n+1} \cdot \boldsymbol{\eta} dA = 0, \ \ \forall \boldsymbol{\eta} \in \mathcal{V}, \tag{5.5}$$

where

$$\mathcal{K}_{n+1} = \left\{ \boldsymbol{u} : \bar{\Omega}_0 \to \mathcal{R}^3 | \boldsymbol{u}\left(\boldsymbol{X}\right) = \bar{\boldsymbol{u}}_{n+1}\left(\boldsymbol{X}\right),\ \boldsymbol{X} \in \partial\Omega_0^u \right\}, \tag{5.6}$$

being $\bar{\boldsymbol{u}}_{n+1}$ the prescribed displacement at $t_{n+1}$.

Within the present framework, the deformation gradient $\boldsymbol{F}_{n+1}$ must determine the stress $\boldsymbol{P}_{n+1}$ uniquely through specific integration algorithm (to be described in Section 5.2). This requirement is the numerical counterpart of the principle of thermodynamic determinism stated in Subsection 3.1.5. In other words, the integration algorithm defines an incremental constitutive function $\bar{\boldsymbol{P}}$ given in terms of both $\boldsymbol{F}_{n+1}$ and $\boldsymbol{\alpha}_n$:

$$\boldsymbol{P}_{n+1} = \bar{\boldsymbol{P}}\left(\boldsymbol{F}_{n+1}, \boldsymbol{\alpha}_n\right). \tag{5.7}$$

The resulting numerical stress tensor $\boldsymbol{P}_{n+1}$ tends to converge to an exact solution as the number of time intervals $N$ increases [de Souza Neto et al., 2008, p.95].

Even adopting a numerical formulation, satisfying the incremental equilibrium equation (5.1) requires the solution to a nonlinear initial boundary value problem, since the incremental constitutive function (5.7) consists of a set of nonlinear equations to be solved. An iterative procedure for solving Eq. (5.5) is then adopted, specifically the *Newton-Raphson* method described in the sequel.

### 5.1.3 *Newton-Raphson* Method

Employing the *Newton-Raphson* method to solve $\mathscr{R}\left(\boldsymbol{u}_{n+1}, \boldsymbol{\eta}\right) = 0$ in Eq. (5.5) consists of an iterative solution strategy in with the method is started by assuming a trial solution corresponding to an iteration $k = 0$:

$$\boldsymbol{u}_{n+1}^k = \boldsymbol{u}_n,\ \ k = 0,\ \ \forall \boldsymbol{X} \in \Omega_0 \cup \partial\Omega_0^t \tag{5.8}$$

and

$$\boldsymbol{u}_{n+1}^k = \bar{\boldsymbol{u}}_{n+1},\ \ k = 0,\ \ \forall \boldsymbol{X} \in \partial\Omega_0^u, \tag{5.9}$$

where $\boldsymbol{u}_n$ is the converged solution at $t_n$, and $\bar{\boldsymbol{u}}_{n+1}$ is the prescribed displacement at time $t_{n+1}$. At iteration $k$, one should determine $\Delta\boldsymbol{u}_{n+1}^k$ satisfying condition

$$\mathscr{R}\left(\boldsymbol{u}_{n+1}^{k+1}, \boldsymbol{\eta}\right) = \mathscr{R}\left(\boldsymbol{u}_{n+1}^k + \Delta\boldsymbol{u}_{n+1}^k, \boldsymbol{\eta}\right) = 0,\ \ \forall \boldsymbol{\eta} \in \mathcal{V}, \tag{5.10}$$

where $\boldsymbol{u}_{n+1}^{k+1} = \boldsymbol{u}_{n+1}^k + \Delta\boldsymbol{u}_{n+1}^k$ is the approximated solution. Expanding $\mathscr{R}\left(\boldsymbol{u}_{n+1}^{k+1}, \boldsymbol{\eta}\right)$ according to a *Taylor* series around $\boldsymbol{u}_{n+1}^k$, and keeping only the first-order terms, yields

$$\mathscr{R}\left(\boldsymbol{u}_{n+1}^k + \Delta\boldsymbol{u}_{n+1}^k, \boldsymbol{\eta}\right) \approx \mathscr{R}\left(\boldsymbol{u}_{n+1}^k, \boldsymbol{\eta}\right) + D\mathscr{R}\left(\boldsymbol{u}_{n+1}^k, \boldsymbol{\eta}\right)\left[\Delta\boldsymbol{u}_{n+1}^k\right] = 0,\ \ \forall \boldsymbol{\eta} \in \mathcal{V}, \tag{5.11}$$

and consequently

$$D\mathscr{R}\left(\boldsymbol{u}_{n+1}^{k},\boldsymbol{\eta}\right)\left[\Delta\boldsymbol{u}_{n+1}^{k}\right]=-\mathscr{R}\left(\boldsymbol{u}_{n+1}^{k},\boldsymbol{\eta}\right),\ \ \forall\boldsymbol{\eta}\in\mathcal{V}. \tag{5.12}$$

Term $D\mathscr{R}\left(\boldsymbol{u}_{n+1}^{k},\boldsymbol{\eta}\right)\left[\Delta\boldsymbol{u}_{n+1}^{k}\right]$ stands for the directional derivative of $\mathscr{R}$ at $\boldsymbol{u}_{n+1}^{k}$ in the direction of increment $\Delta\boldsymbol{u}_{n+1}^{k}$. The formal definition of this derivative is [Bonet and Wood, 1997; de Souza Neto et al., 2008; Simo and Hughes, 1998]:

$$D\mathscr{R}\left(\boldsymbol{u},\boldsymbol{\eta}\right)\left[\Delta\boldsymbol{u}\right]=\left.\frac{d}{d\epsilon}\mathscr{R}\left(\boldsymbol{u}+\epsilon\Delta\boldsymbol{u},\boldsymbol{\eta}\right)\right|_{\epsilon=0}. \tag{5.13}$$

Considering the incremental equilibrium integral of Eq. (5.5) and the definition given in Eq. (5.13), linearized equation (5.12) then becomes [de Souza Neto et al., 2008; dos Santos, 2012]

$$D\mathscr{R}\left(\boldsymbol{u}_{n+1}^{k},\boldsymbol{\eta}\right)\left[\Delta\boldsymbol{u}_{n+1}^{k}\right]=\int_{\Omega_0}\mathbb{M}_{n+1}^{k}:\nabla_{\boldsymbol{X}}\left(\Delta\boldsymbol{u}_{n+1}^{k}\right):\nabla_{\boldsymbol{X}}\boldsymbol{\eta}dV,\ \ \forall\boldsymbol{\eta}\in\mathcal{V}, \tag{5.14}$$

where term

$$\mathbb{M}_{n+1}^{k}\coloneqq\left.\frac{d\boldsymbol{P}}{d\boldsymbol{F}}\right|_{\boldsymbol{u}_{n+1}^{k}}, \tag{5.15}$$

is the consistent tangent modulus calculated in terms of displacement $\boldsymbol{u}_{n+1}^{k}$. An explicit expression for $\mathbb{M}_{n+1}$ is going to be derived in Subsection 5.2.2. Hence, expression of the linearized virtual work equation at an iteration $k$ and a time instant $t_{n+1}$ is given by

$$\int_{\Omega_0}\mathbb{M}_{n+1}^{k}:\nabla_{\boldsymbol{X}}\left(\Delta\boldsymbol{u}_{n+1}^{k}\right):\nabla_{\boldsymbol{X}}\boldsymbol{\eta}dV=-\mathscr{R}\left(\boldsymbol{u}_{n+1}^{k},\boldsymbol{\eta}\right),\ \ \forall\boldsymbol{\eta}\in\mathcal{V}, \tag{5.16}$$

with

$$\mathscr{R}\left(\boldsymbol{u}_{n+1}^{k},\boldsymbol{\eta}\right)=\int_{\Omega_0}\boldsymbol{P}_{n+1}^{k}:\nabla_{\boldsymbol{X}}\boldsymbol{\eta}dV-\int_{\Omega_0}\rho_0\bar{\boldsymbol{b}}_{n+1}\cdot\boldsymbol{\eta}dV-\int_{\partial\Omega_0^t}\bar{\boldsymbol{t}}_{n+1}\cdot\boldsymbol{\eta}dA. \tag{5.17}$$

These last two equations have to be solved in terms of increment $\Delta\boldsymbol{u}_{n+1}^{k}$, which then provides the next iterative displacement

$$\boldsymbol{u}_{n+1}^{k+1}\leftarrow\boldsymbol{u}_{n+1}^{k}+\Delta\boldsymbol{u}_{n+1}^{k}. \tag{5.18}$$

We remember that both $\boldsymbol{u}_{n+1}^{k}$ and $\boldsymbol{u}_{n+1}^{k+1}$ must satisfy the imposed essential boundary conditions. Knowing the new incremental displacement, a new residual $\mathscr{R}\left(\boldsymbol{u}_{n+1}^{k+1},\boldsymbol{\eta}\right)$ is therefore computed and checked against the tolerance $e_{tol}$, that is, if condition

$$\mathscr{R}\left(\boldsymbol{u}_{n+1}^{k+1},\boldsymbol{\eta}\right)<e_{tol} \tag{5.19}$$

holds, then convergence of the algorithm is achieved, and the new attempt is taken as the

current solution:

$$\boldsymbol{u}_{n+1} \leftarrow \boldsymbol{u}_{n+1}^{k+1}. \tag{5.20}$$

Otherwise,

$$\boldsymbol{u}_{n+1}^{k} \leftarrow \boldsymbol{u}_{n+1}^{k+1} \text{ and } k \leftarrow k+1, \tag{5.21}$$

and the algorithm is restarted.

### 5.1.4 Spatial discretization using the FEM

In order to solve the linearized equation (5.16) in terms of $\Delta\boldsymbol{u}_{n+1}^{k}$, the finite element method is employed in this work. Its simplicity and generality makes this method attractive to a wide range of nonlinear boundary value problems [Oden, 1972]. Thereby, this topic is intended to succinctly describe the FE implementation for solving equilibrium problems in the solid mechanics field. For a detailed discussion on the subject, standard textbooks as those of Oden, 1972, Bonet and Wood, 1997, Belytschko et al., 2000, Hughes, 2000, and Zienkiewicz and Taylor, 2000b, are referred to. Yet, for details on the FE implementation and elements technology, see work of Dhatt and Touzot, 1984, for example.

Let be a continuum vector function $\boldsymbol{a} : \Omega_0 \rightarrow \mathcal{R}^{n_d}$, where $1 \leq n_d \leq 3$ is the dimension of vector field $\boldsymbol{a}$. Considering the FEM approach, continuum function $\boldsymbol{a}(\boldsymbol{X})$ is then approximated following a discrete procedure. In a simplified way, the discretization consists of selecting a finite number $n_N$ of points (nodes) in $\bar{\Omega}_0$. At these nodes the respective values of function $\boldsymbol{a}(\boldsymbol{X})$ are specified. The real function domain $\bar{\Omega}_0$ is then approximately represented by a finite number $n_e$ of non-overlapping subdomains (elements) $\bar{\Omega}_0^{(e)}$ connected by their boundary nodes, such that

$$\bar{\Omega}_0 \approx {}^{h}\bar{\Omega}_0 = \bigcup_{e=1}^{n_e} \bar{\Omega}_0^{(e)}. \tag{5.22}$$

Function $\boldsymbol{a}(\boldsymbol{X})$ can be locally approximated within each subdomain $\bar{\Omega}_0^{(e)}$ by using its nodal values and specific base (or interpolation) functions associated to each element node, in the following manner:

$$\boldsymbol{a}(\boldsymbol{X}) \approx {}^{h}\boldsymbol{a}(\boldsymbol{X}) = \sum_{i=1}^{n_n} \boldsymbol{a}^i N_i^{(e)}(\boldsymbol{X}), \tag{5.23}$$

where $\boldsymbol{a}^i$ is the value of function $\boldsymbol{a}(\boldsymbol{X})$ evaluated at a node $i$ whose coordinate is $\boldsymbol{X}^i$, i.e.,

$$\boldsymbol{a}^i \coloneqq \boldsymbol{a}\left(\boldsymbol{X}^i\right). \tag{5.24}$$

Term $n_n$ represents the number of nodes of a given element, $N_i^{(e)}(\boldsymbol{X})$ is the interpolation

function associated with node $i$ of an element $e$.[5] This function has compact support, that is, it has a non-null values only over element $\Omega_0^{(e)}$. Furthermore, $N_i^{(e)}(\boldsymbol{X})$ is defined in order to comply with

$$N_i^{(e)}\left(\boldsymbol{X}^j\right) = \delta_{ij}. \tag{5.25}$$

In addition, functions $N_i^{(e)}(\boldsymbol{X})$ are partitions of unity (PU):

$$\sum_{i=1}^{n_n} N_i^{(e)}(\boldsymbol{X}) = 1, \ \ \forall \boldsymbol{X} \in \Omega_0^{(e)}. \tag{5.26}$$

The global field $\boldsymbol{a}(\boldsymbol{X})$ on ${}^h\Omega_0$ is represented by means of a piecewise approximation using $n_N$ global interpolation functions $N_i^g(\boldsymbol{X})$ related to each node $i$. This function has non-null values only on the elements connected by this same node, see Figure 5.1. Thus, the approximate form of $\boldsymbol{a}(\boldsymbol{X})$ in ${}^h\bar{\Omega}_0$ is given by

$${}^h\boldsymbol{a}(\boldsymbol{X}) = \sum_{i=1}^{n_N} \boldsymbol{a}^i N_i^g(\boldsymbol{X}). \tag{5.27}$$

Sometimes Eq. (5.27) is conveniently written in a matrix form:

$${}^h\boldsymbol{a}(\boldsymbol{X}) = \mathsf{N}^g(\boldsymbol{X})\,\vec{a}, \tag{5.28}$$

where $\vec{a}$ stands for a vector containing the nodal values of function $\boldsymbol{a}(\boldsymbol{X})$:

$$\vec{a}^T = \left[a_1^1, ..., a_{n_d}^1, ....., a_1^{n_N}, ..., a_{n_d}^{n_N}\right] \tag{5.29}$$

in which $a_i^j$ is the $i-$th component of vector field $\boldsymbol{a}$ related to a global node $j$. In addition, $\mathsf{N}^g(\boldsymbol{X})$ is the global interpolation matrix. For a domain with dimension $n_d$, $\mathsf{N}^g(\boldsymbol{X})$ is given by

$$\mathsf{N}^g(\boldsymbol{X}) = \left[\text{diag}\left[N_1^g(\boldsymbol{X})\right] \ \text{diag}\left[N_2^g(\boldsymbol{X})\right] \ ... \ \text{diag}\left[N_{n_N}^g(\boldsymbol{X})\right]\right], \tag{5.30}$$

where $\text{diag}\left[N_1^g(\boldsymbol{X})\right]$ denotes a $n_d \times n_d$ diagonal matrix defined as

$$\text{diag}\left[N_i^g(\boldsymbol{X})\right] = \begin{bmatrix} N_i^g(\boldsymbol{X}) & 0 & \cdots & 0 \\ 0 & N_i^g(\boldsymbol{X}) & \cdots & 0 \\ \vdots & \vdots & \ddots & 0 \\ 0 & 0 & \cdots & N_i^g(\boldsymbol{X}) \end{bmatrix}. \tag{5.31}$$

[5] Here an element of class $\mathcal{C}^o$ is considered.

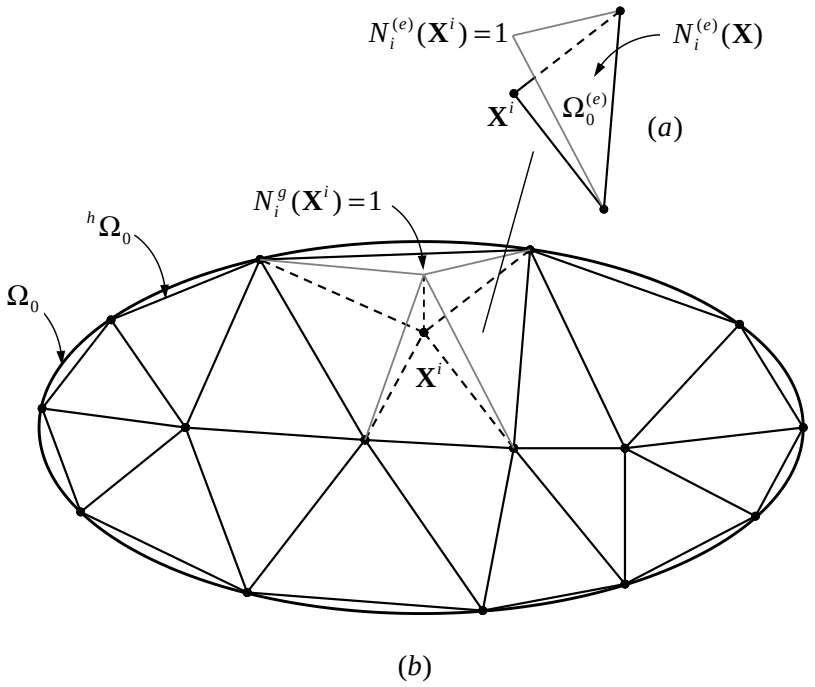


Figure 5.1: Finite element interpolation. (a) Local interpolation function; (b) Global interpolation function.

### 5.1.5 FEM solution of incremental Virtual Work equation

Numerical FEM solution of Eq. (5.16) consists of substituting the set $\mathcal{K}_{n+1}^k$ and space $\mathcal{V}$ by the corresponding finite element counterparts ${}^h\mathcal{K}_{n+1}^k$ and ${}^h\mathcal{V}$ , defined respectively as [de Souza Neto et al., 2008, p.85]

$$ {}^h\mathcal{K}_{n+1}^k \coloneqq \left\{ {}^h\boldsymbol{u}\left(\boldsymbol{X}\right) = \sum_{i=1}^{n_N} \boldsymbol{u}^i N_i^g\left(\boldsymbol{X}\right) | \boldsymbol{u}^i = \bar{\boldsymbol{u}}_{n+1},\ \boldsymbol{X}^i \in \partial\Omega_0^u \right\}, \tag{5.32} $$

and

$$ {}^h\mathcal{V} \coloneqq \left\{ {}^h\boldsymbol{\eta}\left(\boldsymbol{X}\right) = \sum_{i=1}^{n_N} \boldsymbol{\eta}^i N_i^g\left(\boldsymbol{X}\right) | \boldsymbol{\eta}^i = \boldsymbol{0},\ \boldsymbol{X}^i \in \partial\Omega_0^u \right\}. \tag{5.33} $$

It is recalled that both $\mathcal{K}$ and $\mathcal{V}$ refer to kinematically admissible fields related respectively to displacements and virtual displacements. Note that definitions related to the subsets ${}^h\mathcal{K}_{n+1}^k$ and ${}^h\mathcal{V}$ make use of result given in Eq. (5.27), that is, by substituting $\mathcal{K}_{n+1}^k$ and $\mathcal{V}$ by their discrete versions in Eq. (5.16), one assumes

$$ \Delta\boldsymbol{u}_{n+1}^k\left(\boldsymbol{X}\right) \approx \Delta^h\boldsymbol{u}_{n+1}^k\left(\boldsymbol{X}\right) = \sum_{i=1}^{n_N} \left(\Delta\boldsymbol{u}^i\right)_{n+1}^k N_i^g\left(\boldsymbol{X}\right), \tag{5.34} $$

and

$$ \boldsymbol{\eta}\left(\boldsymbol{X}\right) \approx^h \boldsymbol{\eta}\left(\boldsymbol{X}\right) = \sum_{i=1}^{n_N} \boldsymbol{\eta}^i N_i^g\left(\boldsymbol{X}\right). \tag{5.35} $$

Furthermore, analogously to Eq. (5.28), expressions given in Eq. (5.34) and (5.35) can be rewritten following a matrix descriptions, such as

$$\Delta^h \boldsymbol{u}^k_{n+1}(\boldsymbol{X}) = \mathsf{N}^g(\boldsymbol{X})\,\Delta\vec{u}^k_{n+1}, \tag{5.36}$$

and

$$^h\boldsymbol{\eta}(\boldsymbol{X}) = \mathsf{N}^g(\boldsymbol{X})\,\vec{\eta}, \tag{5.37}$$

where $\Delta\vec{u}^k_{n+1}$ and $\vec{\eta}$ are global vectors containing the nodal values of $\Delta\boldsymbol{u}^k_{n+1}(\boldsymbol{X})$ and $\boldsymbol{\eta}(\boldsymbol{X})$, respectively.

Matrix notation facilitates a compact numerical formulation and further computational implementation. Matrix forms presented earlier refer to a problem dealing with a vector field with dimension $n_d$ evaluated at $n_N$ nodes, i.e., the discrete problem has a total of $n_d.n_N$ degrees of freedom. In what follows, this quite general notation is therefore particularized by introducing plane and axisymmetric assumptions. Consequently, specific matrix forms for operator $\nabla_{\boldsymbol{X}}(\cdot)$ and stress tensor $\boldsymbol{P}$ are given. Those descriptions are required in order to provide the matrix formulation and FE implementation associated with Eq. (5.16).

**Plane problems.** By assuming $n_d = 2$, displacement vector $\boldsymbol{u}(\boldsymbol{X})$ becomes

$$\boldsymbol{u}^T(\boldsymbol{X}) = \left[u_1(\boldsymbol{X}),\ u_2(\boldsymbol{X})\right], \tag{5.38}$$

where $u_1(\boldsymbol{X})$ and $u_2(\boldsymbol{X})$ are displacements along directions 1 and 2, respectively. For a vector field $\boldsymbol{a} = \mathsf{N}^g\vec{a} : {}^h\bar{\Omega}_0 \to \mathcal{R}^2$, its gradient $\nabla_{\boldsymbol{X}}(\boldsymbol{a})$ is written in a vector form as

$$\nabla_{\boldsymbol{X}}\boldsymbol{a}(\boldsymbol{X}) \to \mathsf{G}^g(\boldsymbol{X})\,\vec{a} = \begin{bmatrix} a_{1,1} \\ a_{1,2} \\ a_{2,1} \\ a_{2,2} \end{bmatrix} = \begin{bmatrix} (\nabla^s\boldsymbol{a})_{11} \\ (\nabla^s\boldsymbol{a})_{12} \\ (\nabla^s\boldsymbol{a})_{21} \\ (\nabla^s\boldsymbol{a})_{22} \end{bmatrix}, \tag{5.39}$$

where

$$\mathsf{G}^g(\boldsymbol{X}) = \left[\begin{array}{cc|cc|c|cc} N^g_{1,1} & 0 & N^g_{2,1} & 0 & \cdots & N^g_{n_N,1} & 0 \\ N^g_{1,2} & 0 & N^g_{2,2} & 0 & \cdots & N^g_{n_N,2} & 0 \\ 0 & N^g_{1,1} & 0 & N^g_{2,1} & \cdots & 0 & N^g_{n_N,1} \\ 0 & N^g_{1,2} & 0 & N^g_{2,2} & \cdots & 0 & N^g_{n_N,2} \end{array}\right], \tag{5.40}$$

is the discrete global gradient operator, where notation $(\cdot)_{i,j} = \frac{\partial(\cdot)_i}{\partial X_j}$ is employed. The stress tensor $\boldsymbol{P}$ is given in a vector form by

$$\boldsymbol{P} \to \vec{P}^T = \begin{bmatrix} P_{11} & P_{12} & P_{21} & P_{22} \end{bmatrix}. \tag{5.41}$$

We remark that, for plane strain cases, stress component $P_{33}$ is generally non-zero. In this case, the stress is stored but is not include in product operations.

**Axisymmetric problems.** In order to develop the axisymmetric model, cylindrical coordinates $\{r, z, \theta\}$ are considered. The vector formulation considering a cylindrical system assumes a position vector $\boldsymbol{X} : \bar{\Omega}_0 \to \mathcal{R}^3$ and a vector field $\boldsymbol{a} = \mathsf{N}^g \vec{a} : {}^h\bar{\Omega}_0 \to \mathcal{R}^3$ whose components are respectively

$$X_1 = r, \quad X_2 = z, \quad X_3 = \theta, \tag{5.42}$$

and

$$a_1 = a_r, \quad a_2 = a_z, \quad a_3 = a_\theta. \tag{5.43}$$

By adopting the axisymmetric hypothesis, the field $\boldsymbol{a}$ assumes the specific form

$$a_r = a_r\left(r, z\right), \quad a_z = a_z\left(r, z\right), \quad a_\theta = 0, \tag{5.44}$$

and its gradient $\nabla_{\boldsymbol{X}}\left(\boldsymbol{a}\right)$, according to a cylindrical system, reads

$$\nabla_{\boldsymbol{X}}\left(\boldsymbol{a}\right) = \begin{bmatrix} a_{r,r} & a_{r,z} & 0 \\ a_{z,r} & a_{z,z} & 0 \\ 0 & 0 & \frac{a_r}{r} \end{bmatrix}. \tag{5.45}$$

Which, following a matrix description, can be rewritten as

$$\nabla_{\boldsymbol{X}}\boldsymbol{a}\left(\boldsymbol{X}\right) \to \mathsf{G}^g\left(\boldsymbol{X}\right)\vec{a} = \begin{bmatrix} a_{r,r} \\ a_{r,z} \\ a_{z,r} \\ a_{z,z} \\ \frac{a_r}{r} \end{bmatrix} = \begin{bmatrix} \left(\nabla^s \boldsymbol{a}\right)_{11} \\ \left(\nabla^s \boldsymbol{a}\right)_{12} \\ \left(\nabla^s \boldsymbol{a}\right)_{21} \\ \left(\nabla^s \boldsymbol{a}\right)_{22} \\ \left(\nabla^s \boldsymbol{a}\right)_{33} \end{bmatrix}, \tag{5.46}$$

with

$$\mathsf{G}^g\left(\boldsymbol{X}\right) = \left[\begin{array}{cc|cc|c|cc} N^g_{1,r} & 0 & N^g_{2,r} & 0 & \cdots & N^g_{n_N,r} & 0 \\ N^g_{1,z} & 0 & N^g_{2,z} & 0 & \cdots & N^g_{n_N,z} & 0 \\ 0 & N^g_{1,r} & 0 & N^g_{2,r} & \cdots & 0 & N^g_{n_N,r} \\ 0 & N^g_{1,z} & 0 & N^g_{2,z} & \cdots & 0 & N^g_{n_N,z} \\ \frac{N_1}{r} & 0 & \frac{N_2}{r} & 0 & & \frac{N_{n_N}}{r} & 0 \end{array}\right]. \tag{5.47}$$

Within this context, tensor $\boldsymbol{P}$ assumes the following vector form:

$$\boldsymbol{P} \to \vec{P}^T = \begin{bmatrix} P_{11} & P_{12} & P_{21} & P_{22} & P_{33} \end{bmatrix}. \tag{5.48}$$

Spatial discretization

Making use of results given in Eqs. (5.36), (5.37), (5.39) and (5.41) for plane problems, or Eqs. (5.46) and (5.48) for axisymmetric problems, in Eq.(5.16), after some algebraic manipulations, the following discrete equations is then obtained

$$\int_{\Omega_0} (\mathsf{G}^g)^T \, \mathsf{M}^k_{n+1} \mathsf{G}^g dV \Delta \vec{u}^k_{n+1} = -\vec{R}\left(\vec{u}^k_{n+1}\right), \tag{5.49}$$

with

$$\vec{R}\left(\vec{u}^k_{n+1}\right) = \int_{\Omega_0} (\mathsf{G}^g)^T \, \vec{P}^k_{n+1} dV - \int_{\Omega_0} (\mathsf{N}^g)^T \, \bar{\boldsymbol{b}}_{n+1} dV - \int_{\partial\Omega^t_0} (\mathsf{N}^g)^T \, \bar{\boldsymbol{t}}_{n+1} dA, \tag{5.50}$$

where $\mathsf{M}^k_{n+1}$ is the matrix counterpart of tangent modulus $\mathbb{M}^k_{n+1}$ given in Eq. (5.15). The global internal force $\vec{f}_{int}$, the global external force $\vec{f}_{ext}$, and the global stiffness tangent matrix $\mathsf{K}_T$, at $t_{n+1}$ for an iteration $k$, are respectively defined as

$$\left(\vec{f}_{int}\right)^k_{n+1} \coloneqq \int_{\Omega_0} (\mathsf{G}^g)^T \, \vec{P}^k_{n+1} dV, \tag{5.51}$$

$$\left(\vec{f}_{ext}\right)_{n+1} \coloneqq \int_{\Omega_0} (\mathsf{N}^g)^T \, \bar{\boldsymbol{b}}_{n+1} dV + \int_{\partial\Omega^t_0} (\mathsf{N}^g)^T \, \bar{\boldsymbol{t}}_{n+1} dA, \tag{5.52}$$

and

$$(\mathsf{K}_T)^k_{n+1} \coloneqq \int_{\Omega_0} (\mathsf{G}^g)^T \, \mathsf{M}^k_{n+1} \mathsf{G}^g dV. \tag{5.53}$$

Thus, the displacement increment $\Delta\vec{u}^k_{n+1}$ is finally computed by

$$\Delta\vec{u}^k_{n+1} = -\left[(\mathsf{K}_T)^k_{n+1}\right]^{-1} \left[\left(\vec{f}_{int}\right)^k_{n+1} - \left(\vec{f}_{ext}\right)_{n+1}\right]. \tag{5.54}$$

**Contribution of each finite element.** Considering the FE framework, an important aspect to be highlighted is the determination of global quantities $\vec{f}_{int}$, $\vec{f}_{ext}$, and $\mathsf{K}_T$ from the superimposed local contribution of each finite element, what is performed in the following manner:

$$\vec{f}_{int} = \mathop{\mathsf{A}}_{e=1}^{n_e} \left(\vec{f}^{(e)}_{int}\right), \quad \vec{f}_{ext} = \mathop{\mathsf{A}}_{e=1}^{n_e} \left(\vec{f}^{(e)}_{ext}\right), \quad \text{and} \quad \mathsf{K}_T = \mathop{\mathsf{A}}_{e=1}^{n_e} \left(\mathsf{K}^{(e)}_T\right), \tag{5.55}$$

where operator $\mathsf{A}$ stands for a finite element assembling operator, which allows that each global quantity, $\vec{f}_{int}$, $\vec{f}_{ext}$, and $\mathsf{K}_T$, associated with each global node can be computed from the sum of local contributions associated with elements connected by that node. Terms $\vec{f}^{(e)}_{int}$, $\vec{f}^{(e)}_{ext}$, and $\mathsf{K}^{(e)}_T$ are computed respectively by

$$\vec{f}^{(e)}_{int} \coloneqq \int_{\Omega^{(e)}} \left(\mathsf{G}^{(e)}\right)^T \vec{P}^k_{n+1} dV, \tag{5.56}$$

$$\vec{f}_{ext}^{(e)} \coloneqq \int_{\Omega^{(e)}} \left(\mathsf{N}^{(e)}\right)^T \bar{\boldsymbol{b}} dV - \int_{\partial\Omega^{t(e)}} \left(\mathsf{N}^{(e)}\right)^T \boldsymbol{t} dA, \tag{5.57}$$

and

$$\mathsf{K}_T^{(e)} \coloneqq \int_{\Omega^{(e)}} \left(\mathsf{G}^{(e)}\right)^T \mathsf{M}\mathsf{G}^{(e)} dV. \tag{5.58}$$

Considering a generic element $e$ with $n_n$ nodes, the local interpolation matrix $\mathsf{N}^{(e)}$ is given by

$$\mathsf{N}^{(e)}(\boldsymbol{X}) = \left[\text{diag}\left[N_1^{(e)}(\boldsymbol{X})\right] \ \text{diag}\left[N_2^{(e)}(\boldsymbol{X})\right] \ \ldots \ \text{diag}\left[N_{n_n}^{(e)}(\boldsymbol{X})\right]\right], \tag{5.59}$$

and the local gradient matrix $\mathsf{G}^{(e)}$ (considering plane analysis) has the form

$$\mathsf{G}^{(e)}(\boldsymbol{X}) = \left[\begin{array}{cc|cc|c|cc} N_{1,1}^{(e)} & 0 & N_{2,1}^{(e)} & 0 & \cdots & N_{n_n,1}^{(e)} & 0 \\ N_{1,2}^{(e)} & 0 & N_{2,2}^{(e)} & 0 & \cdots & N_{n_n,2}^{(e)} & 0 \\ 0 & N_{1,1}^{(e)} & 0 & N_{2,1}^{(e)} & \cdots & 0 & N_{n_n,1}^{(e)} \\ 0 & N_{1,2}^{(e)} & 0 & N_{2,2}^{(e)} & \cdots & 0 & N_{n_n,2}^{(e)} \end{array}\right]. \tag{5.60}$$

Considering axisymmetric problems, $\mathsf{G}^{(e)}(\boldsymbol{X})$ follows analogously to $\mathsf{G}^{g}(\boldsymbol{X})$ given in Eq. (5.47).

The size of matrix $\mathsf{N}^{(e)}$ and mathematical features associated with functions $N_i^{(e)}(\boldsymbol{X})$ depend on the type of employed finite element. A rich description on a variety of finite elements can be found in Dhatt and Touzot, 1984. In the present work the following elements will be used: 6th-node triangular element, and 4th-node quadrilateral element, both pertaining to the class of $\mathcal{C}^0$-elements. Normally, within a finite element context, Eqs. (5.56), (5.57), and (5.58) are numerically integrated by means of the traditional *Gauss* quadrature. This choice is motivated by the fact that in general $N_i^{(e)}(\boldsymbol{X})$ are polynomial functions, and using the appropriate number of integration points, the *Gauss* method is able of exactly integrating this kind of functions. For more details, see, e.g., Hughes, 2000, and Zienkiewicz and Taylor, 2000a.

## 5.2 Local integration algorithm

This section describes numerical strategy used for solving the local constitutive problem formulated in Chapter 3, more specifically Eqs. (3.107)-(3.115). Determining the local quantities is required in order to obtain the current stress state $\boldsymbol{P}_{n+1}$ and to compute the consistent tangent modulus $\mathbb{M}_{n+1}$ needed for solving the global equilibrium problem described in preceding section. The local numerical scheme relies upon the same time discretization described in Subsection 5.1.2. Consequently, considering a given subinterval $(t_n, t_{n+1}]$, the rate of a given variable $(\cdot)$ is approximated as

$$\frac{d(\cdot)}{dt} \approx \frac{(\cdot)_{n+1} - (\cdot)_n}{\Delta t}, \ \text{ for } \ t \in (t_n, t_{n+1}], \tag{5.61}$$

where $\Delta t \coloneqq t_{n+1} - t_n$ is the time increment. Hence, the evolution of the accumulated viscoplastic strain $\varepsilon$ given in Eq. (3.108) is approximated based on a backward *Euler* method

$$\varepsilon_{n+1} = \varepsilon_n + \sqrt{\frac{2}{3}}\Delta\lambda \tag{5.62}$$

in which the incremental viscoplastic multiplier $\Delta\lambda$ must satisfy

$$\Delta\lambda = 0, \;\; \text{for} \;\; f_{n+1} \leq 0, \tag{5.63}$$

and in view of Eq. (3.70)

$$f\left(\bar{\boldsymbol{\tau}}_{n+1}, A_{n+1}\right) = \left\|\bar{\boldsymbol{\tau}}^D_{n+1}\right\| - \sqrt{\frac{2}{3}}\left(\sigma_y + A_{n+1}\right) = \bar{\Theta}^{-1}\left(\Delta\lambda, A_{n+1}\right), \tag{5.64}$$

for $f_{n+1} > 0$. Function $\bar{\Theta}^{-1}$ is the algorithmic form of $\Theta^{-1}$ given in Eq. (3.70), and specialized in Eqs. (3.99), (3.101), and (3.102). To compute the evolution of hardening variable $A$ given in Eq. (3.63) together with Eqs. (3.110) and (3.111), a constant rate $\dot{\varepsilon} \approx \frac{\varepsilon_{n+1}-\varepsilon_n}{\Delta t}$ is assumed within time step $(t_n, t_{n+1}]$. Then, Eq. (3.84) can be used considering $t_n$ as the initial state and $t_{n+1}$ as the current state, leading to

$$A_{n+1} = A_n + \bar{A}_{\infty_{n+1}} c\left(\varepsilon_{n+1} - \varepsilon_n\right) + \left[\bar{A}_{\infty_{n+1}}\left(1 + c\varepsilon_n\right) - A_n\right]\left\{1 - \exp\left[-\delta\left(\varepsilon_{n+1} - \varepsilon_n\right)\right]\right\}, \tag{5.65}$$

where parameters $\delta$ and $\bar{A}_\infty$ are calculated at $t_{n+1}$ making use of Eqs. (3.91), (3.112), (3.114), and (3.115), what yield the respective equations:

$$\delta_{n+1} = \delta^{lwr} + \left[\frac{1}{\Delta t}\left(\frac{\varepsilon_{n+1} - \varepsilon_n - \Delta t\dot{\varepsilon}_{lwr}}{\dot{\varepsilon}_{up} - \dot{\varepsilon}_{lwr}}\right)\right]^{\xi_1}\left(\delta^{up} - \delta^{lwr}\right) \tag{5.66}$$

and

$$\bar{A}_{\infty_{n+1}} = \frac{\varepsilon_n}{\varepsilon_{n+1}}\bar{A}_{\infty_n} + \left(1 - \frac{\varepsilon_n}{\varepsilon_{n+1}}\right)A_{\infty_{n+1}}, \tag{5.67}$$

with

$$A_{\infty_{n+1}} = A^{lwr}_\infty + \left[\frac{1}{\Delta t}\left(\frac{\varepsilon_{n+1} - \varepsilon_n - \Delta t\dot{\varepsilon}_{lwr}}{\dot{\varepsilon}_{up} - \dot{\varepsilon}_{lwr}}\right)\right]^{\xi_2}\left(A^{up}_\infty - A^{lwr}_\infty\right). \tag{5.68}$$

An important aspect related to numerical integration to be highlighted lies on the fact that, employing a standard procedure to numerically integrate Eq. (3.107), may originate significant precision loss when solving constitutive equations of incompressible (visco)plastic models. As a matter of fact, by using a standard implicit integration method in large strain problems, the plastic flow incompressibility can not be ensured (see for instance discussion of de Souza Neto et al., 2008, p.592). This problem can be overcome by employing an integration based on a backward exponential mapping as proposed by Eterovic and Bathe, 1990, and Weber and Anand, 1990, which then provides the following

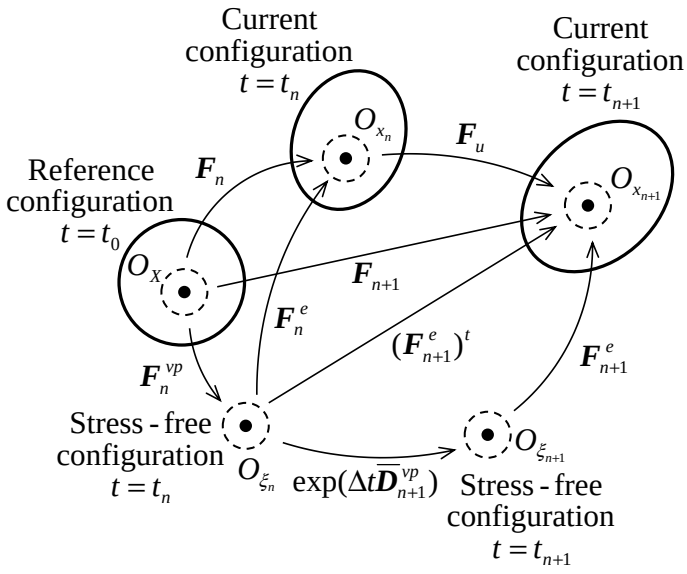


Figure 5.2: Schematic representation of incremental configuration mappings between time instants $t_n$ and $t_{n+1}$.

incremental equation associated with Eq. (3.107):

$$\boldsymbol{F}_{n+1}^{vp} = \exp\left(\Delta t \bar{\boldsymbol{D}}_{n+1}^{vp}\right) \boldsymbol{F}_n^{vp} \rightarrow \boldsymbol{F}_{n+1}^{vp} = \exp\left(\Delta\lambda \boldsymbol{N}_{\bar{\boldsymbol{\tau}}_{n+1}}\right) \boldsymbol{F}_n^{vp}. \tag{5.69}$$

where $\boldsymbol{N}_{\bar{\boldsymbol{\tau}}_{n+1}} = \frac{\bar{\boldsymbol{\tau}}_{n+1}^D}{\|\bar{\boldsymbol{\tau}}_{n+1}^D\|}$. Based upon the present incremental formulation, numerical mappings relating the reference, current, as well as the stress-free configurations considering a time subinterval $(t_n, t_{n+1}]$ are shown in Figure 5.2. Term $\boldsymbol{F}_u = \boldsymbol{F}_{n+1}\boldsymbol{F}_n^{-1}$ is the deformation increment from $t_n$ to $t_{n+1}$.

Now a numerical method have to be employed for solving the system of nonlinear equations (5.62)-(5.69)$_2$ in terms of unknowns

$$\left\{\boldsymbol{F}_{n+1}^{vp}, \varepsilon_{n+1}, \Delta\lambda, A_{n+1}, \delta_{n+1}, \bar{A}_{\infty_{n+1}}\right\}, \tag{5.70}$$

with (see Eq. (3.105)$_1$)

$$\bar{\boldsymbol{\tau}}_{n+1} = \mathbb{D}^e : \boldsymbol{E}_{n+1}^e. \tag{5.71}$$

In view of Eqs. (5.63) and (5.64), and considering a given prescribed deformation increment $\boldsymbol{F}_u = \boldsymbol{F}_{n+1}\boldsymbol{F}_n^{-1}$ within time interval $(t_n, t_{n+1}]$, the corresponding local constitutive problem has two possible solutions: (i) a pure elastic solution, which results in a null viscoplastic multiplier: $\Delta\lambda = 0$; (ii) an elastic-viscoplastic solution in which the viscoplastic deformation characterized by $\Delta\lambda > 0$ proceeds. The algorithm employed to solve the present problem has to address these two conditions and to provide the correct solution.

### 5.2.1 Elastic prediction and viscoplastic correction algorithm

The nature of the above problem motivates the establishment of a two-step algorithm in which the two possible solutions are considered sequentially and the final solution is the unique valid one [Simo and Hughes, 1998; de Souza Neto et al., 2008]. The two steps consist of: (i) elastic prediction; and (ii) viscoplastic correction. In the elastic prediction step, a fully elastic deformation increment is assumed, then providing the formal condition

$$\dot{\boldsymbol{F}}^{vp} = \boldsymbol{0} \text{ and } \dot{A} = 0 \tag{5.72}$$

and its incremental counterpart

$$\boldsymbol{F}_{n+1}^{vp^{trial}} = \boldsymbol{F}_{n}^{vp} \text{ and } A_{n+1}^{trial} = A_n. \tag{5.73}$$

From these conditions, the *trial elastic state* is defined in terms of elastic deformation gradient and elastic logarithmic strain measure,

$$\boldsymbol{F}_{n+1}^{e^{trial}} = \boldsymbol{F}_{n+1}\left(\boldsymbol{F}_{n+1}^{vp^{trial}}\right)^{-1} \quad \rightarrow \quad \boldsymbol{E}_{n+1}^{e^{trial}} = \frac{1}{2}\ln\left(\boldsymbol{C}_{n+1}^{e^{trial}}\right), \tag{5.74}$$

with $\boldsymbol{C}_{n+1}^{e^{trial}} = \left(\boldsymbol{F}_{n+1}^{e^{trial}}\right)^{T}\boldsymbol{F}_{n+1}^{e^{trial}}$. Therefore, the trial stress state is computed using Eqs. $(3.55)_1$: $\bar{\boldsymbol{\tau}}_{n+1}^{trial} = \mathbb{D}^e : \boldsymbol{E}_{n+1}^{e^{trial}}$. If this state complies with condition

$$f\left(\bar{\boldsymbol{\tau}}_{n+1}^{trial}, A_{n+1}^{trial}\right) \leq 0, \tag{5.75}$$

then it is considered as the unique possible solution, consequently variables at $t_{n+1}$ are updated,

$$(\cdot)_{n+1} = (\cdot)_{n+1}^{trial}, \tag{5.76}$$

and the algorithm has converged, thus proceeding to the next deformation increment. Otherwise, the plastic correction is required when

$$f\left(\bar{\boldsymbol{\tau}}_{n+1}^{trial}, A_{n+1}^{trial}\right) > 0. \tag{5.77}$$

System of nonlinear equations (5.62)-$(5.69)_2$ has therefore to be solved. Making use of Eq. $(5.74)_1$ into Eq. $(5.69)_2$ reads

$$\boldsymbol{F}_{n+1}^{e} = \boldsymbol{F}_{n+1}^{e^{trial}} \exp\left\{-\Delta\lambda \boldsymbol{N}_{\bar{\boldsymbol{\tau}}_{n+1}}\right\}. \tag{5.78}$$

Moreover, after some manipulations Eq. (5.78) reduces to (see for instance deductions in works of Eterovic and Bathe, 1990, Eterovic and Bathe, 1990, or dos Santos, 2012)

$$\boldsymbol{E}_{n+1}^{e} = \boldsymbol{E}_{n+1}^{e^{trial}} - \Delta\lambda \boldsymbol{N}_{\bar{\boldsymbol{\tau}}_{n+1}}. \tag{5.79}$$

Actually, when the constitutive formulation is restricted to elastic and inelastic isotropy, equivalence of Eqs. $(5.69)_2$ and (5.79) is exact. Otherwise, Eq. (5.79) is in fact an approximation based on moderately small elastic strains with a second-order error on elastic strains. These conditions are needed to obtain the relation $\boldsymbol{R}^e_{n+1} = \boldsymbol{R}^{e^{trial}}_{n+1}$ for elastic rotation tensor [Eterovic and Bathe, 1990; Weber and Anand, 1990].

The return mapping algorithm consists therefore in solving the system of nonlinear equations (5.62)-(5.68) and (5.79) with respect to the set of unknowns $\left\{\boldsymbol{E}^e_{n+1},\, \varepsilon_{n+1},\, \Delta\lambda,\, A_{n+1},\, \delta_{n+1}, \bar{A}_{\infty_{n+1}}\right\}$. However, equality $\boldsymbol{N}_{\bar{\boldsymbol{\tau}}_{n+1}} = \boldsymbol{N}_{\bar{\boldsymbol{\tau}}^{trial}_{n+1}}$ can be established in the context of *von Mises* criterion stated in Eq. (3.67). Equations (5.62)-(5.64) and (5.79) thus reduce to the scalar equation (see deduction in B.2):

$$\left\|\bar{\boldsymbol{\tau}}^{D^{trial}}_{n+1}\right\| - \Delta\lambda 2\mu - \sqrt{\frac{2}{3}}\left(\sigma_y + A_{n+1}\right) = \bar{\Theta}^{-1}\left(\Delta\lambda, A_{n+1}\right), \tag{5.80}$$

with unknowns $\Delta\lambda$ and $A_{n+1}$. Furthermore, inserting Eq. (5.62) into Eqs. (5.65), (5.66), (5.67), and (5.68) yields the respective equations

$$A_{n+1} = A_n + \bar{A}_{\infty_{n+1}} c\sqrt{\frac{2}{3}}\Delta\lambda + \left[\bar{A}_{\infty_{n+1}}\left(1 + c\varepsilon_n\right) - A_n\right]\left[1 - \exp\left(-\delta_{n+1}\sqrt{\frac{2}{3}}\Delta\lambda\right)\right], \tag{5.81}$$

$$\delta_{n+1} = \delta^{lwr}_{\infty} + \left[\frac{1}{\Delta t}\left(\frac{\sqrt{\frac{2}{3}}\Delta\lambda - \Delta t\dot{\varepsilon}_{lwr}}{\dot{\varepsilon}_{up} - \dot{\varepsilon}_{lwr}}\right)\right]^{\xi_1}\left(\delta^{up}_{\infty} - \delta^{lwr}_{\infty}\right), \tag{5.82}$$

and

$$\bar{A}_{\infty_{n+1}} = \frac{\varepsilon_n}{\sqrt{\frac{2}{3}}\Delta\lambda + \varepsilon_n}\bar{A}_{\infty_n} + \left(1 - \frac{\varepsilon_n}{\sqrt{\frac{2}{3}}\Delta\lambda + \varepsilon_n}\right) A_{\infty_{n+1}}, \tag{5.83}$$

with

$$A_{\infty_{n+1}} = A^{lwr}_{\infty} + \left[\frac{1}{\Delta t}\left(\frac{\sqrt{\frac{2}{3}}\Delta\lambda - \Delta t\dot{\varepsilon}_{lwr}}{\dot{\varepsilon}_{up} - \dot{\varepsilon}_{lwr}}\right)\right]^{\xi_2}\left(A^{up}_{\infty} - A^{lwr}_{\infty}\right). \tag{5.84}$$

Then, the reduced return mapping algorithm consists of solving Eqs. (5.80)-(5.84) with respect to unknowns $\left\{\Delta\lambda, A_{n+1}, \delta_{n+1}, \bar{A}_{\infty_{n+1}}\right\}$. Derivatives of Eqs. (5.80)-(5.84) with respect to $\Delta\lambda$, $A_{n+1}$, $\delta_{n+1}$, and $\bar{A}_{\infty_{n+1}}$, required in the *Newton-Raphson* method described in B.1, are given in Appendix B.3 and are employed to solve this set of nonlinear equations. After solution in terms of unknowns $\left\{\Delta\lambda, A_{n+1}, \delta_{n+1}, \bar{A}_{\infty_{n+1}}\right\}$, mechanical quantities are then updated at $t_{n+1}$:

$$\bar{\boldsymbol{\tau}}^{D}_{n+1} = \left(\bar{\boldsymbol{\tau}}^{D^{trial}}_{n+1}\right)^t - \Delta\lambda 2\mu \boldsymbol{N}_{\bar{\boldsymbol{\tau}}^{trial}_{n+1}}, \tag{5.85}$$

$$\bar{\boldsymbol{\tau}}_{n+1} = \bar{\boldsymbol{\tau}}^{D}_{n+1} + \frac{1}{3}\mathrm{tr}\left(\bar{\boldsymbol{\tau}}^{trial}_{n+1}\right)\boldsymbol{I}, \tag{5.86}$$

$$\boldsymbol{\tau}_{n+1} = \boldsymbol{R}^{e^{trial}}_{n+1}\bar{\boldsymbol{\tau}}_{n+1}\left(\boldsymbol{R}^{e^{trial}}_{n+1}\right)^T, \tag{5.87}$$

$$\boldsymbol{P}_{n+1} = \boldsymbol{\tau}_{n+1}\boldsymbol{F}_{n+1}^{-T}, \tag{5.88}$$

$$\boldsymbol{E}_{n+1}^{e} = \boldsymbol{E}_{n+1}^{e^{trial}} - \Delta\lambda \boldsymbol{N}_{\bar{\boldsymbol{\tau}}_{n+1}^{trial}}, \tag{5.89}$$

$$\varepsilon_{n+1} = \varepsilon_{n+1}^{trial} + \sqrt{\frac{2}{3}}\Delta\lambda, \tag{5.90}$$

and

$$\boldsymbol{F}_{n+1}^{vp} = \exp\left(\Delta\lambda \boldsymbol{N}_{\bar{\boldsymbol{\tau}}_{n+1}^{trial}}\right)\boldsymbol{F}_{n}^{vp}. \tag{5.91}$$

### 5.2.2 Consistent tangent modulus

The consistent tangent modulus $\mathbb{M}_{n+1} \coloneqq \left(\frac{d\boldsymbol{P}}{d\boldsymbol{F}}\right)_{n+1}$ previously introduced in Eq. (5.15), can be written as:

$$M_{ijkl_{n+1}} = \left(\frac{\partial \tau_{ip}}{\partial F_{kl}}F_{jp}^{-1} - \tau_{ip}F_{jk}^{-1}F_{lp}^{-1}\right)_{n+1}, \tag{5.92}$$

since $\boldsymbol{P} = \boldsymbol{\tau}\boldsymbol{F}^{-T}$, as indicated in Eq. $(3.45)_2$, computation of $\mathbb{M}_{n+1}$ requires thus the derivative of $\boldsymbol{\tau}$ with respect to $\boldsymbol{F}$. However, expressing $\boldsymbol{\tau}$ in terms of the rotated *Kirchhoff* stress tensor $\bar{\boldsymbol{\tau}}$ (see Eq. (3.43)) provides an alternative way to compute this derivative. Within a time interval $(t_n, t_{n+1}]$, tensor $\bar{\boldsymbol{\tau}}_{n+1}$, similarly to $\boldsymbol{P}_{n+1}$ of Eq. (5.7), is given by a numerical constitutive function $\tilde{\bar{\boldsymbol{\tau}}}$ expressed in terms input variables $\boldsymbol{E}_{n+1}^{e^{trial}}$ and $\boldsymbol{\alpha}_n$: $\bar{\boldsymbol{\tau}}_{n+1} = \tilde{\bar{\boldsymbol{\tau}}}\left(\boldsymbol{E}_{n+1}^{e^{trial}}, \boldsymbol{\alpha}_n\right)$. Recalling that $\boldsymbol{\alpha}_n$ remains fixed within $(t_n, t_{n+1}]$ and exploiting the chain rule, the derivative of $\bar{\boldsymbol{\tau}}_{n+1}$ with respect to $\boldsymbol{F}_{n+1}$ can be calculated as:

$$\tilde{\mathbb{D}}_{n+1} = \frac{\partial \bar{\boldsymbol{\tau}}_{n+1}}{\partial \boldsymbol{F}_{n+1}} = \mathbb{D}_{n+1} : \mathbb{P}_{n+1} : \mathbb{Q}_{n+1}, \tag{5.93}$$

where $\mathbb{D}_{n+1} = \frac{\partial \bar{\boldsymbol{\tau}}_{n+1}}{\partial \boldsymbol{E}_{n+1}^{e^{trial}}}$, $\mathbb{P}_{n+1} = \frac{\partial \boldsymbol{E}_{n+1}^{e^{trial}}}{\partial \boldsymbol{C}_{n+1}^{e^{trial}}}$ and $\mathbb{Q}_{n+1} = \frac{\partial \boldsymbol{C}_{n+1}^{e^{trial}}}{\partial \boldsymbol{F}_{n+1}}$.

Observing that $\boldsymbol{C}_{n+1}^{e^{trial}} = \left(\boldsymbol{F}_{n+1}^{e^{trial}}\right)^{T}\boldsymbol{F}_{n+1}^{e^{trial}}$, the components of the fourth-order tensor $\mathbb{Q}_{n+1}$ read

$$Q_{ijkl_{n+1}} = F_{li_n}^{vp^{-1}}F_{kj_{n+1}}^{e^{trial}} + F_{ki_{n+1}}^{e^{trial}}F_{lj_n}^{vp^{-1}}. \tag{5.94}$$

The fourth-order tensor $\mathbb{P}_{n+1}$ is computed as

$$\mathbb{P}_{n+1} = \frac{\partial}{\partial \boldsymbol{C}_{n+1}^{e^{trial}}}\ln\left(\boldsymbol{U}_{n+1}^{e^{trial}}\right) = \frac{1}{2}\frac{\partial}{\partial \boldsymbol{C}_{n+1}^{e^{trial}}}\ln\left(\boldsymbol{C}_{n+1}^{e^{trial}}\right). \tag{5.95}$$

The terms $\mathbb{P}_{n+1}$ and $\mathbb{Q}_{n+1}$ are geometrical quantities related to finite strains, while the tangent operator $\mathbb{D}_{n+1}$ is the unique term of $\tilde{\mathbb{D}}_{n+1}$ depending on material response. In the elastic range, $\mathbb{D}_{n+1}$ turns to be coincident with the elastic stiffness $\mathbb{D}^e$, while it becomes the elastic-viscoplastic tangent operator

$$\mathbb{D}_{n+1}^{vp} = \frac{\partial \bar{\boldsymbol{\tau}}_{n+1}}{\partial \boldsymbol{E}_{n+1}^{e^{trial}}} \tag{5.96}$$

in the inelastic range. Evaluation of $\mathbb{D}^{vp}_{n+1}$ is obtained from linearization of Eqs. (5.79), (5.64), (5.84) and (5.81), what yields (see derivation in Appendix B.4)

$$\mathbb{D}^{vp}_{n+1} = \frac{\partial \bar{\boldsymbol{\tau}}_{n+1}}{\partial \boldsymbol{E}^{e^{trial}}_{n+1}} = \left( \mathbb{D}^{e^{-1}} + \Delta\lambda \frac{\partial \boldsymbol{N}_{\bar{\boldsymbol{\tau}}_{n+1}}}{\partial \bar{\boldsymbol{\tau}}_{n+1}} + \frac{1}{\chi} \boldsymbol{N}_{\bar{\boldsymbol{\tau}}_{n+1}} \otimes \boldsymbol{N}_{\bar{\boldsymbol{\tau}}_{n+1}} \right)^{-1}, \tag{5.97}$$

where

$$N_{A_{n+1}} = \frac{\partial f_{n+1}}{\partial A_{n+1}} \text{ and } \chi = \left[ \frac{\partial \bar{\Theta}^{-1}}{\partial \Delta\lambda} + \left( \frac{\partial \bar{\Theta}^{-1}}{\partial A_{n+1}} - N_{A_{n+1}} \right) \Lambda \right], \tag{5.98}$$

in which

$$\frac{\partial \bar{\Theta}^{-1}}{\partial \Delta\lambda} = \sqrt{\frac{2}{3}} \left( \sigma_y + A_{n+1} \right) \left[ \frac{1}{m} \frac{\vartheta_1}{\Delta t} \left( 1 + \vartheta_1 \frac{\Delta\lambda}{\Delta t} \right)^{\frac{1}{m}-1} + \frac{\vartheta_2}{\Delta t} \right], \tag{5.99}$$

$$\frac{\partial \bar{\Theta}^{-1}}{\partial A_{n+1}} = \sqrt{\frac{2}{3}} \left[ \left( 1 + \vartheta_1 \frac{\Delta\lambda}{\Delta t} \right)^{\frac{1}{m}} + \vartheta_2 \frac{\Delta\lambda}{\Delta t} - 1 \right], \tag{5.100}$$

and

$$\begin{aligned} \Lambda \quad = \quad & \sqrt{\frac{2}{3}} \left\{ \delta_{n+1} \left[ \bar{A}_{\infty_{n+1}} \left( 1 + c\varepsilon_n \right) - A_n \right] \varphi + \bar{A}_{\infty_{n+1}} c \right\} + \dots \\ \dots + \quad & \sqrt{\frac{2}{3}} \Delta\lambda \left[ \bar{A}_{\infty_{n+1}} \left( 1 + c\varepsilon_n \right) - A_n \right] \varphi\omega_1 + \dots \qquad (5.101) \\ \dots + \quad & \left[ \left( 1 + c\varepsilon_n \right) \left( 1 - \varphi \right) + c\sqrt{\frac{2}{3}} \Delta\lambda \right] \omega_2, \qquad (5.102) \end{aligned}$$

with

$$\omega_1 = \sqrt{\frac{2}{3}} \frac{\xi_1}{\Delta t} \left( \frac{\delta^{up} - \delta^{lwr}}{\dot{\varepsilon}_{up} - \dot{\varepsilon}_{lwr}} \right) \left[ \frac{1}{\Delta t} \left( \frac{\sqrt{\frac{2}{3}} \Delta\lambda - \Delta t \dot{\varepsilon}_{lwr}}{\dot{\varepsilon}_{up} - \dot{\varepsilon}_{lwr}} \right) \right]^{\xi_1 - 1}, \tag{5.103}$$

$$\omega_2 = \frac{\sqrt{\frac{2}{3}} \varepsilon_n}{\left( \sqrt{\frac{2}{3}} \Delta\lambda + \varepsilon_n \right)^2} \left( A_{\infty_{n+1}} - \bar{A}_{\infty_n} \right) + \left( 1 - \frac{\varepsilon_n}{\sqrt{\frac{2}{3}} \Delta\lambda + \varepsilon_n} \right) \frac{\partial A_{\infty_{n+1}}}{\partial \Delta\lambda}, \tag{5.104}$$

where $A_{\infty_{n+1}}$ is given in Eq. (5.84),

$$\frac{\partial A_{\infty_{n+1}}}{\partial \Delta\lambda} = \sqrt{\frac{2}{3}} \frac{\xi_2}{\Delta t} \left( \frac{A^{up}_{\infty} - A^{lwr}_{\infty}}{\dot{\varepsilon}_{up} - \dot{\varepsilon}_{lwr}} \right) \left[ \frac{1}{\Delta t} \left( \frac{\sqrt{\frac{2}{3}} \Delta\lambda - \Delta t \dot{\varepsilon}_{lwr}}{\dot{\varepsilon}_{up} - \dot{\varepsilon}_{lwr}} \right) \right]^{\xi_2 - 1}, \tag{5.105}$$

and

$$\varphi = \exp\left( -\delta_{n+1} \sqrt{\frac{2}{3}} \Delta\lambda \right). \tag{5.106}$$

# 6 NUMERICAL RESULTS

This chapter presents the results obtained by employing the local and global numerical formulation developed earlier. Each simulation performed in this chapter considers the elastic-viscoplastic model developed in this work and the parameters given in Table 4.3, which were obtained for the aluminum AA1050. Simulations are performed in order to numerically explore the constitutive features associated with the present proposal. Furthermore, to assess the numerical performance related to the employed framework, local and global convergence studies are also performed. Convergence criterion is the number of iterations ($n_{iter}$) to reach a *Newton-Raphson* residue $\|\boldsymbol{r}\|_{(\cdot)}$ lower than an admissible error of $e_{tol} = 10^{-6}$. In a local analysis the residue is the *Euclidean* norm ($\|\cdot\|$) of vector $\boldsymbol{f}_{n+1}$, in which corresponding components are equations $f_{n+1_i}$, $i = \{1, 2, ..., 5\}$, given in Appendix B.3. The finite element residue is the infinity norm ($\|\cdot\|_{\infty}$) of the classical vector $\vec{R}_{n+1} = \vec{f}_{int_{n+1}} - \vec{f}_{ext_{n+1}}$, in which $\vec{f}_{ext_{n+1}}$ and $\vec{f}_{int_{n+1}}$ are respectively the external and internal finite element force vectors at $t_{n+1}$ (see Eq. (5.50)).

In order to verify the numerical implementation, numerical solutions associated with simple homogeneous deformation problems are first compared with the analytical solutions previously developed. Evaluation consists of comparing both numerical and analytical flow stress-strain, as well as hardening curves considering distinct strain-rates. In these preliminary simulations, the whole loading-history consists of a constant strain-rate loading followed by a stress relaxation phase.

In a second step of verification procedure, billet upsetting simulations considering frictional contact conditions are also performed. These cases are evaluated in order to assess the overall numerical framework in a non-homogeneously deforming structural problem, and also to discuss on the deformation homogeneity hypothesis, adopted in the analysis of experimental data and in model calibration procedure, when compared with numerical results in which frictional conditions are considered.

## 6.1 Homogeneous deformation simulations

The homogeneous deformation cases considered herein consist of solving the axisymmetric finite element problem showed in Figure (6.1), where the mesh composed by a single 4th-node quadrilateral element and imposed boundary conditions are illustrated. The simulation consists of homogeneously imposing a compressive strain of $E_{11_f} = -0.5$ according to distinct constant strain-rates $\bar{D}_{11} = K < 0$. In this case, the prescribed displacement $\bar{u}(t) \leq 0$ follows the time history given in Eq. (4.6):

$$\bar{u}(t) = l_0 \left[\exp(Kt) - 1\right] \leq 0. \tag{6.1}$$

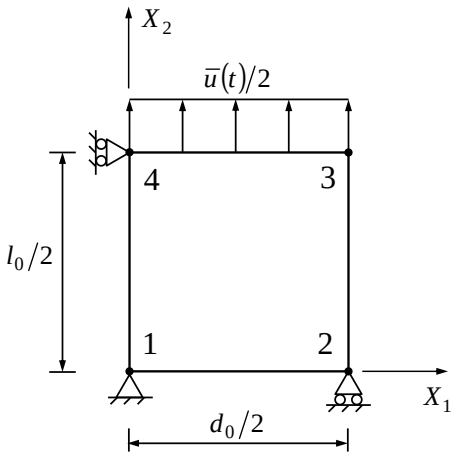


Figure 6.1: Finite element mesh (single 4th-noth quadrilateral element) and boundary conditions considered in homogeneous deformation simulations.

To impose a given strain of $E_{11_f} = -0.5$ at a time $t = t_f$, a total displacement $\bar{u}_f = l_0 \left[\exp\left(E_{11_f}\right) - 1\right] = -2.3608\,\text{mm}$ have to be prescribed at this time. In order to perform subsequent stress relaxation test, the prescribed displacement is then maintained constant for $t \geq t_f$. Accordingly, the overall loading process is defined as follows:

$$\bar{u}(t) = \begin{cases} l_0 \left[\exp(Kt) - 1\right] & 0 \leq t < t_f \\ \bar{u}_f & t_f \leq t < \infty \end{cases}, \tag{6.2}$$

with $\bar{u}_f = l_0 \left[\exp(Kt_f) - 1\right]$. For a constant strain-rate case, final loading time is computed according to $t_f = \frac{E_{11_f}}{K}$. Furthermore, it is possible to show that during the loading phase the prescribed displacement can be described according to the following relation given in terms of the ratio $\frac{t}{t_f}$:

$$\bar{u}(t) = l_0 \left[\left(\frac{\bar{u}_f}{l_0} + 1\right)^{\frac{t}{t_f}} - 1\right], \tag{6.3}$$

satisfying $\bar{u} = 0$ for $\frac{t}{t_f} = 0$, and $\bar{u} = \bar{u}_f$ for $\frac{t}{t_f} = 1$. The numerical simulations consist therefore of incrementally imposing $\bar{u}(t)$ in $N = 20$ subsequent equal time steps following the absolute strain-rates $|K|$ given in Table 6.1, where the time instant $t_f$, the total strain $E_{11_f}$ and related prescribed displacement $\bar{u}_f$, as well as the specimen dimensions, $l_0$ and $d_0$, are summarized.

Simulation results are displayed in Figures 6.2. Figure 6.2(a) compares flow stress-strain numerical results with corresponding analytical solutions obtained from Eq. (4.14). Although good correspondences are verified through the whole compression, slightly higher differences are observed at small strain levels. This is due to significant elastic contribution at the beginning of the deformations, once the elastic behavior is not accounted for in the rigid-viscoplastic analytical solution. Figure 6.2(b) shows the stress

Table 6.1: Parameters used in homogeneous numerical simulations.

| | $\lvert K\rvert$ [$s^{-1}$] | $t_f$ [s] | $E_{11_f}$ | $\bar{u}_f$ [mm] | $l_0$ [mm] | $d_0$ [mm] |
|---|---|---|---|---|---|---|
| Case 01 (Q-S) | $10^{-2}$ | $5 \times 10^{1}$ | $-0.5$ | $-2.36$ | 6.0 | 6.0 |
| Case 02 | $10^{0}$ | $5 \times 10^{-1}$ | $-0.5$ | $-2.36$ | 6.0 | 6.0 |
| Case 03 | $10^{2}$ | $5 \times 10^{-3}$ | $-0.5$ | $-2.36$ | 6.0 | 6.0 |
| Case 04 | $10^{4}$ | $5 \times 10^{-5}$ | $-0.5$ | $-2.36$ | 6.0 | 6.0 |

relaxation behavior associated with the present model. An important result to be highlighted is the fact that, depending on the previous loading-rates, different stress levels are asymptotically reached during the relaxation phase. The higher the loading-rate the higher the equilibrium stress state. This behavior, similar to the sequential strain-rate tests presented in Subsection 2.3.3, illustrates the strain-rate influence on corresponding material hardening response. The latter feature is readily evidenced in Figure 6.2(c), where the strain-rate influence on the hardening variable $A$ is evaluated. However, in contrast to the flow stress, which is instantaneously affected by the current deformation velocity, the hardening behavior does not depend on the instantaneous strain-rate, but on the whole past strain-rate-history. Thus, when the imposed deformation holds constant, the corresponding material hardening does not change during the relaxation phase, see Figure 6.2(d).

In summary, comparison between numerical and analytical results of Figures 6.2(a) and (c) shows the correct numerical implementation considering the present constitutive model. Furthermore, in order to evaluate the corresponding convergence, and how it is influenced by the imposed deformation velocity, local and global convergence analyzes, considering the lowest (Case 01) and the highest (Case 04) loading-rates, are depicted in Figures 6.3. Local analysis shows that by increasing the loading-rate induces a slight increase in the number of iterations needed to achieve the convergence criterion. Considering Case 01, in which a low strain-rate of $10^{-2}\,s^{-1}$ is imposed, 4 iterations were needed to converge in every load step, $\frac{t}{t_f} \in \{0.1, 0.2, 0.5, 1.0\}$. However, in every load steps, Case 04 has achieved convergence in 7 iterations. On the other hand, global analysis does not have demonstrated significant difference between the convergence behavior associated to cases 01 and 04. Considering this simple problem, both cases have reached the convergence criterion in 5 iterations.

## 6.2 Billet upsetting

This section has the goal of evaluating the overall numerical framework considering a more complex problem. Corresponding simulation consists of compressing a cylindrical specimen considering both contact and friction conditions, see Figure 6.4(a). This problem was chosen in order to achieve two main goals. The first one is to employ the present

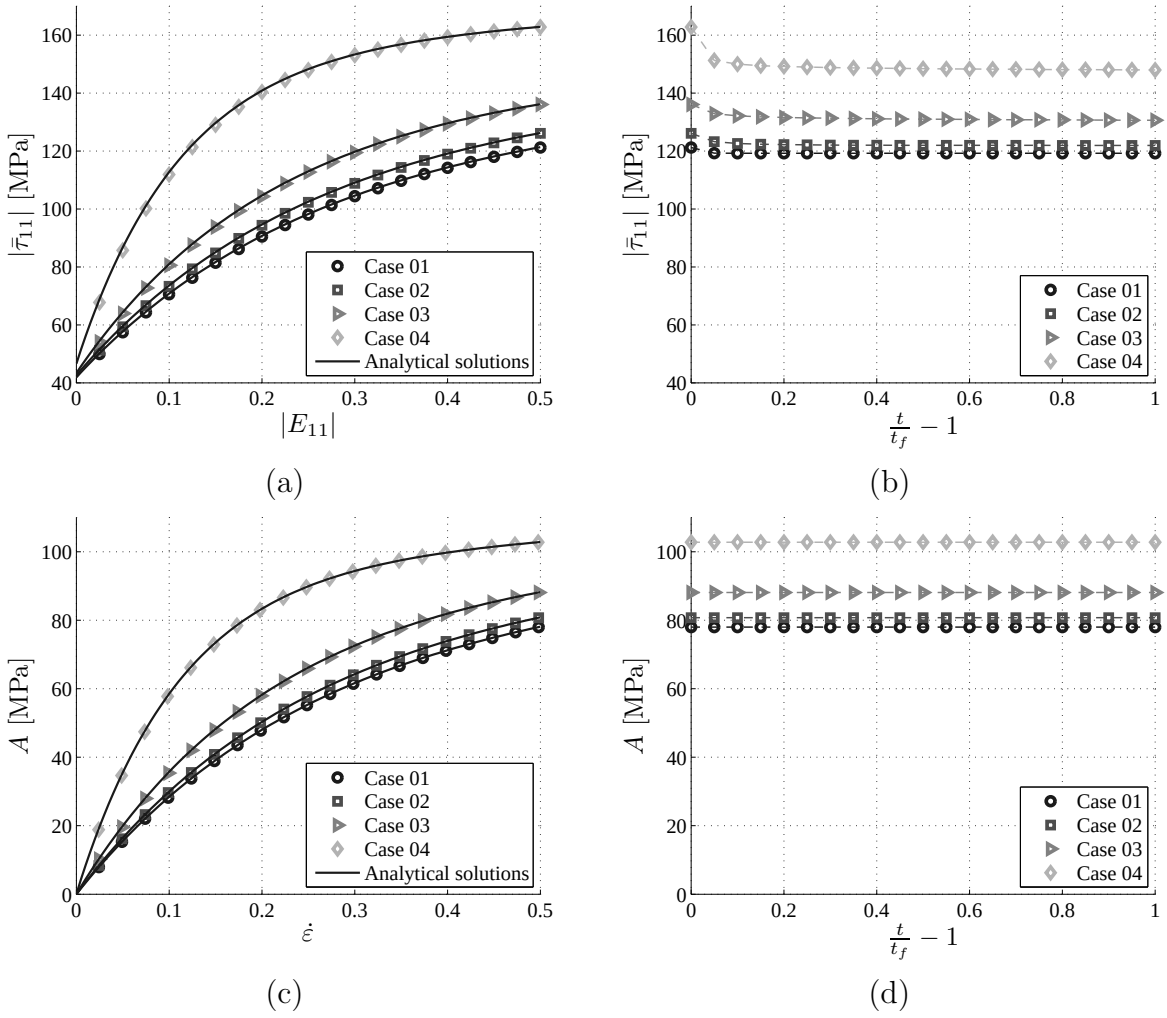


Figure 6.2: (a) Comparison of flow stress-strain numerical results with analytical solution of Eq. (4.14); (b) Stress relaxation numerical curves; (c) Comparison of hardening vs. accumulated viscoplastic strain numerical curves with analytical solution of Eq. (4.13); (d) Material hardening behavior during stress relaxation process.

constitutive procedure in a non-homogeneous deformation process, when there is a non-null friction between specimen and compression platens. The second goal is to evaluate the hypothesis concerning homogeneous deformation conditions adopted to analyze the experimental data and also to adjust the proposed constitutive model. Throughout this section, numerical results are also compared to analytical solutions considering flow stress, Eq. (4.14), and material hardening responses, Eq. (4.13).

Figure 6.4(a) schematically presents the axisymmetric model considered for analysis, where upper and lower gray regions represent rigid platens. The specimen dimensions, $l_0$ and $r_0 = \frac{d_0}{2}$, are the same given in Table 4.3. Due to symmetry conditions, only a quarter of the whole problem is simulated, see Figure 6.4(b). Finite element discretization consists of 1600 6th-node triangular elements (3281 nodes). Material parameters are also those of Table 4.3. The contact formulation is based on the *Signorini* condition and friction is modeled by the regularized *Coulomb* model with a friction coefficient of $f_c = 0.1$ and

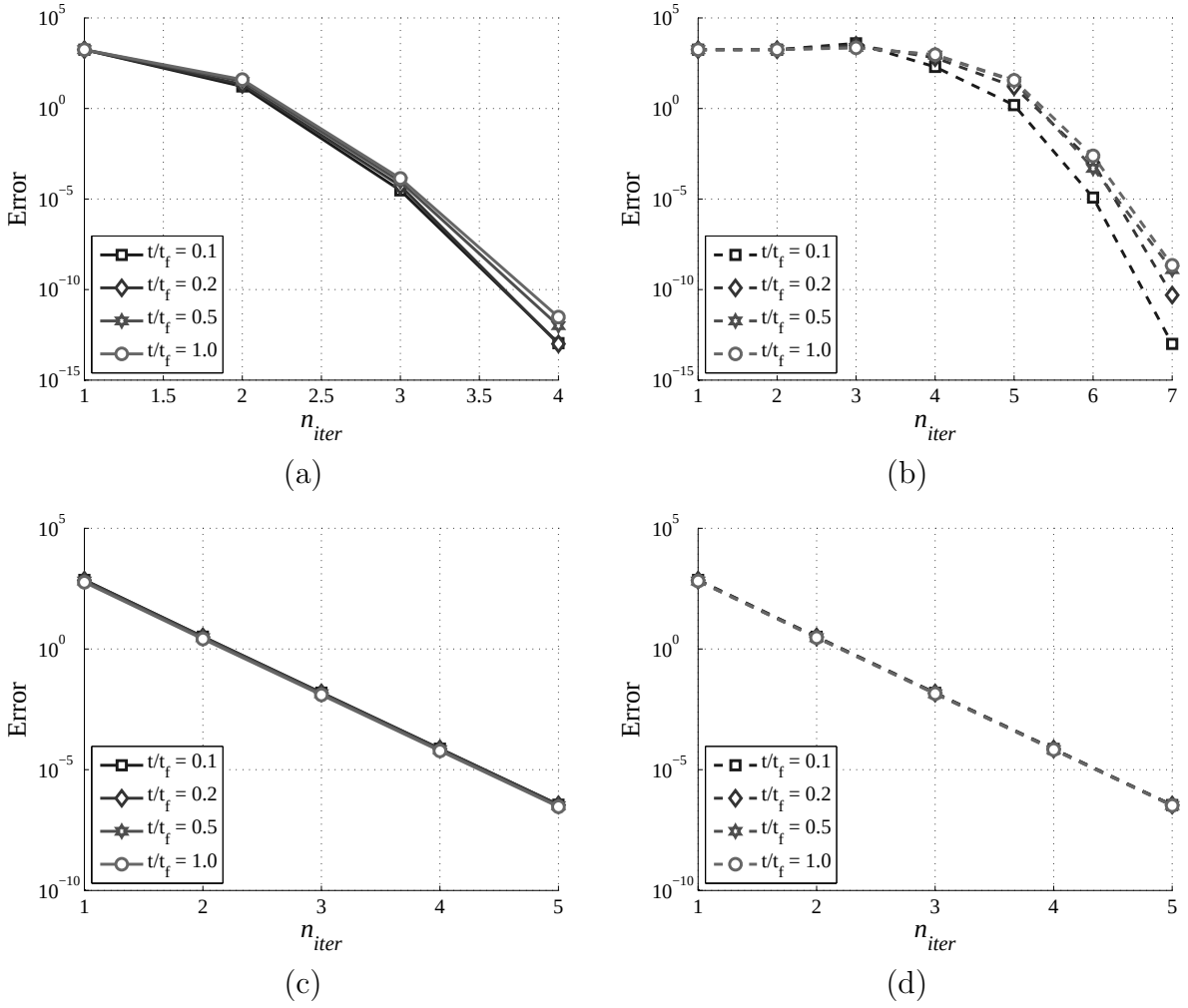


Figure 6.3: Local convergence analyzes considering (a) Case 01 and (b) Case 04. Global convergence analyzes considering (c) Case 01 and (d) Case 04.

regularization parameter $\epsilon_T = 10^{-4}$. The *Augmented Lagrangian* algorithm [Rossi et al., 2008, 2009] is employed to impose the contact, and penalty parameter associated with the impenetrability condition is set as $\epsilon_v = 10^{-7}$. The main focus of the present simulation is to analyze the structural response in frictional compression tests. However, the simulation with $f_c = 0$ shall also be performed and corresponding compression force predictions compared to the frictional response and analytical results. Starting from $\bar{u}\,(t = 0) = 0$, the prescribed displacement is given according to Eq. (6.2), which corresponds in a frictionless problem to a homogeneous axial strain-rate of $\bar{D}_{11} = K < 0$. Loading conditions consider the extreme cases of Table 6.1, namely Case 01 and Case 04. The total prescribed displacement $\bar{u}_f = -2.36\,\text{mm}$ is applied and maintained in 400 equal time steps (200 for loading stage and 200 for stress relaxation phase). Referring to the friction case, the prescribed displacement $\bar{u}_f = -2.36\,\text{mm}$ induces a non-homogeneous strain field $\varepsilon$ in the specimen whose maximum magnitude is in all cases lower than 0.6.

Friction conditions along loaded faces induce a heterogeneous strain field in the spec-

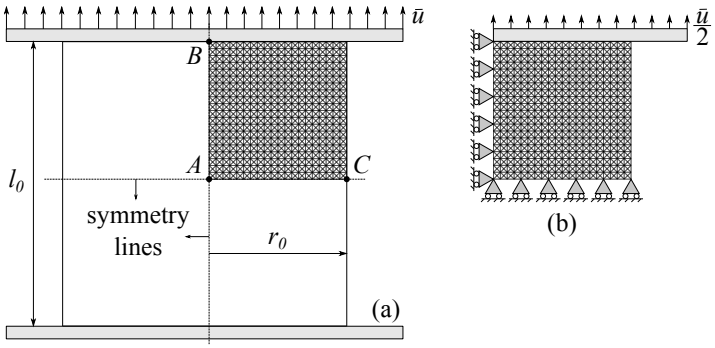


Figure 6.4: (a) Axisymmetric billet upsetting model; (b) Finite element mesh (1600 6th-node triangular elements) and boundary conditions for a quarter of workpiece.

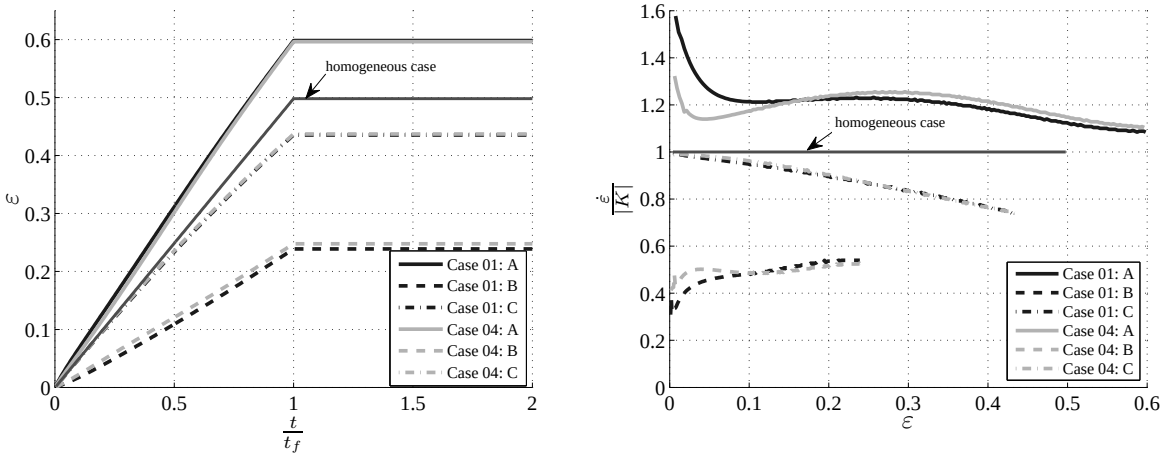


Figure 6.5: Influence of loading-rate on (a) inelastic deformation histories, $\varepsilon$ vs. $\frac{t}{t_f}$, and on (b) inelastic strain-rate vs. accumulated viscoplastic strain curves of points $A$, $B$, and $C$ (friction cases).

imen. This aspect will be characterized considering three distinct points ($A$, $B$, and $C$) of the discretized workpiece, see Figure 6.4(a). The loading-rate influence on axial strain-history of points $A$, $B$, and $C$ is depicted in Figure 6.5(a). The latter figure shows the influence of loading rate parameter $|K|$ on axial strain response vs. normalized time $\frac{t}{t_f}$. Due to friction effects, which restrict the radial displacement at platen-specimen interface, point $B$ undergoes the smallest strain levels (total strain close to 0.25) when compared to points $A$ and $C$. In contrast, the highest strain level is experienced by point $A$ (total strain of $\approx 0.6$). However, none of the evaluated points experiences the strain-history corresponding to a homogeneous (frictionless) compression (total strain of 0.5). While strains imposed on point $A$ are higher than those of homogeneous case, points $B$ and $C$ experience lower strain levels. In addition, one notes that, by increasing the imposed strain-rate, a slight decrease in axial strain of point $A$ is observed, while it induces a small increase in axial strain of $B$ and minor rate effects are observed in point $C$.

Another aspect concerning the heterogeneous compression is the strain-rate-history

experienced by the three points during deformation. Figure 6.5(b) shows evolutions of normalized strain-rate $\frac{\dot{\varepsilon}}{|K|}$ in terms of accumulated viscoplastic strain $\varepsilon$ reached on points $A$, $B$, and $C$, considering cases 01 and 04. These comparisons with the nominal (homogeneous) loading-rate $|K|$ demonstrate that, in a heterogeneous deformation process, strain-rates lower (points $B$ and $C$) and higher (point $A$) than $|K|$ are observed throughout the sample. Furthermore, as large as the imposed strain proceeds, a transient behavior corresponding to the strain-rate-history is evidenced, although this fact is not clear in Figure 6.5(a). For example, point $C$ at the beginning of the compression process experiences a strain-rate very close to the nominal value, and as the strain level increases, the strain-rate related to $C$ decreases. In addition, the results of Figure 6.5(a) are reflecting that no significant difference is observed when comparing responses of $C$ related to cases 01 and 04. In contrast, when compared with Case 01, Case 04 presents lower (resp. higher) values of $\frac{\dot{\varepsilon}}{|K|}$ associated with point $A$ (resp. $B$) at the deformation beginning. However, this behavior changes for strains between 0.1 and 0.2. For both cases 01 and 04, the strain-rate experienced by point $A$ presents a significant fast decrease as the compression is started, followed by a smooth oscillation around 1.2 when the deformation exceeds 0.1. Regarding point $B$, a rapid slight increase in the strain-rate is first induced by the imposed deformation, and parameter $\frac{\dot{\varepsilon}}{|K|}$ tends to values close to 0.5 for strain values greater than 0.1.

As it can be expected, the heterogeneous deformation field imposed on the compressed specimen has a direct consequence on the stress and hardening fields. The axial rotated *Kirchhoff* stress vs. strain curves of points $A$, $B$, and $C$ are displayed in Figures 6.6(a) and (b), respectively for cases 01 and 04. In addition to results obtained from numerical simulations of frictional compressions, these figures also show the the analytical solution of Eq. (4.14) considering parameters of Table 4.3. For both cases 01 and 04, the response of points $A$ and $C$ remains close to corresponding analytical flow stress-strain curves until strain levels between 0.1 and 0.2. Beyond this strain range, the response in friction cases present a major deviation from respective reference situations. In contrast, due to confined strain state, stress triaxiality appears in the vicinity of point $B$ (Figure 6.7(b)) right after the loading process has been started, leading to lower strain and higher axial stress levels than at points $A$ and $C$. This restriction associated with the strain field around point $B$ is clearly evidenced in corresponding strain-history and associated strain-rate-history showed respectively in Figures 6.5(a) and (b).

Comparisons between cases 01 and 04, whose axial rotated *Kirchhoff* stress vs. logarithmic strain curves are shown respectively in Figures 6.6(a) and (b) for frictional compression test, indicate that increasing the value of $|K|$ induces higher absolute stress levels in the specimen. However, as already evidenced in Figure 6.5(a), the maximum strain level slightly decreases with $|K|$ at point $A$, while it exhibits opposite trend at point $B$. No significant rate influence is observed in point $C$.

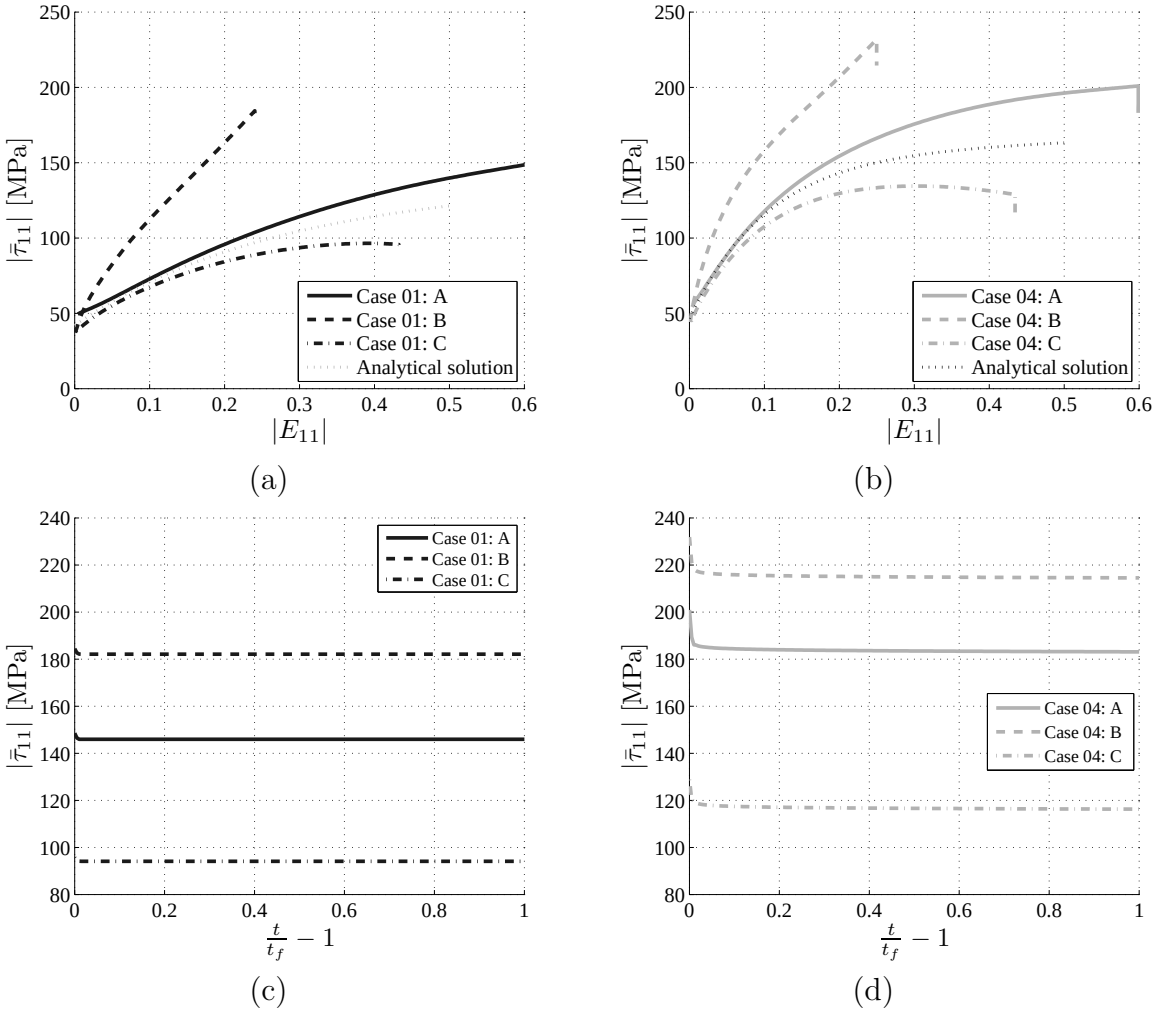


Figure 6.6: Comparison of numerical axial stress vs. strain curves associated with points $A$, $B$, and $C$ with analytical solution of Eq. (4.14): (a) Case 01, $|K| = 10^{-2}\,\mathrm{s}^{-1}$; (b) Case 04, $|K| = 10^{4}\,\mathrm{s}^{-1}$. Stress relaxation curves: (c) Case 01, $|K| = 10^{-2}\,\mathrm{s}^{-1}$; (d) Case 04, $|K| = 10^{4}\,\mathrm{s}^{-1}$. Numerical results consider only frictional simulations.

The analysis performed during loading phase ($t \leq t_f$) suggests that, due to instantaneous material rate-sensitivity, significant effects of strain-rate on flow stress rise at high strain-rates. This feature is also corroborated in the relaxation phase imposed to specimen. Figures 6.6(c) and (d) respectively present the stress relaxation curves of cases 01 and 04, considering points $A$, $B$, and $C$, i.e., evolution of axial rotated *Kirchhoff* stress vs. dimensionless time $\frac{t}{t_f}$. It is observed from these figures that the equilibrium stress state reached after relaxation process is generally sensitive to previous loading-rate. This fact is evidenced when comparing corresponding asymptotic stress states associated with Case 01 and Case 04. As it would be expected, the equilibrium stress reached in Case 04 is always higher than that corresponding to Case 01, thus reflecting the strain-rate influence on observed material hardening behavior.

Stress triaxiality effects associated with points $A$ and $B$ are demonstrated respectively

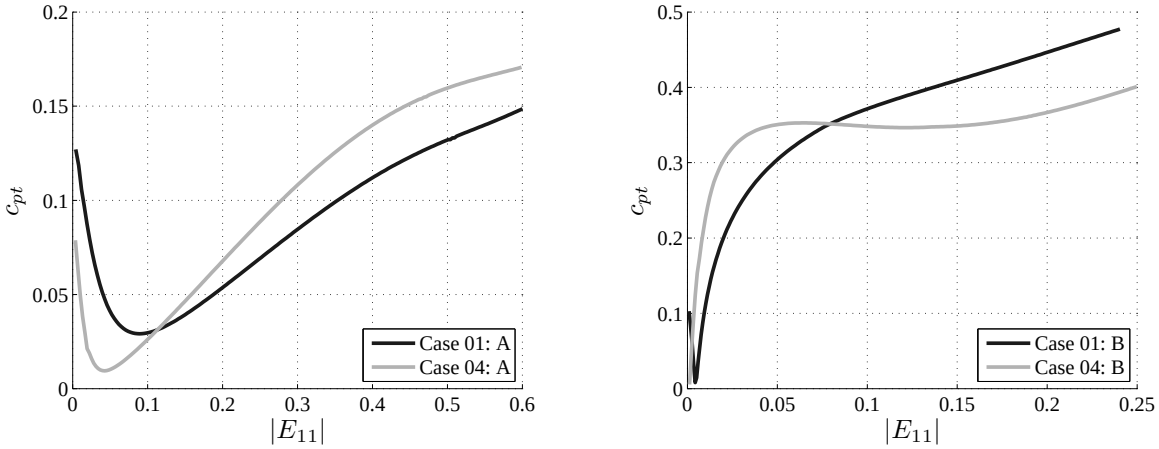


Figure 6.7: Influence of loading-rate parameter $K$ on pressure transmission coefficient $c_{pt} := \frac{\bar{\tau}_{22}}{\bar{\tau}_{11}}$ vs. strain curves (friction cases): (a) Point $A$; (b) Point $B$.

in Figures 6.7(a) and (b), where the pressure transmission coefficients[1] $c_{pt} = \frac{\bar{\tau}_{22}}{\bar{\tau}_{11}}$ at these points are plotted against the absolute axial strain. Scalars $\bar{\tau}_{11}$ and $\bar{\tau}_{22}$ refer to axial and radial rotated *Kirchhoff* stresses, respectively. For strains lower than 0.1, Case 01 presents higher values of $c_{pt}$ in $A$, while opposite trend is observed for strains exceeding this level. This fact can explain a higher deviation from the analytical solution associated with point $A$ of Case 01 at the beginning of loading phase showed in Figure 6.6(a). As the stress triaxiality reduces, the numerical curve approaches the analytical solution for strains near 0.1, and tends to deviate again as the deformation and parameter $c_{pt}$ increases. A similar behavior is observed in Figure 6.6(b) corresponding to point $A$ of Case 04. However, due to small initial stress triaxialities, a lower difference between numerical and analytical curves is evidenced as the loading is started. Furthermore, when the strain level exceeds the value of 0.1, ratio $c_{pt}$ increases and higher deviations from analytical curve are verified. In contrast, for both cases 01 and 04, ratio $c_{pt}$ associated with point $B$ increases rapidly with strain within the small range (until $\approx 0.005$), followed by a moderate smooth increasing with strain level in Case 01, and a smooth oscillation near $c_{pt} = 0.4$ in Case 04, see Figure 6.7(b). Still referring to point $B$, Figure 6.7(b) shows higher values of $c_{pt}$ for Case 04 until strains of $\approx 0.08$, and for deformations higher than this value, Case 01 presents the highest values of ratio $c_{pt}$.

The capability of the proposed constitutive model to capture the effects of strain-rate on flow stress response has been illustrated in Figures 6.6, which indicate that axial stress-strain curves are significantly affected by the value of imposed loading rate $|K|$. As already discussed, the overall stress rate-sensitivity is the result of instantaneous and microstructural rate-effects. The effect of strain-rate on the material hardening response,

[1]It is worth to recall that for axisymmetric deformation the value $c_{pt} = 0$ indicates an axial stress state and $c_{pt} = 1$ a hydrostatic one.

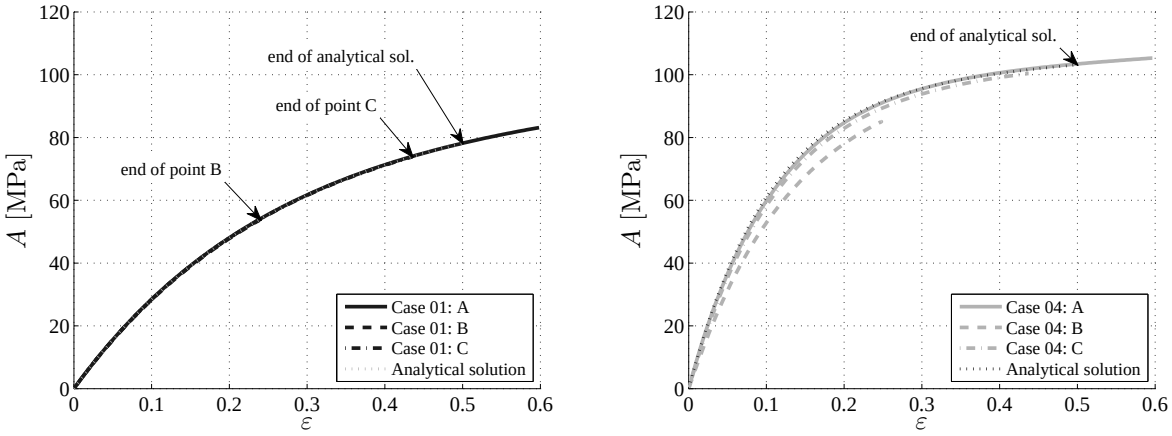


Figure 6.8: Comparison of numerical hardening curves with analytical solution of Eq. (4.13): (a) Case 01, $|K| = 10^{-2}\,\mathrm{s}^{-1}$; (b) Case 04, $|K| = 10^{4}\,\mathrm{s}^{-1}$. Numerical results consider only the frictional simulations.

is demonstrated in Figures 6.8(a) and (b) considering frictional compressions. Comparison between these figures emphasize that, for a given accumulated viscoplastic strain, by increasing the value of $|K|$, a larger material hardening is induced. In addition, Figures 6.8(a) and (b) show the difference between the hardening induced by heterogeneous deformation fields in the distinct points: $A$, $B$, and $C$. Considering Case 01 in Figure 6.8(a), when low loading-rates are imposed, no significant difference is observed between hardening curves associated with points $A$, $B$, and $C$, although the difference in strain levels. In contrast, due to the high strain-rate levels, as a result of the distinct strain-rate-history imposed on each point (Figure 6.5(b)), different hardening curves are obtained for Case 04 in Figure 6.8(b). Due to lower strain-rate levels, point $B$ presents the lowest hardening. In contrast, as higher deformation velocities are imposed on $A$, higher hardening values are observed at this point.

An alternative way to illustrate the strain-rate-history effects on specimen response consists of visualizing the contours of *von Mises* equivalent stress, as displayed in Figures 6.9(a) and (b) respectively for cases 01 and 04. Two particular instants are considered for each case, namely at the onset of stress relaxation ($t = t_f$) and at the relaxed state. As expected, no noticeable change is observed between the "before relaxation" and "after relaxation" states associated with Case 01. In contrast, significant changes between the "before relaxation" and "after relaxation" states are observed for Case 04, in which $|K| = 10^{4}\,\mathrm{s}^{-1}$ was set. On one hand, the significant difference between *von Mises* stress contours, corresponding to the two states showed in Figure 6.9(b), is due to instantaneous viscous effects. On the other hand, as already discussed, no major changes on the hardening contours is observed for both cases 01 and 04, as displayed respectively in Figures 6.9(c) and (d). Furthermore, comparison of all "after relaxation" states indicates that Case 04

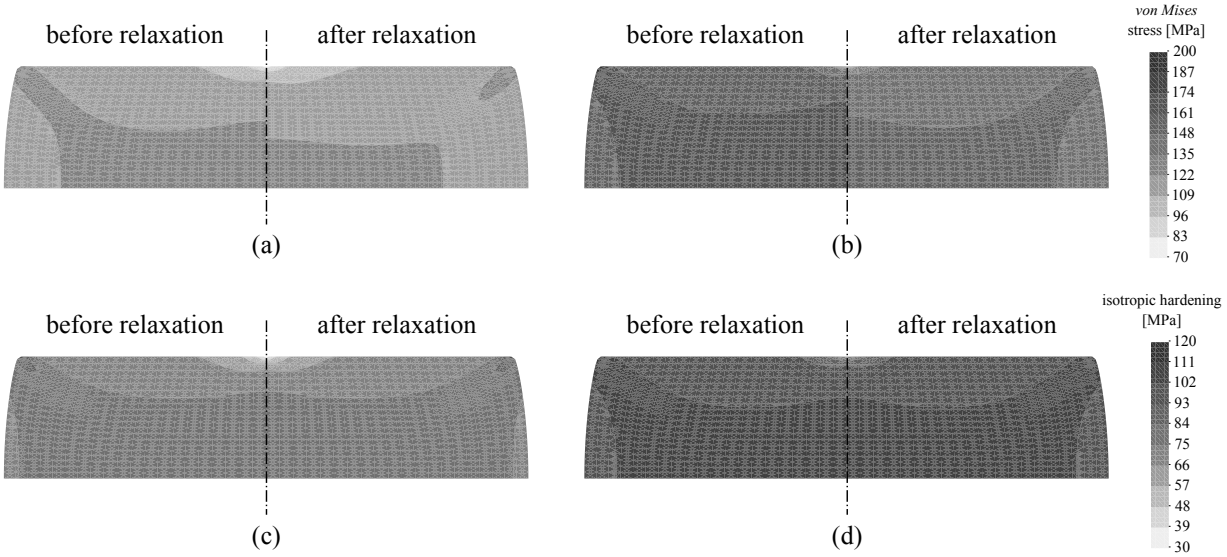


Figure 6.9: Contours of *von Mises* equivalent stress [MPa], before stress relaxation $\left(\frac{t}{t_f} = 1\right)$ and after stress relaxation: (a) Case 01, $|K| = 10^{-2}\,\mathrm{s}^{-1}$; (b) Case 04, $|K| = 10^{4}\,\mathrm{s}^{-1}$. Contours of isotropic hardening $A$ [MPa], before stress relaxation $\left(\frac{t}{t_f} = 1\right)$ and after stress relaxation: (c) Case 01, $|K| = 10^{-2}\,\mathrm{s}^{-1}$; (d) Case 04, $|K| = 10^{4}\,\mathrm{s}^{-1}$.

relaxes to a state far from that of Case 04, that is, higher values of $|K|$ leads to higher *von Mises* stress and hardening fields.

Based upon the preceding results and discussions, one has to keep in mind the real heterogeneity induced by frictional contact effects when adopting the homogeneous deformation hypothesis. Throughout the body deformed under friction conditions, points experiencing lower and higher stress levels, when compared with the idealized homogeneous case, are evidenced. However, overall result of this compression simulation presenting heterogeneous stress and strain fields is the force-displacement response. The difference of considering or not frictional effects on the overall behavior of the structure may be characterized by means of the evolution of resultant vertical force applied to specimen with respect to prescribed displacement. Figure 6.10(a) compares both frictional and frictionless results obtained from numerical simulations with analytical solution corresponding to a homogeneous compression, which is obtained from stress solution of Eq. (4.14):

$$|f_1| = \frac{V_0}{l}\,|\bar{\tau}_{11}|\,, \tag{6.4}$$

where $|f_1|$ is the resultant compression force, $V_0$ is the initial specimen volume and $l$ is the current length of workpiece. While the numerical frictionless results are very close to the analytical solutions, slight friction effects are observed when prescribed displacement increases. It is emphasized that the whole results should be interpreted keeping in mind that the considered value of friction coefficient is rather small ($f_c = 0.1$). This fact em-

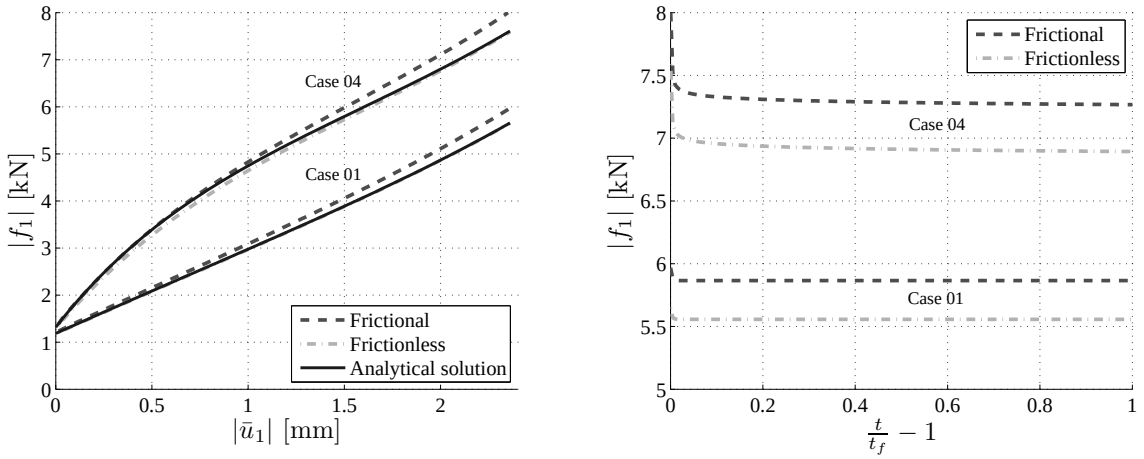


Figure 6.10: (a) Comparison of numerical compression forces with analytical solution of Eq. (6.4); (b) Numerical force relaxation curves. Numerical results concern both frictional and frictionless simulations, considering loading data of Case 01 and Case 04 of Table 6.1.

phasizes the importance of using lubricant in platen-specimen interfaces. Regarding the influence of loading-rate parameter $|K|$, Figure 6.10(a) demonstrate that, in addition to inducing higher compression forces to impose a given displacement, increasing the loading rate $|K|$ increases the difference between homogeneous (frictionless) and heterogeneous (frictional) deformation curves. Although there are differences between the frictional and frictionless responses, they are not higher than 5%.

Since the prescribed displacement holds constant after the desired compression is reached, a force relaxation is expected for $\frac{t}{t_f} \geq 1$. Results considering cases 01 and 04, with and without friction, are displayed in Figure 6.10(b). Based on these results, one can clearly observe that, even after the relaxation phase, the frictional cases present residual forces when compared with frictionless simulations. While Case 01 does not present a significant force relaxation (for both $f_c = 0.1$ and $f_c = 0$), results corresponding to Case 04 present a significant load reduction while the prescribed displacement is maintained constant. Observed force reduction is due to instantaneous viscous effects induced by high deformation velocities imposed during the loading step. Furthermore, in addition to instantaneous rate effects, Figure 6.10(b) also demonstrates effects associated with strain-rate-hardening behavior. These effects become clear by noting that the asymptotic load response related to Case 04 does not recover the respective curve corresponding to Case 01.

The performance of numerical procedure is assessed by means of convergence analyzes in both Case 01 and Case 04. The results are summarized in Table 6.2 for $\frac{t}{t_f} \in \{0.005, 0.2, 0.5, 1.0\}$ considering frictionless ($f_c = 0$) and frictional ($f_c = 0.1$) compressions. In this table term $AL_i$ stands for the number of iterations to reach convergence

Table 6.2: Number of iterations required for convergence of frictionless and frictional contact algorithm.

| $\frac{t}{t_f}$ - (step number) | $AL_i$ | Case 01 | | Case 04 | |
|---|---|---|---|---|---|
| | | $n_{iter}$ | | $n_{iter}$ | |
| | | $f_c = 0$ | $f_c = 0.1$ | $f_c = 0$ | $f_c = 0.1$ |
| 0.005 - (1) | 1 | 5 | 10 | 5 | 7 |
| | 2 | 3 | 6 | 3 | 5 |
| | 3 | – | 3 | – | 3 |
| 0.2 - (40) | 1 | 4 | 6 | 5 | 5 |
| 0.5 - (100) | 1 | 5 | 7 | 5 | 6 |
| 1.0 - (200) | 1 | 5 | 11 | 4 | 8 |
| | 2 | – | 8 | – | 6 |

in the *Augmented Lagrangian* algorithm employed to solve contact problem [Rossi et al., 2008, 2009] and $n_{iter}$ for the number of iterations to reach finite element equilibrium $\left(\left\|\vec{R}_{n+1}\right\|_\infty \leq 10^{-6}\right)$, see Eq. (5.50). The end of loading phase ($t = t_f$) in Case 01 corresponds to the higher number of iterations required for numerical convergence ($n_{iter} = 11$). Table 6.2 also indicates that convergence is enhanced with higher loading rate $|K|$.

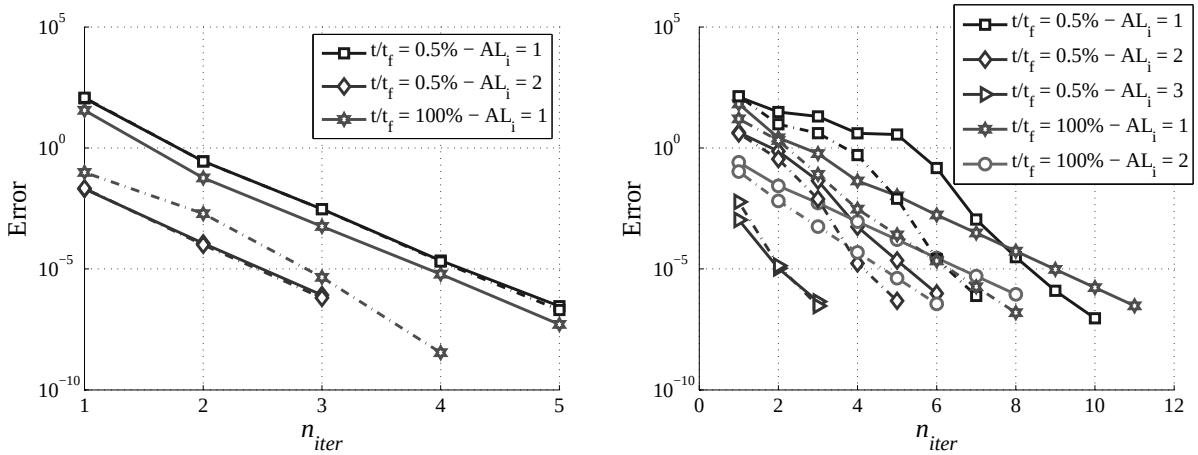


Figure 6.11: Convergence curves for Case 01 (solid lines) and Case 04 (dash-doted lines): (a) Frictionless compression; (b) Frictional compression.

Convergence curves are displayed in Figures 6.11(a) and (b) for simulations considering smooth and frictional contact in the low (Case 01) and high (Case 04) strain-rate conditions. Two particular instants were examined, namely $\frac{t}{t_f} = 0.005$ and $\frac{t}{t_f} = 1.0$. Figure 6.11(a) shows that there is no significant difference between Case 01 and Case 04 for frictionless compression simulations. On the other hand, it is observed in Figure 6.11(b) that the convergence is improved when imposing a higher strain-rate in the case of frictional compression test. As a matter of fact, the number of iterations for convergence drops from 10 (11) to 7 (8) at instant $\frac{t}{t_f} = 0.005$ $\left(\frac{t}{t_f} = 1.0\right)$ and iteration $AL_i = 1$ of *Aug-*

*mented Lagrangian* algorithm. Furthermore, the results for frictional simulations shown in Figure 6.11(b) indicate that both cases 01 and 04 present a varying convergence-rate at the beginning of deformation $\left(\frac{t}{t_f} = 0.005\right)$, while for the other time steps a *quasi*-constant convergence-rate is observed.

# 7 CONCLUSIONS

The present work has been devoted to the experimental and constitutive characterization of the mechanical behavior of polycrystalline FCC metals when subjected to high strain-rate finite deformations. As an specific case of study, experimental characterization was conducted by means of compression and microhardness tests on samples of aluminum AA1050. During compressions, work pieces were subjected to finite strains covering a wide strain-rate range: from *quasi*-static to high strain-rate ($\dot{\varepsilon} \approx 10^4\,\mathrm{s}^{-1}$) conditions. From specific constant strain-rate experiments, complying with a primary objective, the main constitutive features associated with the high strain-rate cold deformation of polycrystalline FCC metals were evidenced: (i) strain-hardening; (ii) strain-rate-hardening; and (iii) instantaneous rate-sensitivity. Strain-rate-history effects on material hardening and material hardness evolution were evidenced by means of sequential strain-rate experiments. Based on obtained experimental results, as well as on micro and macroscopic experiments available in the literature, an isothermal semi-physical elastic-viscoplastic model was proposed. Constitutive formulation was carried out within a finite strain framework, and proposed model was intended to represent the constitutive features cited above. Furthermore, an alternative model describing the material hardness evolution in terms of strain and strain-rate histories was also provided. Taking advantage of the experimental data for aluminum AA1050, proposed models were adjusted and then validated. Regarding the general validation of the constitutive modeling at material level, both stress and hardness predictions have presented reasonable agreement with experimental results. At the structural level, corresponding global and local stress-strain numerical formulations were developed within the finite element framework. The constitutive ability and accuracy of numerical procedures were assessed by simulating a homogeneous deformation compression as well as a frictional billet upsetting. Numerical results have demonstrated the ability of the constitutive modeling to appropriately capturing the main features of FCC metals in structural analysis. Furthermore, numerical efficiency and robustness associated with the employed numerical procedures were assessed by means of local and global convergence analyses. From a general view point, the main contribution of the present work is the experimental characterization, mathematical constitutive formulation at finite strain, and associated finite element implementation with account for high strain-rate effects. In this respect, an isothermal simplified constitutive proposal, presenting considerable constitutive capabilities for solving engineering problems considering high strain-rate loadings, was provided.

Based on experimental results obtained at the material level, one can realize the strain-rate-dependent material behavior observed at different strain-rate levels. A rather significant hardening rate-sensitivity was evidenced when comparing low and high strain-rate

responses, in the sense that, for a given strain level, by increasing the corresponding strain-rate higher stress hardening are reached. Furthermore, a pronounced flow stress increasing is observed when strain-rates exceeding $10^3\,s^{-1}$ are imposed. From these observations, one readily finds the importance of accounting for both hardening and flow stress rate-dependences. For example, supposing that a constitutive model not accounting for strain-rate-induced hardening have been adjusted by using low to moderate strain-rate experiments for a given metal. If the adjusted model is employed to simulate the corresponding material behavior under high strain-rate conditions, it will underestimate the material hardening promoted by the high velocity plastic deformation imposed. In addition, the flow stress will also be underestimated if the model does not account for strain-rate-sensitivity changes according to imposed strain-rate range, since the calibration procedure was performed considering low to moderate strain-rate experimental results. Each one of preceding constitutive deficiencies will result in drawbacks associated with the overall structural response. Reasoning on a mechanical component which is processed according to a high velocity manufacturing process (such as machining, rolling, forging, or compaction). If the strain-rate material hardening is not accounted for, the mechanical strength associated with the processed component will be underestimated. Consequently, based on the predicted material strength, on one hand an over-sized component will be designed for further engineering application. On the other hand, the machine and tools will be undersized for processing the component in question.

In view of the aforementioned high strain-rate effects, one realizes practical cases in which the constitutive model proposed in this work has direct applicability. Since, in addition to account for both rate-dependences associated with hardening and flow stress responses, it has a simplified character towards simpler numerical implementation and numerical efficiency. Another aspect favoring the utilization of the proposed model concerns the easier model calibration performed in subsequent steps. In contrast, the isothermal approach followed by the present development restricts the continuously imposed strain level when working at high strain-rate situations, since adiabatic thermal effects are not accounted for by the present model. Other limitation associated with the formulation developed in this work, concern the hypotheses on permanent elastic and plastic isotropy. This features, mainly the plastic one, will results in prediction drawbacks if one wish to apply the model for describing plastic process in which strain path changes or reversal loadings are present.

Concerning future studies on the present subject, at the structural level, straightforward continuation of the present work is the global formulation and associated numerical implementation accounting for inertial effects. In addition, reasoning on advancing the present constitutive modeling, thus reducing its limitations, the results that have been obtained motivate future developments including: (i) thermo-mechanical coupling, which is expected to enhance the rate-effects on viscoplastic deformations and to allow for large

strain, high strain-rate predictions, and (ii) formulation of micromechanically-based models accounting for microstructural mechanisms responsible for the overall macroscopic response, such as the plastically-induced crystallographic texture and anisotropy.

## BIBLIOGRAPHIC REFERENCES

Alfano, G.; Angelis, F. D.; Rosati, L. General solution procedures in elasto/viscoplasticity. **Computer Methods in Applied Mechanics and Engineering**, v. 190, p. 5123–5147, 2001.

Anand, L. Constitutive equations for hot-working of metals. **International Journal of Plasticity**, v. 1, p. 213–231, 1985.

Andrade-Campos, A.; Menezes, L. F.; Teixeira-Dias, F. Large deformation processes on aa1050-o aluminium at elevated temperatures. In **Advanced Materials Forum II**, v. 455 of **Materials Science Forum**, p. 723–727. Trans Tech Publications, 5 2004.

Argon, A. **Strengthening Mechanisms in Crystal Plasticity**. Oxford Series on Materials Modelling. OUP Oxford, 2012.

Argon, A.; Haasen, P. A new mechanism of work hardening in the late stages of large strain plastic flow in F.C.C. and diamond cubic crystals. **Acta Metallurgica et Materialia**, v. 41, p. 3289–3306, 1993.

Arias, Á.; López-Puente, J.; Loya, J. A.; Varas, D.; Zaera, R. **Constitutive Relations under Impact Loadings: Experiments, Theoretical and Numerical Aspects**, chapter Analysis of high-speed impact problems in the aircraft industry, p. 137–207. Springer Vienna, Vienna, 2014.

Armstrong, R.; Arnold, W.; Zerilli, F. Dislocation mechanics of shock-induced plasticity. **Metallurgical and Materials Transactions A**, v. 38, p. 2605–2610, 2007.

Asaro, R. J. Micromechanics of crystals and polycrystals. v. 23 of **Advances in Applied Mechanics**, p. 1–115. Elsevier, 1983.

Baig, M.; Khan, A. S.; Choi, S.-H.; Jeong, A. Shear and multiaxial responses of oxygen free high conductivity OFHC copper over wide range of strain-rates and temperatures and constitutive modeling. **International Journal of Plasticity**, v. 40, p. 65–80, 2013.

Bailey, R. Note on the softening of strain hardened metals and its relation to creep. **J. Inst. Metals**, v. 25, p. 27, 1926.

Bamman, D. J.; Chiesa, M. L.; Johnson, G. C. Modeling large deformation and failure in manufacturing process. In T. Tatsumi, E. W.; Kambe, T., editors, **Theoretical and Applied Mechanics**, p. 359–376, 1996.

Barlat, F. Crystallographic texture, anisotropic yield surfaces and forming limits of sheet metals. **Materials Science and Engineering**, v. 91, p. 55–72, 1987.

Barlat, F.; Duarte, J. F.; Gracio, J.; Lopes, A.; Rauch, E. Plastic flow for non-monotonic loading conditions of an aluminum alloy sheet sample. **International Journal of Plasticity**, v. 19, p. 1215–1244, 2003.

Barlat, F.; Vincze, G.; Grácio, J.; Lee, M.-G.; Rauch, E.; Tomé, C. Enhancements of homogenous anisotropic hardening model and application to mild and dual-phase steels. **International Journal of Plasticity**, v. 58, p. 201 – 218, 2014.

Bataille, J.; Kestin, J. General Forms of the Dissipation Inequality. **Journal of Non Equilibrium Thermodynamics**, v. 1, p. 25–32, 1976.

Bataille, J.; Kestin, J. Irreversible Processes and Physical Interpretation of Rational Thermodynamics. **Journal of Non Equilibrium Thermodynamics**, v. 4, p. 229–258, 1979.

Bay, B.; Hansen, N.; Kuhlmann-Wilsdorf, D. Microstructural evolution in rolled aluminium. **Materials Science and Engineering: A**, v. 158, p. 139–146, 1992.

Belytschko, T.; Liu, W. K.; Moran, B. **Nonlinear finite elements for continua and structures**. Wiley, 2000.

Beyerlein, I. J.; Tomé, C. N. Modeling transients in the mechanical response of copper due to strain path changes. **International Journal of Plasticity**, v. 23, p. 640–664, 2007.

Bhattacharyya, A.; Rittel, D.; Ravichandran, G. Effect of strain rate on deformation texture in OFHC copper. **Scripta Materialia**, v. 52, p. 657–661, 2005.

Bodelot, L.; Escobedo-Diaz, J. P.; Trujillo, C. P.; Martinez, D. T.; Cerreta, E. K.; Gray III, G. T.; Ravichandran, G. Microstructural changes and in-situ observation of localization in OFHC copper under dynamic loading. **International Journal of Plasticity**, v. 74, p. 58–74, 2015.

Bodner, S. R.; Partom, Y. Constitutive Equations for Elastic-Viscoplastic Strain-Hardening Materials. **Journal of Applied Mechanics**, v. 42, p. 385, 1975.

Bodner, S. R.; Rubin, M. B. Modeling of hardening at very high strain rates. **Journal of Applied Physics**, v. 76, p. 2742–2747, 1994.

Bonet, J.; Wood, R. **Nonlinear Continuum Mechanics for Finite Element Analysis**. Cambridge University Press, 1997.

Borodin, E.; Mayer, A.; Petrov, Y.; Gruzdkov, A. Maximum yield strength under quasi-static and high-rate plastic deformation of metals. **Physics of the Solid State**, v. 56, p. 2470–2479, 2014.

Brown, S. B.; Kim, K. H.; Anand, L. An internal variable constitutive model for hot working of metals. **International Journal of Plasticity**, v. 5, p. 95–130, 1989.

Brünig, M.; Driemeier, L. Numerical simulation of taylor impact tests. **International Journal of Plasticity**, v. 23, p. 1979–2003, 2007.

Busby, J. T.; Hash, M. C.; Was, G. S. The relationship between hardness and yield stress in irradiated austenitic and ferritic steels. **Journal of Nuclear Materials**, v. 336, p. 267 – 278, 2005.

Cáceres, C.; Griffiths, J.; Pakdel, A.; Davidson, C. Microhardness mapping and the hardness-yield strength relationship in high-pressure diecast magnesium alloy AZ91. **Materials Science and Engineering: A**, v. 402, p. 258 – 268, 2005.

Campbell, J. **Dynamic Plasticity of Metals: Course Held at the Department for Mechanics of Deformable Bodies, July 1970**. CISM International Centre for Mechanical Sciences. Springer Vienna, 1972.

Chaboche, J. L. Constitutive equations for cyclic plasticity and cyclic viscoplasticity. **International Journal of Plasticity**, v. 5, p. 247–302, 1989.

Chaboche, J. L. A review of some plasticity and viscoplasticity constitutive theories. **International Journal of Plasticity**, v. 24, p. 1642–1693, 2008.

Cheval, F.; Priester, L. Effect of strain rate on the dislocation substructure in deformed copper polycrystals. **Scripta Metallurgica**, v. 23, p. 1871–1876, 1989.

Chiem, C.; Duffy, J. Strain rate history effects and observations of dislocation substructure in aluminum single crystals following dynamic deformation. **Materials Science and Engineering**, v. 57, p. 233–247, 1983.

Ciarlet, P. **Three-Dimensional Elasticity**. Number v. 1 in Studies in mathematics and its applications. Elsevier Science, 1988.

Coleman, B. D.; Gurtin, M. E. Thermodynamics with Internal State Variables. **Reports on Progress in Physics**, v. 47, p. 597–613, 1967.

de Angelis, F. An internal variable variational formulation of viscoplasticity. **Computer Methods in Applied Mechanics and Engineering**, v. 190, p. 35–54, 2000.

de Souza Neto, E. A.; Perić, D.; Owen, D. R. J. **Computational Methods for Plasticity: Theory and Applications**. John Wiley & Sons, 2008.

Dhatt, G.; Touzot, G. **The finite element method displayed**. (A Wiley-Interscience publication). Wiley, 1984.

Dieter, G. **Mechanical metallurgy**. McGraw-Hill series in materials science and engineering. McGraw-Hill, 1986.

Dirras, G.; Chauveau, T.; Abdul-Latif, A.; Ramtani, S.; Bui, Q.-H. Microstructure characterization of high-purity aluminum processed by dynamic severe plastic deformation. **physica status solidi (a)**, v. 207, p. 2233–2237, 2010.

dos Santos, T. **Implementação e avaliação de modelos constitutivos viscoplásticos em pequenas e grandes deformações utilizando o MEF**. Master's thesis, Universidade Federal do Rio Grande do Sul, Brasil, 2012.

dos Santos, T.; Alves, M. K.; Rossi, R. A constitutive formulation and numerical procedure to model rate effects on porous materials at finite strains. **International Journal of Mechanical Sciences**, v. 93, p. 166–180, 2015a.

dos Santos, T.; Ramos, G. R.; Rossi, R. A note on overstress and overthermodynamic forces derivation for elasto-viscoplastic media: Thermodynamic analysis of an isothermal relaxation process. **International Journal of Engineering Science**, v. 93, p. 13–30, 2015b.

dos Santos, T.; Rosa, P. A.; Maghous, S.; Rossi, R. A simplified approach to high strain rate effects in cold deformation of polycrystalline FCC metals: Constitutive formulation and model calibration. **International Journal of Plasticity**, v. 82, p. 76–96, 2016.

Duffy, J. Strain rate history effects and dislocation substructure at high strain rates. In Mescall, J.; Weiss, V., editors, **Material Behavior Under High Stress and Ultrahigh Loading Rates**, v. 29 of **Sagamore Army Materials Research Conference Proceedings**, p. 21–37. Springer US, 1983.

Duvaut, G.; Lions, J. **Inequalities in mechanics and physics**. Grundlehren der mathematischen Wissenschaften. Springer-Verlag, 1976.

Dym, C.; Shames, I. **Solid mechanics: a variational approach**. Advanced engineering series. McGraw-Hill, 1973.

Erlich, D. C.; Shockey, D. A.; Seaman, L. Symmetric rod impact technique for dynamic yield determination. In **American Institute of Physics Conference Series**, v. 78 of **American Institute of Physics Conference Series**, p. 402–406, April 1982.

Estrin, Y.; Mecking, H. A unified phenomenological description of work hardening and creep based on one-parameter models. **Acta Metallurgica**, v. 32, p. 57–70, 1984.

Estrin, Y.; Mecking, H. An extension of the bodner-partom model of plastic deformation. **International Journal of Plasticity**, v. 2, p. 73–85, 1986.

Eterovic, A. L.; Bathe, K.-J. A hyperelastic-based large strain elasto-plastic constitutive formulation with combined isotropic-kinematic hardening using the logarithmic stress and strain measures. **International Journal for Numerical Methods in Engineering**, v. 30, p. 1099–1114, 1990.

Eve, R. A.; Gültop, T.; Reddy, B. D. An internal variable finite strain theory of elastoplasticity within the framework of convex analysis. **Quarterly of Applied Mathematics**, v. 48, p. 625–643, 1990a.

Eve, R. A.; Reddy, B. D.; Rockafellar, R. T. An internal variable theory of elastoplasticity based on the maximum plastic work inequality. **Quarterly of Applied Mathematics**, v. 48, p. 59–83, 1990b.

Fajoui, J.; Gloaguen, D.; Courant, B.; Guillén, R. Micromechanical modelling of the elastoplastic behaviour of metallic material under strain-path changes. **Computational Mechanics**, v. 44, p. 285–296, 2009.

Farbaniec, L.; Abdul-Latif, A.; Gubicza, J.; Dirras, G. High purity ultrafine-grained nickel processed by dynamic plastic deformation: Microstructure and mechanical properties. **Advanced Engineering Materials**, v. 14, p. 1027–1033, 2012.

Follansbee, P. S. 24 - high strain rate deformation of fcc metals and alloys. In Murr, L. E.; Staudhammer, K. P.; ; Meyers, M. A., editors, **Metallurgical Applications of Shock-Wave and High-Strain Rate Phenomena**, p. 451–479. Marcel Dekker Inc., New York, 1986.

Follansbee, P.; Gray III, G. Dynamic deformation of shock prestrained copper. **Materials Science and Engineering: A**, v. 138, p. 23–31, 1991.

Follansbee, P.; Kocks, U. A constitutive description of the deformation of copper based on the use of the mechanical threshold stress as an internal state variable. **Acta Metallurgica**, v. 36, p. 81–93, 1988.

François, D.; Pineau, A.; Zaoui, A. **Mechanical Behaviour of Materials: Volume 1: Micro- and Macroscopic Constitutive Behaviour**. Mechanical Behaviour of Materials. Springer, 2012.

Gao, C.; Zhang, L. Constitutive modelling of plasticity of fcc metals under extremely high strain rates. **International Journal of Plasticity**, v. 32-33, p. 121–133, 2012.

Gao, X.-L.; Jing, X.; Subhash, G. Two new expanding cavity models for indentation deformations of elastic strain-hardening materials. **International Journal of Solids and Structures**, v. 43, p. 2193 – 2208, 2006.

Gazder, A. A.; Cao, W.; Davies, C. H.; Pereloma, E. V. An EBSD investigation of interstitial-free steel subjected to equal channel angular extrusion. **Materials Science and Engineering: A**, v. 497, p. 341–352, 2008.

Geier, M.; José, M.; Rossi, R.; Rosa, P.; Martins, P. Interference-fit joining of aluminium tubes by electromagnetic forming. **Advanced Materials Research**, v. 853, p. 488–493, 2014.

Germain, P.; Son Nguyen, Q.; Suquet, P. Continuum thermodynamics. **Journal of Applied Mechanics**, v. 50, p. 1010–1020, 1983.

Godfrey, A.; Cao, W. Q.; Liu, Q.; Hansen, N. Stored energy, microstructure, and flow stress of deformed metals. **Metallurgical and Materials Transactions A**, v. 36, p. 2371–2378, 2005.

Gurtin, M. E. **An Introduction to Continuum Mechanics**. Mathematics in Science and Engineering. Academic Press, 1981.

Gurtin, M.; Fried, E.; Anand, L. **The Mechanics and Thermodynamics of Continua**. The Mechanics and Thermodynamics of Continua. Cambridge University Press, 2010.

Hall, E. O. The deformation and ageing of mild steel: Iii discussion of results. **Proceedings of the Physical Society. Section B**, v. 64, p. 747, 1951.

Halphen, B.; Son Nguyen, Q. Sur les matériaux standard généralisés. **Journal de Mécanique**, v. 14, p. 39–63, 1975.

Hansen, N.; Barlow, C. 17 - plastic deformation of metals and alloys. In Hono, D. E. L., editor, **Physical Metallurgy (Fifth Edition)**, p. 1681–1764. Elsevier, Oxford, fifth edition edition, 2014.

Hansen, N. Hall-petch relation and boundary strengthening. **Scripta Materialia**, v. 51, p. 801–806, 2004.

Hansen, N.; Mehl, R.; Medalist, A. New discoveries in deformed metals. **Metallurgical and Materials Transactions A**, v. 32, p. 2917–2935, 2001.

Haupt, P. **Continuum mechanics and theory of materials**. Advanced texts in physics. Springer, 2000.

Haupt, P.; Lion, A. Experimental identification and mathematical modeling of viscoplastic material behavior. **Continuum Mechanics and Thermodynamics**, v. 7, p. 73–96, 1995.

Hill, R. A theory of the yielding and plastic flow of anisotropic metals. **Proceedings of the Royal Society of London A: Mathematical, Physical and Engineering Sciences**, v. 193, p. 281–297, 1948.

Hill, R. Theoretical plasticity of textured aggregates. **Mathematical Proceedings of the Cambridge Philosophical Society**, v. 85, p. 179, 1979a.

Hill, R. Aspects of invariance in solid mechanics. v. 18 of **Advances in Applied Mechanics**, p. 1–75. Elsevier, 1979b.

Hopkinson, B. **A Method of Measuring the Pressure Produced in the Detonation of High Explosives Or by the Impact of Bullets**. Philos. trans. 1914.

Horstemeyer, M. F.; Bammann, D. J. Historical review of internal state variable theory for inelasticity. **International Journal of Plasticity**, v. 26, p. 1310–1334, 2010.

Huang, F.; Tao, N. Effects of strain rate and deformation temperature on microstructures and hardness in plastically deformed pure aluminum. **Journal of Materials Science & Technology**, v. 27, p. 1–7, 2011.

Huang, M.; del Castillo, P. E. R.-D.; Bouaziz, O.; van der Zwaag, S. A constitutive model for high strain rate deformation in FCC metals based on irreversible thermodynamics. **Mechanics of Materials**, v. 41, p. 982–988, 2009.

Hughes, D. Microstructure evolution, slip patterns and flow stress. **Materials Science and Engineering: A**, v. 319-321, p. 46–54, 2001.

Hughes, D.; Hansen, N. Microstructure and strength of nickel at large strains. **Acta Materialia**, v. 48, p. 2985–3004, 2000.

Hughes, D.; Liu, Q.; Chrzan, D.; Hansen, N. Scaling of microstructural parameters: Misorientations of deformation induced boundaries. **Acta Materialia**, v. 45, p. 105–112, 1997.

Hughes, D.; Kassner, M.; Stout, M.; Vetrano, J. Metal forming at the center of excellence for the synthesis and processing of advanced materials. **JOM**, v. 50, p. 16–21, 1998.

Hughes, T. **The finite element method: linear static and dynamic finite element analysis**. Dover Civil and Mechanical Engineering Series. Dover Publications, 2000.

Hull, D.; Bacon, D. **Introduction to Dislocations**. Materials science and technology. Elsevier Science, 2011.

Johnson, G. R.; Cook, W. H. A constitutive model and data for metals subjected to large strains, high strain rates and high temperatures. In **International Symposium on Ballistics**, p. 541–547, The Hague, The Netherlands, 1983.

Johnson, K. The correlation of indentation experiments. **Journal of the Mechanics and Physics of Solids**, v. 18, p. 115 – 126, 1970.

Jordan, J.; Siviour, C.; Sunny, G.; Bramlette, C.; Spowart, J. Strain rate-dependant mechanical properties of ofhc copper. **Journal of Materials Science**, v. 48, p. 7134–7141, 2013.

Kestin, J.; Rice, J. **Paradoxes in the Application of Thermodynamics to Strained Solids**. Technical report (Brown University. Division of Engineering). Division of Engineering, Brown University, 1969.

Khan, A. S.; Suh, Y. S.; Kazmi, R. Quasi-static and dynamic loading responses and constitutive modeling of titanium alloys. **International Journal of Plasticity**, v. 20, p. 2233–2248, 2004.

**SlimLine Sensors - Measurement of Dynamic and Quasistatic Forces, 0 ... 3 kN up to 0 ... 80 kN**. Kistler Group, 2016.

Klepaczko, J. Thermally activated flow and strain rate history effects for some polycrystalline f.c.c. metals. **Materials Science and Engineering**, v. 18, p. 121–135, 1975.

Klepaczko, J. R. Constitutive relations in dynamic plasticity, pure metals and alloys. In Klepaczko, J. R.; Lodygowski, T., editors, **Advances in Constitutive Relations Applied in Computer Codes**, v. 515 of **CISM International Centre for Mechanical Sciences**, p. 1–146. Springer Vienna, 2009.

Klepaczko, J.; Chiem, C. On rate sensitivity of f.c.c. metals, instantaneous rate sensitivity and rate sensitivity of strain hardening. **Journal of the Mechanics and Physics of Solids**, v. 34, p. 29–54, 1986.

Knezevic, M.; Beyerlein, I. J.; Brown, D. W.; Sisneros, T. A.; Tomé, C. N. A polycrystal plasticity model for predicting mechanical response and texture evolution during strain-path changes: Application to beryllium. **International Journal of Plasticity**, v. 49, p. 185–198, 2013.

Kocks, U. F.; Argon, A. S.; Ashby, M. F. Thermodynamics and kinetics of slip. **Progress in Materials Science**, v. 19, p. 1–271, 1975.

Kocks, U. Laws for work-hardening and low-temperature creep. **Journal of Engineering Materials and Technology, Transactions of the ASME**, v. 98 Ser H, p. 76–85, 1976.

Kocks, U.; Mecking, H. Physics and phenomenology of strain hardening: the FCC case. **Progress in Materials Science**, v. 48, p. 171–273, 2003.

Kok, S.; Beaudoin, A.; Tortorelli, D. On the development of stage IV hardening using a model based on the mechanical threshold. **Acta Materialia**, v. 50, p. 1653–1667, 2002.

Kolsky, H.; Douch, L. Experimental studies in plastic wave propagation. **Journal of the Mechanics and Physics of Solids**, v. 10, p. 195–223, 1962.

Korkut, I.; Kasap, M.; Ciftci, I.; Seker, U. Determination of optimum cutting parameters during machining of AISI 304 austenitic stainless steel. **Materials & Design**, v. 25, p. 303–305, 2004.

Krempl, E.; Gleason, J. M. Isotropic viscoplasticity theory based on overstress (vbo). the influence of the direction of the dynamic recovery term in the growth law of the equilibrium stress. **International Journal of Plasticity**, v. 12, p. 719–735, 1996.

Krempl, E. 6 - a small-strain viscoplasticity theory based on overstress. In Krausz, A. S.; Krausz, K., editors, **Unified Constitutive Laws of Plastic Deformation**, p. 281–318. Academic Press, San Diego, 1996.

Kubin, L. **Dislocations, Mesoscale Simulations and Plastic Flow**. Oxford Series on Materials Modelling. OUP Oxford, 2013.

Kuhlmann-Wilsdorf, D. Theory of plastic deformation: - properties of low energy dislocation structures. **Materials Science and Engineering: A**, v. 113, p. 1–41, 1989.

Kuhlmann-Wilsdorf, D.; Hansen, N. Geometrically necessary, incidental and subgrain boundaries. **Scripta Metallurgica et Materialia**, v. 25, p. 1557–1562, 1991.

Kuhlmann-Wilsdorf, D.; Merwe, J. V. D. Theory of dislocation cell sizes in deformed metals. **Materials Science and Engineering**, v. 55, p. 79–83, 1982.

Lee, E. H. Elastic-Plastic Deformation at Finite Strains. **Journal of Applied Mechanics**, v. 36, p. 1–6, 1969.

Lee, E. H.; Liu, D. T. Finite-Strain Elastic-Plastic Theory with Application to Plane-Wave Analysis. **Journal of Applied Physics**, v. 38, p. 19–27, 1967.

Lemaitre, J.; Chaboche, J. L. **Mechanics of Solid Materials**. Cambridge University Press, 1990.

Leslie, W. Microstructural effects of high strain rate deformation. In Rohde, R.; Butcher, B.; Holland, J.; Karnes, C., editors, **Metallurgical Effects at High Strain Rates**, p. 571–586. Springer US, 1973.

Li, Y.; Zhang, Y.; Tao, N.; Lu, K. Effect of the zener-hollomon parameter on the microstructures and mechanical properties of Cu subjected to plastic deformation. **Acta Materialia**, v. 57, p. 761–772, 2009.

Lima, J.; Ávila, R.; Abrão, A.; Faustino, M.; Davim, J. P. Hard turning: AISI 4340 high strength low alloy steel and AISI D2 cold work tool steel. **Journal of Materials Processing Technology**, v. 169, p. 388–395, 2005.

Lindholm, U. Some experiments with the split hopkinson pressure bar. **Journal of the Mechanics and Physics of Solids**, v. 12, p. 317–335, 1964.

Liu, Q.; Jensen, D. J.; Hansen, N. Effect of grain orientation on deformation structure in cold-rolled polycrystalline aluminium. **Acta Materialia**, v. 46, p. 5819–5838, 1998.

Lubliner, J. On the thermodynamic foundations of non-linear solid mechanics. **International Journal of Non-Linear Mechanics**, v. 7, p. 237–254, 1972.

Lubliner, J. A maximum-dissipation principle in generalized plasticity. **Acta Mechanica**, v. 52, p. 225–237, 1984.

Lubliner, J. Normality rules in large-deformation plasticity. **Mechanics of Materials**, v. 5, p. 29–34, 1986.

Lubliner, J. **Plasticity Theory**. Dover books on engineering. Dover Publications, 2008.

Luo, Z.; Mishin, O.; Zhang, Y.; Zhang, H.; Lu, K. Microstructural characterization of nickel subjected to dynamic plastic deformation. **Scripta Materialia**, v. 66, p. 335–338, 2012a.

Luo, Z.; Zhang, H.; Hansen, N.; Lu, K. Quantification of the microstructures of high purity nickel subjected to dynamic plastic deformation. **Acta Materialia**, v. 60, p. 1322–1333, 2012b.

Lush, A.; Weber, G.; Anand, L. An implicit time-integration procedure for a set of internal variable constitutive equations for isotropic elasto-viscoplasticity. **International Journal of Plasticity**, v. 5, p. 521–549, 1989.

Ma, H.; Huang, L.; Tian, Y.; Li, J. Effects of strain rate on dynamic mechanical behavior and microstructure evolution of 5a02-o aluminum alloy. **Materials Science and Engineering: A**, v. 606, p. 233–239, 2014.

Macdougall, D. Determination of the plastic work converted to heat using radiometry. **Experimental Mechanics**, v. 40, p. 298–306, 2000.

Mamalis, A.; Manolakos, D.; Kladas, A.; Koumoutsos, A. Electromagnetic forming and powder processing: Trends and developments. **Applied Mechanics Reviews**, v. 57, p. 299–324, 2004.

Mandel, J. **Plasticité classique et viscoplasticité: course held at the Department of Mechanics of Solids, September-October, 1971**. Courses and lectures - International Centre for Mechanical Sciences. Springer-Verlag, 1972.

Mánik, T.; Holmedal, B.; Hopperstad, O. S. Strain-path change induced transients in flow stress, work hardening and r-values in aluminum. **International Journal of Plasticity**, v. 69, p. 1–20, 2015.

Marsden, J.; Hughes, T. **Mathematical Foundations of Elasticity**. Dover Civil and Mechanical Engineering Series. Dover, 1994.

McClintock, F.; Argon, A. **Mechanical behavior of materials**. Addison-Wesley series in metallurgy and materials. Addison-Wesley Pub. Co., 1966.

Meyers, M. **Dynamic Behavior of Materials**. Wiley-Interscience publication. Wiley, 1994.

Meyers, M.; Gregori, F.; Kad, B.; Schneider, M.; Kalantar, D.; Remington, B.; Ravichandran, G.; Boehly, T.; Wark, J. Laser-induced shock compression of monocrystalline copper: characterization and analysis. **Acta Materialia**, v. 51, p. 1211–1228, 2003.

Miehe, C.; Schotte, J. **Crystal Plasticity and Evolution of Polycrystalline Microstructure**. John Wiley & Sons, Ltd, 2004.

Miguélez, M.; Soldani, X.; Molinari, A. Analysis of adiabatic shear banding in orthogonal cutting of ti alloy. **International Journal of Mechanical Sciences**, v. 75, p. 212–222, 2013.

Mirzaei, M.; Najafi, M.; Niasari, H. Experimental and numerical analysis of dynamic rupture of steel pipes under internal high-speed moving pressures. **International Journal of Impact Engineering**, v. 85, p. 27–36, 2015.

Mishin, O.; Jensen, D. J.; Hansen, N. Microstructures and boundary populations in materials produced by equal channel angular extrusion. **Materials Science and Engineering: A**, v. 342, p. 320–328, 2003.

Molinari, A.; Ravichandran, G. Constitutive modeling of high-strain-rate deformation in metals based on the evolution of an effective microstructural length. **Mechanics of Materials**, v. 37, p. 737–752, 2005.

Mourad, H.; Bronkhorst, C.; Addessio, F.; Cady, C.; Brown, D.; Chen, S.; Gray III, G. T. Incrementally objective implicit integration of hypoelastic-viscoplastic constitutive equations based on the mechanical threshold strength model. **Computational Mechanics**, v. 53, p. 941–955, 2014.

Muschik, W. Internal Variables in Non-Equilibrium Thermodynamics. **Journal of Non Equilibrium Thermodynamics**, v. 15, p. 127–138, 1990.

Nemat-Nasser, S. **Plasticity: A Treatise on Finite Deformation of Heterogeneous Inelastic Materials**. Cambridge Monographs on Mechanics. Cambridge University Press, 2009.

Nemat-Nasser, S.; Isaacs, J. Direct measurement of isothermal flow stress of metals at elevated temperatures and high strain rates with application to ta and taw alloys. **Acta Materialia**, v. 45, p. 907–919, 1997.

Nemat-Nasser, S.; Li, Y. Flow stress of f.c.c. polycrystals with application to OFHC Cu. **Acta Materialia**, v. 46, p. 565–577, 1998.

Nes, E. Modelling of work hardening and stress saturation in FCC metals. **Progress in Materials Science**, v. 41, p. 129–193, 1997.

Neugebauer, R.; Bouzakis, K.-D.; Denkena, B.; Klocke, F.; Sterzing, A.; Tekkaya, A.; Wertheim, R. Velocity effects in metal forming and machining processes. **CIRP Annals - Manufacturing Technology**, v. 60, p. 627–650, 2011.

Oden, J. T. **Finite elements of nonlinear continua**. Advanced engineering series. McGraw-Hill, 1972.

Ogden, R. W. **Non-Linear Elastic Deformations**. Dover Civil and Mechanical Engineering Series. Dover Publications, 1997.

Orava, R. Metallurgical effects of high energy rate forming. p. 129–155, 1973.

Orowan, E. The creep of metals. **J. of the West Scotland Iron and Steel Institutive**, v. 54, p. 1633, 1945.

Ottosen, N. S.; Ristinmaa, M. **The Mechanics of Constitutive Modeling**. Elsevier, 2005.

Pandey, A.; Khan, A. S.; Kim, E.-Y.; Choi, S.-H.; Gnäupel-Herold, T. Experimental and numerical investigations of yield surface, texture, and deformation mechanisms in AA5754 over low to high temperatures and strain rates. **International Journal of Plasticity**, v. 41, p. 165–188, 2013.

Pavlina, E.; Van Tyne, C. Correlation of yield strength and tensile strength with hardness for steels. **Journal of Materials Engineering and Performance**, v. 17, p. 888–893, 2008.

Perić, D. On a class of constitutive equations in viscoplasticity: Formulation and computational issues. **International Journal for Numerical Methods in Engineering**, v. 36, p. 1365–1393, 1993.

Perzyna, P. Fundamental problems in viscoplasticity. v. 9 of **Advances in Applied Mechanics**, p. 243–377. Elsevier, 1966.

Perzyna, P. Thermodynamic theory of viscoplasticity. v. 11 of **Advances in Applied Mechanics**, p. 313–354. Elsevier, 1971.

Perzyna, P. Internal state variable description of dynamic fracture of ductile solids. **International Journal of Solids and Structures**, v. 22, p. 797–818, 1986.

Petch, N. J. The cleavage strength of polycrystals. **Journal of the Iron and Steel Institute**, v. 174, p. 25–28, 1953.

Plunkett, B.; Lebensohn, R.; Cazacu, O.; Barlat, F. Anisotropic yield function of hexagonal materials taking into account texture development and anisotropic hardening. **Acta Materialia**, v. 54, p. 4159–4169, 2006.

Qi, C.; Wang, M.; Qian, Q. Strain-rate effects on the strength and fragmentation size of rocks. **International Journal of Impact Engineering**, v. 36, p. 1355–1364, 2009.

Qiao, X.; Starink, M.; Gao, N. Hardness inhomogeneity and local strengthening mechanisms of an al1050 aluminium alloy after one pass of equal channel angular pressing. **Materials Science and Engineering: A**, v. 513-514, p. 52–58, 2009.

Ramesh, K. T. **High Rates and Impact Experiments**, p. 929–960. Springer US, Boston, MA, 2008.

Rashid, M. M.; Gray III, G. T.; Nemat-Nasser, S. Heterogeneous deformations in copper single crystals at high and low strain rates. **Philosophical Magazine A**, v. 65, p. 707–735, 1992.

Reddy, J. N. **Applied functional analysis and variational methods in engineering**. McGraw-Hill, 1986.

Reddy, J. N. **Energy Principles and Variational Methods in Applied Mechanics**. Wiley, 2002.

Regazzoni, G.; Kocks, U.; Follansbee, P. Dislocation kinetics at high strain rates. **Acta Metallurgica**, v. 35, p. 2865–2875, 1987.

Reis, A.; Rosa, P.; Ferro, A. **Efeito de escala na resistência mecânica de materiais**. Master's thesis, UTL. Instituto Superior Técnico, Lisboa, 2016.

Rice, J. Inelastic constitutive relations for solids: An internal-variable theory and its application to metal plasticity. **Journal of Mechanics Physics of Solids**, v. 19, p. 433–455, 1971.

Ristinmaa, M.; Ottosen, N. S. Viscoplasticity based on an additive split of the conjugated forces. **European Journal of Mechanics - A/Solids**, v. 17, p. 207–235, 1998.

Ristinmaa, M.; Wallin, M.; Ottosen, N. S. Thermodynamic format and heat generation of isotropic hardening plasticity. **Acta Mechanica**, v. 194, p. 103–121, 2007.

Rodríguez-Martínez, J. **Advanced Constitutive Relations for Modeling Thermo-viscoplastic Behaviour of Metallic Alloys Subjected to Impact Loading**. PhD thesis, 2010.

Rodríguez-Martínez, J.; Rusinek, A.; Klepaczko, J. Constitutive relation for steels approximating quasi-static and intermediate strain rates at large deformations. **Mechanics Research Communications**, v. 36, p. 419–427, 2009.

Rodríguez-Martínez, J.; Rodríguez-Millán, M.; Rusinek, A.; Arias, A. A dislocation-based constitutive description for modeling the behavior of FCC metals within wide ranges of strain rate and temperature. **Mechanics of Materials**, v. 43, p. 901–912, 2011.

Rollett, A.; Kocks, U.; Stout, M.; Embury, J.; Doherty, R. Strain hardening at large strains. In Kettunen, P.; Lepisto, T.; Lehtonen, M., editors, **Strength of Metals and Alloys (ICSMA 8)**, p. 433–438. Pergamon, Oxford, 1989.

Rossi, R.; Alves, M. K.; Al-Qureshi, H. A. A total lagrangian framework for simulation of powder compaction process based on a smooth three-surface cap model and a mesh-free method. **International Journal for Numerical Methods in Engineering**, v. 75, p. 1457–1491, 2008.

Rossi, R.; Alves, M. K.; Al-Qureshi, H. A. An element-free galerkin method for metal forming simulations. **Engineering Computations: International Journal for Computer-Aided Engineering**, v. 26, p. 327–346, 2009.

Rusinek, A.; Jankowiak, T. **Constitutive Relations under Impact Loadings: Experiments, Theoretical and Numerical Aspects**, chapter Dynamic Behavior of Materials. Constitutive Relations and Applications, p. 87–135. Springer Vienna, Vienna, 2014.

Rusinek, A.; Klepaczko, J. Shear testing of a sheet steel at wide range of strain rates and a constitutive relation with strain-rate and temperature dependence of the flow stress. **International Journal of Plasticity**, v. 17, p. 87–115, 2001.

Rusinek, A.; Rodríguez-Martínez, J.; Arias, A. A thermo-viscoplastic constitutive model for FCC metals with application to OFHC copper. **International Journal of Mechanical Sciences**, v. 52, p. 120–135, 2010.

Rusinek, A.; Rodríguez-Martínez, J. Thermo-viscoplastic constitutive relation for aluminium alloys, modeling of negative strain rate sensitivity and viscous drag effects. **Materials & Design**, v. 30, p. 4377–4390, 2009.

Rusty Gray III, G. High-strain-rate deformation: Mechanical behavior and deformation substructures induced. **Annual Review of Materials Research**, v. 42, p. 285–303, 2012.

Schmid, E.; Boas, W. **Kristallplastizität**. Gauthier-Villars, 1935.

Seth, B. R. Generalized strain measure with applications to physical problems. In Reiner, M.; Abir, D., editors, **Second order effects in elasticity, plasticity and fluid dynamics**, p. 162–172, New-York, 1964. McMillan.

Shankaranarayan, H.; Varma, S. K. Strain-rate and grain-size effect on substructures and mechanical properties in OFHC copper during tension. **Journal of Materials Science**, v. 30, p. 3576–3586, 1995.

Shehadeh, M.; Zbib, H.; Diaz De La Rubia, T. Modelling the dynamic deformation and patterning in fcc single crystals at high strain rates: Dislocation dynamics plasticity analysis. **Philosophical Magazine**, v. 85, p. 1667–1685, 2005.

Silva, C.; Rosa, P.; Martins, P. Electromagnetic cam driven compression testing equipment. **Experimental Mechanics**, v. 52, p. 1211–1222, 2012.

Silva, C.; Rosa, P.; Martins, P. **Caracterização mecânica e à fractura de materiais aplicada a processos de deformação plástica e corte**. PhD thesis, UTL. Instituto Superior Técnico, Lisboa, 2013.

Silva, C.; Rosa, P.; Martins, P. Innovative testing machines and methodologies for the mechanical characterization of materials. **Experimental Techniques**, v. p. n/a–n/a, 2014.

Simo, J. C.; Armero, F. Geometrically non-linear enhanced strain mixed methods and the method of incompatible modes. **International Journal for Numerical Methods in Engineering**, v. 33, p. 1413–1449, 1992.

Simo, J. C.; Hughes, T. J. R. **Computational Inelasticity**. Interdisciplinary applied mathematics: Mechanics and materials. Springer, 1998.

Simo, J. C.; Kennedy, J. G.; Govindjee, S. Non-smooth multisurface plasticity and viscoplasticity. loading/unloading conditions and numerical algorithms. **International Journal for Numerical Methods in Engineering**, v. 26, p. 2161–2185, 1988.

Spencer, A. **Continuum Mechanics**. Dover Books on Physics. Dover Publications, 2004.

Tabor, D. **The Hardness of Metals**. Monographs on the physics and chemistry of materials. Oxford, 2000.

Tanner, A. B.; McDowell, D. L. Deformation, temperature and strain rate sequence experiments on OFHC Cu. **International Journal of Plasticity**, v. 15, p. 375–399, 1999.

Tanner, A. B.; McGinty, R. D.; McDowell, D. L. Modeling temperature and strain rate history effects in OFHC Cu. **International Journal of Plasticity**, v. 15, p. 575–603, 1999.

Taylor, G. I. The mechanism of plastic deformation of crystals. part i. theoretical. **Proceedings of the Royal Society of London. Series A, Containing Papers of a Mathematical and Physical Character**, v. 145, p. 362–387, 1934a.

Taylor, G. I. The mechanism of plastic deformation of crystals. part ii. comparison with observations. **Proceedings of the Royal Society of London. Series A, Containing Papers of a Mathematical and Physical Character**, v. 145, p. 388–404, 1934b.

Taylor, G. I. The use of flat-ended projectiles for determining dynamic yield stress. I. theoretical considerations. **Proceedings of the Royal Society of London. Series A. Mathematical and Physical Sciences**, v. 194, p. 289–299, 1948.

Tiryakioglu, M.; Robinson, J.; Salazar-Guapuriche, M.; Zhao, Y.; Eason, P. Hardness-strength relationships in the aluminum alloy 7010. **Materials Science and Engineering: A**, v. 631, p. 196 – 200, 2015.

Tjøtta, S.; Mo, A. A constitutive model for cold deformation of aluminium at large strains and high strain rates. **International Journal of Plasticity**, v. 9, p. 461–478, 1993.

Tome, C.; Canova, G.; Kocks, U.; Christodoulou, N.; Jonas, J. The relation between macroscopic and microscopic strain hardening in f.c.c. polycrystals. **Acta Metallurgica**, v. 32, p. 1637–1653, 1984.

Tong, W.; Clifton, R. J.; Huang, S. Pressure-shear impact investigation of strain rate history effects in oxygen-free high-conductivity copper. **Journal of the Mechanics and Physics of Solids**, v. 40, p. 1251–1294, 1992.

Truesdell, C. Thermodynamics for beginners. In Parkus, H.; Sedov, L., editors, **Irreversible Aspects of Continuum Mechanics and Transfer of Physical Characteristics in Moving Fluids**, IUTAM Symposia, p. 373–389. Springer Vienna, 1968.

Truesdell, C. **Rational thermodynamics**. Springer-Verlag, 1984.

Viatkina, E. M.; Brekelmans, W. A. M.; Geers, M. G. D. Numerical analysis of strain path dependency in FCC metals. **Computational Mechanics**, v. 41, p. 391–405, 2008.

Vilamosa, V.; Clausen, A.; Borvik, T.; Skjervold, S.; Hopperstad, O. Behaviour of Al-Mg-Si alloys at a wide range of temperatures and strain rates. **International Journal of Impact Engineering**, v. 86, p. 223–239, 2015.

Vilamosa, V.; Clausen, A.; Borvik, T.; Holmedal, B.; Hopperstad, O. A physically-based constitutive model applied to {AA6082} aluminium alloy at large strains, high strain rates and elevated temperatures. **Materials & Design**, v. 103, p. 391–405, 2016.

Voce, E. The relationship between stress and strain for homogeneous deformation. **Journal of Institute of Metals**, v. 74, p. 537–562, 1948.

Voyiadjis, G. Z.; Abed, F. H. Microstructural based models for bcc and fcc metals with temperature and strain rate dependency. **Mechanics of Materials**, v. 37, p. 355–378, 2005.

Wang, B.; Liu, Z.; Su, G.; Song, Q.; Ai, X. Investigations of critical cutting speed and ductile-to-brittle transition mechanism for workpiece material in ultra-high speed machining. **International Journal of Mechanical Sciences**, v. 104, p. 44–59, 2015.

Wang, W. M.; Sluys, L. J.; de Borst, R. Viscoplasticity for instabilities due to strain softening and strain-rate softening. **International Journal for Numerical Methods in Engineering**, v. 40, p. 3839–3864, 1997.

Weber, G.; Anand, L. Finite deformation constitutive equations and a time integration procedure for isotropic, hyperelastic-viscoplastic solids. **Computer Methods in Applied Mechanics and Engineering**, v. 79, p. 173–202, 1990.

Winther, G. Effect of grain orientation dependent microstructures on flow stress anisotropy modelling. **Scripta Materialia**, v. 52, p. 995–1000, 2005.

Woods, L. C. On the local form of the second law of thermodynamics in continuum mechanics. **Quarterly of Applied Mathematics**, v. 39, p. 119–126, 1981.

Woods, L. C. Thermodynamic inequalities in continuum mechanics. **IMA Journal of Applied Mathematics**, v. 29, p. 221–246, 1982.

Xu, Z.; Huang, F. Comparison of constitutive models for FCC metals over wide temperature and strain rate ranges with application to pure copper. **International Journal of Impact Engineering**, v. 79, p. 65–74, 2015.

Yan, S.; Yang, H.; Li, H.; Yao, X. A unified model for coupling constitutive behavior and micro-defects evolution of aluminum alloys under high-strain-rate deformation. **International Journal of Plasticity**, v. 85, p. 203–229, 2016.

Yang, Y.; Chen, Y.; Ma, F.; Hu, H.; Zhang, Q.; Tang, T.; Zhang, X. Microstructure evolution of 1050 commercial purity aluminum processed by high-strain-rate deformation. **Journal of Materials Engineering and Performance**, v. 24, p. 4307–4312, 2015.

Yu, S.-S.; Lu, Y.-B.; Cai, Y. The strain-rate effect of engineering materials and its unified model. **Latin American Journal of Solids and Structures**, v. 10, p. 833–844, 2013.

Zaera, R.; Fernández-Sáez, J. An implicit consistent algorithm for the integration of thermoviscoplastic constitutive equations in adiabatic conditions and finite deformations. **International Journal of Solids and Structures**, v. 43, p. 1594–1612, 2006.

Zener, C.; Hollomon, J. H. Effect of strain rate upon plastic flow of steel. **Journal of Applied Physics**, v. 15, 1944.

Zerilli, F.; Armstrong, R. The effect of dislocation drag on the stress-strain behavior of f.c.c. metals. **Acta Metallurgica et Materialia**, v. 40, p. 1803–1808, 1992.

Zhang, B.; Shim, V. Effect of strain rate on microstructure of polycrystalline oxygen-free high conductivity copper severely deformed at liquid nitrogen temperature. **Acta Materialia**, v. 58, p. 6810–6827, 2010.

Zhang, K.; Holmedal, B.; Hopperstad, O.; Dumoulin, S.; Gawad, J.; Bael, A. V.; Houtte, P. V. Multi-level modelling of mechanical anisotropy of commercial pure aluminium plate: Crystal plasticity models, advanced yield functions and parameter identification. **International Journal of Plasticity**, v. 66, p. 3–30, 2015.

Ziegler, H. **An introduction to thermomechanics**. North-Holland series in applied mathematics and mechanics. North-Holland Pub. Co., 1977.

Zienkiewicz, O. C.; Taylor, R. L. **The Finite Element Method: The Basis**. Number v. 1 in The Finite Element Method. Butterworth-Heinemann, 2000a.

Zienkiewicz, O. C.; Taylor, R. L. **The Finite Element Method: Solid mechanics**. Number v. 2 in The Finite Element Method. Butterworth-Heinemann, 2000b.

# APPENDIX A Comparison of viscoplastic models

This topic uniaxial flow stress formulation of the viscoplastic models summarized in Table A.1 of the introductory chapter: the MTS, BPR, MR models and the model of dos Santos et al. [2016]. The corresponding model summary is given in Table A.1, in which the constitutive features outlined are the flow stress, internal state variable evolution, strain-rate-history, and corresponding model parameters.

This chapter has also the aim of comparing the model developed by dos Santos et al., 2016, which is a particular case of the present formulation (see Subsection 3.5.2), with other constitutive proposals, namely the models of Follansbee and Kocks, 1988, MTS, Bamman et al., 1996, BCJ, Bodner and Rubin, 1994, BPR, and Molinari and Ravichandran, 2005, MR. Constitutive approaches are assessed considering experimental results obtained from decremental strain-rate tests (see Figure 1.7(a) and (c)) for an annealed high purity copper.

Two comparisons are carried out. The first one employs the experimental results of Tanner and McDowell, 1999, and compares the models MTS and BCJ adjusted by Tanner et al., 1999, as well as the model of dos Santos et al., 2016, with parameters given in Table A.2. Corresponding loading data and comparison results are presented in Section A.1. The second comparison considers the models BPR and MR adjusted respectively by Bodner and Rubin, 1994, and Molinari and Ravichandran, 2005, employing the experiments of Follansbee and Kocks, 1988, and Follansbee and Gray III, 1991. In this case, the model of dos Santos et al., 2016, uses the parameters of Table A.3. The pertinent loading informations and results are presented in Section A.2.

## A.1 Decremental strain-rate test of Tanner and McDowell, 1999

The decremental strain-rate test performed by Tanner and McDowell, 1999, consisted of:

- *QS*: *quasi*-static test. Material is subjected to a total strain equal to 0.92 at a strain-rate of $\bar{D}_{11} = 4 \times 10^{-4}\,\mathrm{s}^{-1}$;
- *DSR*: decremental strain-rate test. Material is subjected to a high strain-rate of $\bar{D}_{11_1} = 6 \times 10^{3}\,\mathrm{s}^{-1}$ until a partial strain of 0.32 is reached, then the strain-rate is abruptly changed to a lower value $\bar{D}_{11_2} = 4 \times 10^{-4}\,\mathrm{s}^{-1}$ while the strain level reaches 0.79.

The results of each model are depicted in Figure A.1(a). Based on this results one concludes, on one hand, that the MTS model overestimates the hardening rate after flow stress drop while BCJ model underestimates the experimental dropped flow stress. The

latter estimation is closer to the low strain-rate response. On the other hand, the model of dos Santos et al., 2016, produces estimations closer to the experimental data for both high strain-rate loading and dropped flow stress responses.

Table A.1: Summary of some single variable viscoplastic models. Source: dos Santos et al., 2016.

| | |
|---|---|
| **Model proposed by dos Santos et al., 2016** | |
| Flow stress | $\sigma_{flow} = (\sigma_y + A)\left(1 + \sqrt{\frac{3}{2}}\vartheta\dot{\varepsilon}\right)^{\frac{1}{m}}$ |
| ISV evolution | $\dot{A} = \dot{A}_1 + \dot{A}_2$<br>$\dot{A}_1 = \delta\left(A_\infty - A_1\right)\dot{\varepsilon}$ and $A_2 = cA_\infty\varepsilon$<br>$A = A_\infty\left[1 + c\varepsilon - \exp\left(-\delta\varepsilon\right)\right]$ |
| Strain-rate-history | $A_\infty = A_\infty^{lwr} + \left(\frac{\dot{\varepsilon} - \dot{\varepsilon}_{lwr}}{\dot{\varepsilon}_{up} - \dot{\varepsilon}_{lwr}}\right)^{\xi}\left(A_\infty^{up} - A_\infty^{lwr}\right)$ |
| Parameters (10) | $\left\{\sigma_y, \vartheta, m, \delta, c, \dot{\varepsilon}_{lwr}, \dot{\varepsilon}_{up}, A_\infty^{up}, A_\infty^{lwr}, \xi\right\}$ |
| **Molinari-Ravichandran model [Molinari and Ravichandran, 2005]** | |
| Flow stress | $\sigma_{flow} = \hat{\sigma}\left(d\right)\left(\frac{\delta_0}{\delta}\right)\left(\frac{\dot{\varepsilon}}{\dot{\varepsilon}_0}\right)^{\frac{\theta}{A}}$ |
| ISV evolution | $\dot{\delta} = -\frac{\delta_r}{\delta_s}\left(\delta^2 - \delta_s\delta\right)\dot{\varepsilon}$<br>$\delta = \frac{\delta_s}{1 - \left(1 - \frac{\delta_s}{\delta_0}\right)\exp(-\delta_r\varepsilon)}$ |
| Strain-rate-history | $\delta_r = \delta_{r_0}\left[1 + a_r\left(\frac{\dot{\varepsilon}}{\dot{\varepsilon}_{r_0}}\right)^{\xi_r}\left(\frac{\theta}{\theta_0}\right)^{-\nu_r}\right]$ |
| | $\delta_s = \delta_{s_0}\left[1 + a_s\left(\frac{\dot{\varepsilon}}{\dot{\varepsilon}_{s_0}}\right)^{\xi_s}\left(\frac{\theta}{\theta_0}\right)^{-\nu_s}\right]$ |
| Parameters (14) | $\{\hat{\sigma}, \delta_0, A, \dot{\varepsilon}_0, \dot{\varepsilon}_{r_0}, \dot{\varepsilon}_{s_0}, \delta_{r_0}, \delta_{s_0}, a_r, a_s, \xi_r, \xi_s, \nu_r, \nu_s\}$ |
| **Bodner-Partom-Rubin model [Bodner and Rubin, 1994]** | |
| Flow stress | $\sigma_{flow} = \left[2\ln\left(\frac{2\dot{\varepsilon}_0}{\sqrt{3}\dot{\varepsilon}}\right)\right]^{-\frac{1}{2n}} Z$ |
| ISV evolution | $\dot{Z} = m\left(Z_1 - Z\right)\sigma\dot{\varepsilon}$<br>$m = m_b + \left(m_a + m_b\right)\exp\left[-m_c\left(Z - Z_0\right)\right]$ |
| Strain-rate-history | $m_a = M_a\left[1 + \left(\frac{\dot{\varepsilon}}{\dot{\varepsilon}_{s_0}}\right)^{q}\right]$ |
| Parameters (9) | $\{\dot{\varepsilon}_0, n, Z_1, m_a, m_b, m_c, \dot{\varepsilon}_{s_0}, q, Z_0\}$ |
| **MTS model [Follansbee and Kocks, 1988]** | |
| Flow stress | $\sigma = \hat{\sigma}_a + \left(\hat{\sigma} - \hat{\sigma}_a\right)\left\{1 - \left[\frac{k\theta\ln\left(\frac{\dot{\varepsilon}_0}{\dot{\varepsilon}}\right)}{g_0\mu b^3}\right]^{\frac{1}{q}}\right\}^{\frac{1}{p}}$ |
| ISV evolution | $\hat{\sigma} = h_0\left[1 - \tanh\left(2\frac{\hat{\sigma} - \hat{\sigma}_a}{\hat{\sigma}_s - \hat{\sigma}_a}\right)\right]\dot{\varepsilon}$<br>$\varepsilon = \frac{\tanh(2)}{h_0\left[\tanh^2(2) - 1\right]}\left\{\left(\hat{\sigma} - \hat{\sigma}_a\right)\tanh\left(2\right) + \frac{\left(\hat{\sigma}_s - \hat{\sigma}_a\right)}{2}\times\right.$<br>$\left.\times\ln\left[\tanh\left(2\right)\cosh\left(2\frac{\hat{\sigma} - \hat{\sigma}_a}{\hat{\sigma}_s - \hat{\sigma}_a}\right) - \sinh\left(2\frac{\hat{\sigma} - \hat{\sigma}_a}{\hat{\sigma}_s - \hat{\sigma}_a}\right)\right]\right\}\Big|_{\hat{\sigma}_i}^{\hat{\sigma}_f}$ |
| Strain-rate-history | $\hat{\sigma}_s = \hat{\sigma}_{s_0}\exp\left[\frac{k\theta}{A\mu b^3}\ln\left(\frac{\dot{\varepsilon}}{\dot{\varepsilon}_{s_0}}\right)\right]$ and $h_0 = c_1 + c_2\ln\left(\dot{\varepsilon}\right) + c_3\dot{\varepsilon}$ |
| Parameters (14) | $\{\hat{\sigma}_a, k, \mu, b, g_0, p, q, \dot{\varepsilon}_0, \hat{\sigma}_{s_0}, \dot{\varepsilon}_{s_0}, A, c_1, c_2, c_3\}$ |

Table A.2: Material parameters of dos Santos et al., 2016, adjusted using experiments of Tanner and McDowell, 1999.

| $E$ [GPa] | $\nu$ [−] | $\sigma_y$ [MPa] | $\delta$ [−] | $c$ [−] | $A_\infty^{lwr}$ [MPa] | $A_\infty^{up}$ [MPa] | $\dot{\epsilon}_{lwr}$ [$s^{-1}$] | $\dot{\epsilon}_{up}$ [$s^{-1}$] | $\xi$ [−] | $\vartheta$ [s] | $m$ [−] |
|---|---|---|---|---|---|---|---|---|---|---|---|
| 112 | 0.33 | 35 | 6.46 | 0.42 | 233 | 420 | $10^{-4}$ | $10^{4}$ | 3.16 | $1.2 \times 10^{3}$ | 105 |

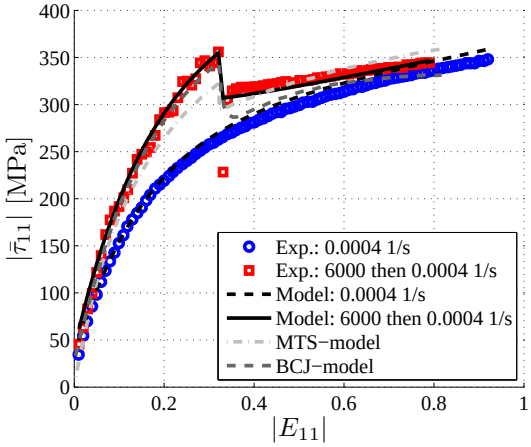


(a)

Figure A.1: Decremental strain-rate test results: (a) Comparison of present model estimation with experiments [Tanner and McDowell, 1999], MTS, and BCJ model predictions presented by Tanner and McDowell [1999]. Source: dos Santos et al., 2016.

## A.2 Decremental strain-rate test of Follansbee and Kocks, 1988

Now, the model of dos Santos et al., 2016, is compared with models of Molinari and Ravichandran, 2005, Figure A.2(a), and Bodner and Rubin, 1994, Figure A.2(b). The calibrated constitutive results are confronted with experiments reported by Follansbee and Kocks, 1988, and Follansbee and Gray III, 1991. The experiments consist of:

- *QS* test: A total strain equal to 0.7 is imposed at a strain-rate of $\bar{D}_{11} = 1.5 \times 10^{-3}\,s^{-1}$;
- *DSR* test: High strain-rate of $\bar{D}_{11_1} = 6 \times 10^{3}\,s^{-1}$ until a partial strain of 0.51. Lower strain-rate of $\bar{D}_{11_2} = 1.5 \times 10^{-3}\,s^{-1}$ to a strain level of 0.7.

Figure A.2(a) shows that the model of dos Santos et al., 2016, provides a better estimation than the MR model. Notice that, the low strain-rate response of the latter overestimates the experimental data, since the behavior predicted by the MR model is higher even than the dropped flow stress after the strain-rate reduction. Further, decremental behavior estimated by the MR model is slightly distant from the experimental response, when compared with the estimation of dos Santos et al., 2016. The results presented in Figure A.2(b) also show that the model of dos Santos et al., 2016, is able to produce better estimations than the BPR model. The latter approximates a low strain-rate response far from the experiments of Follansbee and Gray III, 1991. Still, the BPR

Table A.3: Material parameters of dos Santos et al., 2016, adjusted using experiments of Follansbee and Kocks, 1988.

| $E$ [GPa] | $\nu$ [−] | $\sigma_y$ [MPa] | $\delta$ [−] | $c$ [−] | $A_\infty^{lwr}$ [MPa] | $A_\infty^{up}$ [MPa] | $\dot{\epsilon}_{lwr}$ [$s^{-1}$] | $\dot{\epsilon}_{up}$ [$s^{-1}$] | $\xi$ [−] | $\vartheta$ [s] | $m$ [−] |
|---|---|---|---|---|---|---|---|---|---|---|---|
| 112 | 0.33 | 40 | 7.15 | 0.54 | 230 | 290 | $10^{-4}$ | $10^4$ | 0.35 | $2.7 \times 10^4$ | 215 |

model presents a higher hardening rate than that observed in experimental flow stress after strain-rate decrease. As for Section A.1, the results corresponding to the proposal of dos Santos et al., 2016, present estimations closer to the experimental data for both high strain-rate loading and flow stress dropping responses.

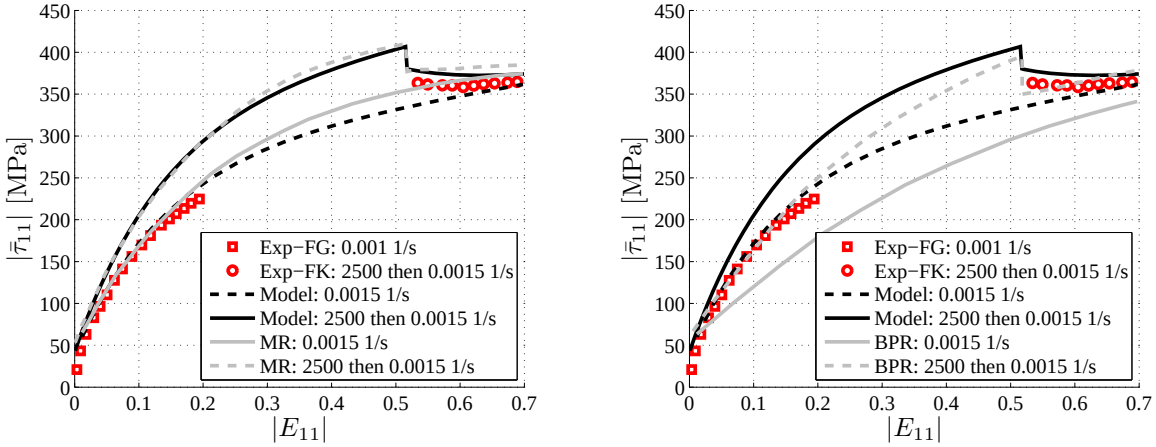


(a) (b)

Figure A.2: Decremental strain-rate test results. Comparison of present model estimation with (a) MR model; and (b) BPR model. Experiments of Follansbee and Kocks, 1988, (FK) and Follansbee and Gray III, 1991, (FG). Source: dos Santos et al., 2016.

# APPENDIX B Numerical aspects

This appendix aims at providing some details on the numerical procedure adopted in this work. First, Section B.1 provides a general description on the *Newton-Raphson* method employed to solve nonlinear equations. Section B.2 outlines the reduction of Eqs. (5.62)-(5.64) and (5.79) into a single equation. In Section B.3 tangent terms required by the *Newton-Raphson* method to solve the local constitutive problem are then described. Section B.4 presents the analytical derivation of the consistent tangent operator associated with the present elastic-viscoplastic model. In Section B.5 a qualitative finite element analysis on the proposed compression tool, evaluating and comparing the compression force applied to the work piece with that dynamically measured by the load cell, is performed considering a high velocity compression.

## B.1 *Newton-Raphson* method

In general, the *Newton-Raphson* method can be stated as in the following. Let be $\boldsymbol{q}$ a vector containing $n$ variables to be found by solving a nonlinear (or even linear) problem:

$$\boldsymbol{q}^T = \left[ \begin{array}{cccccc} q_1 & q_2 & q_3 & , ..., & q_n \end{array} \right]. \tag{B.1}$$

The method starts by assuming an initial estimative $\boldsymbol{q}^t$ for $\boldsymbol{q}$ related to an iteration $k = 0$, i.e.,

$$\boldsymbol{q}^0 \leftarrow \boldsymbol{q}^t. \tag{B.2}$$

Thus, considering an iteration $k$, the problem consists of determining an increment $\Delta\boldsymbol{q}^k$ satisfying

$$\boldsymbol{g}\left(\boldsymbol{q}^{k+1}\right) = \boldsymbol{g}\left(\boldsymbol{q}^k + \Delta\boldsymbol{q}^k\right) = \boldsymbol{0}, \tag{B.3}$$

where $\boldsymbol{g}(\boldsymbol{q})$ is a vector with $n$ nonlinear equations to be solved in terms of the unknown vector $\boldsymbol{q}$. With the aim of determining the increment $\Delta\boldsymbol{q}^k$, an expansion using a *Taylor* series around $\boldsymbol{q}^k$ is employed, which truncating in the first-order terms provides

$$\boldsymbol{g}\left(\boldsymbol{q}^{k+1}\right) = \boldsymbol{g}\left(\boldsymbol{q}^k + \Delta\boldsymbol{q}^k\right) \approx \boldsymbol{g}\left(\boldsymbol{q}^k\right) + \left.\frac{\partial \boldsymbol{g}(\boldsymbol{q})}{\partial \boldsymbol{q}}\right|_k \Delta\boldsymbol{q}^k = \boldsymbol{0}, \tag{B.4}$$

where the tangent matrix is defined as

$$\boldsymbol{M}^k \coloneqq \left.\frac{\partial \boldsymbol{g}(\boldsymbol{q})}{\partial \boldsymbol{q}}\right|_k \Longrightarrow M_{ij}^k \coloneqq \left.\frac{\partial g_i(\boldsymbol{q})}{\partial q_j}\right|_k, \tag{B.5}$$

what allows Eq. (B.4) to be rewritten as

$$\boldsymbol{g}\left(\boldsymbol{q}^k\right) + \boldsymbol{M}^k \Delta \boldsymbol{q}^k = \boldsymbol{0}$$

$$\boldsymbol{M}^k \Delta \boldsymbol{q}^k = -\boldsymbol{g}\left(\boldsymbol{q}^k\right)$$

$$\Delta \boldsymbol{q}^k = -\left(\boldsymbol{M}^k\right)^{-1} \boldsymbol{g}\left(\boldsymbol{q}^k\right). \tag{B.6}$$

By knowing a new increment $\Delta \boldsymbol{q}^k$, the new unknown vector is then updated:

$$\boldsymbol{q}^{k+1} \leftarrow \boldsymbol{q}^k + \Delta \boldsymbol{q}^k. \tag{B.7}$$

Thus, the new values of function $\boldsymbol{g}\left(\boldsymbol{q}^{k+1}\right)$ are calculated. Then, if the new residual $\left\|\boldsymbol{g}\left(\boldsymbol{q}^{k+1}\right)\right\|_{(\cdot)}$ is lower than a given tolerance $e_{tol}$, i.e., if

$$\left\|\boldsymbol{g}\left(\boldsymbol{q}^{k+1}\right)\right\|_{(\cdot)} < e_{tol}, \tag{B.8}$$

the algorithm is finished and the solution is updated:

$$\boldsymbol{q} \leftarrow \boldsymbol{q}^{k+1}. \tag{B.9}$$

Otherwise, if

$$\left\|\boldsymbol{g}\left(\boldsymbol{q}^{k+1}\right)\right\|_{(\cdot)} \geq e_{tol}, \tag{B.10}$$

one assumes

$$\boldsymbol{q}^k \leftarrow \boldsymbol{q}^{k+1} \tag{B.11}$$

$$k \leftarrow k + 1, \tag{B.12}$$

and the algorithm is restarted. Operator $\|\cdot\|_{(\cdot)}$ denotes a given norm.

## B.2 Reduction of return mapping equations for *von Mises* plasticity

By employing the *von Mises* yield criterion given in Eq. (3.67), equations (5.62)-(5.64) and (5.79) can be reduced to a single equation. For this purpose, first the elastic strain tensor is split into its volumetric $\boldsymbol{E}^e_v$ and deviatoric $\boldsymbol{E}^e_d$ parts:

$$\boldsymbol{E}^e = \boldsymbol{E}^e_v + \boldsymbol{E}^e_d, \tag{B.13}$$

where

$$\boldsymbol{E}^e_v = \frac{1}{3}\mathrm{tr}\left(\boldsymbol{E}^e\right). \tag{B.14}$$

Consequently, equation (5.79) is also split into its volumetric and deviatoric parts [Eterovic and Bathe, 1990; Weber and Anand, 1990]:

$$(\boldsymbol{E}_v^e)_{n+1} = (\boldsymbol{E}_v^e)_{n+1}^{trial} \tag{B.15}$$

$$(\boldsymbol{E}_d^e)_{n+1} = (\boldsymbol{E}_d^e)_{n+1}^{trial} - \Delta\lambda \boldsymbol{N}_{\bar{\boldsymbol{\tau}}_{n+1}}. \tag{B.16}$$

These first equation informs that, considering the *von Mises* criterion and an associative flow rule, related viscoplastic correction is performed only on the deviatoric elastic strain. Furthermore, terms $\boldsymbol{E}_v^e$ and $\boldsymbol{E}_d^e$ relate with stress tensor $\bar{\boldsymbol{\tau}}$ according to respective expressions (see Eqs. $(3.55)_1$ and (3.56))

$$\mathrm{tr}\left(\bar{\boldsymbol{\tau}}\right)\boldsymbol{I} = 9\kappa \boldsymbol{E}_v^e \Rightarrow \mathrm{tr}\left(\bar{\boldsymbol{\tau}}\right) = 3\kappa \mathrm{tr}\left(\boldsymbol{E}^e\right), \tag{B.17}$$

and

$$\bar{\boldsymbol{\tau}}^D = 2\mu \boldsymbol{E}_d^e. \tag{B.18}$$

Therefore, by means of last elastic relationship, the deviatoric stress tensor can be calculated as

$$\bar{\boldsymbol{\tau}}_{n+1}^D = \left(\bar{\boldsymbol{\tau}}_{n+1}^D\right)^{trial} - \Delta\lambda 2\mu \boldsymbol{N}_{\bar{\boldsymbol{\tau}}_{n+1}}. \tag{B.19}$$

Manipulating Eq. (B.19), one can show that both current $\bar{\boldsymbol{\tau}}_{n+1}^D$ and trial $\bar{\boldsymbol{\tau}}_{n+1}^{D^{trial}}$ stresses are "collinear" tensors, that is,

$$\boldsymbol{N}_{\bar{\boldsymbol{\tau}}_{n+1}} = \boldsymbol{N}_{\bar{\boldsymbol{\tau}}_{n+1}^{trial}}, \tag{B.20}$$

where $\boldsymbol{N} \coloneqq \frac{\bar{\boldsymbol{\tau}}^D}{\left\|\bar{\boldsymbol{\tau}}^D\right\|}$. This fact, from Eq. (B.19), leads to the following result:

$$\left\|\bar{\boldsymbol{\tau}}_{n+1}^D\right\| = \left\|\left(\bar{\boldsymbol{\tau}}_{n+1}^D\right)^{trial}\right\| - \Delta\lambda 2\mu. \tag{B.21}$$

Substituting Eq. (B.21) into Eq. (5.64) results in the single equation

$$\left\|\bar{\boldsymbol{\tau}}_{n+1}^{D^{trial}}\right\| - \Delta\lambda 2\mu - \sqrt{\frac{2}{3}}\left(\sigma_y + A_{n+1}\right) = \bar{\Theta}^{-1}\left(\Delta\lambda, A_{n+1}\right) \tag{B.22}$$

given in terms of $\Delta\lambda$ and $A_{n+1}$.

### B.3 Tangent terms required in the local problem solution

The return mapping algorithm is used to solve the nonlinear equations (5.80)-(5.84), making use of the *Newton-Raphson* algorithm. In this context, corresponding tangent quantities have to be evaluated. The system of nonlinear linear equations to be solved can be set as

$$f_1 = \left\| \bar{\boldsymbol{\tau}}_{n+1}^{D^{trial}} \right\| - \Delta\lambda 2\mu - \sqrt{\frac{2}{3}} \left( \sigma_y + A_{n+1} \right) - \bar{\Theta}^{-1} \left( \Delta\lambda, A_{n+1} \right) = 0, \tag{B.23}$$

$$f_2 = A_{n+1} - A_n - \bar{A}_{\infty_{n+1}} c \sqrt{\frac{2}{3}} \Delta\lambda - \left[ \bar{A}_{\infty_{n+1}} \left( 1 + c\varepsilon_n \right) - A_n \right] \left[ 1 - \exp\left( -\delta_{n+1} \sqrt{\frac{2}{3}} \Delta\lambda \right) \right] = 0, \tag{B.24}$$

$$f_3 = \delta_{n+1} - \delta^{lwr} - \left[ \frac{1}{\Delta t} \left( \frac{\sqrt{\frac{2}{3}} \Delta\lambda - \Delta t \dot{\varepsilon}_{lwr}}{\dot{\varepsilon}_{up} - \dot{\varepsilon}_{lwr}} \right) \right]^{\xi_1} \left( \delta^{up} - \delta^{lwr} \right) = 0, \tag{B.25}$$

$$f_4 = \bar{A}_{\infty_{n+1}} - \frac{\varepsilon_n}{\sqrt{\frac{2}{3}} \Delta\lambda + \varepsilon_n} \bar{A}_{\infty_n} - \left( 1 - \frac{\varepsilon_n}{\sqrt{\frac{2}{3}} \Delta\lambda + \varepsilon_n} \right) A_{\infty_{n+1}} = 0, \tag{B.26}$$

with

$$A_{\infty_{n+1}} = A_\infty^{lwr} + \left[ \frac{1}{\Delta t} \left( \frac{\sqrt{\frac{2}{3}} \Delta\lambda - \Delta t \dot{\varepsilon}_{lwr}}{\dot{\varepsilon}_{up} - \dot{\varepsilon}_{lwr}} \right) \right]^{\xi_2} \left( A_\infty^{up} - A_\infty^{lwr} \right), \tag{B.27}$$

where involved unknowns are $\left\{ \Delta\lambda, A_{n+1}, \delta_{n+1}, \bar{A}_{\infty_{n+1}} \right\}$. Accordingly, the tangent terms are defined by

$$\frac{\partial f_1}{\partial \Delta\lambda} = -2\mu - \frac{\partial \bar{\Theta}^{-1}}{\partial \Delta\lambda}, \tag{B.28}$$

$$\frac{\partial f_2}{\partial \Delta\lambda} = -\sqrt{\frac{2}{3}} \bar{A}_{\infty_{n+1}} c - \sqrt{\frac{2}{3}} \delta_{n+1} \left[ \bar{A}_{\infty_{n+1}} \left( 1 + c\varepsilon_n \right) - A_n \right] \exp\left( -\delta_{n+1} \sqrt{\frac{2}{3}} \Delta\lambda \right), \tag{B.29}$$

$$\frac{\partial f_3}{\partial \Delta\lambda} = -\sqrt{\frac{2}{3}} \frac{\xi_1}{\Delta t} \left[ \frac{1}{\Delta t} \left( \frac{\sqrt{\frac{2}{3}} \Delta\lambda - \Delta t \dot{\varepsilon}_{lwr}}{\dot{\varepsilon}_{up} - \dot{\varepsilon}_{lwr}} \right) \right]^{\xi_1 - 1} \left( \frac{\delta^{up} - \delta^{lwr}}{\dot{\varepsilon}_{up} - \dot{\varepsilon}_{lwr}} \right), \tag{B.30}$$

$$\frac{\partial f_4}{\partial \Delta\lambda} = \frac{\sqrt{\frac{2}{3}} \varepsilon_n}{\left( \sqrt{\frac{2}{3}} \Delta\lambda + \varepsilon_n \right)^2} \left( \bar{A}_{\infty_n} - A_{\infty_{n+1}} \right) - \left( 1 - \frac{\varepsilon_n}{\sqrt{\frac{2}{3}} \Delta\lambda + \varepsilon_n} \right) \frac{\partial A_{\infty_{n+1}}}{\partial \Delta\lambda}, \tag{B.31}$$

with

$$\frac{\partial A_{\infty_{n+1}}}{\partial \Delta\lambda} = \sqrt{\frac{2}{3}} \frac{\xi_2}{\Delta t} \left[ \frac{1}{\Delta t} \left( \frac{\sqrt{\frac{2}{3}} \Delta\lambda - \Delta t \dot{\varepsilon}_{lwr}}{\dot{\varepsilon}_{up} - \dot{\varepsilon}_{lwr}} \right) \right]^{\xi_2 - 1} \left( \frac{A_\infty^{up} - A_\infty^{lwr}}{\dot{\varepsilon}_{up} - \dot{\varepsilon}_{lwr}} \right), \tag{B.32}$$

$$\frac{\partial f_1}{\partial A_{n+1}} = -\sqrt{\frac{2}{3}} - \frac{\partial \bar{\Theta}^{-1}}{\partial A_{n+1}}, \quad \frac{\partial f_2}{\partial A_{n+1}} = 1, \quad \frac{\partial f_3}{\partial A_{n+1}} = 0, \quad \frac{\partial f_4}{\partial A_{n+1}} = 0, \tag{B.33}$$

$$\frac{\partial f_1}{\partial \delta_{n+1}} = 0, \quad \frac{\partial f_3}{\partial \delta_{n+1}} = 1, \quad \frac{\partial f_4}{\partial \delta_{n+1}} = 0 \tag{B.34}$$

$$\frac{\partial f_2}{\partial \delta_{n+1}} = \left[ \bar{A}_{\infty_{n+1}} \left( 1 + c\varepsilon_n \right) - A_n \right] \sqrt{\frac{2}{3}} \Delta\lambda \exp\left( -\delta_{n+1} \sqrt{\frac{2}{3}} \Delta\lambda \right), \tag{B.35}$$

$$\frac{\partial f_1}{\partial \bar{A}_{\infty_{n+1}}} = 0, \quad \frac{\partial f_3}{\partial \bar{A}_{\infty_{n+1}}} = 0, \quad \frac{\partial f_4}{\partial \bar{A}_{\infty_{n+1}}} = 1, \tag{B.36}$$

$$\frac{\partial f_2}{\partial \bar{A}_{\infty_{n+1}}} = -c\sqrt{\frac{2}{3}}\Delta\lambda - (1 + c\varepsilon_n)\left[1 - \exp\left(-\delta_{n+1}\sqrt{\frac{2}{3}}\Delta\lambda\right)\right]. \tag{B.37}$$

From Eq. (3.102), the derivatives

$$\Theta^{-1}\left(\dot{\lambda}, A\right) = R\left[\left(1 + \vartheta_1\dot{\lambda}\right)^{\frac{1}{m}} + \vartheta_2\dot{\lambda} - 1\right]$$

$$\frac{\partial\bar{\Theta}^{-1}}{\partial\Delta\lambda} = \sqrt{\frac{2}{3}}\left(\sigma_y + A_{n+1}\right)\left[\frac{1}{m}\frac{\vartheta_1}{\Delta t}\left(1 + \vartheta_1\frac{\Delta\lambda}{\Delta t}\right)^{\frac{1}{m}-1} + \frac{\vartheta_2}{\Delta t}\right], \tag{B.38}$$

$$\frac{\partial\bar{\Theta}^{-1}}{\partial A_{n+1}} = \sqrt{\frac{2}{3}}\left[\left(1 + \vartheta_1\frac{\Delta\lambda}{\Delta t}\right)^{\frac{1}{m}} + \vartheta_2\frac{\Delta\lambda}{\Delta t} - 1\right] \tag{B.39}$$

are obtained.

## B.4 Consistent tangent operator

Evaluation of $\mathbb{D}^{vp}$ is obtained from linearization of Eqs. (5.64), (5.79), (5.81), (5.82), and (5.84), what yields

$$\boldsymbol{N}_{\bar{\boldsymbol{\tau}}_{n+1}} : d\bar{\boldsymbol{\tau}}_{n+1} + N_{A_{n+1}}dA_{n+1} = \frac{\partial\bar{\Theta}^{-1}}{\partial\Delta\lambda}d\left(\Delta\lambda\right) + \frac{\partial\bar{\Theta}^{-1}}{\partial A_{n+1}}dA_{n+1}, \tag{B.40}$$

$$d\boldsymbol{E}^{e}_{n+1} + d\left(\Delta\lambda\right)\boldsymbol{N}_{\bar{\boldsymbol{\tau}}_{n+1}} + \Delta\lambda\frac{\partial\boldsymbol{N}_{\bar{\boldsymbol{\tau}}_{n+1}}}{\partial\bar{\boldsymbol{\tau}}_{n+1}} : d\bar{\boldsymbol{\tau}}_{n+1} = d\boldsymbol{E}^{e^{trial}}_{n+1}, \tag{B.41}$$

$$\begin{aligned} dA_{n+1} \quad = \quad & \left[\left(1 + c\varepsilon_n\right)\left(1 - \varphi\right) + c\sqrt{\frac{2}{3}}\Delta\lambda\right]d\bar{A}_{\infty_{n+1}} + \ldots \\ \ldots + \quad & \sqrt{\frac{2}{3}}\left\{\delta_{n+1}\left[\bar{A}_{\infty_{n+1}}\left(1 + c\varepsilon_n\right) - A_n\right]\varphi + \bar{A}_{\infty_{n+1}}c\right\}d\left(\Delta\lambda\right) + \ldots \\ \ldots + \quad & \sqrt{\frac{2}{3}}\Delta\lambda\left[\bar{A}_{\infty_{n+1}}\left(1 + c\varepsilon_n\right) - A_n\right]\varphi d\delta_{n+1}, \end{aligned} \tag{B.42}$$

$$d\delta_{n+1} = \omega_1 d\left(\Delta\lambda\right), \tag{B.43}$$

and

$$d\bar{A}_{\infty_{n+1}} = \omega_2 d\left(\Delta\lambda\right), \tag{B.44}$$

where

$$\frac{\partial\boldsymbol{N}_{\bar{\boldsymbol{\tau}}_{n+1}}}{\partial\bar{\boldsymbol{\tau}}_{n+1}} = \frac{1}{\left\|\bar{\boldsymbol{\tau}}^{D}_{n+1}\right\|}\left(\mathbb{I} - \frac{1}{3}\boldsymbol{I}\otimes\boldsymbol{I} - \boldsymbol{N}_{\bar{\boldsymbol{\tau}}_{n+1}}\otimes\boldsymbol{N}_{\bar{\boldsymbol{\tau}}_{n+1}}\right), \tag{B.45}$$

$$N_{A_{n+1}} = \frac{\partial f_{n+1}}{\partial A_{n+1}} = -\sqrt{\frac{2}{3}}, \tag{B.46}$$

$$\varphi = \exp\left(-\delta_{n+1}\sqrt{\frac{2}{3}}\Delta\lambda\right), \tag{B.47}$$

$$\omega_1 = \sqrt{\frac{2}{3}}\frac{\xi_1}{\Delta t}\left(\frac{\delta^{up}-\delta^{lwr}}{\dot{\varepsilon}_{up}-\dot{\varepsilon}_{lwr}}\right)\left[\frac{1}{\Delta t}\left(\frac{\sqrt{\frac{2}{3}}\Delta\lambda - \Delta t\dot{\varepsilon}_{lwr}}{\dot{\varepsilon}_{up}-\dot{\varepsilon}_{lwr}}\right)\right]^{\xi_1-1}, \tag{B.48}$$

and

$$\omega_2 = \frac{\sqrt{\frac{2}{3}}\varepsilon_n}{\left(\sqrt{\frac{2}{3}}\Delta\lambda+\varepsilon_n\right)^2}\left(A_{\infty_{n+1}} - \bar{A}_{\infty_n}\right) + \left(1 - \frac{\varepsilon_n}{\sqrt{\frac{2}{3}}\Delta\lambda+\varepsilon_n}\right)\frac{\partial A_{\infty_{n+1}}}{\partial\Delta\lambda}, \tag{B.49}$$

in which $A_{\infty_{n+1}}$ is given in Eq. (5.84) and $\frac{\partial A_{\infty_{n+1}}}{\partial\Delta\lambda}$ in Eq. (B.32). Combining Eqs. (B.42), (B.43), and (B.44) reads to

$$dA_{n+1} = \Lambda d\left(\Delta\lambda\right), \tag{B.50}$$

where

$$\begin{aligned}
\Lambda \quad &= \quad \sqrt{\frac{2}{3}}\left\{\delta_{n+1}\left[\bar{A}_{\infty_{n+1}}\left(1+c\varepsilon_n\right) - A_n\right]\varphi + \bar{A}_{\infty_{n+1}}c\right\} + \ldots \\
&\ldots + \quad \sqrt{\frac{2}{3}}\Delta\lambda\left[\bar{A}_{\infty_{n+1}}\left(1+c\varepsilon_n\right) - A_n\right]\varphi\omega_1 + \ldots \qquad \text{(B.51)} \\
&\ldots + \quad \left[\left(1+c\varepsilon_n\right)\left(1-\varphi\right) + c\sqrt{\frac{2}{3}}\Delta\lambda\right]\omega_2. \qquad \text{(B.52)}
\end{aligned}$$

Inserting Eq. (B.50) into Eq. (B.40) reads

$$\boldsymbol{N}_{\bar{\boldsymbol{\tau}}_{n+1}} : d\bar{\boldsymbol{\tau}}_{n+1} = \left[\frac{\partial\bar{\Theta}^{-1}}{\partial\Delta\lambda} + \left(\frac{\partial\bar{\Theta}^{-1}}{\partial A_{n+1}} - N_{A_{n+1}}\right)\Lambda\right] d\left(\Delta\lambda\right)$$

$$d\left(\Delta\lambda\right) = \frac{1}{\chi}\boldsymbol{N}_{\bar{\boldsymbol{\tau}}_{n+1}} : d\bar{\boldsymbol{\tau}}_{n+1}, \tag{B.53}$$

where

$$\chi = \left[\frac{\partial\bar{\Theta}^{-1}}{\partial\Delta\lambda} + \left(\frac{\partial\bar{\Theta}^{-1}}{\partial A_{n+1}} - N_{A_{n+1}}\right)\Lambda\right]. \tag{B.54}$$

Substitution of Eq. (B.53) into Eq. (B.41) provides

$$d\boldsymbol{E}^e_{n+1} + \left(\frac{1}{\chi}\boldsymbol{N}_{\bar{\boldsymbol{\tau}}_{n+1}} : d\bar{\boldsymbol{\tau}}_{n+1}\right)\boldsymbol{N}_{\bar{\boldsymbol{\tau}}_{n+1}} + \Delta\lambda\frac{\partial\boldsymbol{N}_{\bar{\boldsymbol{\tau}}_{n+1}}}{\partial\bar{\boldsymbol{\tau}}_{n+1}} : d\bar{\boldsymbol{\tau}}_{n+1} = d\boldsymbol{E}^{e^{trial}}_{n+1}. \tag{B.55}$$

Observing that $(\boldsymbol{A} \otimes \boldsymbol{G}) : \boldsymbol{K} = (\boldsymbol{G} : \boldsymbol{K})\, \boldsymbol{A}$, the above equation writes

$$d\boldsymbol{E}^{e}_{n+1} + \frac{1}{\chi}\left(\boldsymbol{N}_{\bar{\boldsymbol{\tau}}_{n+1}} \otimes \boldsymbol{N}_{\bar{\boldsymbol{\tau}}_{n+1}}\right) : d\bar{\boldsymbol{\tau}}_{n+1} + \Delta\lambda \frac{\partial \boldsymbol{N}_{\bar{\boldsymbol{\tau}}_{n+1}}}{\partial \bar{\boldsymbol{\tau}}_{n+1}} : d\bar{\boldsymbol{\tau}}_{n+1} = d\boldsymbol{E}^{e^{trial}}_{n+1}\,, \tag{B.56}$$

and from the elastic relationship $d\boldsymbol{E}^{e}_{n+1} = \mathbb{D}^{e^{-1}} : d\bar{\boldsymbol{\tau}}_{n+1}$ Eq. (B.56) can be rearranged as

$$\left(\mathbb{D}^{e^{-1}} + \Delta\lambda \frac{\partial \boldsymbol{N}_{\bar{\boldsymbol{\tau}}_{n+1}}}{\partial \bar{\boldsymbol{\tau}}_{n+1}}\right) : d\bar{\boldsymbol{\tau}}_{n+1} + \frac{1}{\chi}\left(\boldsymbol{N}_{\bar{\boldsymbol{\tau}}_{n+1}} \otimes \boldsymbol{N}_{\bar{\boldsymbol{\tau}}_{n+1}}\right) : d\bar{\boldsymbol{\tau}}_{n+1} = d\boldsymbol{E}^{e^{trial}}_{n+1}\,, \tag{B.57}$$

leading finally to

$$\mathbb{D}^{vp} = \frac{\partial \bar{\boldsymbol{\tau}}_{n+1}}{\partial \boldsymbol{E}^{e^{trial}}_{n+1}} = \left(\mathbb{D}^{e^{-1}} + \Delta\lambda \frac{\partial \boldsymbol{N}_{\bar{\boldsymbol{\tau}}_{n+1}}}{\partial \bar{\boldsymbol{\tau}}_{n+1}} + \frac{1}{\chi}\boldsymbol{N}_{\bar{\boldsymbol{\tau}}_{n+1}} \otimes \boldsymbol{N}_{\bar{\boldsymbol{\tau}}_{n+1}}\right)^{-1}. \tag{B.58}$$

## B.5 Qualitative analysis of compression tool under high strain-rate test

As one can readily observe in Figure 2.2, on one hand, the specimen is positioned on the superior part of the fixed platen. On the other hand, the load cell is assembled under this component. When using this tool considering *quasi*-static loadings, according to equilibrium conditions, the compression force employed on tested specimen is very close to that measured by the load cell. However, this fact can not be readily transported to high velocity compressions, in which dynamic effects due to impact and wave propagation are present. Thus, in order to qualitatively evaluate and compare the compression force applied to the work piece with that dynamically measured by the load cell, a finite element analysis on the compression apparatus considering a high velocity compression is performed. The analysis is conducted making use of software Abaqus explicit. Related model, showing assembled components, as well as employed boundary and initial conditions, is displayed in Figure B.1(a). Material, element type, number of elements employed to each component of Figure B.1 are informed in Table B.1. To the load cell a fictitious material endowed with equivalent elastic modulus ($E = 78\,\mathrm{GPa}$) and equivalent specific mass $\left(\rho_0 = 5273\,\frac{\mathrm{kg}}{\mathrm{m}^3}\right)$ was employed. This values were obtained in order to reproducing the stiffness and total mass of the load cell according to the manufacturer (*Kistler*).

In the present analysis, the specimen was modeled as a viscoplastic material employing the *Johnson-Cook* (JC) model available in Abaqus (see Abaqus manual). Model parameters were adjusted in order to represent the flow stress-strain curves of Figure 2.11(a), what, considering an isothermal analysis, has provided the following JC model constants: $A = 41\,\mathrm{MPa}$, $B = 104\,\mathrm{MPa}$, $n = 0.5543$, and $m = 1$. Contact model and friction parameters used are given in Table B.2. The analysis consists of prescribing an initial velocity of $v_0 = 25\,\frac{\mathrm{m}}{\mathrm{s}}$ to the striker bar, which hits the movable platen, and thus performing the specimen compression. This bar velocity produces a strain-rate of $\approx 4.0 \times 10^3\,\mathrm{s}^{-1}$ on the

Table B.1: Material, element type, and number of elements used in each component. CAX4R refers to a linear quadrilateral element, with reduced integration, used in explicit analysis of Abaqus.

| Component | Material | $E$ [GPa] | $\nu$ [−] | $\rho_0$ $\left[\frac{\text{kg}}{\text{m}^3}\right]$ | Element type | Number of elements |
|---|---|---|---|---|---|---|
| 1 | Brass | 97 | 0.34 | 8500 | CAX4R | 380 |
| 2 | Steel | 200 | 0.3 | 7800 | CAX4R | 5206 |
| 3 | Aluminum | 70 | 0.33 | 2700 | CAX4R | 1800 |
| 4 | Steel | 200 | 0.3 | 7800 | CAX4R | 2330 |
| 5 | Fictitious | 78 | 0.3 | 5273 | CAX4R | 5500 |
| 6 | Steel | 200 | 0.3 | 7800 | CAX4R | 2525 |
| 7 | Steel | 200 | 0.3 | 7800 | CAX4R | 6200 |

Table B.2: Model and friction data used in each contact interface.

| Contact interface | Model | Friction coefficient | Penalty setting |
|---|---|---|---|
| A | Coulomb | Frictionless | Default |
| B | Coulomb | 0.3 | Default |
| C | Coulomb | 0.1 | Default |
| D | Coulomb | 0.1 | Default |
| E | Coulomb | Frictionless | Default |
| F | Coulomb | Frictionless | Default |
| G | Coulomb | Frictionless | Default |

tested material. That velocity was chosen in order to evaluate the tested condition which produces major dynamic effects. The total time interval of the overall analysis is of 1 ms, and a nominal time increment of 1 $\mu$s was set. For this qualitative simulation, convergence criteria and parameters employed were those set by default in Abaqus explicit analysis.

The history associated with the displacement imposed on specimen due to impact is showed in Figure 2.11(d), where a *quasi*-constant displacement-rate is observed. For visualization purposes, both undeformed and deformed configurations are displayed respectively in Figures 2.11(b) and (c), where von Mises stress contours are displayed. In the last configuration, a displacement $\bar{u} \approx 2.4$ is prescribed on specimen, this condition would provide a homogeneous strain of $\varepsilon \approx 0.5$ in a frictionless simulation.

The present evaluation consists of comparing the contact force between the specimen and fixed platen (interface $D$) with that between the load cell and fixed platen (interface $E$), see Figure 2.2. It is worth remark that, in real experiment procedure, the compression displacement is measured directly on the specimen length (distance between interfaces $C$ and $D$), and the data of load is measured by the cell positioned under the fixed platen. During high velocity tests, there is a time delay between these two acquired data, as well as, between the contact forces of interfaces $D$ and $E$, what is shown in Figure B.2(a), where the time delay is 20 $\mu$s. This value corresponds to 16.67% of the compression

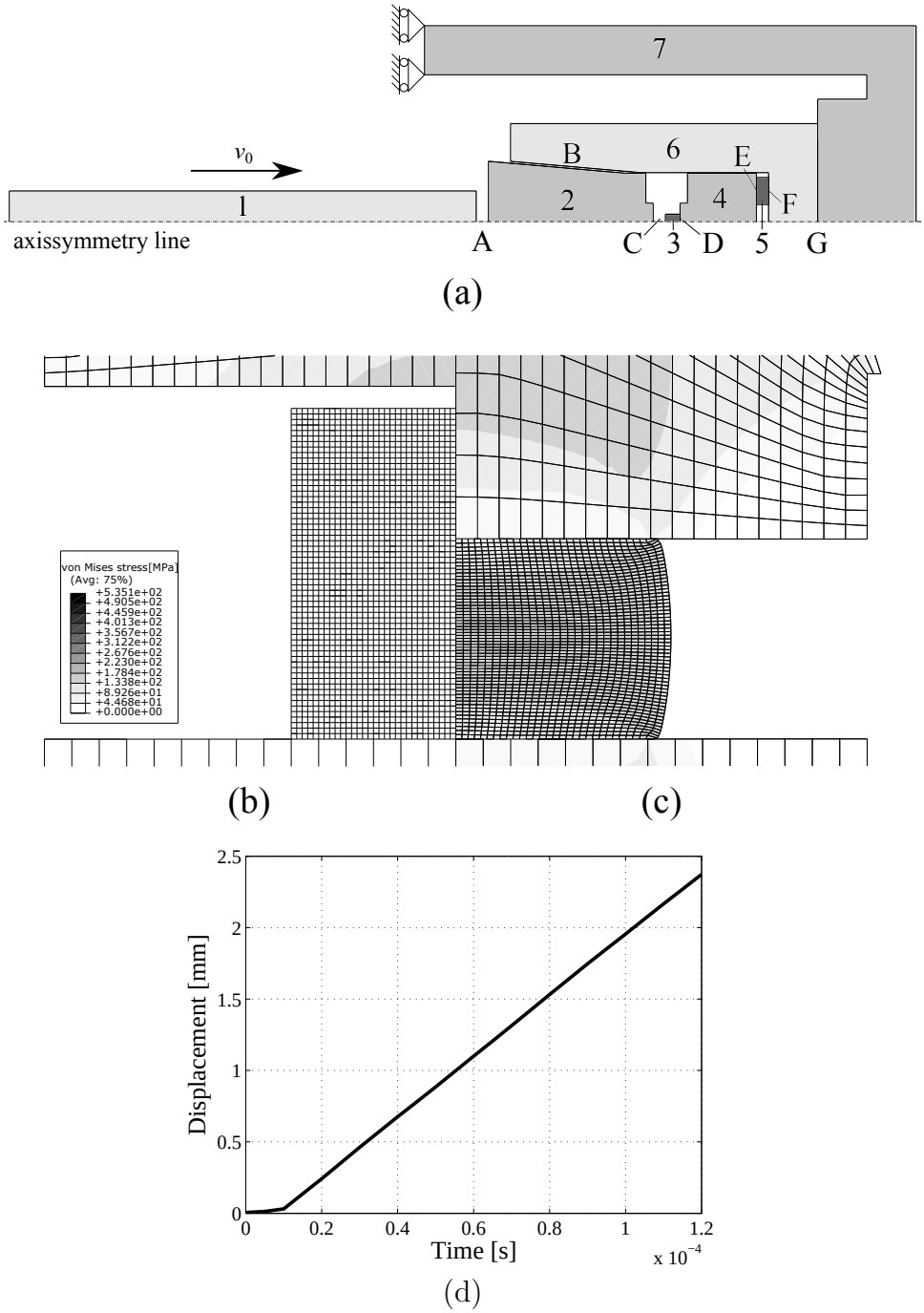


Figure B.1: (a) Simplified model, initial and boundary conditions used for qualitative analysis of compression tool considering dynamic conditions. Detail of specimen in (b) undeformed and (c) deformed ($\bar{u} \approx 2.4$) configurations. (d) Numerical time history of prescribed displacement.

time interval of $120\,\mu$s. Thus, in order to establish a force-displacement relationship from measured experimental data, a correction due to this time delay must be considered. Comparisons between these two contact forces, considering this time correction, are performed in Figures B.2(b) and (c), where force-time and force-displacement data are respectively displayed. For comparison purposes, the experimental curve of Figure 2.11(a)

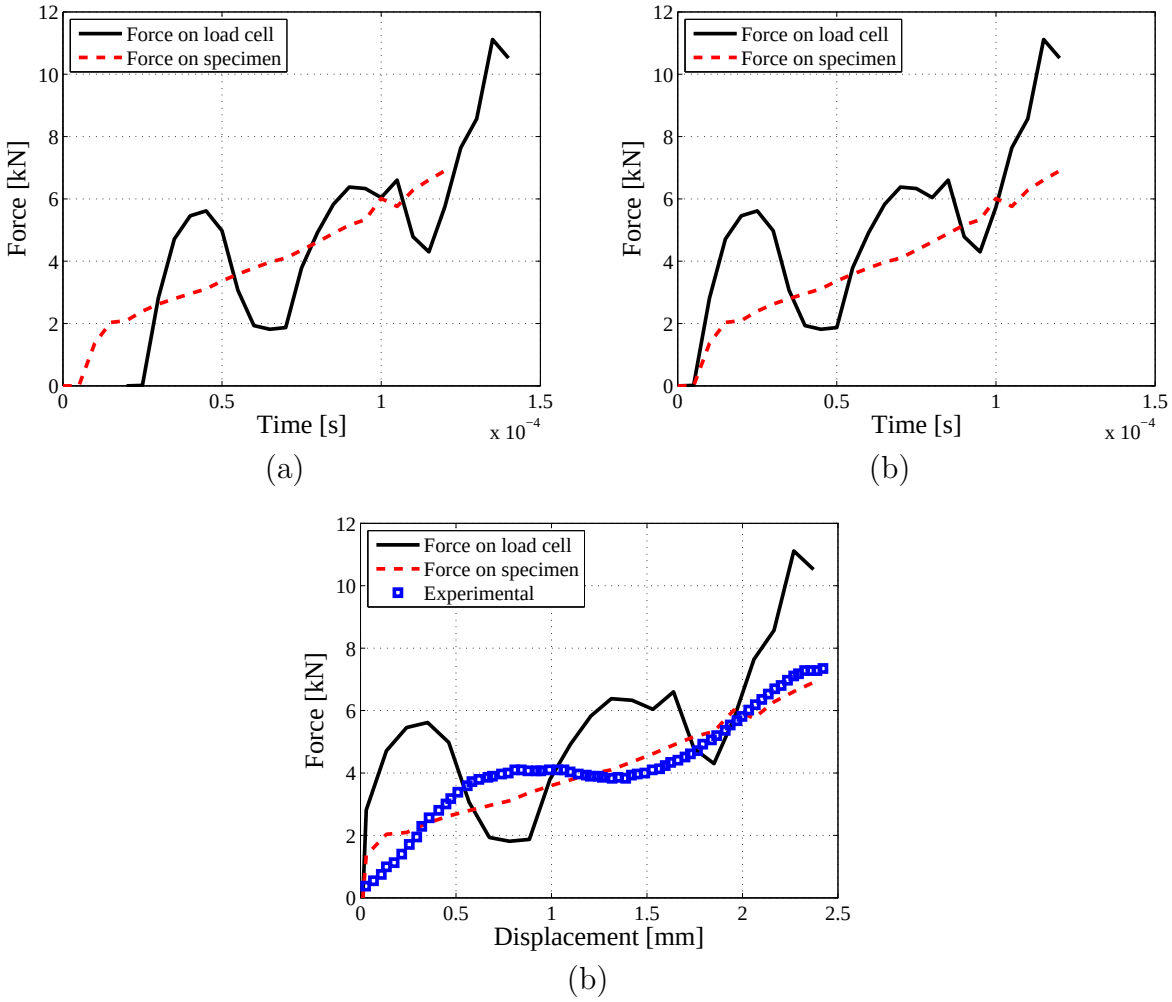


Figure B.2: Numerical comparison between contact forces of interfaces $D$ (force on specimen) and $E$ (force on load cell): (a) Force vs. time curves without time delay correction. (b) Force vs. time with time delay correction; (c) Force vs. displacement curved with time delay correction.

for the strain-rate of $4.0 \times 10^3\,\mathrm{s}^{-1}$ is also plotted. From results, although consisting of a qualitative analysis, one can observe that, despite the oscillation associated with contact force of interface $E$, in an average way there is a good correlation between the contact forces analyzed. Therefore, within the time and displacement ranges considered herein, one concludes that measuring the load data right after the fixed platen, instead of directly on the specimen position, once a suitable time correction is carried out, does not causes major errors in the desired experimental information.